NASA Conference Publication 2138

Heterodyne Systems and Technology

Part II

Proceedings of an
international conference
held at Williamsburg, Virginia
March 25-27, 1980

NASA

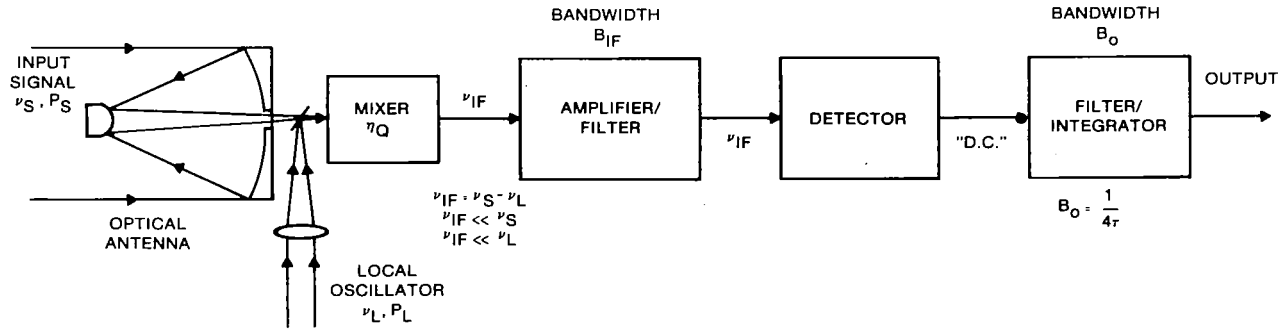

Figure 1.- Block diagram of a representative heterodyne receiver.

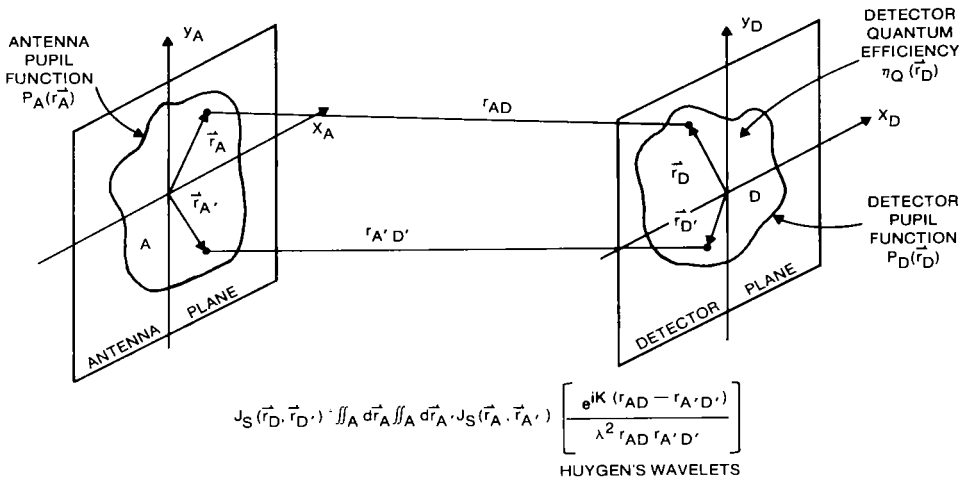

Figure 2.- Huygen's wavelet model for propagation of the mutual intensity function between the antenna and mixer plane.

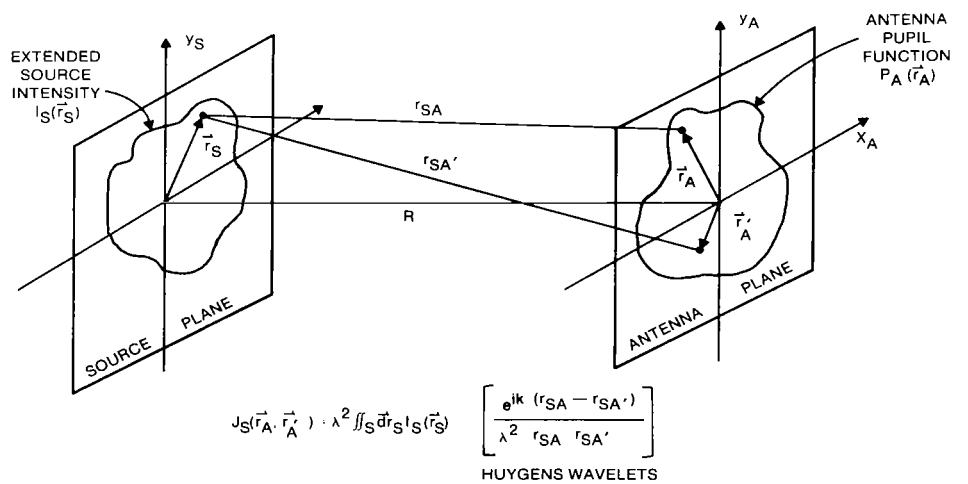

Figure 3.- Huygen's wavelet model for propagation of the mutual intensity from an extended incoherent source.

ERRATA

NASA Conference Publication-2138, Part 2

HETERODYNE SYSTEMS AND TECHNOLOGY

Paper 33 - DESIGN CONSIDERATIONS FOR OPTICAL HETERODYNE RECEIVERS: A REVIEW

BY John J. Degnan

Page 484: Figures 2 and 3 were inadvertently interchanged. Replace page 484 with the corrected page.

NASA Conference Publication 2138

Heterodyne Systems and Technology

Part II

Proceedings of an
international conference
held at Williamsburg, Virginia
March 25-27, 1980

NASA
National Aeronautics
and Space Administration

**Scientific and Technical
Information Branch**

1980

PREFACE

The proceedings of the International Conference on Heterodyne Systems and Technology held in Williamsburg, Virginia March 25-27, 1980, are reported in this NASA Conference Publication. This conference was sponsored by the National Aeronautics and Space Administration.

The conference was the first of its kind, bringing together technologists, systems engineers, and applications scientists to exchange technical information on all aspects of optical heterodyning. Topics covered various aspects of heterodyning throughout the electromagnetic spectrum including detectors, local oscillators, tunable diode lasers, astronomical systems, and environmental sensors, with both active and passive systems represented.

The conference organization consisted of a General Program Chairman, Robert H. Kingston of M.I.T. Lincoln Laboratory, and a Program Committee whose members are listed for reference elsewhere in these proceedings. The conference organizers were Stephen J. Katzberg and James M. Hoell; the conference coordinator was Patricia Hurt. Conference support was led by Jane T. Everett with assistance from Vivian Parrous and Sheila A. Armstrong, all from Langley Research Center.

Stephen J. Katzberg
James M. Hoell

Conference Cochairmen

FOREWORD

Robert H. Kingston
Lincoln Laboratory, Massachusetts Institute of Technology
Lexington, Massachusetts 02173

heterodyne - (hetero + dyne) - separate force

superheterodyne - (super(sonic) + heterodyne)

To introduce the proceedings of this conference, it is interesting to review the origin of the above two words and trace the early history of heterodyne systems up to the first optical heterodyne experiment of 1955. The story begins in 1902 with the issue of a patent to Fessenden with the simple title, Wireless Signaling (1). The invention was the concept of transmitting two separate radio frequencies, receiving the same on two separate antennas and mixing the two to produce an audio frequency. The "mixer" in this case was an iron-core coil driving a telephone diaphragm, and the deflection was proportional to electrical power, thus yielding acoustic output at the difference frequency. A curious and ironic phrase in the patent reads: "By the term 'electromagnetic waves' as used herein is meant electromagnetic waves long in period compared with that are called 'heat-waves' or 'radiant heat'."

It is not clear when the term "heterodyne" was coined, but we find a paper by Hogan (2) in 1913 with the title "The heterodyne receiving system, and notes on the recent Arlington-Salem tests." One section of this paper is particularly significant as it reads, "It is evident that an economy may be brought about by transmitting only one wave and generating the second frequency at the receiving station." And thus came the birth of the local oscillator; "The heterodyne...is seen to consist of a standard receiving set associated with a local generating circuit by means of an inductive coupler. The generator G may be an alternator...which is a 2 K.W. machine capable of generating frequencies up to 100,000 cycles per second." This is probably a record value for local oscillator power, radio or optical. Unfortunately, this first heterodyne system was adequate for c.w. or Morse code signals, but seriously distorted voice communications.

The next step in the development of the heterodyne technique was taken by Armstrong, later the inventor and developer of f.m. broadcasting. During World War I, as a member of the U.S. Army Signal Corps, he devised a technique for receiving and separating signals over a wide range of radio frequencies using a modification of the heterodyne principle. To quote from his 1921 paper (3): "This expedient consists in reducing the frequency of the incoming signal to some predetermined super-audible frequency which can be readily amplified, passing this current through an amplifier, and then detecting or rectifying the amplified current." Thus came the superheterodyne, supersonic being the pre-jet age version of ultrasonic. In a technical discussion still valid today, Armstrong points out the difficulties of r.f. amplification (poor vacuum tube amplifiers) and the difficulties of audio amplification (poor local oscillator stability and high tube noise at audio frequencies). Armstrong's invention was

in response to the problem which he proposed at the beginning of this paper: "The problem may be summed up in the following words -- to construct a receiver for undamped, modulated continuous, and damped oscillations which is substantially equally sensitive over a range of wavelengths from 50 to 600 meters, which is capable of rapid adjustment from one wave to another, and which does not distort or lose any characteristic note or tone inherent in the transmitter." By this time, the mixers were diode rectifiers or vacuum tubes and, since the early thirties, the superheterodyne has been the standard method of radio wave reception.

The next two steps which led to the development of heterodyne systems from the sub-millimeter to the visible occurred in 1955 and 1960. First, Forrester, Gudmundsen, and Johnson (4) demonstrated photoelectric mixing of the Zeeman components of a mercury emission line thus establishing the feasibility of optical heterodyning. Then, in 1960, Maiman (5) gave the first demonstration of optical maser or laser action, thus giving promise of a local oscillator and mixer which in Armstrong's words could "reduce the frequency of the incoming signal to some predetermined super-audible (!) frequency which can be readily amplified."

The papers in these proceedings take up the story from there. The applications are of course much broader than simple signal reception and include spectroscopy, radiometry, communications, and radar. The critical technologies are the design and fabrication of local oscillators and detectors. We are all indebted to the staff of NASA Langley Research Center for initiating and organizing the conference and for the preparation of these proceedings, the first such work devoted exclusively to the exciting field of heterodyne systems at <u>really</u> short wavelengths.

REFERENCES

1. U. S. Patent No,. 706, 740, August 12, 1902.

2. J. L. Hogan, Jr., Proc. I.R.E., <u>1</u>, 75, (1913).

3. E. H. Armstrong, Proc. I.R.E., <u>9</u>, 3, (1921).

4. Forrester, Gudmundsen, and Johnson, Phys. Rev., <u>99</u>, 1691, (1955).

5. T, H,. Maiman, Nature, <u>187</u>, 493, (1960).

CONTENTS

Part 1*

*Papers 1 to 19 are presented under separate cover.

Part 2

SESSION IV - DETECTORS
Chairman: David Spears

SESSION V - LOCAL OSCILLATORS B
Chairman: Aram Mooradian

SESSION VI - COHERENT APPLICATIONS
Chairman: Frank Goodwin

CORRESPONDENCE

n-p (Hg,Cd)Te PHOTODIODES FOR 8-14 MICROMETER HETERODYNE APPLICATIONS

J.F. Shanley and C.T. Flanagan

Honeywell Electro-Optics Center
2 Forbes Road
Lexington, Massachusetts 02173

ABSTRACT

This paper presents experimental results describing the dc and CO_2 laser heterodyne characteristics of a three element n^+-p $Hg_{0.8}Cd_{0.2}Te$ photodiode array and single element and four element n^+-n^--p $Hg_{0.8}Cd_{0.2}Te$ photodiode arrays. The measured data shows that the n^+-p configuration is capable of achieving bandwidths of 475 to 725 MHz and noise equivalent powers of 3.2×10^{-20}W/Hz at 77 K and 1.0×10^{-19}W/Hz at 145 K. The n^+-n^--p photodiodes exhibited wide bandwidths ($\sim$2.0 GHz) and fairly good effective heterodyne quantum efficiencies ($\sim$13-30% at 2.0 GHz). Noise equivalent powers ranging from 1.44×10^{-19}W/Hz to 6.23×10^{-20}W/Hz were measured at 2.0 GHz.

INTRODUCTION

Infrared heterodyne detection as a means of detecting weak signals is useful in many systems applications, such as remote sensing, communications, optical radar range finders, battlefield surveillance, velocity and turbulence measurements and infrared astronomy. Infrared heterodyne receivers which utilize (Hg,Cd)Te photodiodes in a 10.6μm CO_2 laser heterodyne application have been developed for use in these systems. There are two (Hg,Cd)Te photodiode structures which have been designed to meet the needs of various heterodyne applications: the n^+-p photodiode and the n^+-n^--p photodiode.[1-5]

The n^+-p (Hg,Cd)Te photodiode structure was initially designed for use in direct detection systems, and hence, the device detectivity has been optimized.[3-5] There are a number of CO_2 laser heterodyne system applications which require moderate bandwidths ($\sim$500 MHz) and elevated temperature operation ($T \gtrsim 120$ K). The n^+-p photodiode structure is optimum for elevated temperature operation since it is capable of attaining fairly low saturation currents.

It is very difficult to operate n^+-n^--p (Hg,Cd)Te photodiodes at temperatures greater than 110 K due to the low carrier concentration (near intrinsic) contained in the n^--layer. However, the advent of techniques for ultrawideband modulation of CO_2 laser transmitter signals and the requirement to handle large Doppler frequency offsets has created the need for extending the IF bandwidth performance of infrared receivers to at least 2.0 GHz. The n^+-n^--p (Hg,Cd)Te photodiodes are ideally suited for such applications since they are capable of attaining large IF bandwidths.

This paper presents results pertaining to the two diode structures. The n^+-p photodiode attained heterodyne signal frequency response of 475 - 675 MHz at a temperature of 145 K. Also, the n^+-n^--p photodiode demonstrated bandwidths of 2000 MHz when operated in a heterodyne mode at a temperature of 77 K.

HETERODYNE FIGURE OF MERIT

The noise equivalent power (NEP) offers a very convenient figure of merit for evaluating the heterodyne performance of a (Hg,Cd)Te photodiode. The NEP is defined as the incident signal power that must be detected in order to give a signal-to-noise ratio (SNR) of 1.0 in a bandwidth of 1.0 Hz. The NEP per unit bandwidth for an n-p (Hg,Cd)Te photodiode is given by the following expression:

$$\frac{NEP}{B} = \frac{h\nu}{\eta q}\left\{1 + \frac{I_{SAT}}{I_{LO}} + \frac{2k(Tm + T_{IF})}{qI_{LO}}\left(G_D(1+G_DR_S) + \omega^2C^2R_S\right)\right\} \quad (1)$$

where I_{LO} is the laser local oscillator induced current which is related to the incident laser power through the expression:

$$I_{LO} = \frac{h\nu}{\eta q} P_{LO}. \quad (2)$$

where h is Planck's constant, ν is frequency, q is the electron charge, and η is the dc quantum efficiency.

The last two terms in equation (1) establish the criteria for determining the trade-off between the fractional degradation in NEP as a function of the local oscillator power, using the following quantities as parameters:

- The device equivalent circuit parameters (G_D the shunt conductance, R_S the series resistance, and C_D the junction capacitance),
- The photodiode saturation current (I_{SAT}),
- The physical temperature of the photodiode (T_M),
- The device quantum efficiency (η),
- The IF preamplifier characteristics (T_{IF} the equivalent preamplifier noise temperature).

It is instructive to recast equation (1) by defining a minimum detectable signal power $P_{min} = h\nu/\eta q$, an available thermal noise power,

$$P_{th} = 4k(T_m + T_{IF})B$$

and an available shot noise power,

$$P_{sh} = 2qI_{LO}B/\left(G_D\ (1 + G_D R_S) + \omega^2 C_D{}^2 R_S\right)$$

The NEP can then be written as:

$$\frac{NEP}{B} = P_{min}\left(1 + \frac{I_{SAT}}{I_{LO}} + \frac{P_{th}}{P_{sh}}\right) \qquad (3)$$

In order for the NEP to approach the theoretical limit (P_{min}) the photodiode must be operated under the following conditions:

1. $I_{LO} \gg I_{SAT}$
2. $P_{sh} \gg P_{th}$

For the best heterodyne detection sensitivity, the local oscillator induced current (I_{LO}) is fixed so that the shot noise dominates the thermal noise and the photo-induced current dominates the saturation current so that:

$$\frac{NEP}{B} \approx P_{min} = \frac{h\nu}{\eta q} \qquad (4)$$

Under these conditions the device sensitivity is only limited by the dc quantum efficiency. In reality it is very difficult to adjust the incident local oscillator so that it completely dominates the shot noise and the saturation current. Therefore, the observed NEP is

$$\frac{NEP}{B} = \frac{h\nu}{q\eta_{EH}}$$

where the effective heterodyne quantum efficiency η_{EH} includes the effects contributed by the bracketed term in equation (1). The effective heterodyne

quantum efficiency is, thus, a figure-of-merit which describes quantitatively how closely a given infrared heterodyne receiver (i.e., the (Hg,Cd)Te photodiode and amplifier combination) approaches the maximum theoretical efficiency, i.e., η_{EH} = 100% which corresponds to the quantum noise limited NEP of 1.87 X 10^{-20} W/Hz at a wavelength of 10.6 micrometers.

The (Hg,Cd)Te photodiode device parameters (I_{SAT},G_D,R_S, and C_D)are also very important quantities which must be considered in order to optimize the effective heterodyne quantum efficiency. The ideal (Hg,Cd)Te heterodyne photodiode is one in which the thermally generated detector noise is minimized. This means that the saturation current must be limited to very small values by choosing the (Hg,Cd)Te material with the longest possible minority carrier lifetime and the detector configuration with the smallest volume for thermal generation of electron-hole pairs. Thus, if the saturation current is minimized then moderate levels ($\sim$500 microwatts) of local oscillator power are required to overcome the effects of the thermally generated detector noise (I_{SAT}).

Finally, it is noted that the laser induced shot noise power is dependent upon the photodiode shunt conductance, series resistance, and junction capacitance. The maximum shot noise power is obtained when the device possesses a low series resistance ($\backsim$ 5 to 10 ohms), a low capacitance ($\backsim$ 1.0 to 2.0 pF) and a low shunt conductance ($\backsim$ 1.0 X 10^{-3} to 2 X 10^{-4} mhos). Therefore, in designing the best n-p (Hg,Cd)Te photodiode structure it is necessary to reduce the thermal noise contribution to as low a value as is possible and to minimize the G_D, R_S, and C_D parameters.

THE n^+-p $Hg_{0.8}Cd_{0.2}Te$ PHOTODIODE

The n^+-p photodiode structure possesses low saturation currents because the doping levels in the n and p regions are chosen such that the width of the depletion region is reduced. This, in effect, minimizes the generation-recombination current contributed by the depletion layer. The thermal diffusion current from the n-region is minimized by fabricating a fairly thin n^+-layer

(0.3 to 0.7 micrometers). Therefore, the p-region is the primary source of the saturation current. Reducing the volume of the p-region will also help minimize the thermal diffusion current from the p-side. The bandwidth of the n^+-p photodiode is determined by the lifetime of the minority carriers (electrons) diffusing to the junction from the p-region. This implies that the bandwidth of the n^+-p device will be smaller than the n^+-n^--p device since the bandwidth of the n^+-n^--p device is RC limited and the primary collection mechanism is due to the electric field in the depletion region. However, in order to achieve (Hg,Cd)Te photodiodes that are capable of high sensitivity heterodyne detection at elevated temperatures, one must pay the penalty of loss in bandwidth.

Planar processing techniques were used to fabricate the n^+-junctions on a substrate of copper doped p-type ($N_A \backsim 2.0 \times 10^{16} cm^{-3}$) $Hg_{0.8}Cd_{0.2}Te$. The high carrier n^+ layer ($N_D \backsim 1.0 \times 10^{-18} cm^{-3}$) was achieved by the ion implantation of boron, a slowly diffusing donor species, into the p-type substrate. A double boron ion implantation was employed to achieve n^+-junction depths of approximately 0.3 to 0.7 micrometers. The ions were implanted into photolithographically defined areas and the wafers were then subjected to post-implant thermal anneals. The anneals, which reduce implant induced damage that will mask the electrical activity of the impurity species,[4,5] were performed in a reducing atmosphere of forming gas at temperatures ranging from 125 to 175°C with durations of one to three hours.

Front and backside contacts were made subsequent to the post-implant anneals. A thin gold layer was used for the backside contact. Upon completion of the fabrication procedure, the (Hg,Cd)Te wafer was then diced into chips which were then individually affixed to a high frequency mounting structure.

The characterization of the n^+-p photodiode is made through the use of dc characteristics (I-V characteristics, spectral response, and capacitance-voltage measurements) and shot noise and blackbody heterodyne radiometry measurements. The data obtained from these measurements is presented in Table 1.

The current-voltage (I-V) characteristics of the n^+-p $Hg_{0.8}Cd_{0.2}Te$ photodiodes were measured at 77 K and 145 K. The devices exhibited forward resistances of approximately 20 to 40 ohms at both temperatures, and the zero bias resistance was found to vary from 75 to 7000 ohms at 77 K, while at 145 K the zero bias resistance ranged from 30 to 250 ohms. The breakdown voltage, defined to be that voltage at which 1.0 mA of excess reverse current flows in the junction, varied from approximately 0.20 to 0.75 volts at 77 K and from 0.06 to 1.30 volts at 145 K. Figure 1 shows the current-voltage characteristic of element one of the three element array. Spectral response measurements revealed that the photodiodes possessed cutoff wavelengths of approximately 10.31 to 14.1 micrometers and 8.89 to 11.4 micrometers at 77 K and 145 K, respectively.

Blackbody measurements were performed at a frequency of 1.0 kHz to measure the dC quantum efficiencies of the devices. The result of these measurements are shown in Table 1. The devices are seen to exhibit dC quantum efficiencies ranging from 73% to 78%.

Capacitance-voltage measurements were performed on the three elements of the array; the results of the measurements on element one are shown in Figure 2, where a graph of $1/C^2$ versus the reverse bias voltage at 77 K is presented. The straight line plot reveals that the n^+-p junction is abrupt (i.e. $N_D >> N_A$). The net acceptor concentrations in the p-regions of the array were determined from the line slopes to vary from 1.0×10^{16} to 3.1×10^{16} cm^{-3}. This result is consistent with the initial copper concentration ($N_A \sim 2.0 \times 10^{16}$ cm^{-3}) that was introduced during the growth of the p-type $Hg_{0.8}Cd_{0.2}Te$. In addition, Hall measurements performed at 77 K yielded acceptor concentrations of approximately 1.5×10^{16} to 3.4×10^{16} cm^{-3}.

Shot noise and blackbody heterodyne radiometry techniques were used to measure the n^+-p photodiode's frequency response and noise equivalent power (NEP).[1,2,6,7] The measurements were made with a low noise wide bandwidth preamplifier which possessed a net gain of approximately 35 dB, a noise figure of 2.5 dB, and a bandwidth of 5 to 1000 MHz. The shot-noise frequency response was measured by illuminating the photodiode's active area with sufficient chopped CO_2 laser power to overcome the thermal noise. The shot noise spectrum

was determined by slowly scanning a spectrum analyzer over the induced shot noise and synchronously detecting the chopped signal by connecting a lock-in amplifier to the vertical output of the spectrum analyzer.

The measured shot noise frequency response of the n^+-p photodiode array ranged from 581 to 820 MHz for incident CO_2 laser power levels of 175 to 300 microwatts at 77 K and 145 K. The response did not vary as a function of device temperature.

The heterodyne frequency response and sensitivity (represented by either the noise equivalent power, NEP, or the effective heterodyne quantum efficiency, η_{EH}) were measured using the experimental configuration illustrated in Figure 3. A blackbody source (T = 1000 K) beats against the CO_2 laser local oscillator source. The local oscillator power is adjusted so that the shot noise dominates the thermal noise in the receiver. By measuring the signal-to-noise ratio (SNR), the effective heterodyne quantum efficiency can be calculated from the following expression:

$$SNR = 2\eta_{EH}(B\tau)^{\frac{1}{2}} \chi \left[\frac{\varepsilon_{BB}}{\exp(h\nu/kT_{BB}) - 1} - \frac{\varepsilon_r}{\exp(h\nu/kT_r) - 1} \right] \qquad (5)$$

where τ is the post detection integration time, B is the IF bandwidth, χ is the optics transmission factor, T_{BB} and T_r are the blackbody and reference temperatures and ε_{BB} and ε_r are the emissivities of the blackbody and reference.

Figure 4 presents the heterodyne frequency response for element one measured at 145 K. It is seen to be flat to approximately 600 MHz. The right side of Table 1 presents a summary of the heterodyne properties of the three element n^+-p photodiode array. It also lists the operating points (i.e., reverse bias voltage, capacitance and dark current at the bias voltage, and incident CO_2 laser power) at which the heterodyne measurements were made. The data clearly indicates that it is possible to operate the n^+-p photodiode in the heterodyne mode and to obtain moderate bandwidth (475 - 725 MHz) and fairly good sensitivities, $\eta_{EH} \sim 58\%$ and $\eta_{EH} \sim 19\%$, at 77 K and 145 K, respectively.

THE n^+n^--p $(Hg_{0.8}Cd_{0.2})Te$ PHOTODIODE

The n-i-p photodiode is the optimum (Hg,Cd)Te device structure for use as a high speed, i.e., wide bandwidth, CO_2 laser heterodyne detector of infrared radiation.[8,9] The device consists of a slab of nearly intrinsic "i" semiconductor, bounded on one side by a relatively thin layer of very heavily doped n-type material and on the other side by a relatively thick layer of heavily doped p-type semiconductor material. Ohmic contacts to the heavily doped regions serve as a means of applying sufficient dc reverse bias voltage to the structure so that the depletion layer of the junction spreads out to occupy the entire intrinsic or lightly doped n-volume. This volume then becomes a region of high and nearly constant electric field, a region which is swept free of electron-hole pairs, and one which constitutes the active volume of the device.[10,11]

Absorption of infrared radiation in the semiconductor produces electron-hole pairs that are either collected by the drift (electric field) or diffusion mechanism. For high speed devices, the drift mechanism must dominate since the diffusion mechanism only serves to limit the heterodyne device's high frequency sensitivity. For maximum collection efficiency, the intrinsic region must be tailored to be $2/\alpha$ thick, where α is the absorption coefficient of the incident infrared radiation. Thus, diffusion of carriers from the p-side of the junction is minimized by proper placement of the i region below the surface.

In practice, it is very difficult to achieve the idealized intrinsic layer in most semiconductors, i.e., silicon, gallium arsenide, mercury cadmium telluride, etc. Therefore, the "i" region is approximated by either a lightly doped n-layer or a lightly doped p-layer.[8] It is because of the low doping in the i region that most of the potential drop appears across this region. The n^+-n^--p photodiode is the best (Hg,Cd)Te device structure for wide bandwidth CO2 laser heterodyne applications since this configuration is analogous to the n-i-p photodiode.

Planar processing techniques were used to fabricate the lightly doped n^- layers (active area is 1.8×10^{-4} cm^2) on a substrate of p-type ($N_A \sim 1.0 \times 10^{17}$ cm^{-3}) $Hg_{0.8}Cd_{0.2}Te$.[1,2] The substrates are initially doped with a net donor concentration of approximately 1.0×10^{14} cm^{-3}. A mercury diffusion process which compensates the non-stoichiometric defects, presumably mercury vacancies, in the p-type substrate is employed to convert a surface layer of the p-type material to n-type material. Annealing in a mercury atmosphere allows mercury to diffuse into the p-type substrate and this results in the annihilation of the mercury vacancies, thereby allowing the residual donor impurities already present in the substrate to predominate. A shallow n^+-layer ($N_D \sim 5 \times 10^{17}$ to 1.0×10^{18} cm^{-3}) was applied to the surface of n-layer in order to reduce the device's series resistance.

I-V characteristics measured on the n^+-n^--p photodiodes revealed forward resistances of approximately 10 to 35 ohms and zero bias resistances of 180 to 5000 ohms. The breakdown voltage ranged from 630 to 2250 mV for devices possessing cutoff wavelengths of 10.88 to 12.5 micrometers.

C-V measurements were performed on the n^+-n^--p devices and plots of $1/C^2$ versus the reverse bias voltage have resulted in a straight-line behavior. This indicates that the mercury diffusion process creates a one-sided abrupt junction ($N_A >> N_D$). A least square fit applied to the $1/C^2$ data yielded a net donor concentration of approximately 1.1×10^{14} to 1.0×10^{15} cm^{-3} in the n^- layer. The donor concentrations measured by the C-V technique are consistent with the initial donor concentrations that were introduced during the growth of the p-type $(Hg_{0.8}Cd_{0.2})Te$.

Blackbody measurements performed at a frequency of 1 kHz resulted in dC quantum efficiencies ranging from 34% to 65%. The n^+-n^--p photodiodes did not possess anti-reflection coatings on their active areas.

The shot noise and blackbody heterodyne radiometry techniques already discussed were used to characterize the n^+-n^--p photodiode. The results of the shot-noise measurements indicated that many of the photodiodes tested had frequency responses that were flat to 2.0 GHz; no sign of the RC roll-off was

present at this frequency. However, the frequency response was observed to be a function of the applied reverse bias voltage. Increasing the reverse bias voltage increases the depletion width and, hence, reduces the device capacitance. Since the photodiode shot-noise frequency response is RC limited, reducing the capacitance results in increasing the device frequency response.

The shot-noise frequency response of an n^+-n^--p (Hg,Cd)Te photodiode, with a bandwidth greater than 2.0 GHz, is presented in Figure 5. The observed shot-noise signal level presented in Figure 5 changes as the reverse bias voltage is varied since the device impedance is a function of the reverse bias voltage. Network analyzer measurements presented in Figure 6 show that the voltage standing wave ratio changes as a function of the reverse bias voltage. The data presented in Figure 6 was measured using a computer controlled Hewlett-Packard 8542 network analyzer and clearly shows that the device impedance changes as a function of the applied reverse bias voltage. Similar measurements have also demonstrated that the device impedance is also dependent on the incident CO_2 laser power.[6]

Blackbody heterodyne measurements were made on the n^+-n^--p photodiodes. Effective heterodyne quantum efficiencies were measured in the 100 to 2000 MHz frequency region and ranged from 13 to 30%. These values correspond to noise equivalent powers of 1.44×10^{-19} W/Hz to 6.23×10^{-20} W/Hz, respectively. Table 2 presents a summary of the heterodyne characteristics of single element n^+-n^--p photodiodes while Table 3 presents heterodyne data on a 2 x 2 element array. All of the data presented in this paper was measured on devices possessing a square active area of 1.8×10^{-4} cm^2. Both tables list the operating points, i.e., the incident CO_2 laser power, the bias voltage, the dark current, and the local oscillator induced current at which the NEP and effective heterodyne quantum efficiencies were measured.

The effective heterodyne quantum efficiencies have been measured to be fairly flat in the 100 to 2000 MHz frequency range. Figure 7 presents data showing the measured effective heterodyne quantum efficiency as a function of frequency for element 2 of the four element array whose properties are listed in Table 2. The device exhibited an effective heterodyne quantum efficiency of 19%

at 2.0 GHz when reverse biased to 0.450 volts and with 0.641 milliwatts of CO_2 laser power focused onto the photodiode active area.

All of the effective heterodyne quantum efficiencies listed in Tables 2 and 3 were measured at 2.0 GHz. The incident CO_2 laser powers required to provide the listed effective heterodyne quantum efficiencies ranged from approximately 0.295 to 1.090 milliwatts. These power levels resulted in photoinduced currents of 1.4 to 2.5 mA. It is entirely possible to increase the effective heterodyne quantum efficiency by utilizing larger levels of incident CO_2 laser power. However, saturation effects and thermal damage may result from the use of increased laser power levels.

CONCLUSION

The measurements presented for the n^+-p $Hg_{0.8}Cd_{0.2}Te$ photodiode show that it is possible to use it as a moderate bandwidth, 10.6μm CO_2 laser heterodyne detector. This diode may be operated at either 77 K or 145 K with a fairly good sensitivity. By proper adjustment of the (Hg,Cd)Te bandgap and doping levels on either side of the n-p junction, it should be possible to use the n^+-p device structure cooled to the temperature range of 185 to 205 K for 8-14 micrometer infrared heterodyne applications.

Single element and four element n^+-n^--p (Hg,Cd)Te photodiode arrays have been developed for 10.6μm wide bandwidth CO_2 laser heterodyne applications. Effective heterodyne quantum efficiencies of approximately 13 to 30% at 2000 MHz have been exhibited. The photodiode's frequency response and heterodyne sensitivity may be improved by the proper choice of junction geometry, by microwave matching of the photodiode's output to the wide bandwidth preamplifier, by the application of an anti-reflection coating to the photoactive area, and by optimizing the junction depth and the depletion region width.

Current research and development is aimed at developing arrays (12 elements) and increasing the bandwidth and heterodyne sensitivity of the n^+-n^--p$(Hg_{0.8}Cd_{0.2})Te$ photodiode.

REFERENCES

1. J.F. Shanley and L.C. Perry, Proceedings of the IEEE International Electron Devices Meeting, Washington, D.C. (1978), pp. 424-429.

2. D.L. Spears, Proceedings of the IRIS Detector Specialty Group Meeting, U.S. Air Force Academy, CO (1977).

3. A.K. Sood and T.J. Tredwell, Proceedings of the IEEE International Electron Devices Meeting, Washington, D.C. (1978), pp 434-436.

4. A.K. Sood and S.P. Tobin, IEEE Electron Device Letters, EDL-1, No. 1, January 1980.

5. K.J. Riley, J.M. Murosznyk, P.R. Bratt and A.H. Lockwood, Proceedings of the IRIS Detector Specialty Group Meeting, Minneapolis, MN (1979), pp 199-207.

6. J.F. Shanley and C.T. Flanagan, Lasers '79 Conference, Orlando, Florida, 17-21 December 1979.

7. B.J. Peyton, et. al, IEEE J. Quant. Electron., Vol. QE-8, 2, February 1972.

8. G. Lucovsky, M.E. Lasser and R.H. Emmons, Proc. IEEE, 51, 166 (1963).

9. S.M. Sze, Physics of Semiconductor Devices, pp. 663-667, John Wiley and Sons, New York (1969).

10. D.E. Sawyer and R.H. Rediker, Proc. IRE, 46, 1122, June, 1958.

11. R.P. Riesz, Rev Sci Instr. 33, 994, September 1962.

Table 1.

Characteristics Of A Three Element $n^+ - p$ Photodiode Array At Temperatures Of 77 K And 145 K

ELEMENT	TEMPERATURE (K)	CUTOFF WAVELENGTH (μm)	FORWARD RESISTANCE (ohms)	ZERO BIAS RESISTANCE (ohms)	BREAKDOWN VOLTAGE (volts)	DC QUANTUM EFFICIENCY (%)	BIAS VOLTAGE (mV)	CAPACITANCE (pF)	DARK CURRENT (mA)	INCIDENT CO_2 LASER POWER (mwatts)	HETERODYNE SIGNAL FREQUENCY RESPONSE (MHz)	NOISE EQUIV POWER (NEP) (W/Hz)	EFFECTIVE HETERODYNE QUANTUM EFFICIENCY (%)
1	77	13.83	20.5	100	0.240	78	160	20.4	0.55	0.268	625	3.2×10^{-20}	58
	145	11.10	19.38	30	0.046	78	240	27.7	1.85	0.400	675	1.0×10^{-19}	19
2	77	13.66	21.0	102	0.230	73	90	23.9	0.35	0.322	725	8.4×10^{-21}	22
	145	11.07	20.63	40	0.060	74	200	19.1	1.5	0.201	600	1.2×10^{-19}	16
3	77	14.11	19.0	75	0.200	76	55	26.5	0.15	0.263	500	8.8×10^{-20}	21
	145	11.40	18.5	34	0.032	75	250	17.7	1.65	0.180	475	1.3×10^{-19}	14

Table 2.

Summary Of Single Element $n^+ - n - p$ $Hg_{0.8}Cd_{0.2}Te$ Photodiode Low Frequency And Heterodyne Characteristics

MIXER	BREAKDOWN VOLTAGE (VOLTS)	AREA (cm^2)	λ_{peak} (μm)	λ_{co} (μm)	R_o (ohms)	$R_{forward}$ (ohms)	BIAS VOLTAGE (VOLTS)	R_o (ohms)	C (pF)	L (nH)	η_{DC}	BANDWIDTH	I_{LO} mA	P_{LO} (mW)	NEP (J/Hz)	η_{EH}
1	1.72	1.8×10^{-4}	10.0	10.88	410	16	0.75	2000	1.75	0.75	56%	$\geq$ 2.0 GHz	1.4	0.360	1.1×10^{-19}	17%
2	0.86	1.8×10^{-4}	10.5	12.5	180	13.3	0.3	1000	2.8	0.77	62%	$\geq$ 2.0 GHz	1.8	0.295	6.45×10^{-20}	29%
3	0.70	1.8×10^{-4}	10.5	16.06	375	17	0.35	740	1.58	0.67	56%	$\geq$ 2.0 GHz	2.2	0.330	1.24×10^{-19}	15%
4	0.63	1.8×10^{-4}	11.0	11.66	367	20	0.32	600	1.48	0.80	65%	$\geq$ 2.0 GHz	1.8	0.310	1.44×10^{-19}	13%
5	1.49	1.8×10^{-4}	10.5	11.41	778	16	0.34	3330	4.9	3.1	52%	$\geq$ 2.0 GHz	2.0	0.330	6.23×10^{-20}	30%
6	1.76	1.8×10^{-4}	10.5	11.5	775	16	0.33	4680	5.06	3.3	34%	$\geq$ 2.0 GHz	2.5	1.09	7.79×10^{-20}	24%

Table 3.

Summary Of The Heterodyne Characteristics Of A Four Element $n^+ - n^- - p$ $Hg_{0.8}Cd_{0.2}Te$ Photodiode Array

ELEMENT	λ_{co}	λ_p(μm)	η_{DC}	RF (ohms)	R_o (ohms)	BREAKDOWN VOLTAGE (VOLTS)	I_{LO} (mA)	P_{LO} (mA)	V_{BI} (VOLTS)	NEP (W/Hz)	η_{EH}	DARK CURRENT (mA)
1	11.5	10.5	0.375	28.5	270	1.7	2.35	0.716	0.35	6.93×10^{-20}	27%	100
2	11.18	10.5	0.50	33.3	250	1.8	1.98	0.641	0.450	9.84×10^{-20}	19%	100
3	11.5	10.5	0.385	29	270	0.80	2.0	0.633	0.180	1.34×10^{-19}	14%	200
4	11.5	10.5	0.365	25	500	2.1	1.95	0.656	0.530	1.31×10^{-19}	14.3%	50

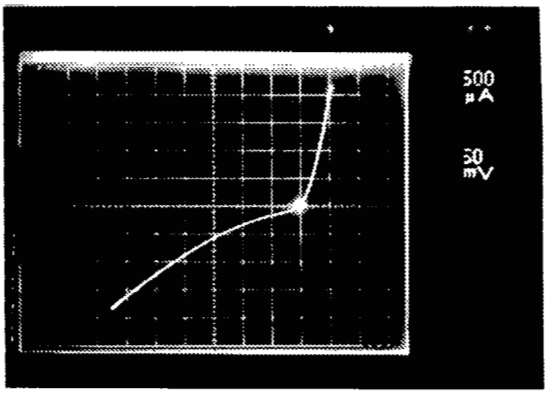

T = 77
λ_{co} = 13.83μm
V_B = 0.240 volts
$R_{FORWARD}$ = 20.5
R_o = 100 ohms
A = 1.8×10^{-4} cm^2

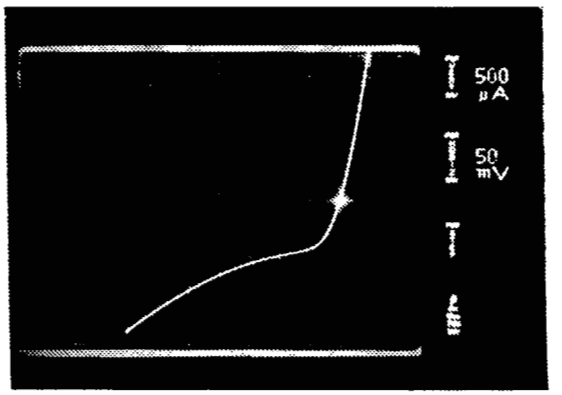

T = 145
λ_{co} = 11.10μm
V_B = 0.046 volts
$R_{FORWARD}$ = 19.38 ohms
R_o = 30 ohms
A = 1.8×10^{-4} cm^2

Figure 1.- I-V characteristics of element 1 measured at 77 K and 145 K.

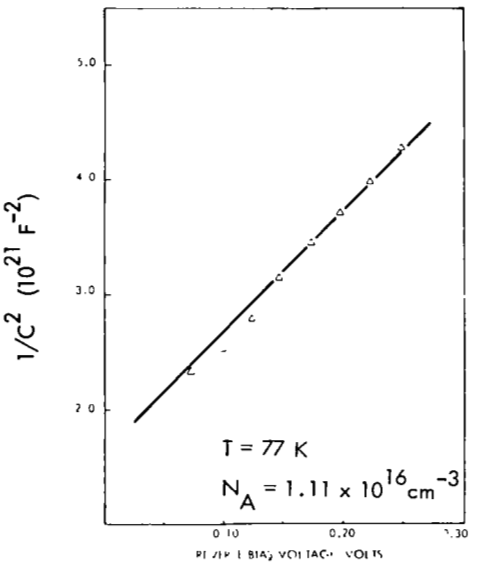

Figure 2.- $1/C^2$ versus reverse bias voltage for element 1.

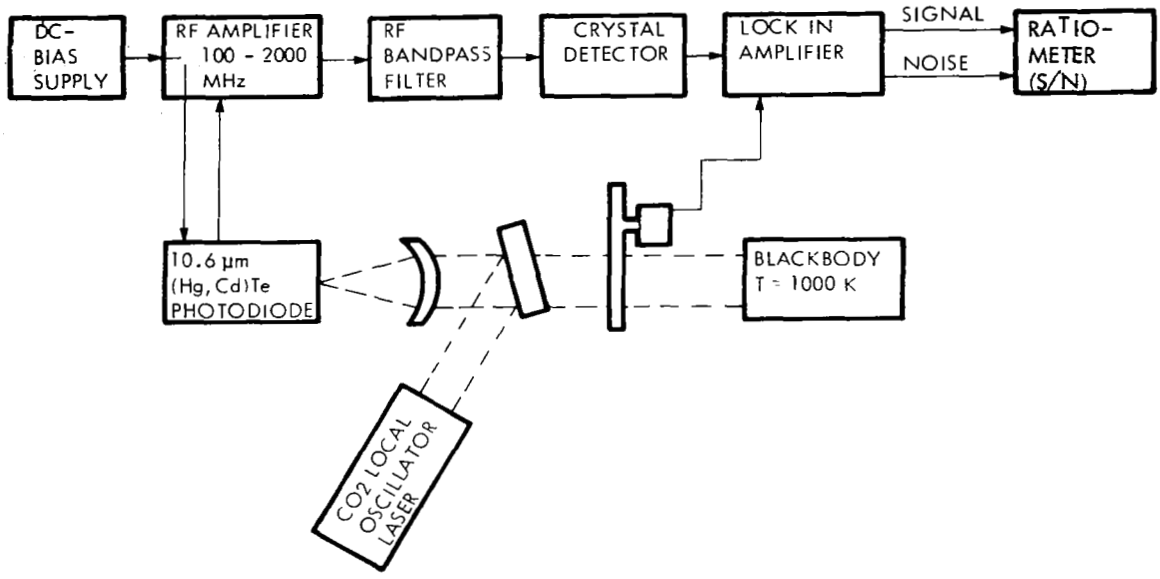

Figure 3.- Heterodyne radiometer.

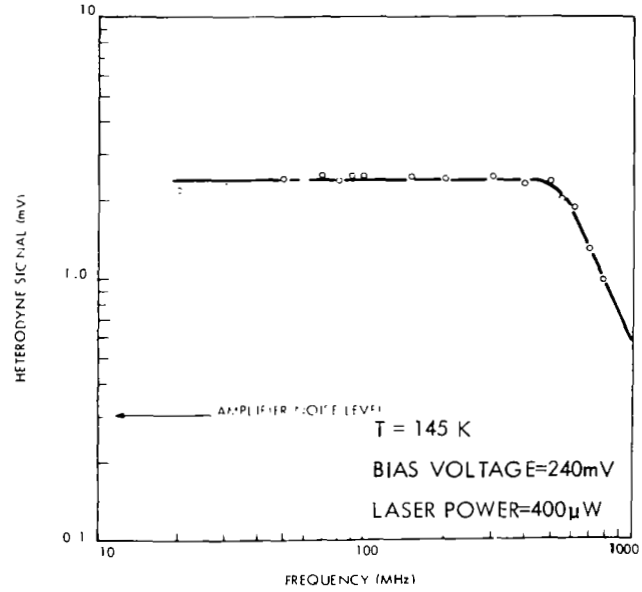

Figure 4.- Heterodyne signal frequency response of element 1 measured at 145 K.

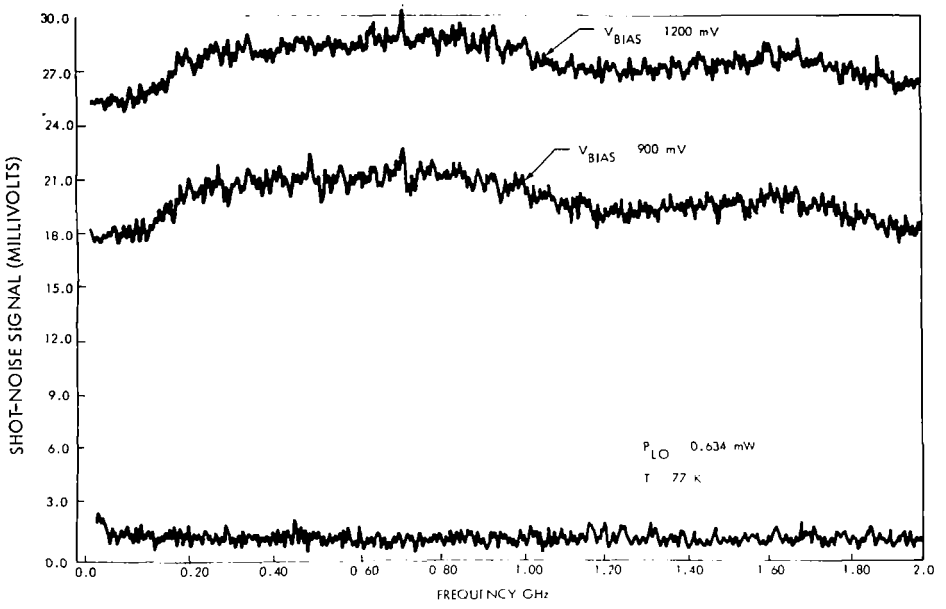

Figure 5.- Shot-noise signal response versus frequency for element 2 of a four element array.

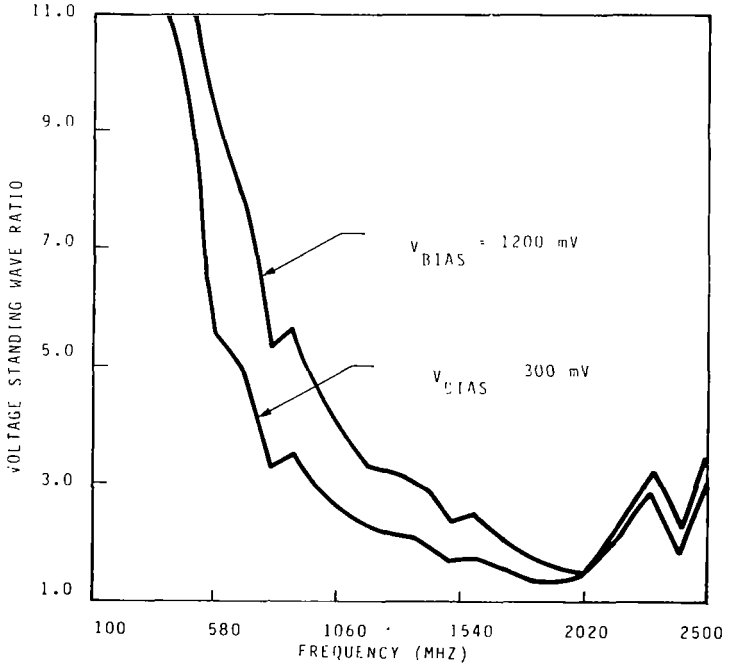

Figure 6.- Voltage standing wave ratio versus frequency for element 2 of a four element array.

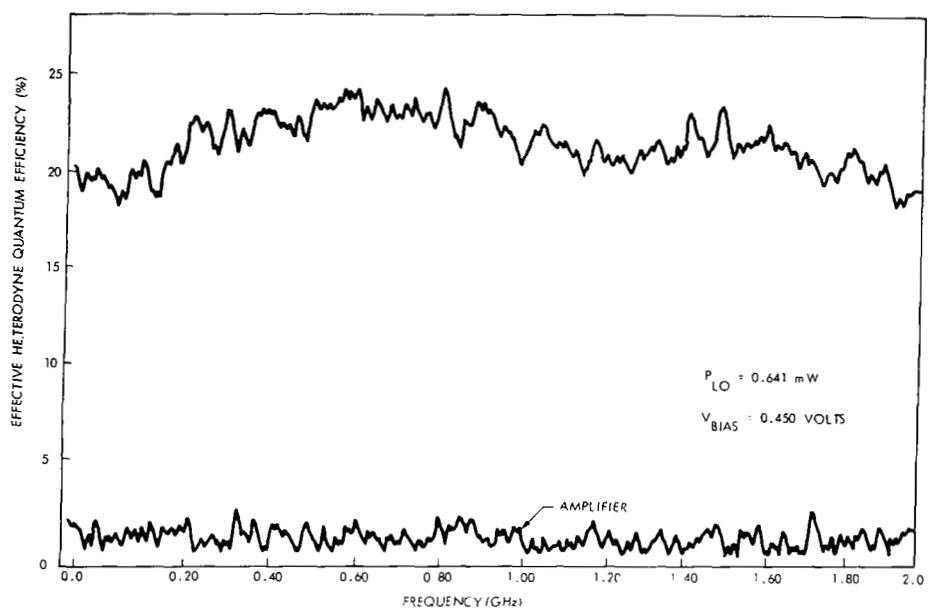

Figure 7.- Effective heterodyne quantum efficiency versus frequency for element 2 of a four element photodiode array.

CONCEPTUAL DESIGN AND APPLICATIONS OF HgCdTe INFRARED PHOTODIODES FOR HETERODYNE SYSTEMS

Michel B. Sirieix
Societe Anonyme de Telecommunications, Paris, France

Henry Hofheimer
ELTEK Corporation, Larchmont NY

SUMMARY

HgCdTe photodiodes represent an important component for heterodyne detection systems operating in the 9 to 11μm CO_2 laser wavelength region. Their successful fabrication requires thorough understanding of the physical properties of the basic materials. The implementation of controlled industrial processes ensures the yield of predictable and repeatable detector characteristics to satisfy today's discriminating systems' demands for high cutoff frequencies, quantum efficiency, and reliability. The most salient production steps and diode characteristics will be described. Measured results from present production units will be presented.

INTRODUCTION

Numerous CO_2 laser applications, in particular those dealing with heterodyne detection at 10.6μm, are largely responsible for the generally increased interest in fast photodiodes for this wavelength region.

As previously reported (1), (2), (3), HgCdTe photodiodes have inherent cutoff frequency capabilities beyond one GHz. This is rendered possible by the normal value of the materials permittivity and the ability to create a junction of very low capacitance. In fact, because of the very high electron mobility in narrow-bandgap semiconductors, the dynamic characteristics of the minority carriers are not expected to become significant limiting mechanisms of the diode. Furthermore, the high value of the absorption coefficient permits excellent optimization of quantum efficiency and cutoff frequency.

The extent of studies conducted during the past decade on the metallurgy of the materials and on the diode technology have enabled us to gain a better understanding of the factors affecting the diode characteristics, performance, and reliability. Thanks to the knowledge gained on the diodes and on their interdependent parameters, it is now possible to optimize the development of a diode for a given application.

PHOTODIODE OPTIMIZATION (77K) FOR A 10.6μm HETERODYNE RECEIVER

The heterodyne receiver signal-to-noise ratio can be expressed using the passive elements of the diode equivalent circuit (Fig.1), including shunt conductance (G_D), junction capacitance (C_D), series resistance (R_s) as well as the signal and noise generators and the preamplifier (4),(5),as shown in Eq.1:

$$\frac{S}{N} = \frac{\eta \; q \; P_{SIG}}{h\nu \; \Delta f \left\{ 1 + \frac{I_d}{I_{Lo}} + \frac{2k\,(T_D + T'_{PA})}{I_{Lo}} \left[G_D(1 + R_S G_D) + R_S C_D^2 \omega^2 \right] \right\}} \qquad (1)$$

where η = the quantum efficiency which must be maximized for the wavelength region of interest

P_{SIG} = signal power

I_d = dark current

I_{LO} = local oscillator induced current

T_D = diode temperature

T'_{PA} = preamplifier noise temperature

Quantum efficiency

Quantum efficieny (η) is defined as the ratio of carriers crossing the junction to the total number of incident photons. It is limited by:

- reflection losses on the semiconductor surface. These losses can be reduced through antireflection coating

- electron-hole recombination in the bulk before reaching the junction. To minimize this effect, the carriers must be generated as close as possible to the junction either through the creation of superficial junctions or by utilizing the transparency effect resulting from the doping of the n-surface of the p-n junction. The transparency effect (1) is particularly prominent in narrow-bandgap semiconductors

- surface recombination which can be reduced through surface passivation or by avoiding carrier generation in the bulk through utilization of the transparency effect

Cutoff Frequency

The HgCdTe detector response varies as a function of frequency. Three factors contribute to the limitation of the usable cutoff frequency (6), (Fig.2):

a. Diffusion effects.

When the depletion region is narrow with respect to the absorption length (case of the very mildly biased junction), only those carriers created within less than one diffusion length will reach the junction and the time required for this action to take place limits the speed. The corresponding cutoff frequency is

$$f_{c_{DIFF}} = \frac{2.4\, D\, \alpha^2}{2\pi} \qquad (2)$$

where D = diffusion coefficient of minority carriers
α = photon absorption coefficient

For example: for $\alpha = 3 \times 10^3\ cm^{-1}$ and D near unity, the cutoff frequency is limited to about 10 MHz.

b. Transit time in the depletion region.

The widening of the depletion region causes an increase in the number of carriers generated. The speed of these carriers is increased by the electric field and the corresponding cutoff frequency is given by

$$f_{C\,DRIFT} = \frac{2.4\, v_s}{2\pi w} \qquad (3)$$

where w = width of the depletion region
v_s = carrier speed, reaching its limit near 10^7 cm s^{-1}

Thus, for w = 3μm, the cutoff frequency is in excess of 10 GHz.

c. Junction capacitance.

The photodiode equivalent circuit (Fig.1) shows the presence of a cutoff frequency limitation through the $R_L C_D$ time constant, wherein R_L is the diode load resistance and C_D the junction capacitance. For a load of 50 ohms and 1 pF capacitance, the cutoff frequency is approximately 3.2 GHz.

The improvement of the cutoff frequency of a photodiode therefore requires the following efforts:

1. Reduction of the junction capacitance by reducing the surface area and the doping level on either side of the junction.

2. Widening of the depletion region and bringing it closer to the surface. This also requires low doping level, a junction depth adapted to the extension of the depletion region and to the absorption length, and elevated breakdown field strength.

These conditions can be simultaneously met, as shown in Fig.3. A doping level of 2 x 10^{14}cm^{-3} and bias of about -1V lead to a depletion region width of about $1/\alpha$, that is, 3μm. This, in turn, results in the following advantages:

- high quantum efficiency, if the junction depth is of the same order of magnitude (3 to 5μm)

- high cutoff frequency resulting from the short transit time in the depletion region (3×10^{-11}s) and the low junction capacitance (1 pF for an area of 2×10^{-4}cm^2)

Planar Technology

The planar technology developed and implemented for the fabrication of HgCdTe photodiode arrays and matrices (7) presents numerous advantages for the manufacture of fast photodiodes, such as:

- protection of the edges around the junction, thus reducing leakage currents and permitting the use of high bias voltages

- passivation of the sensitive area, which reduces internal reflection losses and surface recombination. It also increases the reliability by diminishing the effect of external factors

The p-type HgCdTe material is prepared through recrystallization at the solid state or through epitaxial deposition and isothermal diffusion. The purity of the basic material must be very high in order to attain the desired low doping levels.

Substrate preparation (Fig.4) includes mechanical polishing and cleaning in a bromine-alcohol solution, followed by passivation with a ZnS deposition. The diffusion apertures are developed through localized chemical etching of this layer. Two methods are employed to form the junction: mercury diffusion and ion implantation. A passivation layer of ZnS is then applied which, in turn, is etched to prepare the contacts. The contact areas are formed through a deposit of gold-chromium, and this is followed by overall passivation.

This technology permits the fabrication of all kinds of geometries and photodiode groupings (square, rectangular, or round sensitive areas, single-element detectors, arrays, quadrants, and small matrices).

Photodiode Installation in Cryostat

The method used for mounting the photodiode in its cryostat is of primary importance. On the one hand, one must reduce parasitic capacitance and, on the other hand, it is essential to:

- reduce the inductance of the connections (L_s)
- feed the IF output through the cryostat, using a coaxial cable
- protect the photodiode against electro-magnetic interference

These goals are reached by installing the photodiode in a housing which serves to support and protect it while, at the same time, providing the link to a coaxial output connector (Fig.5). A miniature coaxial cable with a stainless steel sheath connects this housing to the output of the cryostat.

RESULTS

High-speed HgCdTe photodiodes (Class C4) for heterodyne detection at 10.6μm from present production exhibit the following characteristics:

Sensitive area: between $10^{-4}$and 2 x $10^{-4}cm^2$
Quantum efficiency: 50 to 60%
Breakdown field strength (at 1mA): in excess of 2V, reaching or exceeding 3V on certain diodes
Max. reverse dynamic resistance: about 100 kohms
Series resistance: 10 ohms

Analysis of the capacitance variation with increasing bias voltage discloses the presence of a steep junction (varies as $1/c^2$ as a function of reverse bias voltage) (Fig.6) and of a doping level of about 1 to 2 x $10^{14}cm^{-3}$. This confirms the high purity level of the starting material.

The particularly high breakdown field strength which we measured (Fig.7), reveals that the leakage currents around the edges of the junction are minimized by the passivation layer. As predicted by mathematical models, cutoff frequencies in excess of 1 GHz have been achieved with a reverse bias value of -1V (Private communication from Lemaine, Laboratoire de Spectroscopic

Hertzienne, L.A.C.N.R.S. 249 U.S.T.L.)(Fig. 8), while heterodyne detection operation with these detectors was reported at frequencies of 8.7 GHz (8) (Unpublished report by J. P. Sattler et al., U.S. Army, Harry Diamond Laboratories).

Reliability

Reliability tests to military specifications, including cycling up to temperatures of 80°C, which were conducted for periods of several thousand hours without degradation of the diode characteristics, testify to the high degree of reliability of these components. This is further confirmed by the fact that detectors, which have seen operation in the field for over 10 years, are still operating (Private communication from B. J. Peyton of AIL). The use of a passivation layer is primarily responsible for the immunity to external disturbing factors and, in particular, to short wavelength radiation.

Operation at Temperatures in Excess of 77K

The proper operation of a HgCdTe photodiode at temperatures in excess of 77K requires the following conditions:

1. High quantum efficiency at this temperature at 10.6μm. This can be achieved by selecting the composite material so that the absorption coefficient will always be 1000 or higher.

2. Saturation current below the level of the local oscillator current, the latter being generally on the order of 1 to 3 mA.

3. A reverse dynamic resistance (R_D) selected so that:

$$R_D I_{LO} >> \frac{2kT}{q}$$

Numerous studies conducted in our laboratories (DRET contract no. 76/422) on detectors operating at temperatures in excess of 77K enabled us to reach R_oA products at $10^{-2}\Omega cm^{-2}$ at 140K for a spectral peak wavelength of 10.5μm. These detectors can operate in a heterodyne mixer without noticeable degradation of their performance characteristics, when compared to those normally experienced at 77K. "Long wavelength" detectors ($\lambda_p \sim 14\mu m$ at 77K) were measured at temperatures within the operating range of thermoelectric coolers (S.A.T. internal report). In accordance with our predictions regarding the variation of the intrinsic concentration as a function of temperature and based on the characteristics measured at 77K, these detectors exhibit saturation current levels of about

20mA at 200K and reverse dynamic resistance of about 40 ohms. Calculations disclose a degradation of the heterodyne sensitivity on the order of 10 dB under these conditions.

Figure of Merit (Heterodyne Quantum Efficiency)

In order to characterize the performance of a heterodyne detector, one can include all degradation factors into a single parameter: the heterodyne quantum efficiency (η'). Referring back to Eq.1, we obtain:

$$\eta' = \eta \left\{ 1 + \frac{I_d}{I_{Lo}} + \frac{2k\,(T_D + T'_{PA})}{I_{Lo}} \left[G_D (1 + R_S G_D) + R_S C_D^2 \omega^2 \right] \right\}^{-1} \qquad (4)$$

where η' is a function of the local oscillator (L.O.) induced photocurrent, the IF frequency and the detector characteristics. The maximum value for a given intermediate frequency is obtained for optimum local oscillator power and detector reverse bias conditions. It must be noted that it is not possible to indefinitely increase the local oscillator power to minimize the influence of the parasitic effects of the diode and preamplifier, as this would lead to saturation and thus reduce the quantum efficiency. This can occur at local oscillator current levels in excess of a few milliamperes (Fig.9). Degradation of quantum efficiency can also be observed when comparing it to the quantum efficiency measured at very low frequencies. This is caused by the fact that only those carriers generated in the depletion region can be used at very high frequencies. It is, therefore, possible to notice a variation of the heterodyne quantum efficiency as a function of detector reverse bias. The low-frequency value of quantum efficiency is again reached when the depletion region extends very near to the detector surface.

Values of heterodyne quantum efficiency on the order of 40% were measured in the laboratory for detectors whose low-frequency quantum efficiency was 50 to 60%. These figures confirm the fact that, by optimizing the operating point of the photodiode, the degradation will only be very small.

CONCLUSION

HgCdTe photodiodes, optimized for operation at high frequencies, are manufactured through a controlled, repeatable process. They exhibit excellent I-V characteristics which permit the application of high reverse bias voltages, thus yielding at the same time high cutoff-frequency capability and high heterodyne sensitivity.

These detectors can be used in many different systems operating in the 9 to 11μm wavelength region, such as optical radars, telecommunication links, and interferometers. An important fringe benefit lies in their great reliability for terrestrial as well as for aerospace applications.

REFERENCES

(1) C.Verie and M. Sirieix "Gigahertz Cutoff Frequency Capabilities of CdHgTe Photovoltaic Detectors at 10.6μm", IEEE J.Quantum Electronics, Vol.QE-8 No.2,pp.180-191, Feb.1972.

(2) I.Melngailis, T.C.Harman and E.D. Hinkley "High Speed $Hg_{1-x}Cd_xTe$ Photodiodes", Solid-State Research Report, Lincoln Laboratory (MIT 1972), pp.13-14.

(3) J.F.Shanley and L.C.Perry "Wide Bandwidth 10.6μm (HgCd)Te Photodiodes for Infrared Heterodyne Applications",IEDM 78, pp. 424-426.

(4) M.B.Sirieix, Ph.D. Thesis, Universite de Paris, 1971.

(5) B.J.Peyton, A.J.Dinardo, G.M.Kanischak, F.R.Arams, R.A. Lange and E.W.Sard "High Sensitivity Receiver for Infrared Laser Communications", IEEE J.Quantum Electronics, Vol.QE-8 No.2, pp.252-263, Feb. 1972.

(6) S.M.Sze "Physics of Semiconductor Devices", J.Wiley, 1969.

(7) J.Ameurlaine, J.L. Antoniazzi, J.Maille and G.Pichard "Infrared HgCdTe Photovoltaic Detectors by Planar Technology", Tech.Digest IEDM 1978, pp.430-433.

(8) J.P.Sattler, T.L.Worchesky, K.J.Ritter and W.J.Lafferty "Technique for Wideband, Rapid and Accurate Diode-Laser Heterodyne Spectroscopy:Measurements on 1,1-Difluoroethylene, Optics Letters, Vol. 5, No. 1, p.21, January 1980.

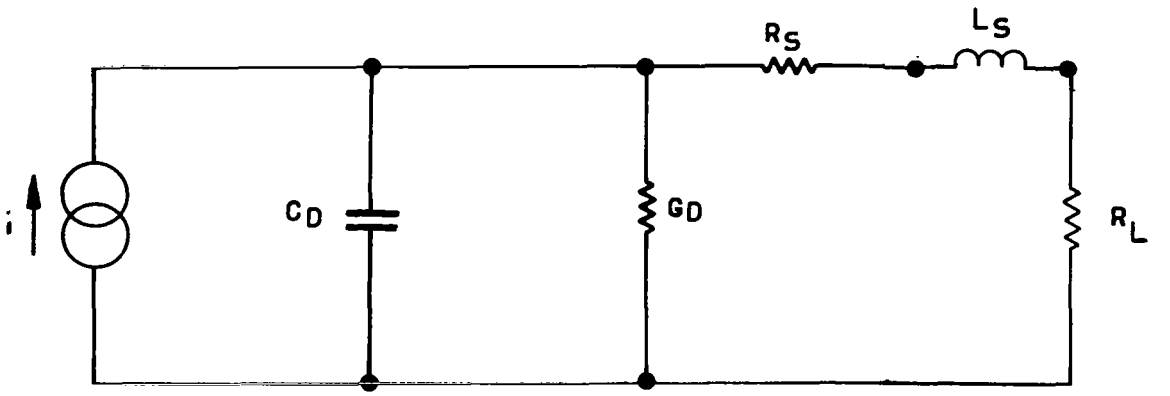

Figure 1.- Photodiode equivalent circuit.

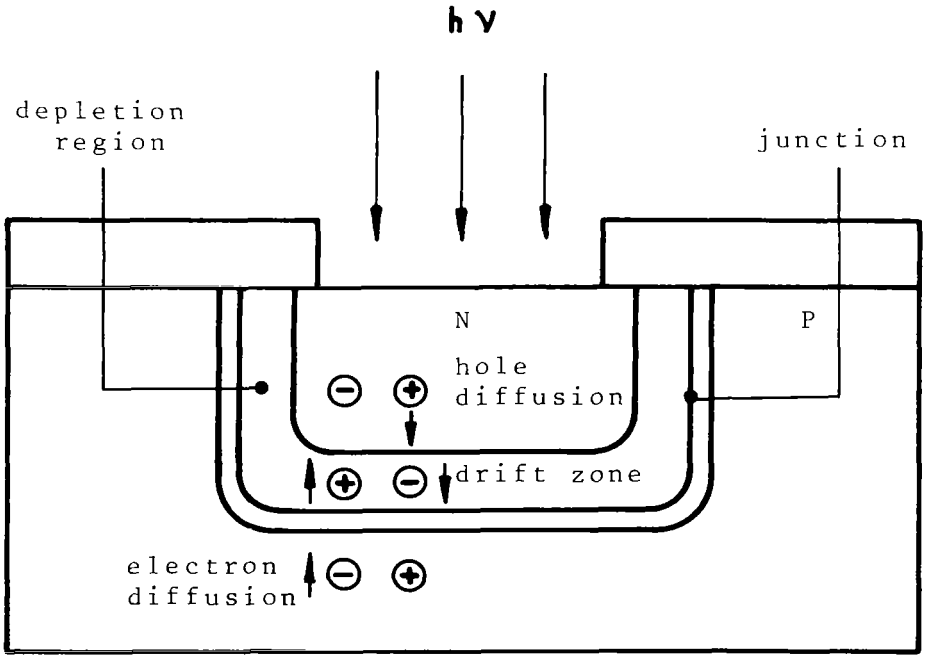

Figure 2.- Photon-induced current generation process in photodiode (junction depth = photon absorption length).

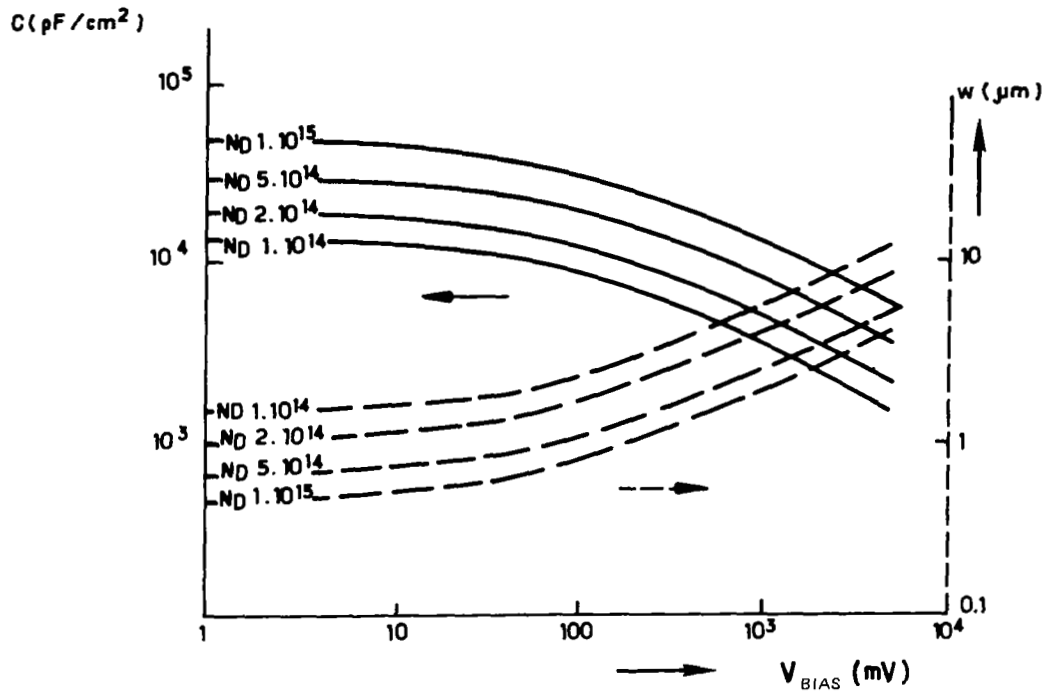

Figure 3.- Junction capacitance and depletion zone width vs. bias voltage for different n. doping levels in HgCdTe photodiode.

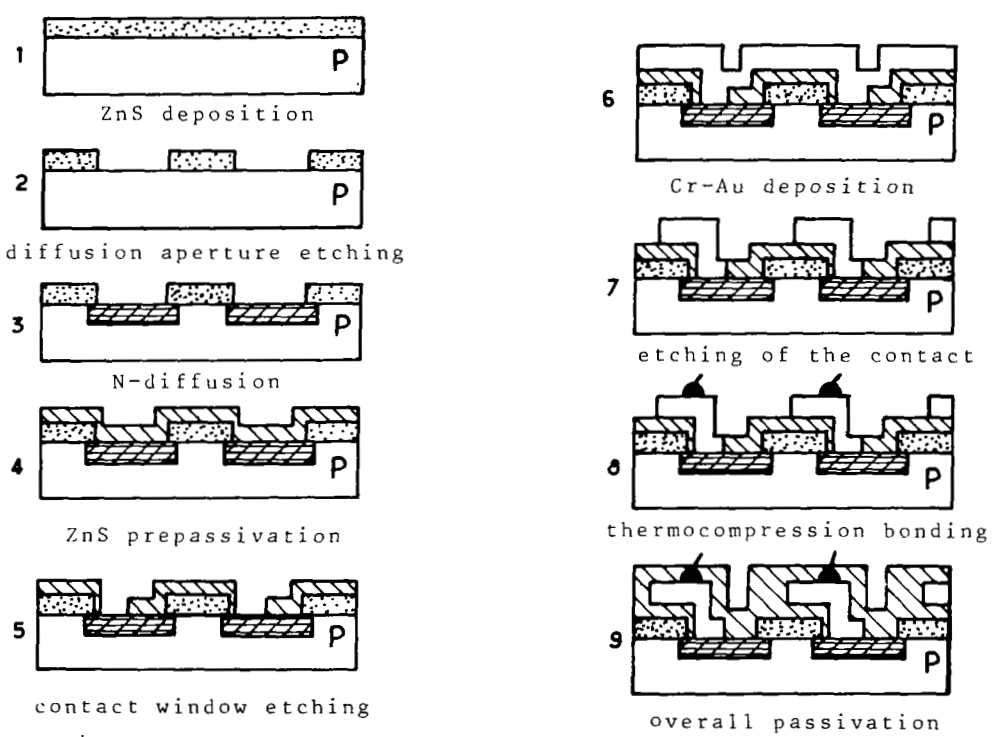

Figure 4.- Planar technology.

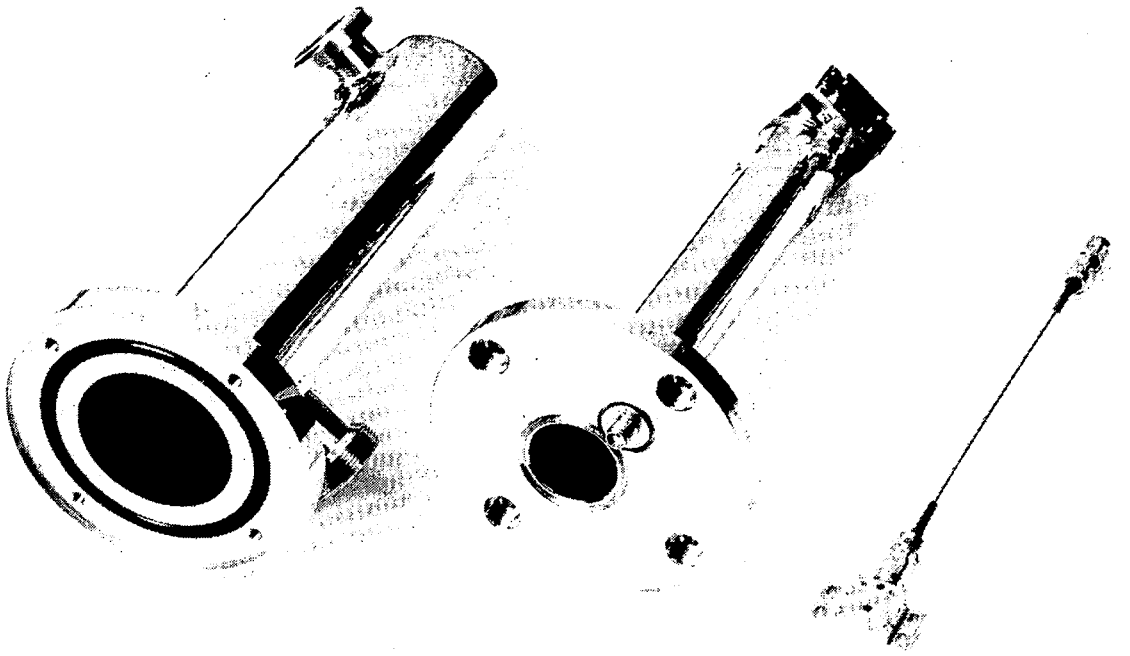

Figure 5.- Detector housing.

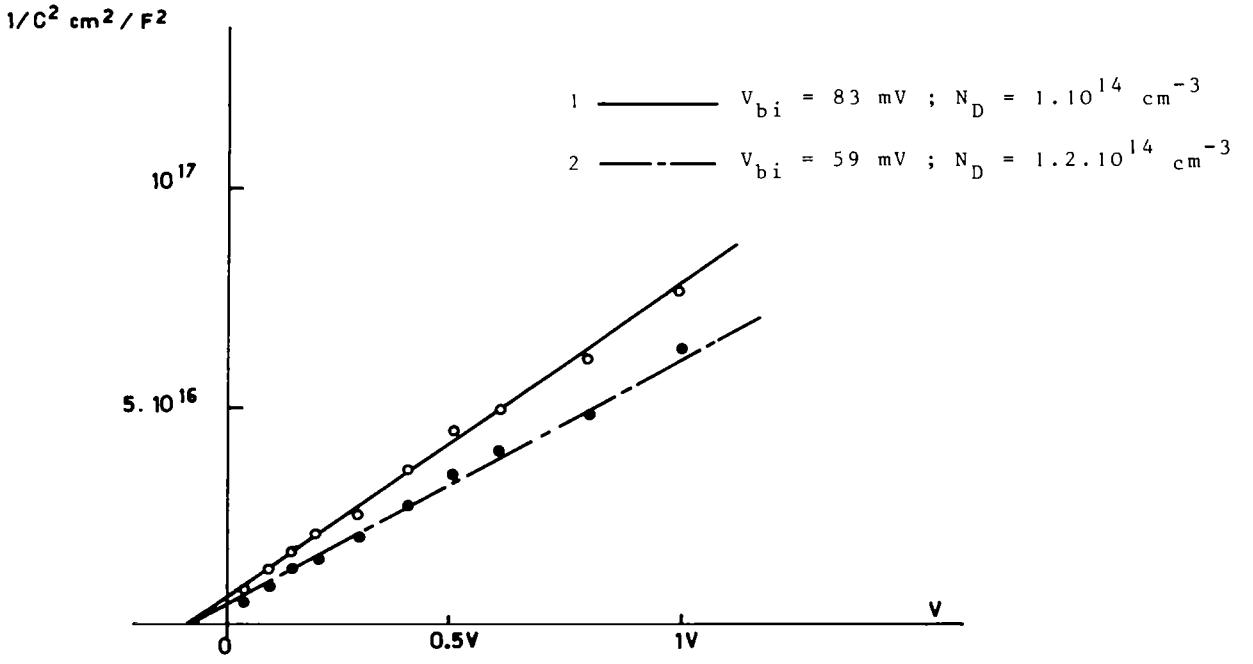

Figure 6.- Doping level calculations from C(V) plots.

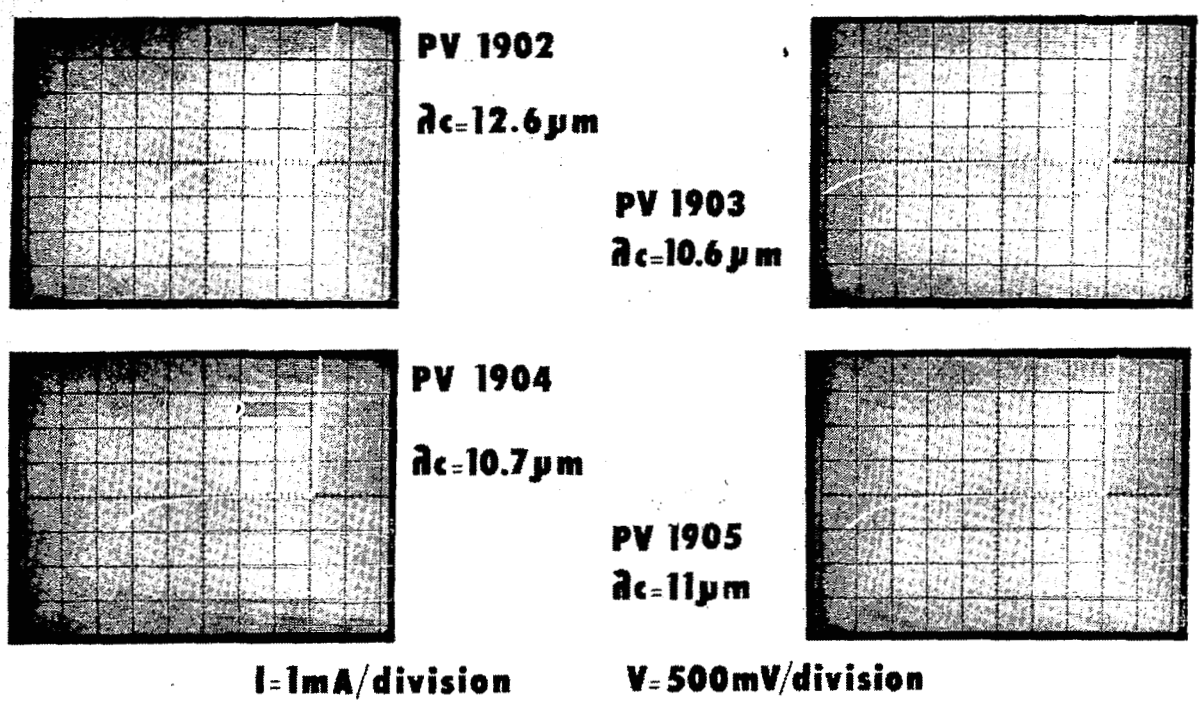

Figure 7.- I(V) characteristics of some wide bandwidth detectors.

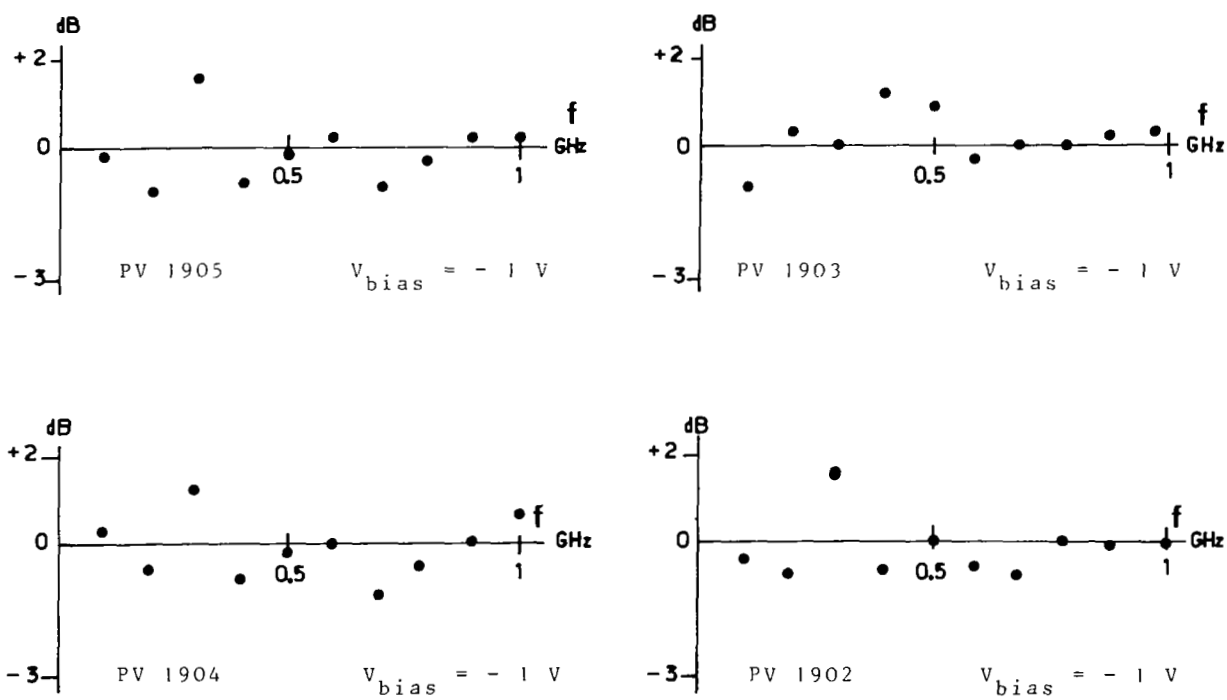

Figure 8.- Frequency response of some 10-μm photodiodes.

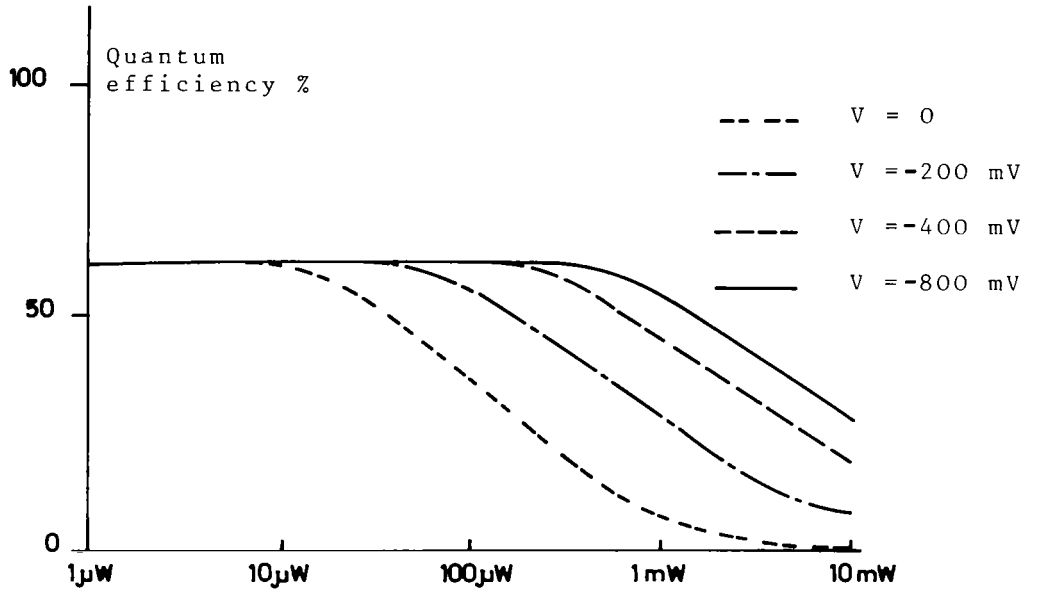

Figure 9.- Quantum efficiency vs. local oscillator power for various values of reverse bias.

COMPARATIVE PERFORMANCE OF HgCdTe PHOTODIODES FOR HETERODYNE APPLICATION

Herbert R. Kowitz
Langley Research Center

SUMMARY

Photodiodes are used as optical photomixers in Laser Heterodyne Spectrometers (LHS) systems to enable high resolution spectroscopy. A very important parameter in any photomixer application is the photodiode's quantum efficiency because of its direct effect on the system's signal-to-noise ratio. Quantum efficiency, however, is usually specified by photodiode manufacturers as the direct current (dc) quantum efficiency. It is important for the LHS application to determine if the quantum efficiency differs for the heterodyne mode of operation and by how much. This paper describes the measurement techniques used by the LHS Conceptual Design Team (CDT) to determine photodiode dc and heterodyne quantum efficiencies. The theory behind these measurements as well as actual measurement data for two currently available HgCdTe photodiodes are presented.

DC QUANTUM EFFICIENCY

The dc quantum efficiency of a photodiode represents a figure of merit of how well the device converts light energy into electrical energy or, more specifically, how many amperes of photocurrent are generated for each watt of optical signal power. The response (R) of a photodiode in amperes/watt is given by

$$R = \eta_{dc} \left(\frac{q}{hf}\right) \tag{1}$$

where:

η_{dc} = dc quantum efficiency
q = electron charge = 1.602 (10^{-19}) Coulombs
h = 6.625 (10^{-34}) Joule-sec
f = 3 $(10^{14})/\lambda$ with the wavelength (λ) expressed in microns

As can be seen by equation (1), the theoretical response is maximum for 100 percent dc quantum efficiency. At a wavelength of 10.6 microns, the maximum response is 8.544 amperes per watt.

The dc quantum efficiency of a given photodiode can be determined by measuring the photocurrent generated for a given signal power impinging on the

photodiode's sensitive area. The difficulty (and any possible inaccuracy) lies in the determination of the factors that influence the amount of signal power. The measurement set-up that was used for photodetector response measurements (see fig. 1) consists of a blackbody radiation source, an optical filter, and focusing mirrors. This set-up was part of an overall LHS layout and not optimized for photodetector response measurements. The chopper and the beam splitter are not required for the dc measurements, but are needed for heterodyne measurements discussed later in this paper.

The blackbody emittance (N_λ) is given by

$$N_\lambda = \frac{c_1 d\lambda}{\pi\lambda^5[\exp(c_2/\lambda T) - 1]} \quad \frac{\text{watts}}{\text{cm}^2 \cdot \text{ster}} \tag{2}$$

where c_1 is 3.7405 (10^4) and c_2 is 1.4388 (10^4) if the wavelength is expressed in microns and the blackbody temperature (T) is in degrees Kelvin. The tests were conducted at 10.6 microns with a 0.3963 micron optical filter resulting in a radiance of 1.866 (10^4) watts/cm^2•ster for the 1273 K source.

The optical power at the detector is related to this radiance by

$$P_{det} = N_\lambda \tau_{CH} \tau_F (\tau_M)^3 \tau_{BS} \tau_{POL} \frac{\pi}{4} \left(\frac{d}{\ell}\right)^2 A_{det} \cos\theta \text{ watts} \tag{3}$$

where:

τ_{CH} = chopper factor = 0.5
τ_F = filter transmission factor = 0.65
τ_M = mirror transmission factor = 0.97
τ_{BS} = beam splitter factor = 0.5
τ_{POL} = polarization factor = 0.5
d = lens diameter = 5.0 cm
ℓ = focal length = 15.2 cm
θ = off normal detector mounting angle = 30°
A_{det} = detector area = 1.21 (10^{-4}) cm^2 for unit (A)
= 1.7 (10^{-4}) cm^2 for unit (B)

Using these given factors in equation (3) results in optical powers of 0.0123 microwatts for unit (A) and 0.0173 microwatts for unit (B). These powers differ because detector (B) has about 40 percent greater sensitive area. To assure a valid comparison the detectors have to be overfilled. This condition was verified by transverse movement of the photodetectors without loss of photocurrent. The measured photocurrents were 0.05 and 0.1 microamperes for detectors (A) and (B), respectively. Application of equation (1) results in η_{dc} = 48 percent for detector (A) and η_{dc} = 68 percent for detector (B).

HETERODYNE QUANTUM EFFICIENCY - THEORY

The heterodyne quantum efficiency is more difficult to ascertain because it involves the heterodyne mode of operation, i.e., the mixing of two optical signals to obtain a "beat signal" in the microwave frequency range. The test set-up used for the heterodyne efficiency measurements (see fig. 2) consists of a blackbody source, a 50 percent duty cycle chopper, focusing optics, and a 50/50 beam splitter to combine the signal (blackbody) with the local oscillator (CO_2 laser). The RF portion consists of a 5 to 550 MHz preamplifier, a 10 to 115 MHz amplifier, and a square-law detector to detect the heterodyne signal power in the midband frequency range (10 to 155 MHz). The detector output is then synchronously demodulated and filtered by a running-mean integrator whose value is read at a 1-second integration time and reset to zero. The chopper rate was chosen to be 1024 Hz to simplify the generation of the required control pulses.

The scheme followed to obtain a heterodyne quantum efficiency measurement is similar to the dc quantum efficiency measurement except that for the heterodyne case, the measured signal-to-noise ratio (SNR) is compared to the maximum theoretical obtainable SNR.

The SNR for the described implementation is given by

$$SNR = \frac{4\,\eta_{Het}\,q\,I_{ph}\,t}{[\exp(hf/kT) - 1]} \cdot \frac{\sqrt{B_{IF}\tau}}{(F-1)\frac{kT_o}{R_{11}} + 2q(I_{ph} + I_d)} \qquad (4)$$

where:

η_{Het} = heterodyne quantum efficiency
I_{ph} = signal induced photocurrent
t = optical transmission factor = 0.093
B_{IF} = IF bandwidth = 105 MHz
τ = post detection integration time = 1 sec
F = noise factor of preamplifier = 1.58 (NF = 2 dB)
T_o = 290 K
R_{11} = equivalent input impedance of preamplifier
I_d = dark photocurrent

As can be seen by equation (4), the SNR is directly dependent on the photodiode's heterodyne quantum efficiency. It should be noted that the optical transmission factor has the same impact on the system SNR as the quantum efficiency indicating that both factors should be maximized. An increase in the IF bandwidth or the integration time, however, has less effect; doubling either only results in a 41.4 percent improvement in the signal-to-noise ratio. Also, integration time is mission dependent and cannot be arbitrarily increased except for static measurements (as in the lab). The IF bandwidth is limited

by two factors: (a) the photomixer's own frequency response limitation, and (b) the increased noise factor of wide bandwidth preamplifiers.

Other important factors that influence the SNR are the temperature of the blackbody source and the effective temperature of the noise sources operating in the LHS system. The blackbody source temperature affects the SNR via the $[\exp(hf/kT) - 1]^{-1}$ factor of equation (4). For example, at 10.6 microns the SNR increases by a factor of approximately 7 when considering the blackbody temperature of the sun at 5600 K versus the temperature of 1273 K of the laboratory source.

The noise sources operating in a LHS system are basically Johnson noise referred to the input of the preamplifier and photodiode shot noise. Their effects are accounted for by the $(F - 1)kT_o/R_{11}$ and $2q(I_{ph} + I_d)$ factors, respectively. Because an unstable reference source will cause an apparent noise component as well, a CO_2 laser was chosen as the local oscillator for the heterodyne quantum efficiency measurements.

HETERODYNE QUANTUM EFFICIENCY MEASUREMENTS - MIDBAND

The heterodyne quantum efficiency measurements for the midband case were conducted in the 10 to 105 MHz frequency range (determined by the amplifier bandwidth of the AIL 2392C radiometer of fig. 2) to assure that the measurement is within the photodetector response bandwidth. It should be noted that the test set-up was part of an overall optical layout for the LHS system and was not optimized for photomixer response measurements. The inability to determine the exact transmission factors, therefore, will cause errors in the absolute measurements, but should be more than adequate for determining heterodyne frequency response rolloff. The SNR was measured by using a microprocessor controlled digital voltmeter (DVM) to measure the average of the RF detector output voltage (1 second integrator) and its standard deviation. The measured SNR was determined as follows:

$$SNR = \frac{V_{LO+BB} - V_{BB}}{\sigma} = \frac{V_{HET}}{\sigma} \qquad (5)$$

where:

V_{LO+BB} = average detected output with the CO_2 laser and BB heterodyning
V_{BB} = average detected output with the CO_2 laser path blocked
σ = standard deviation of detected output during heterodyning
V_{HET} = heterodyne signal output

The SNR was measured for photocurrents up to about 1 milliampere. The test results are provided in table I for both available photomixers. It should be noted that the photocurrents shown are above the photomixer dark currents. Table II depicts the parameter values used and the theoretical SNR calculation

results. It should be noted that for photomixer (B), the dark durrent parameter value used in the theoretical SNR calculations was about 50 percent of the measured dark current because it was found that only about half of the dark current for this photomixer contributed to shot noise. This phenomenon needs further investigation but is outside the scope of this paper. Figure 3 shows both the measured and the calculated values for the SNR in the 10 to 115 MHz band. A comparison between the theoretical and the measured SNR's results in heterodyne quantum efficiencies of 16.5 percent for photomixer (A) and about 62 percent for photomixer (B).

HETERODYNE QUANTUM EFFICIENCY VERSUS FREQUENCY

The quantum efficiency for photodiode (A) decreased from 48 percent at dc to 16.5 percent in the 10 to 115 MHz band and photodiode (B) decreased from 68 percent to 62 percent. This prompted implementation of the test set-up shown in figure 4 to enable a heterodyne frequency response check. The results of these tests are shown in figure 5 for photomixer (A) and in figure 6 for photomixer (B). Because the dc response cannot be obtained with this test implementation, no direct comparison to the dc quantum efficiency can be made. Also, this implementation introduces its own signature on the overall frequency response because of VSWR, amplifier in-band ripple, and RF mixer response effects. These effects have been "backed out" resulting with the corrected response curves shown in figures 5 and 6. It is seen that photomixer (A) has a roll-off in the 10 to 110 MHz band that is not as pronounced for photomixer (B). Photomixer (A) appears to be at its half power point at about 450 MHz. Photomixer (B) has not approached its half power points at the 500 MHz limitation of the test set-up and requires a wider bandwidth implementation to investigate.

CONCLUSIONS

Photodiodes used as photomixers in LHS systems exhibit quantum efficiencies in the heterodyne mode of operation that are lower than their dc quantum efficiencies. Also, this heterodyne efficiency is not constant over the photodiodes specified bandwidth, but exhibits a gentle roll-off with frequency. Consequently, photodiodes that are to be used in heterodyne applications should be tested in that mode and a minimum heterodyne quantum efficiency specified at the upper frequency of interest. These tests require much care, however, due to the signature of the RF components in the test setup.

BIBLIOGRAPHY

1. Hans Melchior, Mahlon B. Fisher, and Frank R. Arams, "Photodetectors For Optical Communication Systems," Proceedings of the IEEE, Vol. 58, No. 10, October 1970.

2. T. B. Blaney, "Signal-to-Noise Ratio and Other Characteristics of Heterodyne Radiation Receivers," Space Science Reviews 17 (1975), pp. 691-702.

3. M. E. Tiuri, "Radio Astronomy Receivers," IEEE Transactions on Antennas and Propagation, Dec. 1964, pp. 930-938.

4. Bernard J. Peyton, Anthony J. DiNardo, Steven C. Cohen, John McElroy, and Robert J. Coates, "An Infrared Heterodyne Radiometer for High Resolution Measurements of Solar Radiation and Atmopsheric Transmission," IEEE Journal of Quantum Electronics, Vol. QE-11, No. 8, Aug. 1975.

TABLE I.- SNR MEASUREMENTS (MIDBAND)

	I_{ph}*	$V_{LO} + V_{BB}$	V_{BB}	σ	SNR
Photo-mixer (A) *I_d = 38 μa	124 μa	1.11 V	0.688 V	0.0087 V	48.5
	209	1.487	0.688	0.0097	82.4
	276	1.55	0.645	0.0116	78.0
	298	1.539	0.641	0.0096	93.5
	409	1.73	0.614	0.0085	131.3
	603	2.063	0.615	0.0114	127.0
	833	1.967	0.54	0.0109	130.9
	1034	2.182	0.538	0.0113	145.5
Photo-mixer (B) *I_d = 375 μa	60	1.72	0.86	0.0118	72.9
	105	2.06	0.80	0.0103	122.3
	210	2.87	0.74	0.0108	197.2
	335	3.49	0.70	0.0082	340.2
	445	4.14	0.69	0.01	345.0
	575	4.26	0.65	0.0087	414.9
	655	4.64	0.65	0.0096	415.6
	900	4.99	0.614	0.01	437.6
	1020	5.30	0.61	0.0098	478.6

TABLE II.- SNR CALCULATIONS

PARAMETER	DET. (A)	DET. (B)	I_{ph}	SNR (A)	SNR (B)
BB Temperature (K)	1273	1273	100 μa	88	170
η_{HET}	0.25	0.75	200	130	277
t	0.093	0.093	300	155	351
NF (dB)	2.0	2.0	400	171	404
R_{11} (ohms)	50	50	500	183	447
Dark Current (μa)	38	195*	600	191	478
B (MHz)	105	105	700	198	504
τ (sec)	1.0	1.0	800	203	525
			900	207	543
			1000	211	559

*Portion of 375 μa dark current that contributes to shot noise.

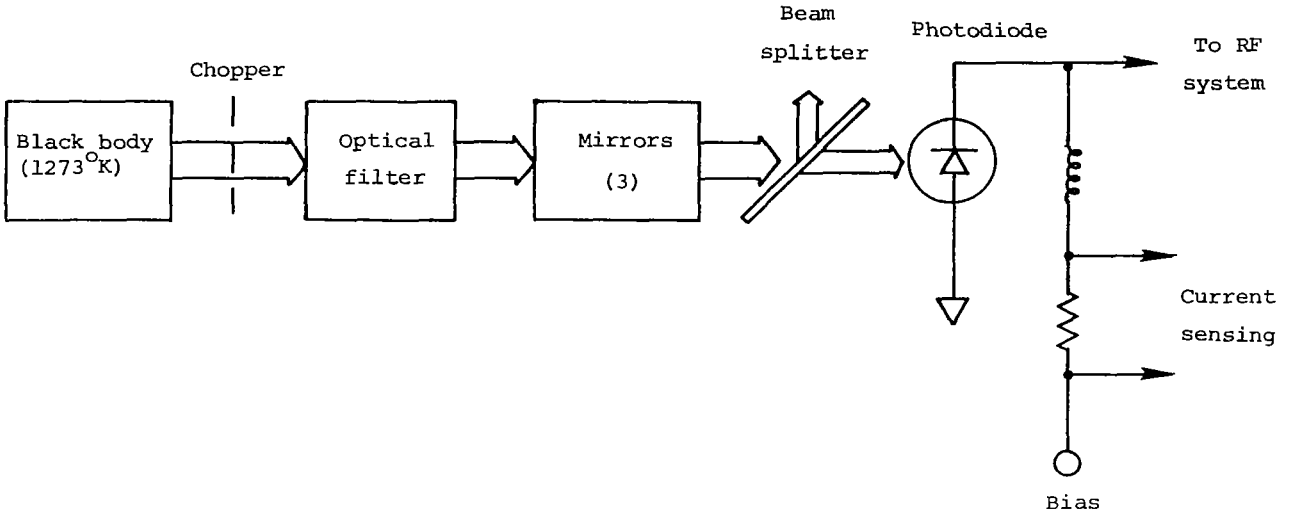

Figure 1.- Photodetector dc response test.

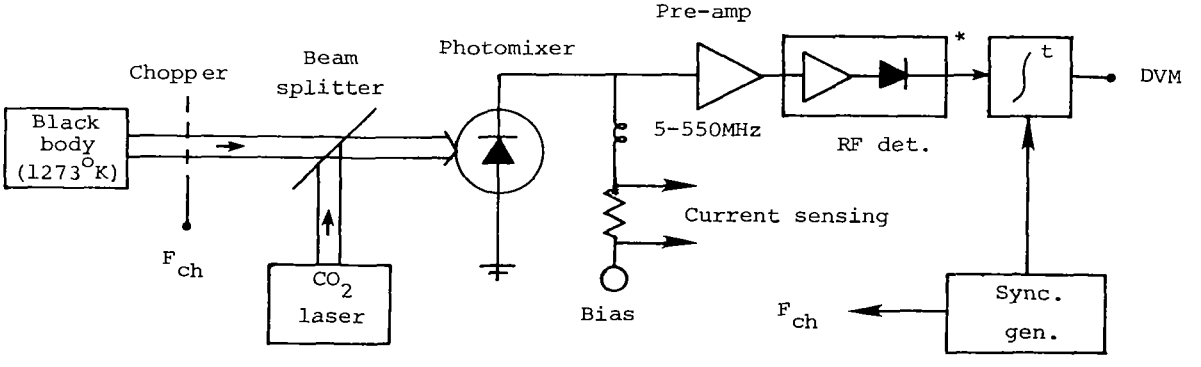

* Portion of AIL type 2392C radiometer: BW = 10 to 115 MHz

Figure 2.- Photomixer heterodyne response test set-up.

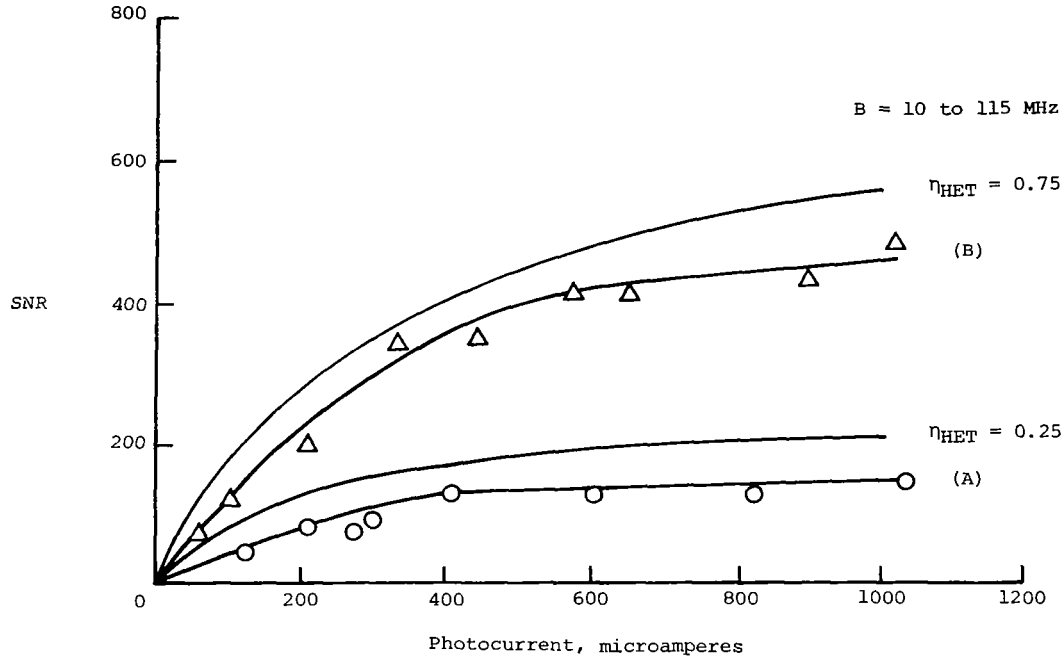

Figure 3.- Measured versus theoretical SNR.

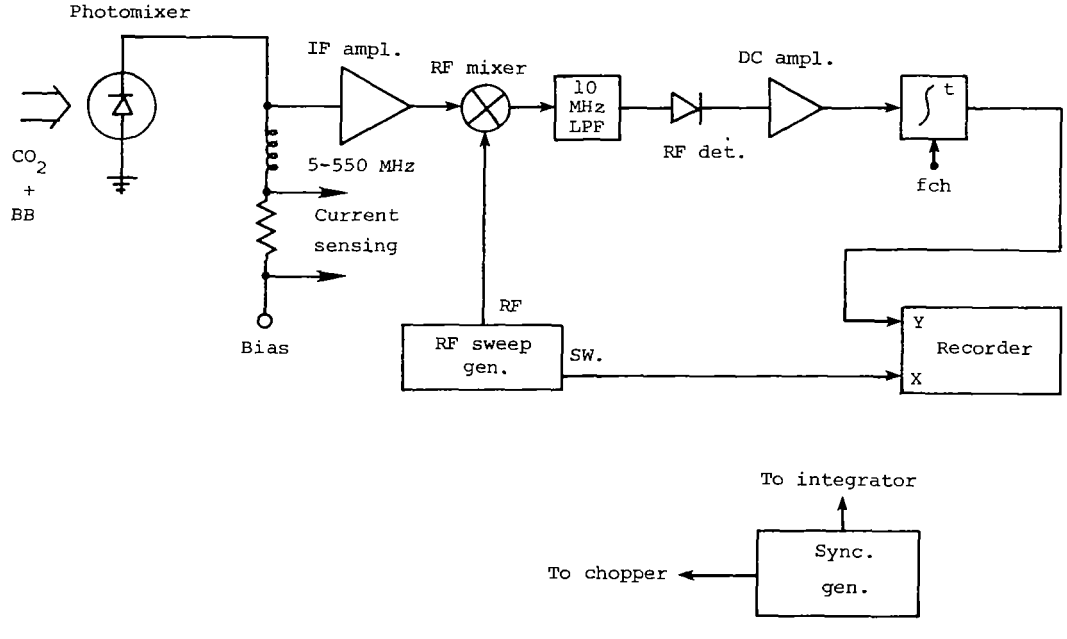

Figure 4.- Swept frequency response test set-up.

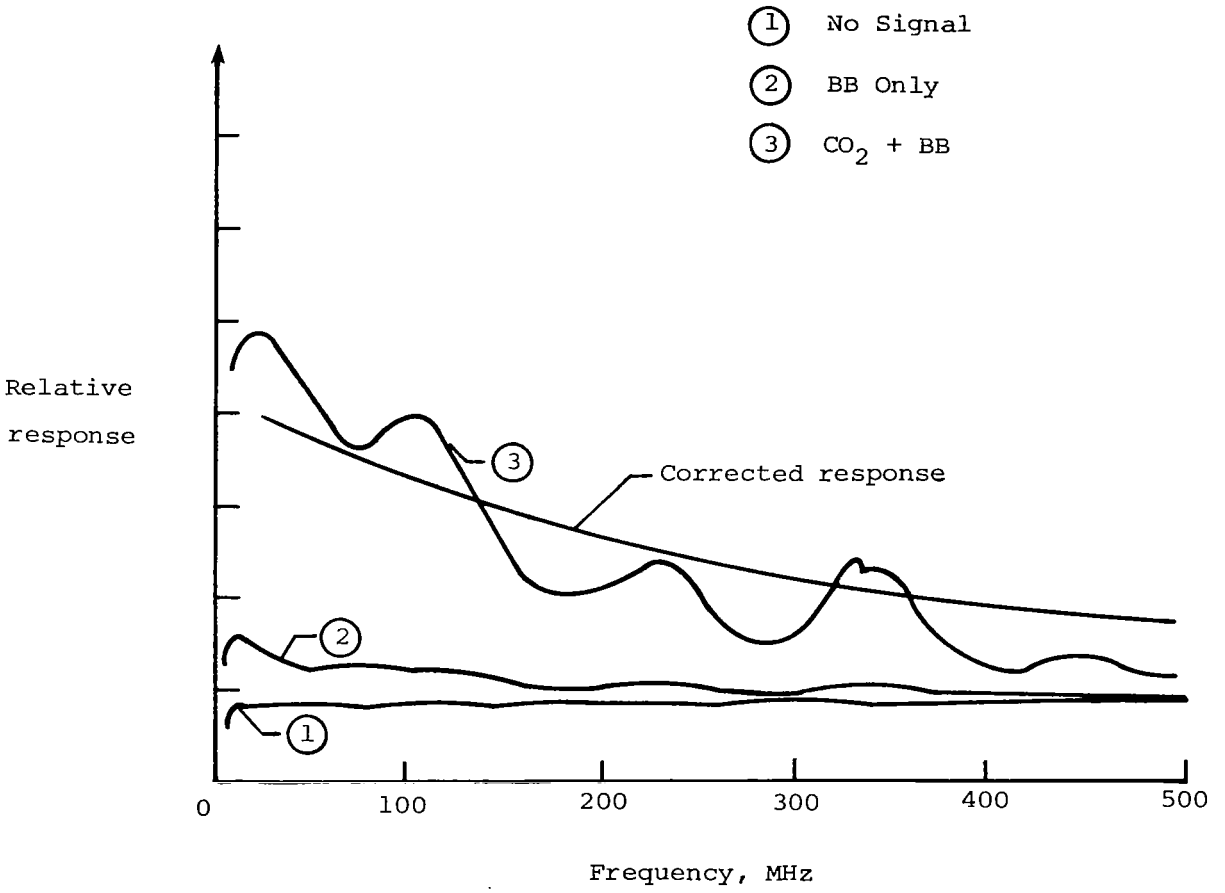

Figure 5.- Photomixer (A) response - 300 μα.

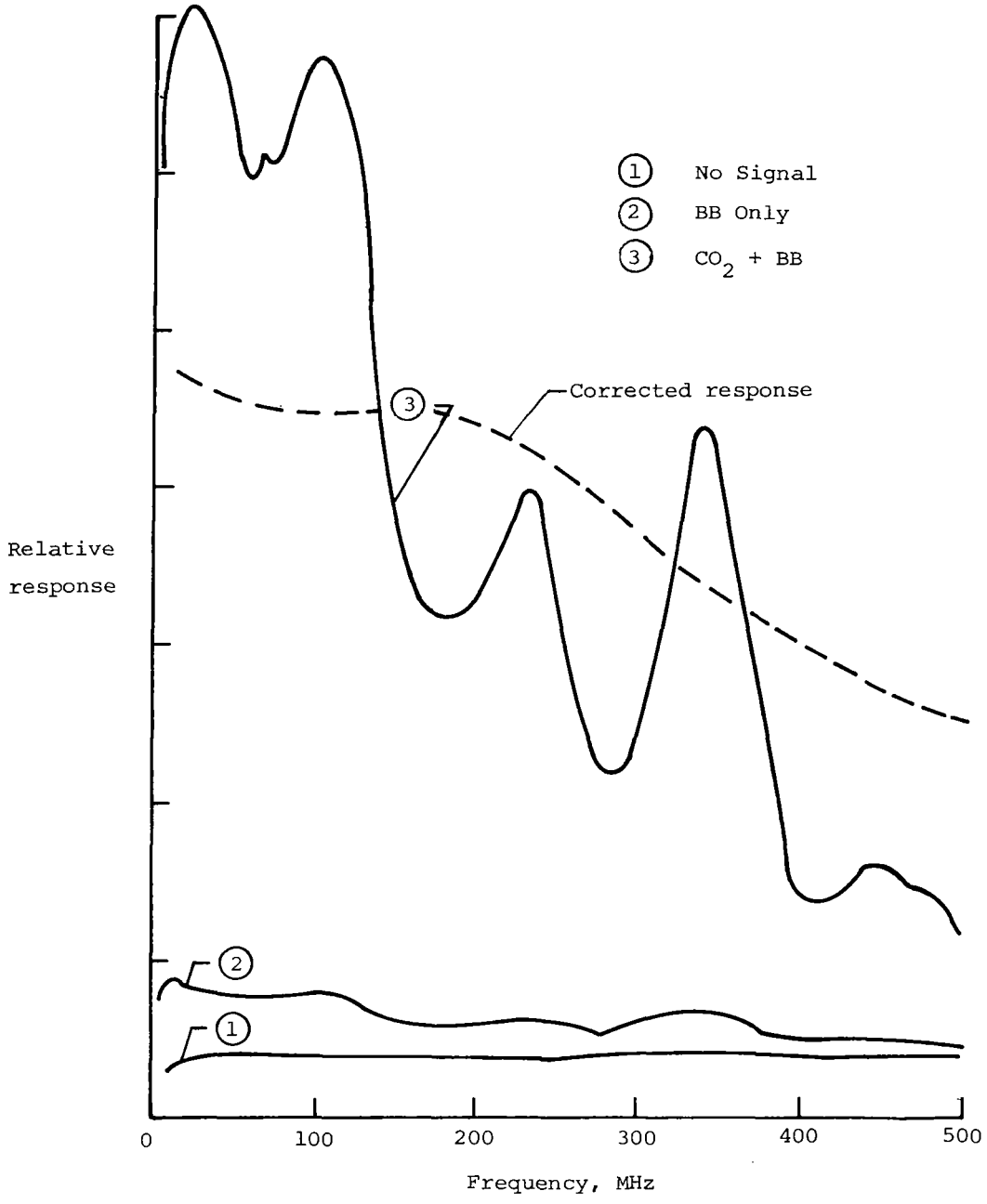

Figure 6.- Photomixer (B) response - 300 μα.

EXTENDING THE OPERATING TEMPERATURE, WAVELENGTH AND FREQUENCY RESPONSE OF HgCdTe HETERODYNE DETECTORS*

D. L. Spears
Lincoln Laboratory, Massachusetts Institute of Technology
Lexington, Massachusetts 02173

ABSTRACT

Near-ideal optical heterodyne performance has been obtained at GHz IF frequencies in the 10-μm-wavelength region with liquid-nitrogen-cooled HgCdTe photodiodes. Heterodyne NEP's as low as 2.7×10^{-20} W/Hz at 100 MHz, 5.4×10^{-20} W/Hz at 1.5 GHz, and 9.4×19^{-20} W/Hz at 3 GHz have been achieved. Various physical phenomena which occur within a photodiode and affect heterodyne operation have been examined in order to assess the feasibility of extending the operating temperature, wavelength, and frequency response of these HgCdTe photomixers. Hole transit time is seen to limit the fundamental bandwidth of 10-μm HgCdTe photodiodes to about 5 GHz. Long optical absorption lengths and small depletion widths of 30-μm photodiodes lead to a response limited by minority electron diffusion. High dark current, very small depletion widths, and slow ambipolar diffusion affect the sensitivity and speed of high-temperature 10-μm HgCdTe photodiodes. For $T \gtrsim 200$ K, p-type HgCdTe photoconductors should outperform photodiodes as moderately-wide-bandwidth photomixers.

INTRODUCTION

In recent years the liquid-nitrogen-cooled HgCdTe photodiode has emerged as the superior wide-bandwidth infrared heterodyne detector in the 10-μm-wavelength region (refs. 1 and 2). High dc quantum efficiencies (75% to 90%) and RC roll-off frequencies in excess of 2 GHz have been routinely achieved (ref. 3). These devices have been used as photomixers at IF frequencies as high as 60 GHz (ref. 2). Quadrantal arrays (ref. 4) have been used in a monopulse CO_2 radar system (ref. 5) for the past five years, tracking at IF frequencies over 1.25 GHz at distances of over 1000 km. The field of laser heterodyne radiometry has made extensive use of these high-sensitivity HgCdTe photomixers for such applications as profiling gas distributions and wind velocities on planets (refs. 6 and 7), measuring ozone (ref. 8) and chlorine monoxide (ref. 9) concentrations in the earth's stratosphere, and stellar heterodyne interferometry (ref. 10).

In this paper, the state-of-the-art performance of HgCdTe photodiode heterodyne receivers and the physics associated with their operation will be discussed. Optical absorption coefficient, intrinsic carrier concentration,

*This work was sponsored by the National Aeronautics and Space Administration, the Defense Advanced Research Projects Agency, and the Department of the Air Force.

interband tunneling, minority-carrier diffusion, and hole transit time will be shown to present limitations and performance trade-offs for a HgCdTe photodiode heterodyne receiver operating at a frequency of 10 GHz, a wavelength of 30 μm, or a temperature near 200K. A discussion of p-type HgCdTe photoconductors for use as elevated-temperature CO_2-laser photomixers is also presented.

STATE OF THE ART

During the past ten years, high-performance HgCdTe photodiodes and photodiode arrays have been developed at Lincoln Laboratory (ref. 3) for use as wide-bandwidth heterodyne receivers. Numerous test measurements were also developed to evaluate these photodiodes and characterize their sensitivity and bandwidth in the heterodyne mode of operation. The blackbody heterodyne measurement has proven to be the most direct and reliable method for determining the heterodyne NEP at high frequencies. Here the measured signal-to-noise ratio is compared with that calculated for an ideal photomixer in order to obtain an effective heterodyne quantum efficiency η_{EH} (refs. 11 and 12) from which the NEP can be determined using the expression NEP = $h\nu B/\eta_{EH}$, where B (noise bandwidth) is usually normalized to 1 Hz. In figure 1 are shown the best values of NEP obtained to date (ref. 3) as a function of IF frequency from 10 MHz to 4 GHz. At 1 GHz the NEP is only about a factor of 2 above the quantum limit of an ideal photodiode-receiver system. A sensitivity of 6.2×10^{-20} W/Hz has also been reported (ref. 13) at 2 GHz. As the IF frequency increases, RC roll-off, diffusion effects, and higher preamplifier noise figures all contribute to a degradation in NEP of present HgCdTe photomixers. (The noise figures of the decade-bandwidth preamplifiers used to obtain the data in figure 1 ranged from about 1.1 dB at 10 MHz to 4.5 dB at 4 GHz.) The best results currently are below 1.5 GHz where most of the effort has been concentrated. Twelve-element arrays with <u>average</u> sensitivities of 7.1×10^{-20} W/Hz at 1.5 GHz and 4.3×10^{-20} W/Hz at 0.76 GHz have been demonstrated (refs. 3 and 14).

The values of NEP in figure 1 were obtained under optimum conditions of bias V_a (typically 0.3 to 0.7 volts) and LO power P_{LO} (typically 0.2 to 0.5 mW). In figure 2 is shown the NEP of a typical high-performance diode as a function of photocurrent ($I_{PC} = \eta(o) q P_{LO}/h\nu$, where $\eta(o)$ is the dc quantum efficiency) at 0.76 GHz and 1.5 GHz. The solid curves were calculated from the simple asymptotic expression (ref. 15) for NEP shown in figure 2, containing the ratios of preamplifier noise to shot noise and dark-current noise to shot noise. T_a is the effective noise temperature of the photodiode and preamplifier, and R_L is the effective load resistance. For a 10.6-μm photodiode at 77K, the dark-current term is almost always negligible at wide bandwidths. (Not all sources of dark current are noisy at high frequencies.) These calculated curves provide a good fit to the data up to $I_{PC} = 1$ mA. Beyond that, the NEP saturates at a value higher than given by the simple expression. In some photodiodes, the NEP <u>increases</u> with increasing photocurrent. This saturation is a result of physical changes within the photodiode caused by the intense optical flux $\phi \approx 1 \times 10^{20}$ photons/cm^2-sec. These processes are complicated, are not well understood, and vary considerably with detector geometry, impurity doping levels, and energy gap ε_g. Bandfilling, increased recombination, ambipolar effects, increased tunneling current, and simple heating can all contribute. These will be described in more

detail below. The effects are more important at high frequencies where larger values of photocurrent are required to overcome higher amplifier noise. By simple narrow-band impedance matching, we have been able to reduce the LO power requirement at 0.76 GHz from 150 μW (1 mA) as shown in figure 2 to about 50 μW (0.3 mA). This is very difficult to do for multioctave bandwidths, however.

PHOTODIODE PHYSICS

Basic Device Operation

Several effects can contribute to the response of a p-n junction photodiode: RC roll-off, the transit time of electrons and holes across the depletion region, the diffusion of holes from the n-type region to the space-charge region, and the diffusion of electrons from the p-type region to the space-charge region. The diffusion time can be as long as the lifetime of the minority carriers, which for 0.1-eV HgCdTe can be several microseconds (ref. 16). Obviously, such slow diffusion effects must be minimized for high-performance wide-bandwidth operation. The most successful wide-bandwidth HgCdTe detector structure to date has been the shallow-junction n^+n^-p geometry (ref. 4), a cross section of which is shown in figure 3. Here the junction depth is about 3 μm, and under reverse bias the depletion width is about 2 μm, leaving a 1-μm region of undepleted n-type material at the surface. Also shown in figure 3 is the expected absorption profile for 10.6-μm radiation, where the absorption coefficient α is about 3000 cm^{-1} (ref. 17).

Electron-hole pairs are created in all three regions, giving rise to several different response mechanisms. Holes produced in the n-type region must diffuse to the edge of the space-charge region and drift across in order to generate current. This diffusion time is approximately equal to $(\delta x)^2/D$, where δx is the distance from the space-charge layer where the electron-hole pair is produced and $D = \mu kT/q$ is the minority-carrier diffusion coefficient (ref. 18). Hole diffusion is a slow process as $D_h^{-1} \approx 2$ nsec/$(\mu m)^2$ at 77K, and only those holes produced within a fraction of a μm of the space-charge region will respond in 0.3 nsec (i.e., 1 GHz bandwidth). The diffusion length of holes (i.e., the average distance they can diffuse before they recombine) can be as long as 10 μm, so $\eta(o)$ could be very high for a junction as deep as 10 μm. However, such a device would have a very slow response, even though the junction capacitance may be small. For electron concentrations greater than about 10^{16} cm^{-3} the conduction band becomes degenerate and this band filling reduces the absorption near the cutoff wavelength in the n^+ layer and improves the high frequency performance (refs. 1 and 17).

The transit time across the depletion region is given by

$$t_t = \int_{w_D - x'}^{w_D} v(x')^{-1}\, dx' \qquad (1)$$

where w_D is the depletion width, x' is the position within the depletion region, and $v(x')$ is the local carrier drift velocity in the depletion region. At very low

fields, electrons in HgCdTe reach a scattering-limited saturation velocity due to their high mobility (ref. 16) and, consequently, travel across the space-charge region with constant velocity of about 2×10^7 cm/sec or $v_e^{-1} = 0.005$ nsec/μm. If electron transit were the only limitation, a 10-GHz bandwidth could be obtained with depletion widths as large as 6 μm. However, holes must also transit the space-charge region and they have a relatively small mobility ($\mu_h = 600$ cm^2/V-sec at 77K) and their drift velocity v_h is a function of position. For a 0.1-eV photodiode, v_h^{-1} is expected to vary from 0.02 nsec/μm to 2 nsec/μm.

Carriers generated in the p-type region are controlled by electron diffusion which can be relatively fast. Assuming $\mu_e = 30\ 000$ cm^2/V-sec in the p-type region, we obtain $D_e^{-1} = 0.05$ nsec/(μm)^2, which means that electron-hole pairs created in the p-type region within a few micrometers of the junction can respond at 1 GHz. However, if the minority-electron concentration approaches 1% of the hole density (by either thermal generation or the local-oscillator flux), ambipolar effects (ref. 19) enter and begin to slow this diffusion process.

The response of any given photodiode will be a composite of all the above effects and the RC roll-off due to the external circuit and the junction capacitance. The relative importance of each of these processes will depend on the precise junction depth, doping levels, HgCdTe alloy composition, and the local-oscillator flux level.

Slow diffusion, which can frequently be seen as a tail on the pulse response of a photodiode, is particularly detrimental to heterodyne operation. This diffusion not only gives rise to a loss in signal at high frequency, but gives additional noise, as the slowly diffusing carriers have the same shot-noise spectra as the fast ones (ref. 20). The shot-noise-limited NEP in the presence of diffusion is given by

$$\mathrm{NEP}_{\min} = \frac{h\nu B}{\eta(0)}\left[\frac{\eta(0)}{\eta(f)}\right]^2 \tag{2}$$

where $\eta(f)$ is the quantum efficiency at frequency f. In a planar diode, laterial diffusion from around the perimeter can degrade its high-frequency performance. To get maximum sensitivity, the local oscillator should be confined to within the junction area. A steep mesa diode does not have this lateral diffusion problem.

Optical-Absorption Coefficient

A high value of optical absorption coefficient α is desirable in a wide-bandwidth photodiode in order to localize the photocarrier generation. However, in small-energy-gap material, α is not very large. In figure 4 is shown the wavelength dependence of α as given by the Kane theory (ref. 17) for HgCdTe with energy gaps of 0.1 eV and 0.035 eV, required for 10.6-μm and 30-μm photodiodes, respectively. Accurate experimental values have been reported only for $\alpha < 1000$ cm^{-1}. However, these calculated curves are consistent with all published

data and with transmission measurements made at Lincoln Laboratory on thin epitaxial samples. The solid curves do not take into account effects of charge carriers, impurities, or lattice vibrations, all of which tend to "smear out" the absorption edge. Band filling occurs in narrow-energy-gap HgCdTe with relatively low electron concentrations due to the small density of states in the conduction band. This produces a Burstein-Moss shift in the absorption edge as indicated by the dashed curves in figure 4, which show the effects of 1×10^{16} electrons/cm^3 in 0.1-eV HgCdTe and 1×10^{15} electrons/cm^3 in 0.035-eV HgCdTe. These electron densities are similar to those optically generated by a 100-μm-diameter LO beam producing $I_{PC} = 1$ mA. Thus if the background doping does not render the n-type region transparent near the absorption edge, the LO flux most likely will. At a wavelength of 10 μm, the absorption length $1/\alpha$ is about 3 μm, whereas for $\lambda = 30$ μm, $1/\alpha$ is about 10 μm. Confinement of the photocarrier generation is particularly difficult at 30 μm.

Tunneling Breakdown

The fundamental breakdown mechanism in a reverse-biased, narrow-energy-gap photodiode is the tunneling of electrons from the valence band to the conduction band due to the high field in the space-charge region. In a one-sided abrupt junction this field varies linearly across the depletion layer with a peak value of $2V/w_D$, where V is the sum of the external bias and the built-in junction potential ($\sim \varepsilon_g/2q$). The depletion width is given by

$$w_D = (2\kappa V/qN)^{1/2} \qquad (3)$$

where κ is the dielectric constant (~18.6 for $Hg_{0.8}Cd_{0.2}Te$) and N is the carrier concentration on the lightly-doped side of the junction. The value of w_D at breakdown sets a limit to the RC roll-off frequency of the device. In figure 5 is shown the calculated depletion width at a tunnel-current density of 1 A/cm^2 as a function of N for energy gaps of 0.1 eV and 0.035 eV, according to equation 16 of reference 21. The peak field at breakdown E_{max} is a strong function of energy gap ($E_{max} \propto \varepsilon_g^{5/3}$) but is relatively independent of N. E_{max} at $J_T = 1$ A/cm^2 is about 1 V/μm for $\varepsilon_g = 0.1$ eV and 0.17 V/μm for $\varepsilon_g = 0.035$ eV. As can be seen in figure 5, w_D at breakdown is a strong function of N and ε_g, varying approximately as $\varepsilon_g^{1.43}/N^{0.9}$. For $\varepsilon_g = 0.1$ eV, depletion widths in excess of 6 μm should be obtainable with present HgCdTe material technology ($N \sim 1 \times 10^{14}$ cm^{-3}). In high-performance wide-bandwidth photodiodes, w_D has been typically in the range of 2 to 3 μm at breakdown. A 1-GHz RC roll-off frequency into 50 Ohms for a 100-μm-diameter photodiode requires $w_D > 0.4$ μm, which is achieveable with $N = 2 \times 10^{15}$ cm^{-3} in 0.1-eV material. Clearly very high RC roll-off frequencies are possible with carrier concentrations in the low 10^{14} cm^{-3} range. A device sensitive at a wavelength of 30 μm, however, requires N to be less than 3×10^{14} cm^{-3} for a 1-GHz RC roll-off.

Intrinsic Carrier Concentration

A high density of carriers can be generated thermally in small-energy-gap semiconductors. In figure 6 is shown this intrinsic carrier concentration n_i as a function of temperature for $\varepsilon_g = 0.1$ eV and $\varepsilon_g = 0.035$ eV (ref. 22). For good diode characteristic, n_i should be much less than the doping levels on either side of the junction. For a wide-bandwidth 30-μm photodiode, this requires operation below about 50K to achieve n_i less than 10^{14} cm^{-3}, as seen from figure 6. Similarly a 10-GHz 10.6-μm diode must be operated below about 100K. Note as the 0.1-eV material approaches 200K, n_i becomes greater than 10^{16} cm^{-3}. Thus from figure 5 we see that the depletion width at breakdown in a high-temperature 10.6-μm photodiode will be much less than 1 μm and, since $1/\alpha >$ 3 μm, its response will be diffusion limited.

Photogenerated Carriers

The LO flux can cause enormous changes in the minority (and majority) electron and hole concentrations in a photodiode. In the absence of drift and diffusion effects, the steady-state excess photocarrier concentration is given simply by $\alpha \phi \tau$, where τ is the minority-carrier lifetime. In lightly doped 0.1-eV n-type HgCdTe, τ_h is of the order of 10^{-6} sec (ref. 16), so $\alpha \phi \tau_h \approx 3 \times 10^{17}$ cm^{-3} for $\phi = 10^{20}$ photons/cm^2-sec. This electron concentration would clearly give strong band filling (see figure 4) and render the material transparent near the absorption edge. Near a p-n junction, diffusion and drift effects must be considered, however (see reference 19). The excess minority-electron concentration δn in the p-type side of an n-p junction illuminated from the n-type side is given by

$$\delta n(x) = \alpha \phi \tau_e \quad (\exp(-x/L_e) - \exp(-\alpha x))/(\alpha^2 L_e^2 - 1) \qquad (4)$$

$$\alpha L_e \neq 1$$

where x is the distance from the space-charge region, and $L_e = (D_e \tau_e)^{1/2}$ is the minority-electron diffusion length. Figure 7 shows $\delta n(x)$ calculated using parameters appropriate for a typical 10.6-μm HgCdTe photodiode at moderate LO flux. The minority-electron lifetime τ_e is a strong function of hole concentration and 10 nsec is believed appropriate for a hole concentration p in the region of 3×10^{16} cm^{-3} at 77K (ref. 23). Note, the calculated photoelectron density peaks at a value of about 1×10^{14} cm^{-3} at a distance from the junction about equal to the absorption length. At this concentration, these minority electrons contribute significantly to the conductivity due to the high electron-to-hole mobility ratio b (~100 in HgCdTe). In this ambipolar regime (ref. 19), the diffusion coefficient is given by

$$D_a = D_e \, (1 + n/p)/(1 + b \, n/p) \qquad (5)$$

where $n = \delta n + n_0$. As n approaches p/b, D_a decreases, slowing down the diffusion process, which in turn reduces the frequency response and quantum

efficiency. For low values of p, ambipolar effects enter in at lower values of optical flux. In the very-strong-flux limit, the lifetime, the mobility, and the absorption coefficient are all expected to be functions of LO power, and a self-consistent calculation of $\delta n(x)$ is very difficult.

ULTRAWIDE-BANDWIDTH PHOTODIODES

With increasing bandwidth, hole transit time begins to affect the response of a 10-μm HgCdTe photodiode, as the hole velocity v_h within the space-charge region is low and a function of position, $v_h(x) = \mu_h E(x)$. In the case of a one-sided abrupt junction, $E(x)$ varies linearly across the space-charge region. If we assume $v_h(x) = (x/w_D)\, v_m + v_o$, then integrating equation 1 we obtain the transit time,

$$t_t(x) = \frac{w_D}{v_m} \ln \left\{ \frac{w_D}{x} \left(\frac{1 + v_o/v_m}{1 + (v_o/v_m)(w_D/x)} \right) \right\} \qquad (6)$$

for a hole generated within the space-charge region a distance x from the n-type side. Using this expression we have made numerous numerical calculations of the step response of photodiodes assuming: 1) the photogeneration varies exponentially into the device as $e^{-\alpha x}$ and 2) the delay in the response of each of these photogenerated carriers is given by the sum of their diffusion time $(\delta x)^2/D$ and transit time, i.e. the time required for holes to reach the p-type region and electrons to reach the n-type region. For $1/\alpha \ll w_D$ (which is the common situation for wide-energy-gap, high-speed photodiodes), a shallow-junction p^+-n^- device is the best structure for minimizing hole-transit effects as the electron-hole pairs are generated near the p^+ side of the depletion layer and only electron transit is involved. However, for small absorption coefficients, such as here at $\lambda \approx 10\mu m$, the difference between an n-p and p-n diode structure is small. The step response calculated for two n^+n^-p photodiodes with depletion widths of 4 μm are shown in figure 8. Here the RC time constant is assumed zero and the undepleted n^+-region is assumed transparent, i.e. no hole-diffusion effects. The curve on the right is for a simple triangular field profile (E_{max} = 1 V/μm). Electrons generated near the p side of the space-charge region give the initial response after a 15-psec transit time delay. The slower rise continuing to about 120 psec is the delayed response of holes produced throughout the space-charge region. If the thickness of the n^- region is only 4 μm and very lightly doped (i.e. pin-type device), "punch through" can occur well before breakdown, giving a more uniform field profile as shown in the diagram on the left in figure 8. If the average field is 75% of the breakdown field (i.e. 0.75 V/μm), the step response on the left is calculated. The very slow rise at the top is due to the comparatively slow diffusion of photoelectrons produced in the p-type region. Transit time could be reduced by decreasing the width of the space-charge layer; however, this would result in a loss in quantum efficiency and increased junction capacitance. We chose w_D = 4 μm here because it is greater than $1/\alpha$ and gives a 10-GHz RC roll-off frequency for a 100-μm-diameter photodiode. Judging from the step response shown in figure 8, a 10-GHz bandwidth (which requires a 30-psec rise time) does

not appear possible in a 10.6-μm HgCdTe photodiode. The fundamental bandwidth limit will be about 5 GHz. However, since the shot noise spectra is also influenced by transit time (ref. 24) (both the signal and the shot noise will roll off between 5 and 10 GHz), reasonably good sensitivity (1×10^{-19} W/Hz) may be possible at 10 GHz in an optimized device.

LONG-WAVELENGTH PHOTODIODES

In figure 9 is shown the reverse-bias I-V characteristic calculated for a 100-μm-diameter, 0.035-eV n^--p photodiode at 40K with $n^- = 2 \times 10^{14}$ cm^{-3}. For the case of Auger-limited lifetimes (refs. 16 and 23) used here, the dominant diffusion component is from the p-type side and given by

$$I_D = A\,(n_i^2/p)\,e(D_e/L_e) \qquad (7)$$

where A is the photodiode area. As seen from figure 9, this current is small ($\sim$0.1 A/cm^2) at 40K. The tunnel current I_T shows a characteristic soft breakdown. The magnitude of I_T is not a problem for V < 100 mV; however, for the impedance dV/dI to be greater than 50 Ohms, the bias must be below about 60 mV, where w_D = 0.7 μm. Since $1/\alpha \gtrsim 10$ μm, essentially all of the photocarrier generation takes place in the p-type region. In a thick photodiode, the frequency response limited by electron diffusion is approximately $\alpha^2 D_e$ (ref. 24), which for T = 40K, μ_e = 50 000 cm^2/V-sec and α = 1000 cm^{-1}, is about 250 MHz. A diffusion-limited bandwidth of 1 GHz could be obtained by thinning the p-type region to about 3 μm. With a reflecting contact to increase the absorption, a quantum efficiency of 40% should be possible. However, a very important question remains. The minority electron mobility μ_e is expected to be a function of hole concentration. Can μ_e = 50 000 cm^2/V-sec be obtained with $p = 1 \times 10^{16}$ cm^{-3} in 0.035-eV HgCdTe ? A concentration much less than this will be susceptible to strong ambipolar effects. If these parameters are consistent, then an NEP of about 5×10^{-20} W/Hz at 1 GHz should be possible at 30 μm.

ELEVATED-TEMPERATURE PHOTODIODES

There has been great interest in developing CO_2 laser photomixers operating at temperatures in the region of 200K where thermoelectric coolers are convenient, reliable and reasonably efficient. At elevated temperatures, narrow-energy-gap photodiodes are subject to very high dark current in reverse bias due to diffusion, drift and/or tunneling. If the minority-carrier recombination times in a 0.1-eV photodiode are Auger-limited (refs. 16 and 23), then electron-diffusion current from the p-side of the junction is the dominant diffusion component and relatively independent of p. In the Auger limit, τ_e varies as $1/p^2$ (see reference 23). In figure 10 is shown this diffusion current (calculated from equation 7) as a function of temperature for energy gaps of 0.11 eV and 0.14 eV, corresponding to α = 1000 cm^{-1} at 11 μm and 9 μm (ref. 25), respectively. Also shown are data taken on a photodiode with a cutoff wavelength of about 9 μm at 185K, which are in reasonable agreement with these calculations. Diffusion current can be reduced by thinning the p-type region in order to limit the diffusion volume (ref. 19). However, diffusion-current

values below these curves in figure 10 are yet to be reported. Also, this simple theory is not strictly valid at these very high current densities ($\sim$100 A/cm^2). If either n or p is close to the value of n_i, a large component of drift current also flows across the junction; whereas if n and p are both much greater than n_i, tunneling current becomes excessive at even very low biases. In both of these cases, the calculated maximum reverse-bias resistance of a 200K 0.12-eV HgCdTe photodiode is only a few ohms. The frequency response at high temperatures of an optimally designed shallow-junction n-p photodiode is determined by minority-electron diffusion, which is in the strong ambipolar regime. Here, as seen from equation 5, D_a approaches 2 D_e/b and the absorption-limited diffusion time increases into the range of 10 to 50 nsec. Faster response can be achieved by heavily doping the p-type region and reducing the lifetime of the minority electrons, but this is at the expense of quantum efficiency.

At 173K, we have measured an NEP of 4 x 10^{-19} W/Hz at 9.3 μm for a 90-MHz photodiode, and an NEP of 8 x 10^{-19} W/Hz at 10.6 μm has been reported (ref. 26) also at 173K for a 23-MHz device. With further development, NEPs approaching 1 x 10^{-19} W/Hz and bandwidths approaching 100 MHz should be realized in 180K photodiodes. This performance will be very sensitive to temperature, however.

p-TYPE HgCdTe PHOTOCONDUCTORS

As the performance of HgCdTe photodiodes degrades with increasing temperatures, the p-type HgCdTe photoconductor becomes very attractive as a moderately-wide-bandwidth CO_2-laser photomixer. In this device, the bandwidth and photoresponse are determined by the lifetime τ_e and mobility μ_e of the minority electrons. In addition, the resistance can be reasonably high at 200K due to the low mobility of holes. In order to obtain quantum-noise-limited performance in a p-type photoconductor (NEP = 2 $h\nu B/\eta$), the LO power must be such that (1) the density of photoelectrons greatly exceeds the background minority electron density (n_i^2/p) and (2) the associated g-r noise greatly exceeds the Johnson or thermal noise 4kT/R of the detector and preamplifier (ref. 24). Both of these requirements are very sensitive to n_i, μ_e, and τ_e. The dashed curve in figure 11 shows the photoconductor bandwidth $(2\pi\tau_e)^{-1}$ determined from the calculated Auger-limited lifetime (ref. 23) as a function of hole concentration at 200K for 0.12-eV HgCdTe (n_i = 1 x 10^{16} cm^{-3}). Using this theoretical lifetime and assuming μ_e = 10 000 cm^2/V-sec, we have calculated (unpublished work of D. L. Spears, P. E. Duffy, and C. D. Hoyt) the LO power required in order to achieve a photoelectron concentration equal to the background electron concentration and a g-r noise equal to the thermal noise. These values of P_{LO} are a strong function of p as shown by the solid curves in figure 11. A minimum in the calculated LO power occurs for p = 3 x 10^{16} cm^{-3}, with a corresponding bandwidth of 12 MHz. Note, for a 100 MHz bandwidth, the calculated CO_2 LO power is about 10 mW. The over-100-mW requirement at 1 GHz is unreasonable, as excessive heating (ΔT > 100K) would surely occur in these small-area (100 μm x 100 μm) devices.

P-type photoconductors we have fabricated have shown a 9.3-μm NEP of about 2 x 10^{-19} W/Hz at 38 MHz at 200K, with a bandwidth of over 50 MHz and a LO power requirement of 7 mW. Other devices with bandwidths in excess of

150 MHz have shown NEPs better than 4×10^{-19} W/Hz at 200K. With the optimum geometry, energy gap, and hole concentration, we expect that an NEP of about 1×10^{-19} W/Hz at 100 MHz could be achieved in a 200K photoconductor with a total power dissipation of 10 mW, which is compatible with a 1-watt TE cooler.

REFERENCES

1. C. Verie and M. Sirieix "Gigahertz Cutoff Frequency Capabilities of CdHgTe Photovoltaic Detectors at 10.6 μm," IEEE J. Quantum Electron., vol. QE-8, pp. 180-191, Feb. 1972.

2. D. L. Spears and C. Freed "HgCdTe Varactor Photodiode Detection of cw CO_2 Laser Beats Beyond 60 GHz." Appl. Phys. Lett., vol. 23, pp. 445-447, Oct. 1973.

3. Solid State Research Reports, Lincoln Laboratory, M.I.T. (1970:4), (1973:2), (1974:4), (1975:3), (1976:3), (1977:1), (1977:4), (1978:1) and (1978:3).

4. D. L. Spears "Planar HgCdTe Quadrantal Heterodyne Arrays with GHz Response at 10.6 μm," Infrared Phys., vol. 17, pp. 5-8, Jan. 1977.

5. R. Teoste, W. J. Scouler and D. L. Spears "Coherent Monopulse Tracking with a 10.6-μm Radar," Digest of Technical Papers, 1977 IEEE/OSA Conf. on Laser Engineering and Applications, pp. 40-41, June 1-3, 1977, Washington, D.C. (IEEE, New York, 1977).

6. A. L. Betz, R. A. McLaren, E. C. Sutton and M. A. Johnson "Infrared Heterodyne Spectroscopy of CO_2 in the Atmosphere of Mars," Icarus, vol. 30, pp. 650-662, 1977.

7. T. Kostiuk, M. J. Mumma, J. J. Hillman, D. Buhl, L. W. Brown, J. L. Faris and D. L. Spears "NH_3 Spectral Line Measurements on Earth and Jupiter using a 10-μm Superheterodyne Receiver," Infrared Phys., vol. 17, p. 431-439, Nov. 1977.

8. M. A. Frerking and D. J. Muehlner "Infrared Heterodyne Spectroscopy of Atmospheric Ozone," Appl. Optics, vol. 16, pp. 526-528, Mar. 1977.

9. R. T. Menzies "Remote Measurement of ClO in the Stratosphere," Geophys. Res. Lett., vol. 6, p. 151-154, Mar. 1979.

10. E. C. Sutton, J. W. V. Storey, A. L. Betz, C. H. Townes and D. L. Spears "Spatial Heterodyne Interferometry of VY Canis Majoris, Alpha Orionis, Alpha Scorpii, and R Leonis at 11 Microns," Astrophys. J. (Letters), vol. 217, pp. L97-L100, Oct. 1977.

11. B. J. Peyton, A. J. DiNardo, S. C. Cohen, J. H. McElroy and R. J. Coates "An Infrared Heterodyne Radiometer for High-Resolution Measurements of Solar Radiation and Atmospheric Transmission," IEEE J. Quantum Electron., vol. QE-11, pp. 569-574, Aug. 1975.

12. R. T. Ku and D. L. Spears "High-Sensitivity Infrared Heterodyne Radiometer Using a Tunable-Diode-Laser Local Oscillator," Optics Lett., vol. 1, pp. 84-86, Sept. 1977.

13. J. F. Shanley and L. C. Perry "Wide Bandwidth 10.6 μm (Hg,Cd)Te Photodiodes for Infrared Heterodyne Applications," Tech. Digest of the Int. Electron Device Meeting, pp. 424-429, Dec. 1978, Washington, D.C.

14. D. L. Spears "Wide Bandwidth CO_2 Laser Photomixers," Proc. of the S.P.I.E., vol. 227, 1980.

15. B. J. Peyton, A. J. DiNardo, G. M. Kanischak, F. R. Arams, R. A. Lang and E. W. Sard "High-Sensitivity Receiver for Infrared Laser Communications," IEEE J. Quantum Electron., vol. QE-8, pp. 252-263, Feb. 1972.

16. R. Dornhous and G. Nimtz "The Properties and Applications of the $Hg_{1-x}Cd_xTe$ Alloy System," in Solid State Physics 78, G. Hohler, ed. (Springer-Verlag, New York, 1966).

17. M. D. Blue "Optical Absorption in HgTe and HgCdTe," Phys. Rev., vol. 134, p. A226-A234, Apr. 1964.

18. D. E. Sawyer and R. H. Rediker, "Narrow Base Germanium Photodetectors," Proc. IRE, vol. 46, pp. 1122-1130, June 1958.

19. John P. McKelvey, Solid State and Semiconductor Physics (Harper and Row, New York, 1966).

20. D. L. Spears and R. H. Kingston "Anomalous Noise Behavior in Wide Bandwidth Photodiodes in Heterodyne and Background-Limited Operation," Appl. Phys. Lett., vol. 34, pp. 589-590, May 1979.

21. W. W. Anderson "Tunnel Current Limitations of Narrow Bandgap Infrared Charge Coupled Devices," Infrared Phys., vol. 17, pp. 147-164, Mar. 1977.

22. Y. Nemirovsky and E. Finkman "Intrinsic Carrier Concentration of $Hg_{1-x}Cd_xTe$," J. Appl. Phys., vol. 50, pp. 8107-8111, Dec. 1979.

23. T. N. Casselman and P. E. Peterson "A Comparison of the Dominant Auger Transitions in p-type (Hg,Cd)Te," Solid State Comm., vol. 33, pp. 615-619, Feb. 1980.

24. R. H. Kingston, Detection of Optical and Infrared Radiation, (Springer-Verlag, New York, 1978).

25. E. Finkman and Y. Nemirovsky "Infrared Optical Absorption of $Hg_{1-x}Cd_xTe$," J. Appl. Phys., vol. 50, pp. 4356-4361, June 1979.

26. T. Koehler "10.6 Micron (Hg,Cd)Te Photodiode Module," Research and Development Report, Honeywell Radiation Center, ECOM-71-0236-F, Oct. 1976.

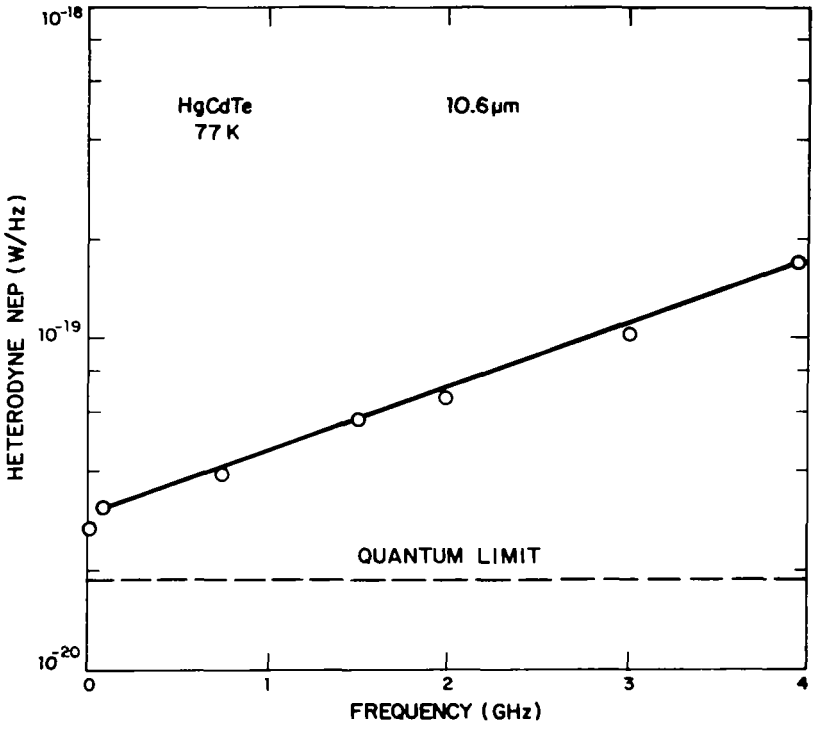

Figure 1.- State-of-the-art heterodyne NEP at 10.6 μm as function of IF frequency.

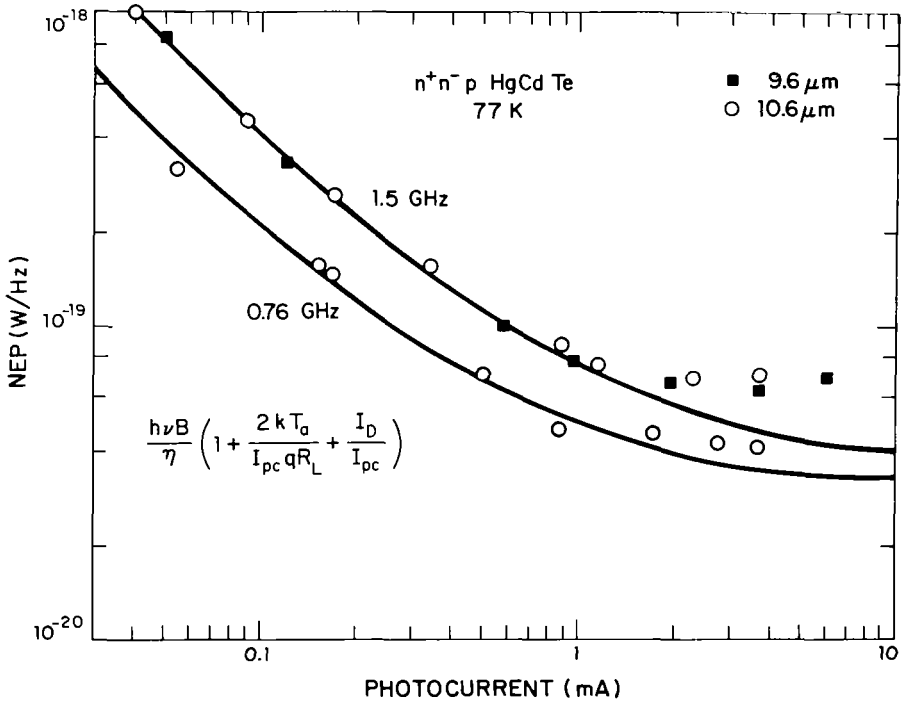

Figure 2.- Heterodyne NEP as function of LO-induced photocurrent for high-performance HgCdTe photodiode.

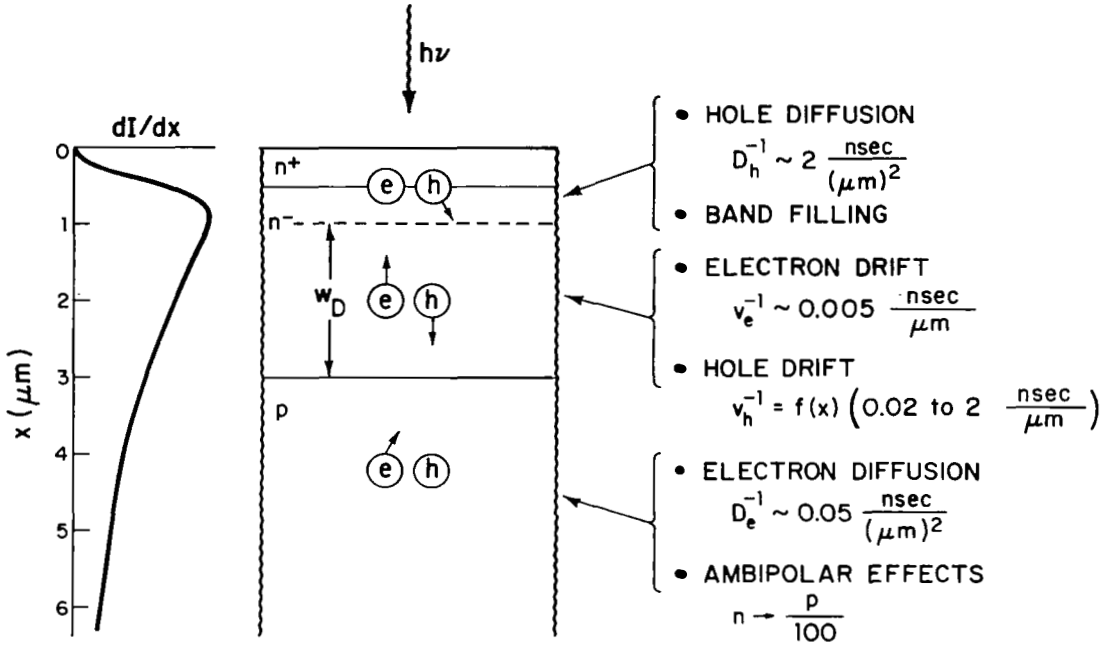

Figure 3.- Cross section of n^+n^-p HgCdTe photodiode showing absorption profile at 10.6 μm and drift and diffusion parameters at 77 K.

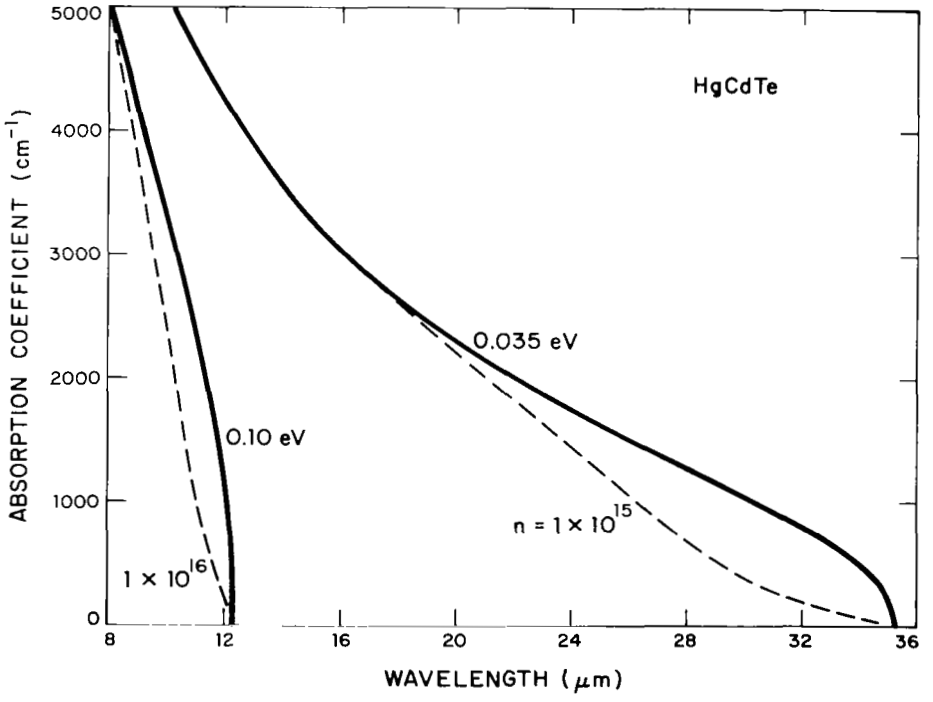

Figure 4.- Calculated optical absorption coefficient as function of wavelength for HgCdTe with energy gaps of 0.1 and 0.035 eV.

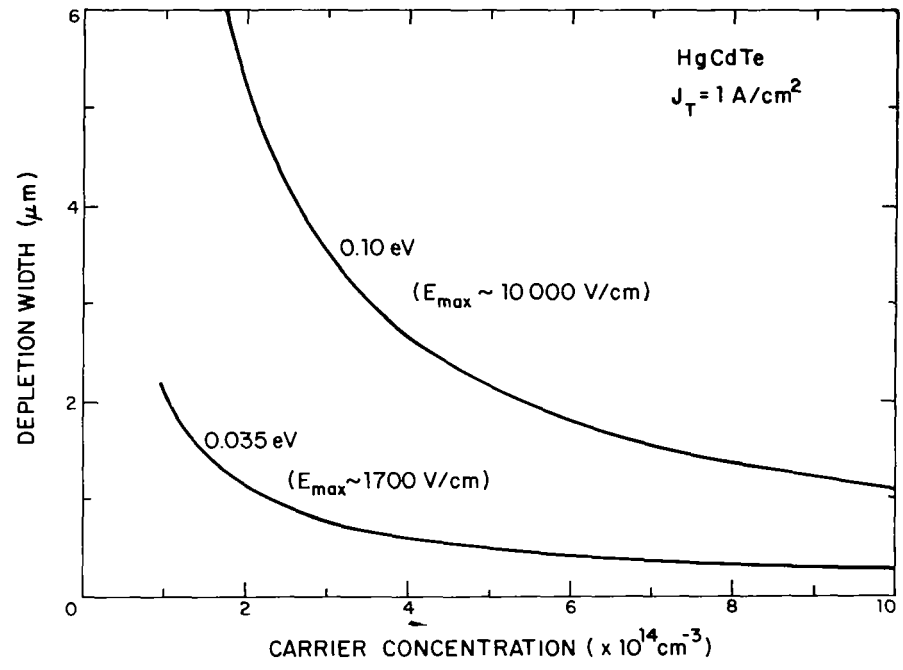

Figure 5.- Calculated junction depletion width at tunnel current density of 1 A/cm^2 as function of carrier concentration for one-sided abrupt junctions in HgCdTe with energy gaps of 0.1 and 0.035 eV.

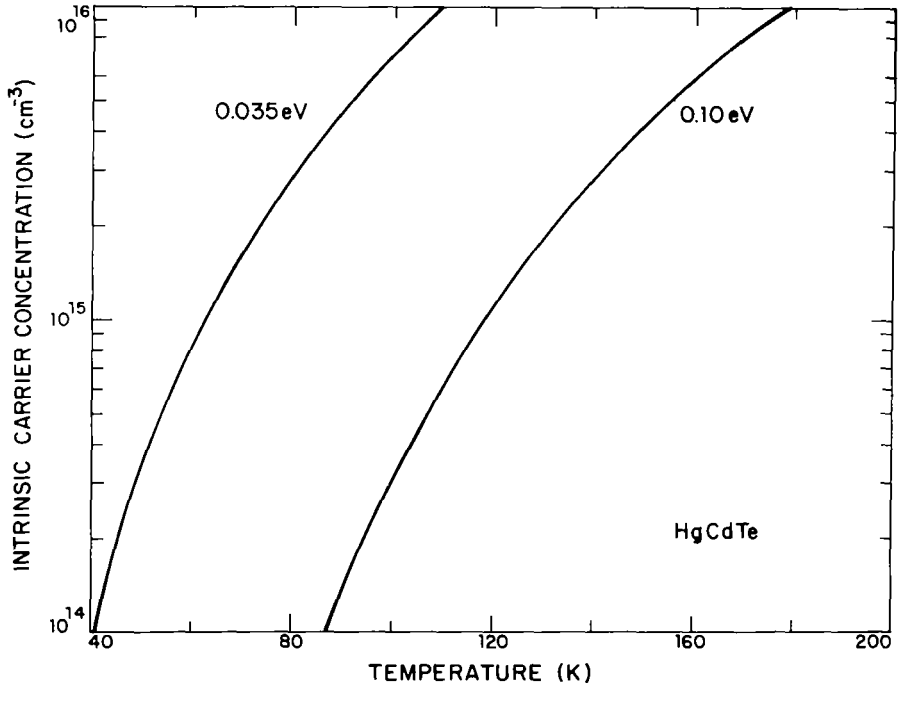

Figure 6.- Intrinsic carrier concentration as function of temperature for HgCdTe with energy gaps of 0.1 and 0.035 eV (ref. 22).

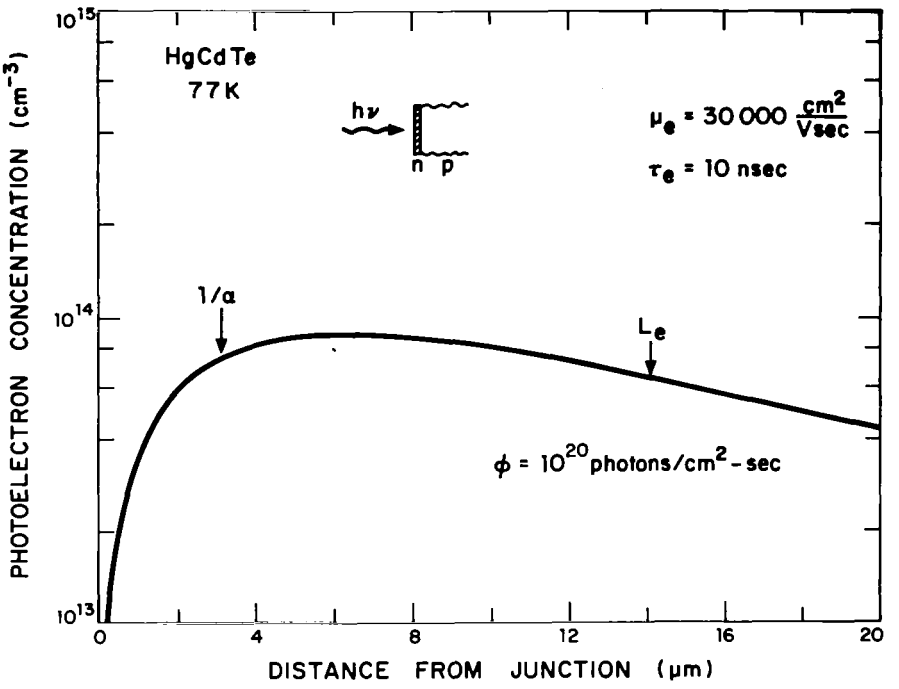

Figure 7.- Calculated steady-state minority electron distribution in n-p HgCdTe photodiode for typical LO flux level.

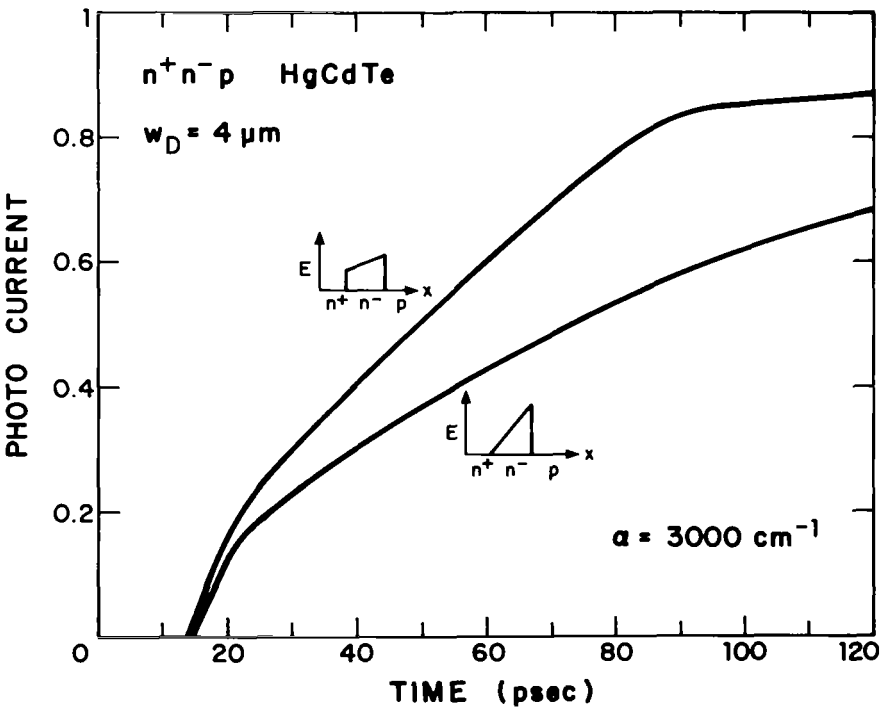

Figure 8.- Calculated step response of two reverse-biased n^+n^-p HgCdTe photodiodes (assuming RC = 0) showing transit time delays.

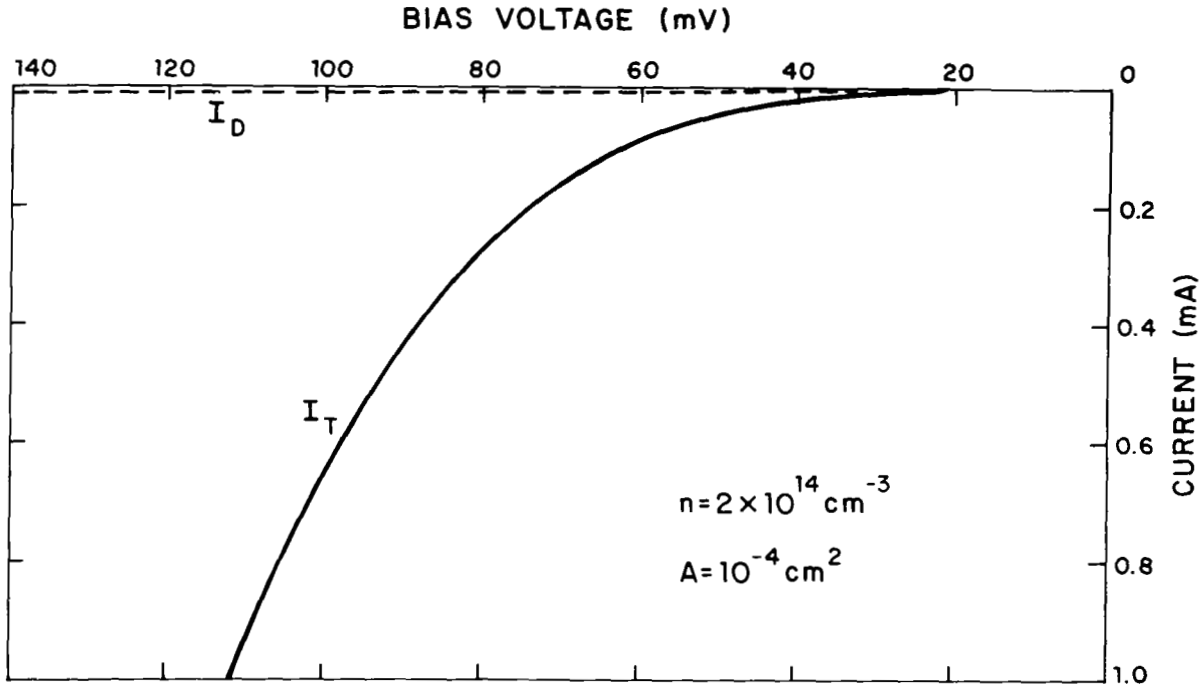

Figure 9.- Calculated reverse-bias I-V characteristic for 30-μm HgCdTe photodiode at 40 K.

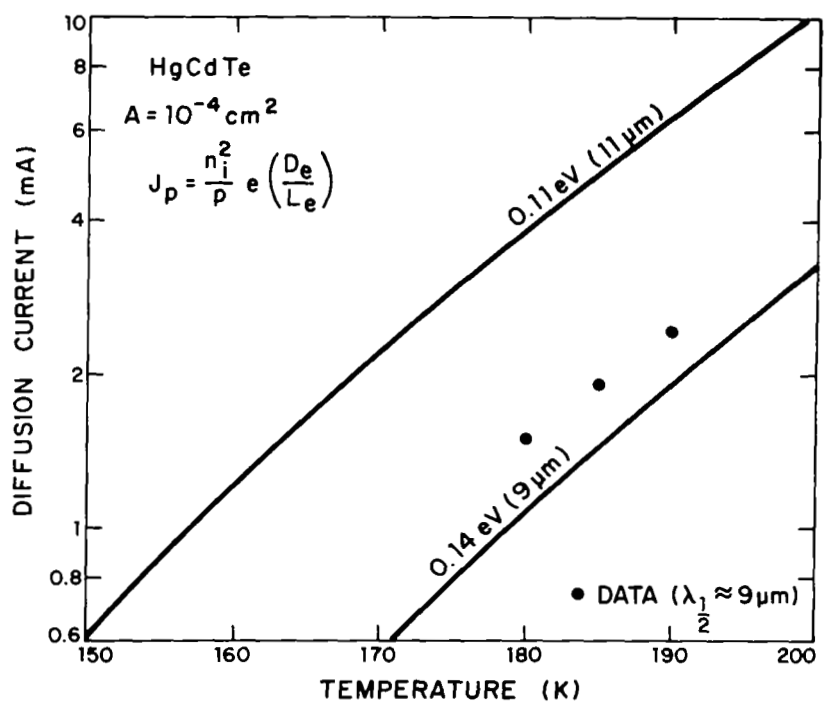

Figure 10.- Calculated diffusion current as function of temperature for HgCdTe photodiodes with energy gaps of 0.11 and 0.14 eV, along with data for 9-μm photodiode.

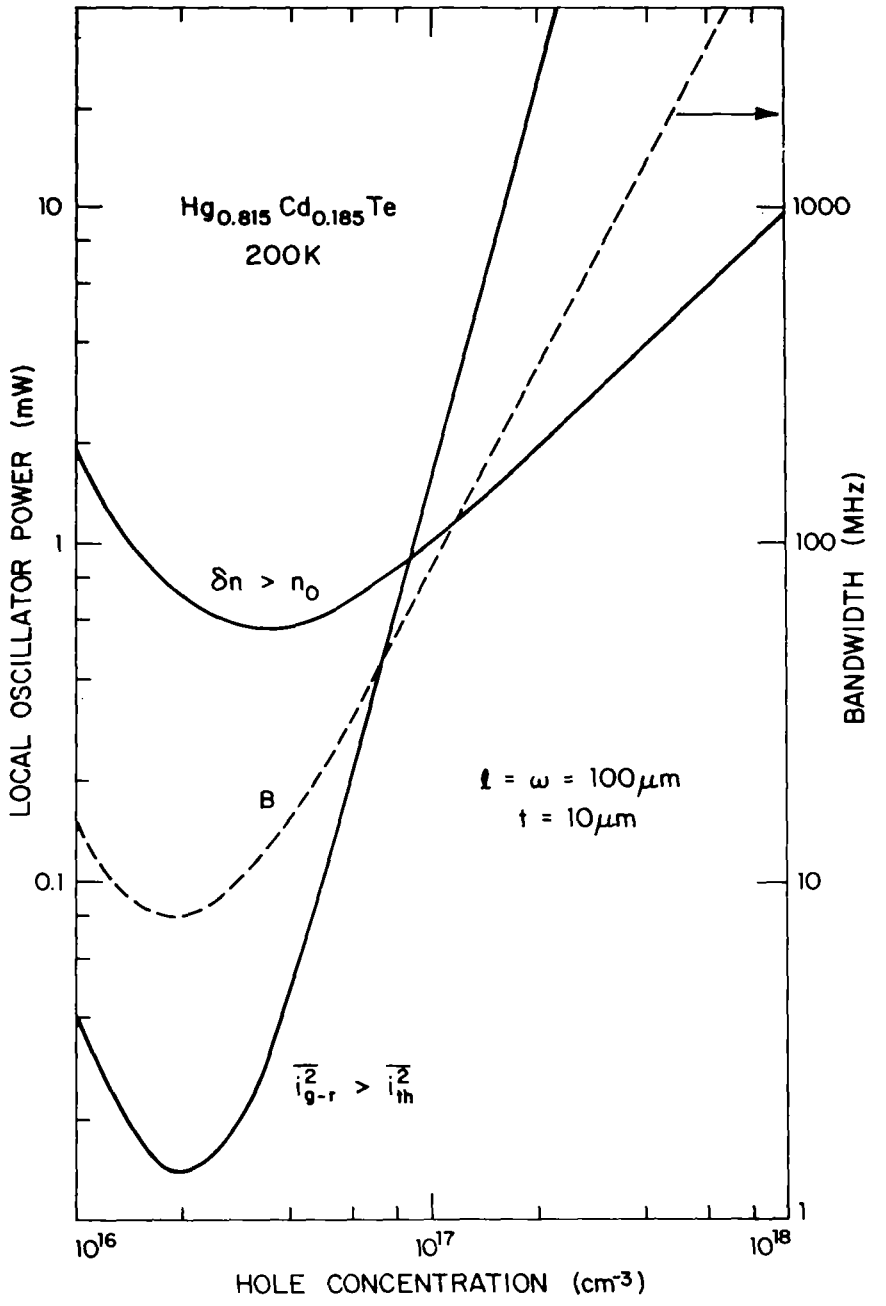

Figure 11.- Calculated bandwidth and heterodyne LO power requirements at 200 K as function of hole concentration for p-type HgCdTe photoconductors.

INFRARED HETERODYNE RECEIVERS WITH IF RESPONSES APPROACHING 5 GHz*

J.M. Wolczok and B.J. Peyton
Eaton Corporation, AIL Division, Melville, NY 11747

SUMMARY

Laser probing of high density tokamak plasmas has led to the development of specialized coherent 10.6 μm infrared receivers with IF frequency responses approaching 5 GHz. CO_2 lasers are employed for these applications because of their availability, stability, and high average-power levels. The use of a high-power laser probing source and a highly scattering plasma requires the use of a photomixer which can detect weak laser signals in the presence of high stray-laser levels. Accordingly, heterodyne receivers which employ extrinsic photoconductive Ge:Cu(Sb) mixers have been developed for measurements of CO_2 laser scattering to determine: (1) the driven lower-hybrid wave density fluctuations, and (2) the plasma ion temperature of dense tokamak plasmas.

The liquid helium cooled Ge:Cu(Sb) detectors are operated in a high photogain mode in which the photomixer impedance is approximately 1200 ohms. This paper reports on IF impedance matching techniques which are aimed at optimizing: (1) the power transfer between the photomixer and the IF preamplifier, and (2) the receiver sensitivity over the IF frequency range of interest. In particular, cooled 1200 to 50 ohm impedance matching networks have been employed to optimize heterodyne receiver performance. Although this work has been carried out with Ge:Cu photomixers, these IF impedance matching techniques are also applicable to other wideband infrared photomixers, such as PV:HgCdTe.

Two relatively narrow band 10.6 μm heterodyne receivers with IF center frequencies near 2.5 and 4.6 GHz have been developed for lower-hybrid wave density fluctuation measurements in tokamak plasmas. The 2.5 GHz response heterodyne receiver provides an NEP of 2×10^{-19} W/Hz for an applied dc bias power of 104 mW, while the 4.6 GHz response heterodyne receiver provides an NEP of 4.4×10^{-19} W/Hz for an applied dc bias power of 150 mW. A broadband 10.6 μm heterodyne receiver has also been developed for remote ion temperature measurements of a tokamak plasma. This receiver operates over the 200 to 1300 MHz IF frequency range and provides an NEP as low as 1.5×10^{-19} W/Hz with an applied dc bias power of only 60 mW.

*This work was supported by the United States Energy Research and Development Administration.

PLASMA PROBING

CO_2 laser scattering of quasi-free electrons in a dense tokamak plasma (ref. 1) permits the remote determination of: (1) the amplitude and spectral and spatial distributions of driven lower-hybrid wave fluctuations (ref. 2 and 3), and (2) the plasma ion temperature (ref. 4 and 5). The use of a 100 W CW CO_2 laser radiation results in a forward scattering angle of about 1° and a relatively large amount (1 to 3 mW) of stray laser radiation at the infrared detector. However, the overall heterodyne sensitivity is relatively unaffected by the stray laser radiation because the diagnostic receiver utilizes: (1) transmitter and local oscillator (LO) sources which operate at the same frequency, and (2) an extrinsic photoconductive mixer which utilizes an incident laser LO level of between 50 and 100 mW (ref. 6). (It has also been suggested (ref. 7) that CO_2 laser diagnostics will permit the remote measurement of the poloidal-field in a tokamak plasma.)

An important method of heating tokamak plasma involves the application of RF energy which generates lower hybrid waves that propagate to the center of the plasma and deposit energy into the ions and electrons (ref. 3). At the MIT Alcator tokamak, 50 kW of CW microwave radiation is coupled into the core at a plasma wave resonant frequency of 2.5 (or 4.6) GHz (ref. 2). A coherent 100 W CO_2 laser beam probes the plasma to determine the depth of the RF energy penetration and a wideband heterodyne receiver has been developed for plasma diagnostic measurements. A microwave antenna is used to direct the RF radiation toward the plasma. Two CO_2 beams (a 100 W transmitter and a 1 W LO) from a common laser source are coupled into the plasma at right angles to the microwave radiation (fig. 1). The two laser beams are adjusted to cross in a small spatial cross-section (1 mm X 1 mm) of the plasma (ref. 8). The interaction of the microwave radiation and the transmit laser beam in the nonlinear plasma results in both a spatial and Doppler spectral shift in the tramsitter laser radiation. The shifted laser beam and the unshifted laser LO beam are spatially aligned to fall on the wideband photomixer. The measured intensity of the frequency shifted (2.5 or 4.6 GHz offset) laser beam across the plasma provides information on the RF mismatch at the turbulent vacuum-plasma boundary layer, and the measured frequency spread of the shifted laser beam provides information on the boundary layer physics.

The ion temperature measurement setup employs a pulsed CO_2 laser beam with a peak transmit power level near 5×10^5 W. From a single particle perspective, the electrons radiate a Doppler shifted frequency which is related to its velocity compared to the incident and scattered laser beams. The average of all such scattering events leads to a scattered spectrum whose width is related to the plasma ion temperature. The actual average Doppler shift is due to the ion motion in the plasma rather than the electron motion because the laser scattering is from the electron shield that surrounds each ion. The width of the scattered spectrum in the 300 to 1300 MHz frequency range is determined using IF channelizer techniques.

HETERODYNE RECEIVER DESIGN

The sensitivity (NEP) and the available conversion gain (G) for an infrared heterodyne receiver which uses an extrinsic photoconductive mixer are given (ref. 9) by

$$NEP = \frac{2h\upsilon B}{\eta} + \frac{k\,(T_m + T'_{IF})\,B}{GC} = \frac{2h\nu B}{\eta'} \tag{1}$$

$$G = \frac{\eta q V}{2h\upsilon}\left(\frac{\tau}{T}\right)\frac{1}{1+\omega^2\tau^2} \tag{2}$$

where h is Planck's constant, υ is the infrared frequency, B is the IF bandwidth, η is the photomixer quantum efficiency, k is Boltzmann's constant, T_m is the photomixer temperature, T'_{IF} is the effective IF amplifier noise figure, C is the IF impedance matching efficiency, η' is the effective heterodyne quantum efficiency, q is the electronic charge, V is the mixer bias voltage, τ is the photomixer carrier lifetime, T is the photomixer transit time, and ω is the angular IF frequency.

Optimum heterodyne receiver performance is achieved by minimizing the thermal noise term in equation (1). This term can be minimized by: (1) using a low noise IF preamplifier, (2) increasing the photomixer gain, and (3) maximizing the impedance matching efficiency by using a matching network.

The photomixer conversion gain [equation (2)] can be increased by increasing the applied dc bias voltage. However, the photomixer must be operated in a linear portion of its current-voltage (I-V) characteristic. It should be noted that the photomixer transit time varies directly with the photomixer interelectrode spacing and inversely with the applied bias voltage. The $(1 + \omega^2\tau^2)^{-1}$ term in equation (2) represents the finite photomixer IF frequency response.

The photomixer IF output resistance, R_o, is given (ref. 8) by

$$R_o = \frac{L^2\, h\nu_{LO}}{q\mu\eta P_{LO}} \tag{3}$$

where L is the photomixer interelectrode spacing, μ is the mobility of principal carriers, and P_{LO} is the incident laser LO power. As can be seen, the photomixer IF output resistance varies inversely as the square of the photomixer interelectrode spacing. Accordingly, a photomixer height of L = 250 μm was selected for the plasma probing applications to: (1) ease the impedance matching network requirements, and (2) increase the photomixer gain by decreasing the photomixer transit time.

Substituting equation (3) into equation (2), the photomixer conversion gain is

$$G = \frac{P_{dc}}{2P_{LO}} \left(\frac{1}{1+\omega^2\tau^2} \right) \tag{4}$$

From equations (3) and (4), the photomixer gain and the photomixer resistance both increase inversely with LO power. Therefore, a tradeoff is required to select the incident laser LO power level which will result in sufficient overall photomixer gain and a photomixer resistance which can be efficiently matched to the 50-ohm IF preamplifier. The photomixer resistance is typically 12 megohms with no incident LO power and is reduced to approximately 1200 ohms with applied laser LO power. A cooled microwave impedance matching network is used to obtain nearly optimum power transfer between the photomixer and IF preamplifier over the IF frequency range of interest.

Ge:Cu(Sb) PHOTOMIXERS

As has been mentioned, wideband extrinsic germanium photomixers are used for CO_2 laser plasma probing diagnostics because the stray laser radiation would saturate and possibly damage available wideband PV:HgCdTe photomixers. Measured carrier lifetimes of Ge:Au and Ge:Cu photomixers are given in figure 2. As can be seen, the carrier lifetime varies with donor concentration and applied electric field (ref. 10, 11, and 12). Typical Ge:Cu characteristics for a highly doped photomixer which exhibits wideband performance are given in table I. To our knowledge, this photomixer cutoff frequency (set by the carrier lifetime) is the highest value reported for Ge:Cu(Sb) photomixers. The photomixer IF response is flat to 300 MHz, 3-dB down at 800 MHz, and 10-dB down at 2500 MHz.

The measured photomixer I-V characteristic (fig. 3) demonstrates that an applied voltage of 15 volts, and above, can be used in the positive biasing direction to maximize the photoconductive gain [equation (2)]. For heterodyne receiver operation at lower IF frequencies, special attention must be given to minimize the contact (1/f) noise at high bias levels by utilizing good ohmic contacts.

IF IMPEDANCE MATCHING

It has been demonstrated (ref. 10) that wideband infrared receivers which have impedance mismatches between the photomixer output and the IF preamplifier

will exhibit significant variations in sensitivity with changing IF frequency. These sensitivity variations are exaggerated by the use of a fixed (50 ohm) impedance transmission line between the photomixer and IF preamplifier. A previously developed (ref. 13) wideband IF preamplifier was mounted in a liquid nitrogen (T_m = 77K) Dewar flask and interfaced directly with a PV:HgCdTe photomixer. The cooled IF preamplifier utilized an input impedance matching network and operated over the 10 to 2200 MHz frequency range.

Cooled preamplifiers are not suitable for laser plasma probing applications because they presently do not operate at the liquid helium temperature levels (T_m = 4.2K) of extrinsic germanium photomixers. Therefore, cooled impedance matching networks have been developed which transform the photomixer impedance to approximately match the 50-ohm impedance characteristics of the interconnecting transmission line and the IF preamplifier. A microwave network analyzer is employed to determine the real and imaginary components of the photomixer impedance in its operating mode. A cooled microwave matching network which operates over the IF band of interest is then designed and incorporated between the photomixer output and the input to the 50-ohm preamplifier for maximum IF power transfer. A cooled impedance matching network for Ge:Cu photomixers was previously developed (ref. 14) for CO_2 laser radar applications.

A typical matching network for a photomixer with R_o = 1200 ohms* and C_o = 0.05 pF (fig. 4) utilizes a multipole filter and a quarter-wave transformer type microstrip circuit on an alumina substrate. The cooled matching circuit connects directly to the photomixer. A Kovar housing is employed becuase of: (1) its similarity to the thermal characteristics of alumina, and (2) its low thermal expansion. These factors are important because of the large amount of temperature cycling that is required between room temperature and liquid helium temperature over a 6 to 12 month test period. A typical block diagram of the CO_2 laser heterodyne receiver is given in figure 5 and a photograph of the receiver package is shown in figure 6. An RFI shielded enclosure and a fiber optic data link are used to minimize RF pickup in the infrared receiver.

RECEIVER SENSITIVITY MEASUREMENTS

The receiver sensitivity (NEP) has been determined using: (1) an indirect g-r noise measurement technique, and (2) a direct signal-to-noise ratio (SNR) measurement using a blackbody source. The noise measurement technique consists of irradiating the photomixer with the laser LO and measuring the g-r

* For a 50-ohm IF preamplifier, this represents a VSWR of 24:1. The VSWR is the ratio of the reflected and transmitted waves. Maximum power transfer occurs for VSWR = 1:1.

noise and the receiver thermal noise as a function of applied dc bias (ref. 9). The direct SNR measurement technique (ref. 15) utilizes a spectrally broadband blackbody source and a single frequency laser LO in a heterodyne configuration.

1300-MHZ RECEIVER

The measured heterodyne sensitivity and matching network performance as a function of IF frequency for the 1300-MHz response receiver is given in figure 7. The impedance matching network provides a VSWR of 3:1 between the photomixer and the IF preamplifier over the 400 to 1500-MHz band (fig. 7) and the measured receiver NEP is less than 2×10^{-19} W/Hz over the 300 to 1300 MHz IF frequency range for an applied bias voltage of 10 volts. The upper end of the measured heterodyne response (fig. 7) is limited by the IF amplifier gain roll-off.

2500-MHZ RECEIVER

The measured heterodyne sensitivity and matching network performance as a function of IF frequency for the 2500-MHz response receiver is given in figure 8. The impedance matching network provides a VSWR of 1.5:1 between the photomixer and the IF preamplifier over the 2100- to 2300-MHz band. As can be seen, an NEP $\approx 2 \times 10^{-19}$ W/Hz was obtained at an IF = 2.3 GHz ± 200 MHz and the data is in good agreement for the two measurement techniques.

Improved heterodyne receiver sensitivity and higher photomixer gain can be obtained by increasing the dc bias power at the photomixer (equations (1) and (4)). The maximum applied dc bias power (P_{dc} = 350 mW) is fixed by the diameter of the gold wire between the photomixer and the impedance matching network. Receiver sensitivity measurements as a function of dc bias power resulted in a receiver NEP improvement from NEP = 2×10^{-19} W/Hz for P_{dc} = 100 mW, to NEP = 1.35×10^{-19} W/Hz for P_{dc} = 250 mW.

4600-MHZ RECEIVER

The measured heterodyne sensitivity and matching network performance as a function of IF frequency for the 4600-MHz response receiver is given in figure 9. An NEP of 4.4×10^{-19} W/Hz was obtained at an IF of 4.5 GHz for P_{dc} = 150 mW and the IF heterodyne sensitivity is in good agreement with the spectral characteristics of the impedance matching network.

CONCLUSION

The use of selected wideband germanium photomixers and cooled impedance matching networks has permitted the development of high sensitivity heterodyne receivers with IF responses of 1.3, 2.5, and 4.6 GHz. The heterodyne receivers use microwave techniques to optimize the infrared performance over a specific IF frequency interval and have achieved effective heterodyne quantum efficiencies of: (1) $\eta' = 30\%$ at IF's which are three times the photomixer 3-dB cutoff frequency, and (2) $\eta' = 8.5\%$ at IF's which are about six times the photomixer 3-dB cutoff frequency.

The resultant infrared heterodyne receivers have permitted unique CO_2 laser diagnostic probing measurements of tokamak plasmas. Some initial measurements have resulted in the determination of the penetration depth of the RF heating source and information which is being used to model the interaction mechanism at the turbulent plasma boundary (ref. 3). Plasma ion temperature measurements are presently in progress.

Heterodyne operation at higher IF frequencies, as well as other diagnostic applications, are presently being investigated. The reported impedance matching techniques are believed to be applicable at IF frequencies as high as 8 GHz. In addition, the IF impedance matching techniques are applicable to other types of infrared photomixers.

REFERENCES

1. Sheffield, J.: Plasma Scattering of Electromagnetic Radiation. Academic Press, 1975.

2. Slusher, R.E. et al,: Bull. Phy. Soc., no. 23, 1976, p. 765.

3. Surko, C.M.; Slusher, R.E.: Study of Driven Lower-Hybrid Waves in the Alcator Tokamak Using CO_2 Laser Scattering. Phys. Rev. Lett. no. 43, 1979, p. 1016.

4. Holzhauer, E.; and Massig, J.H.: An Analysis of Optical Mixing in Plasma Scattering Experiments. Plasma Phys., no. 20, 1978, p. 867.

5. Massig, J.H.: Light Scattering From Thermal Density Fluctuations Using a CW-CO_2 Laser and Heterodyne Detection. Phys. Lett. no. 66A, 1978, p. 207.

6. Wolczok, J.; and Peyton, B.J.: Diagnostic Laser Probing of the Alcator Tokamak. Infrared Phys., no. 19, 1979, pp. 447-454.

7. Kunz, W.: Measurement of Paloidal-Field Induced Faraday Rotation in a Tokamak Plasma. Nuclear Fusion Lett. no. 18, 1978, p. 1729.

8. Slusher, R.E.; and Surko, C.M.: Study of Density Fluctuations in the Absorption of Oxygen on Silicon. Phys. Rev. Lett. no. 40, 1978, pp. 400-403.

9. Arams, F.R.; Sard, E.W.; Peyton, B.J.; and Pace, F.P.: Infrared 10.6 Micron Heterodyne Detection With Gigahertz IF Capability. IEEE J. Quantum Elec., QE-3, 1967, pp. 484-492.

10. Arams, F.R.; Peyton, B.J.; Sard, E.W.; and Pace, F.P.: Semiconductors and Semimetals, Infrared Detectors. Academic Press, NY, vol. 5, 1970, p. 10.

11. Picus, G.S.: Carrier Generation and Recombination Processes in Copper-Doped Germanium Photoconductors. J. Phys. Chem. Solids, no. 23, 1962, p. 1753.

12. Yardley, J.T.; and Moore, C.B.: Response Times of Ge:Cu Infrared Detectors. Appl. Phys. Lett. no. 311, 1965.

13. Peyton, B.J.; Lange, R.A.; Savage, M.; Hoell, J.; and Allario, F.: Remote Airborne Measurements of Stratospheric Ozone, Proceedings of Laser '79 Conference, Orlando, Fla., 1979.

14. Lange, R.A.; Kalisiak, P.; Rubinstein, I.; and Pace, F.P.: 10.6 Micron Heterodyne Monopulse Receiver with Doppler Tracking Capability. IEEE J. of Quantum Elec., QE-9, 1973.

15. Peyton, B.J.; DiNardo, A.J.; Cohen, S.C.; McElroy, J.H.; and Coates, R.J.: An Infrared Heterodyne Radiometer for High-Resolution Measurements of Solar Radiation and Atmospheric Transmission. IEEE J. of Quantum Elec., QE-11, 1975.

TABLE I. MEASURED Ge:Cu(Sb) PHOTOMIXER CHARACTERISTICS

Mixer operator temperature, T_m	4.2K
Electric field, E	500 V cm^{-1}
3-dB cutoff frequency, f_c	800 MHz
Power handling capabiltity	500 mW
Carrier lifetime, τ	2 x 10^{-10} sec
Mixer dc resistance, R_o	1200 ohms (with LO applied)
Quantum efficiency, η	0.55
Photo gain, τ/T	0.011

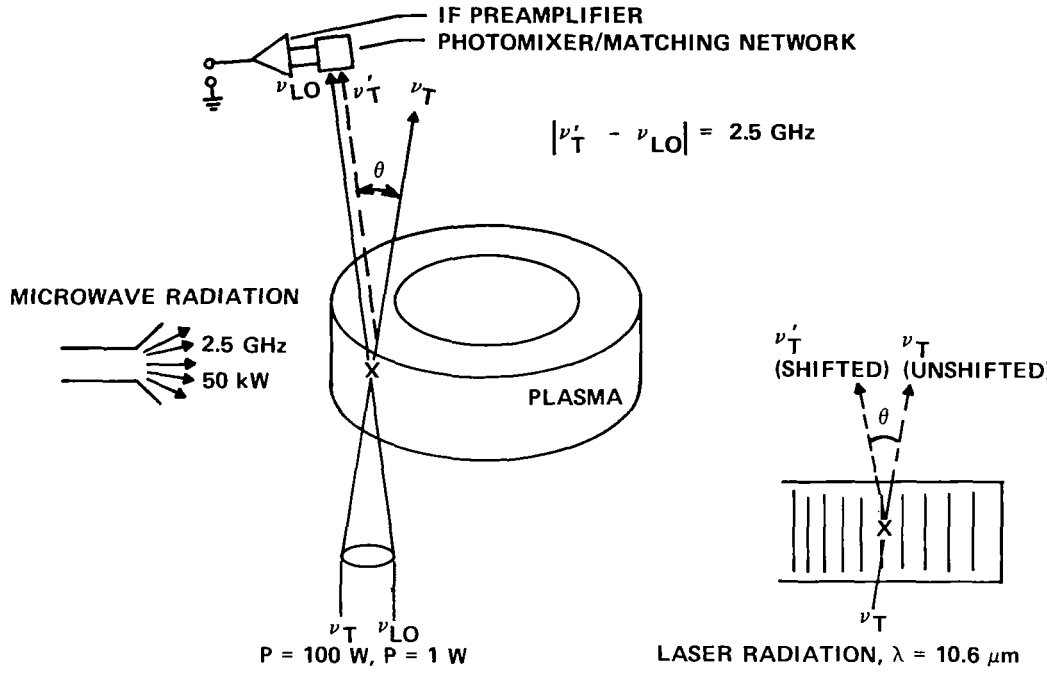

Figure 1.- Plasma probing technique.

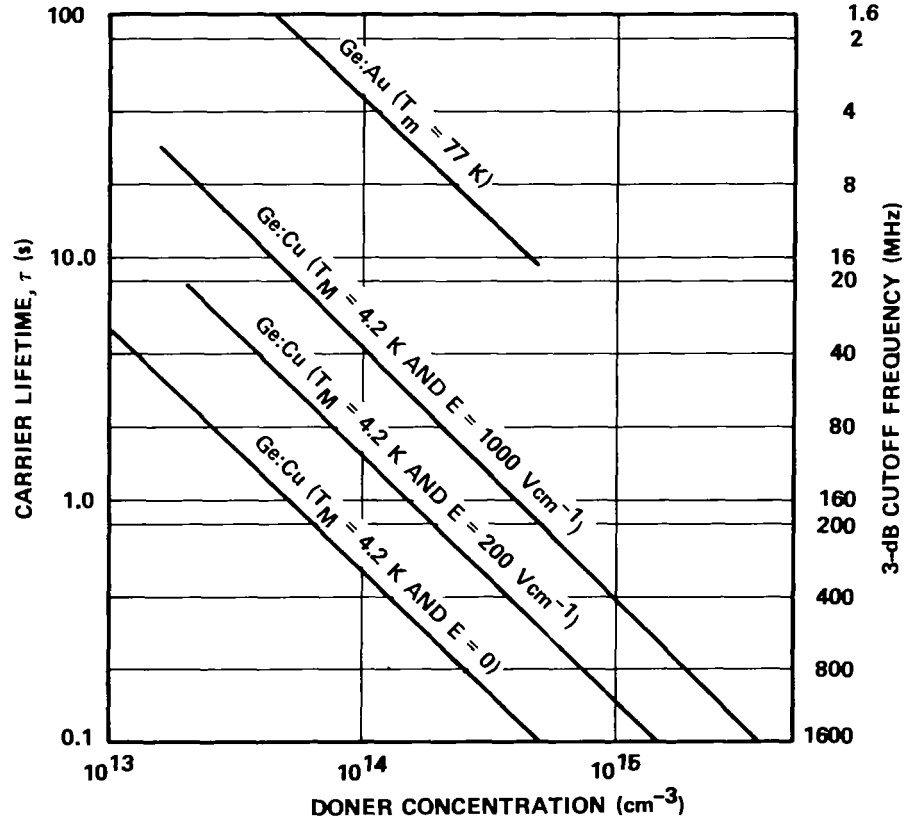

Figure 2.- Measured variation of carrier lifetime with doner concentration for extrinsic germanium photoconductors.

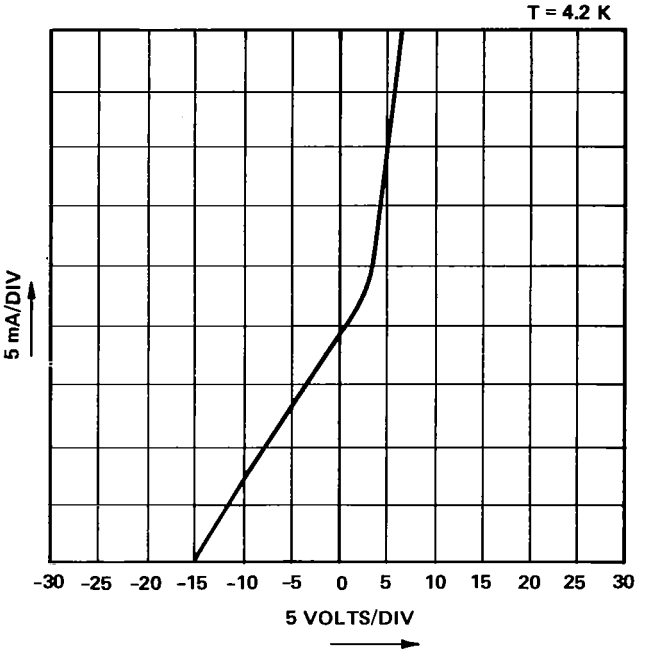

Figure 3.- I-V characteristics of Ge:Cu(Sb) photomixer.

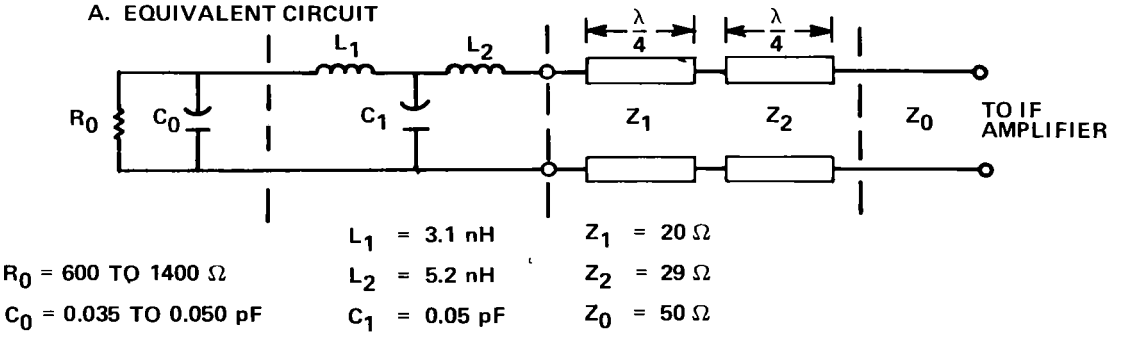

B. PHOTOMIXER/MATCHING NETWORK MOUNT

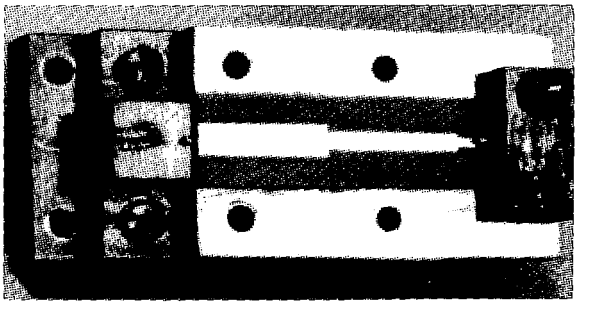

Figure 4.- Cooled mixer impedance matching network for 2.5-GHz infrared heterodyne receiver.

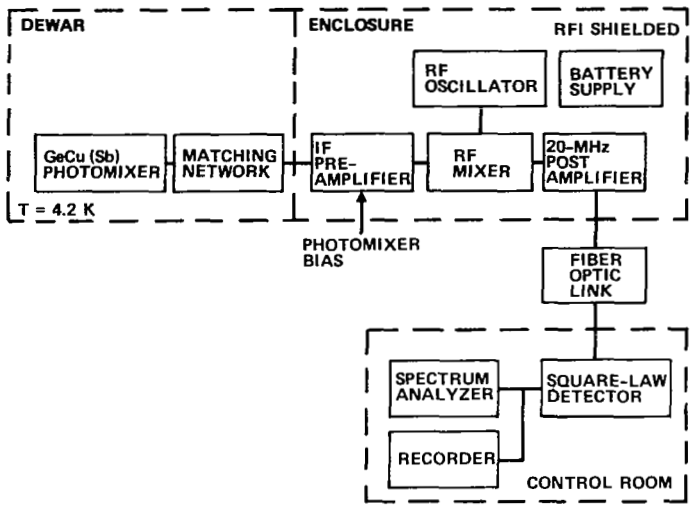

Figure 5.- CO_2 laser infrared heterodyne receiver for lower hybrid heating diagnostics.

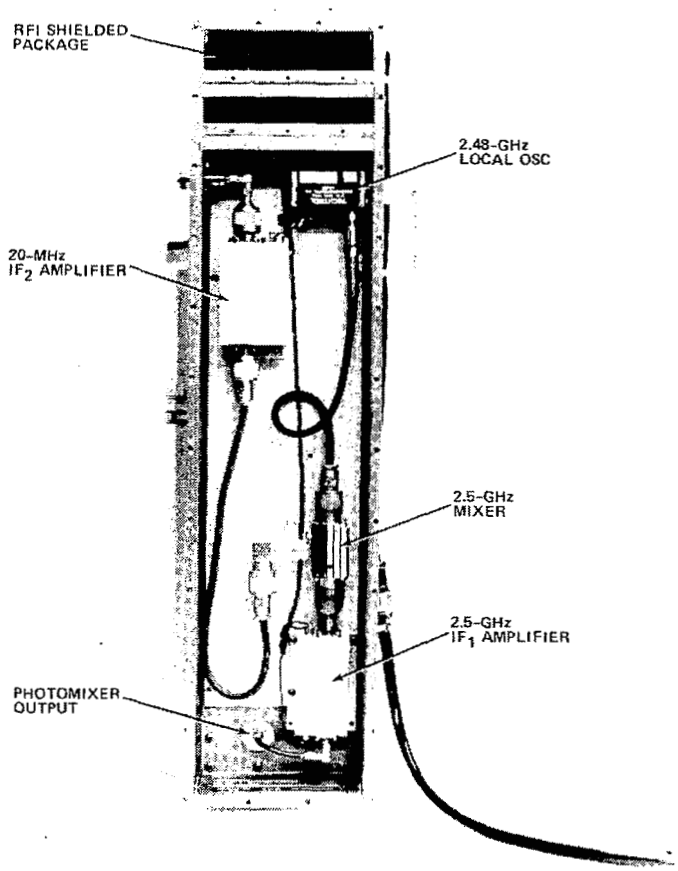

Figure 6.- Packaged infrared heterodyne receiver for lower hybrid heating diagnostics.

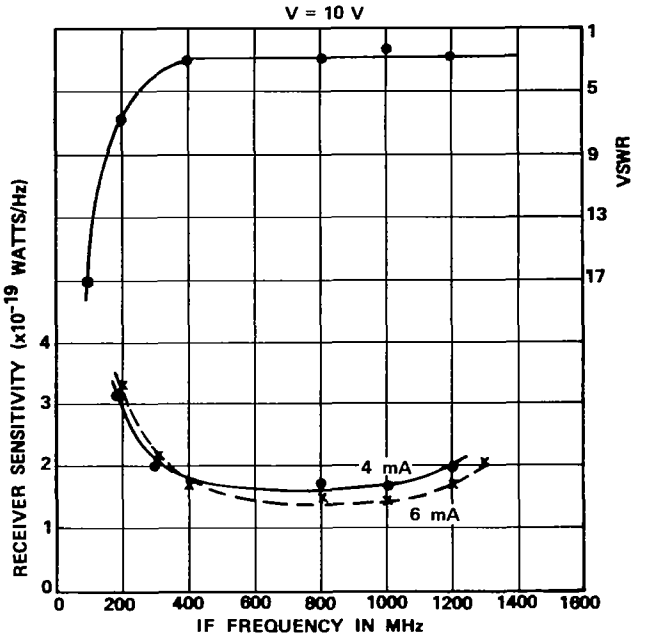

Figure 7.- Measured NEP and matching network performance versus IF frequency for 1300 MHz response infrared heterodyne receiver.

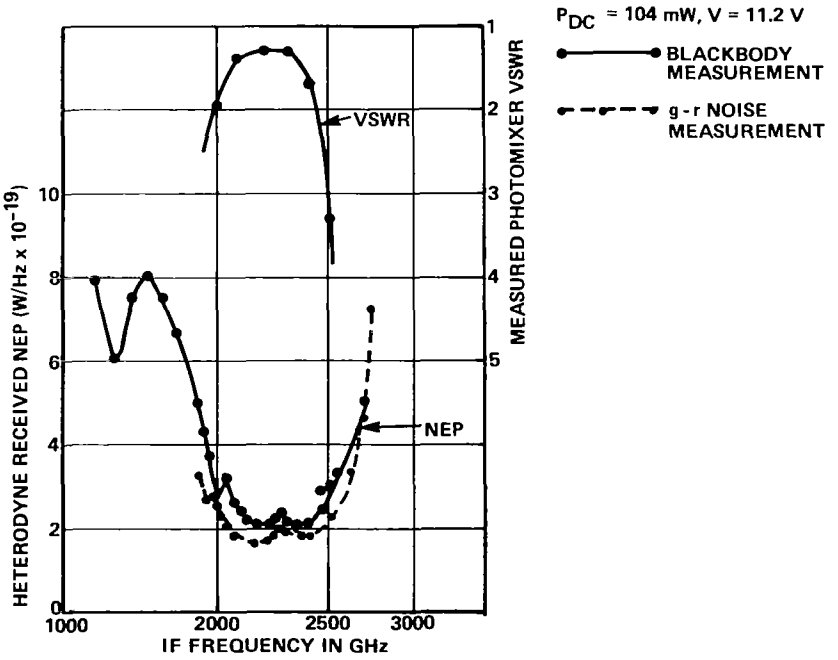

Figure 8.- Measured heterodyne receiver sensitivity versus IF frequency.

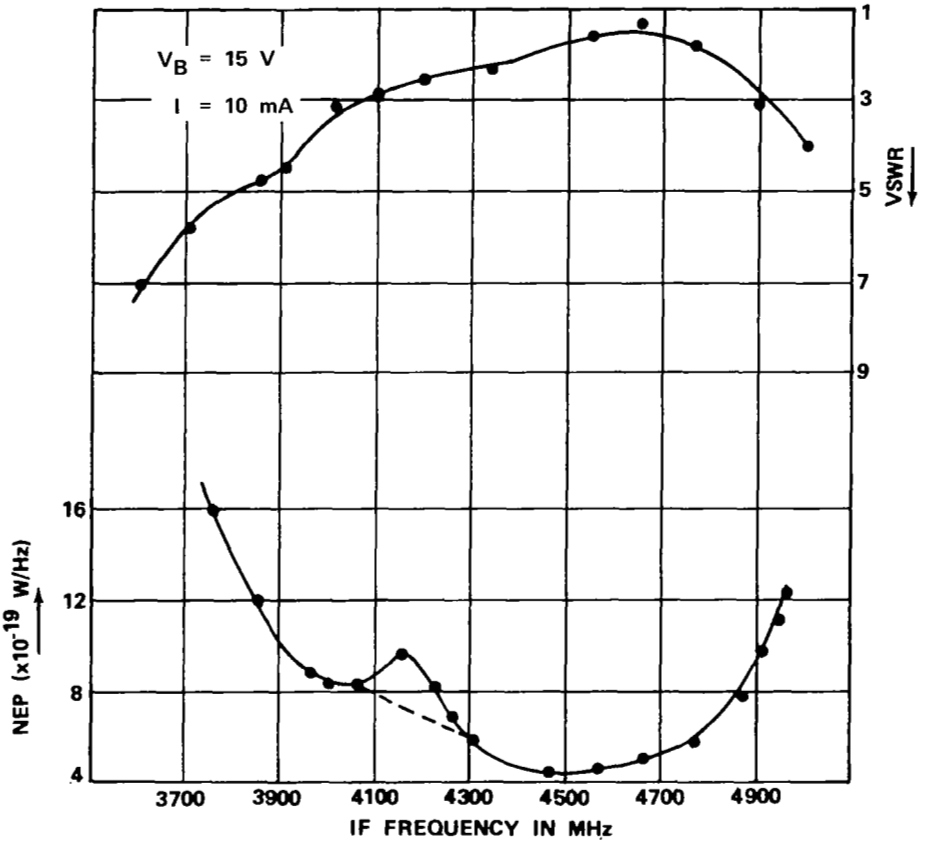

Figure 9.- Measured NEP and matching network performance for 4600 MHz response infrared heterodyne receiver.

FAR INFRARED HETERODYNE SYSTEMS

P. E. Tannenwald
Lincoln Laboratory,* Massachusetts Institute of Technology
Lexington, Massachusetts 02173

ABSTRACT

Three far infrared detectors, the InSb hot electron bolometer, the GaAs Schottky diode and the Josephson point contact junction, have been incorporated as mixers into sensitive heterodyne systems. The performances of existing heterodyne receivers/radiometers using these detectors are described and compared. Other applications of submillimeter heterodyne techniques are discussed.

I. INTRODUCTION

Over the last few years three far infrared detectors (ref. 1) have been developed into useful mixers that are presently being used in a number of applications: InSb, the GaAs Schottky diode, and the Josephson junction. InSb, which acts by way of a hot electron mechanism, has shown itself to be a highly sensitive heterodyne detector between 1 mm and 600 μm. Its very low LO requirement permits a variety of tunable klystron harmonics to be used, and the needed low temperature environment has not been particularly troublesome. InSb's outstanding limitation is its slow relaxation time (10^{-7} sec), leading to a quite narrow IF bandwidth of 1-2 MHz.

The GaAs Schottky diode has proved to be a highly useful room temperature mixer over a wide spectral range with exceedingly broad band IF capability limited to 40 GHz only by IF circuit parameters (ref. 2). In the millimeter region it has been engineered to a high state of perfection in low noise receivers and radiometers, while at submillimeter wavelengths it is just becoming a practical mixer when used in conjunction with quasi-optical techniques. For example, figure 1 shows the design of the Lincoln Laboratory quasi-optical diode mount that covers the range 1 mm to 100 μm with appropriately scaled antenna lengths (see ref. in table I, Fetterman et al.) At the lower frequencies the mixer design problem is relatively much easier inasmuch as waveguide techniques can be employed, and harmonics of tunable klystrons can be used as local oscillators. At far infrared wavelengths, the much more cumbersome optically pumped far infrared lasers are used as LOs, and

*Supported in part by the U. S. Army Research Office and the Department of the Air Force.

their fixed frequency output makes the wideband IF capability of the Schottky diode imperative.

The superconducting point contact or Josephson junction (JJ) is also just being readied as a mixer in radiometers for field experiments. The planar superconductor-insulator-superconductor (SIS) junction has not yet been operated beyond mm frequencies (ref. 3). JJ receiver systems have excellent sensitivity, but their operational restriction to liquid He temperature and the attendant temperature recycling could be troublesome. One great advantage of JJs is their exceedingly low LO requirement. They have a moderate IF bandwidth of around 100 MHz.

II. FAR IR HETERDOYNE RADIOMETERS/RECEIVERS

Table I lists all the currently operational heterodyne radiometer/receiver systems from 1.3 mm (230 GHz) to 119 μm (2521 GHz). The dots (•) denote that the detector was cooled. Some estimates and interpolations were made from the information reported in the literature in order to achieve moderate compactness of the data.

The DSB systems noise temperatures from table I are plotted in figure 2 as a function of wavelength. The solid or half-solid points represent low temperature measurements, the open points room temperature operation. The range of currently reported best values of DSB system temperature at 3 mm for both cooled (solid bar) and uncooled (open bar) mixers are also shown for comparison. For room temperature mixers there is a roughly linear trend with unity slope; there is no fundamental basis for this, but it is nevertheless an interesting guide, especially since all the room temperature mixers are GaAs Schottky diodes.

The plot shown in figure 2 makes no allowance for the instantaneous bandwidth available with each detector when estimating signal-to-noise ratios obtainable from observation of sources whose spectral features are moderately broad. To the extent that the observed object exceeds 1 MHz in spectral width, performance of the broad band Schottky diodes increases proportionally as compared with the 1 MHz wide InSb detectors. In other words, in the InSb case a single post-detection channel must be scanned sequentially across the spectral line, while with the Schottky diode the broad band IF can feed a multi-channel filter bank, thus integrating over the whole spectral feature simultaneously. Of course, if the signal intensity is so small as to give only a marginally usable S/N ratio with InSb, then no spectral characteristics would be resolvable with Schottky diodes. This is especially true at the very short wavelengths where optically pumped lasers must be used as LOs, and the system's stability over long integration times has yet to be demonstrated. In the case of superconducting junctions, with their $\sim$100 MHz bandwidth, the situation falls somewhere in between, but closer to the Schottkys.

III. OTHER HETERODYNE APPLICATIONS

Tunable Far Infrared Sources

Low power ($\sim 10^{-7}$ W) tunable sources are now available throughout the submillimeter region by means of tunable sideband generation. In such schemes a tunable millimeter klystron or tunable microwave source is mixed with a fixed frequency optically pumped far infrared laser in a GaAs Schottky diode (refs. 4, 5). The narrow linewidths of these sideband sources make them quite suitable for far infrared spectroscopy. In one particularly sophisticated arrangement, shown in figure 3, the detector in the far IR spectrometer consists of a complete heterodyne receiver that utilizes as LO the same laser with which the source sidebands are generated (ref. 5).

Planar Diode Technology

In the next generation of Schottky diode detectors, discrete whisker contact diodes will be supplanted by a new type of device -- the planar, surface-oriented Schottky diode. This device is fabricated by means of photolithographic techniques in conjunction with ion implantation and proton bombardment (ref. 6). Figure 4 shows a simplified sketch of a whisker contact diode and a planar diode. The surface-oriented character of the planar diode is clearly evident in that both ohmic connecting contacts are brought out in the same surface plane. A photomicrograph of a single diode is shown in figure 5, one of many devices made on a single GaAs chip. Although the sensitivity of planar diodes is presently limited by inefficient coupling of radiation into them, they are used routinely in high-order harmonic mixing and direct heterodyne experiments between 1 mm and 100 μm. They are more rugged and reliable, and ultimately will lend themselves to mass fabrication of integrated antennas, mixer diodes and IF amplifiers on the same chip, and to array configurations for heterodyne imaging in the far infrared.

Frequency Standards

It is generally desirable to measure frequencies of visible lasers in terms of microwave standards. This has been possible with the metal-oxide-metal (MOM) diode, which can mix visible lasers with harmonics of far IR lasers, which in turn are locked to microwave standards (ref. 7). Two improvements over such a scheme would be advantageous: a replacement of the MOM diode by a more reproducible and stable mixing element, and the elimination of the chain of intermediate far IR lasers.

One step in such a direction has been the mixing of a He-Ne laser with a cw dye laser with approximately 80 GHz frequency offset in a reverse-biased GaAs Schottky diode (ref. 8). The beat frequency detector in this case was a sensitive 80 GHz heterodyne receiver. Thus large frequency differences between lasers emitting in the visible can be determined with the high accuracy inherent in heterodyning techniques.

Another step has been the high-order harmonic mixing of a stabilized X-band source with a far IR laser in a planar Schottky diode -- e.g., most recently the 145th harmonic of 12 GHz with a 170 μm formic acid laser (ref. 9). The desirability of extending this to 10 μm or even 1 μm is obvious.

Finally, it has been possible to extend the GaAs diode mixer operation up to 30 THz (ref. 10). Two laser lines in the 10 μm regime from a single stabilized laser cavity, which included two cells filled with CO_2 and isotopic CO_2, respectively, were mixed in both whisker point contact and planar diodes. Figure 6 shows the heterodyne signal produced at 15.6 GHz, with second heterodyning with a microwave LO down to a 50 MHz IF taking place either in the Schottky diode itself or in an external microwave mixer diode. Further experiments are underway to clarify the mixing process at these high frequencies, which could be RC roll-off of thermionic emission or perhaps field emission.

IV. SUMMARY

Three far infrared heterodyne detectors have been developed into useful mixers that are presently being used in radio astronomical experiments and other applications. The lowest system noise temperatures have been obtained with the liquid helium cooled InSb hot electron bolometer. Its principal drawback is the narrow IF bandwidth of 1-2 MHz imposed by the slow electron relaxation time. The superconducting point contact or Josephson junction will probably approach this performance, with somewhat less convenience and perhaps less reliability, but with $\sim$ 100 MHz bandwidth. Both InSb and the JJs require extremely little LO power (microwatts).

The exceedingly impressive performance obtained earlier from GaAs Schottky diodes at 3 mm [room temperature T (system) DSB $\sim 300^{\circ}$K; cooled T (system) DSB 200°K] is gradually being extended to shorter wavelengths [at 1 mm, T (system) DSB $\sim 2000^{\circ}$K]. The two principal advantages of GaAs Schottky diode mixers are room temperature operation and, inherently, unlimited IF bandwidth. Further extension of Schottky diode mixers in heterodyne systems to wavelengths as short as 119 μm has also been recently accomplished using quasi-optional techniques, with performance falling off roughly linearly with increasing frequency. In order to fully utilize these advances in detector technology for various radiometric applications, it is now desirable to achieve equal progress in the devlopment of tunabe far infrared LOs, especially solid state sources.

REFERENCES

1. P. E. Tannenwald, "Far Infrared Heterodyne Detectors", Intern. J. of Infrared and Millimeter Waves, Vol. 1, No. 2 (1980).

2. B. J. Clifton, "Schottky Diode Receivers for Operation in the 100-1000 GHz Region", Radio and Electronic Engineer, IREE (UK), Vol. 49, pp. 333-346, July/August 1979.

3. G. J. Dolan, T. G. Phillips and D. P. Woody, Appl. Phys. Lett. 34, 347 (1979).

4. D. D. Bićanić, B. F. J. Zuidberg and A. Dymanus, Appl. Phys. Lett. 32, 367 (1978).

5. W. A. M. Blumberg, H. R. Fetterman, D. D. Peck and P. F. Goldsmith, Appl. Phys. Lett. 35, 582 (1979).

6. R. A. Murphy, C. O. Bozler, C. D. Parker, H. R. Fetterman, P. E. Tannenwald, B. J. Clifton, J. P. Donnelly and W. T. Lindley, IEEE Trans. Microwave Theory and Tech., Vol. MTT-25, pp. 494-495, June 1977.

7. K. M. Evenson, D. A. Jennings, F. R. Petersen and J. S. Wells, in Laser Spectroscopy III, J. L. Hall and J. L. Carlsten, Eds. (Springer, Berlin, 1977), p. 56.

8. B. Burghardt, H. Hoeffgen, G. Meisel, W. Reinert and B. Vowinkel, Appl. Phys. Lett. 35, 498 (1979).

9. G. A. Koepf, "Submillimeter Laser Local Oscillators: Design Criteria and Results", Heterodyne Systems and Technology Conference, NASA CP-2138, 1980. (Paper 32 of this compilation).

10. H. R. Fetterman, P. E. Tannenwald, B. J. Clifton, C. Freed and R. G. O'Donnell, Lincoln Laboratory, M.I.T. Solid State Research Report (1980:1).

References for Table I

N. R. Erickson, 1978 IEEE MTT-S International Microwave Symposium Digest, pp. 438-439, Ottawa, June 1978. Ibid, Washington, DC, May 1980.

E. R. Carlson and M. V. Schneider, IVth Intern. Conf. on IR and Mm Waves and Their Applications, Miami, FL, December 1979, Conference Digest, p. 82.

T. G. Phillips and K. B. Jefferts, IEEE Trans. Microwave Theory and Tech., Vol. MTT-22, pp. 1290-1292, December 1974.

J. Edrich, IVth Intern. Conf. on IR and Mm Waves and Their Applications, Miami, FL, December 1979, Conference Digest, p. 152.

ESA/ESTEC: A. H. F. van Vliet, Th. deGraauw, and H. J. Schötzau, 3rd Intern. Conf. on Submillimeter Waves and Their Applications, Guilford, England, March 1978, Conference Digest, p. 248; and A. H. F. van Vliet, Th. deGraauw, S. Lidholm and H. v. d. Stadt, IVth Intern. Conf. on IR and Mm Waves and Their Applications, Miami, FL, December 1979, Post-Deadline Conference Digest, p. 40.

T. G. Phillips, P. J. Huggin, G. Neugebauer and M. W. Werner, Astrophys. J. 217, L161, 1977.

T. G. Blaney, N. R. Cross and R. G. Jones, 3rd Intern. Conf. on Submillimeter Waves and Their Applications, Guilford, England, March 1978, Conference Digest, p. 258.

Lincoln Lab: H. R. Fetterman, P. F. Goldsmith, B. J. Clifton, C. D. Parker and P. E. Tannenwald, presented at the IVth Intern. Conf. on IR and Mm Waves and Their Applications (no Digest paper).

H. R. Fetterman, P. E. Tannenwald, B. J. Clifton, C. D. Parker, W. D. Fitzgerald and N. R. Erickson, Appl. Phys. Lett. 33, 151 (1978).

TABLE I.- OPERATIONAL HETERODYNE SYSTEMS
(dots • denote receivers that use cooled mixers)

FREQUENCY (GHz)	λ	DETECTOR	NOISE T [DSB]	AUTHORS	LO POWER	IF FREQUENCY	CONV. LOSS	COMMENTS
230	1.3 mm	GaAs S.D.	1250 °K	Erickson*	2 mW	1.3 GHz		2 × klystron
230	1.3 mm	GaAs S.D.	1500	Carlson & Schneider	<10 mW	1.4 GHz	8 dB	subharm. pump
• 230	1.3 mm	InSb	300	Phillips & Jefferts	10^{-4} mW	2 MHz	<10 dB	2 × klystron •
285	1.05 mm	GaAs S.D.	1450	Erickson	1 mW	1.3 GHz	T_{IF} = 50°K	3 × klystron
• 300	1.0 mm	Nb pt. contact	500	Edrich et al.	4 × klystron	1.3 GHz		Cooled FET, T_N = 45°K •
• 300	1.0 mm	InSb	600	ESA/ESTEC	10^{-3} mW			Carcinotron •
342	877 μm	GaAs S.D.	2200	Erickson	~10 mW	1.7 GHz	7 dB	Carcinotron
• 346	870 μm	InSb	2000	Phillips et al.		1 MHz		3 × klystron •
• 452	660 μm	Nb pt. contact	2100	Blaney et al.	10^{-4} mW	100 MHz	11 dB	OP laser, T_{IF} = 110°K •
• 460	652 μm	InSb	650	ESA/ESTEC	10^{-3} mW			Carcinotron •
• 492	608 μm	InSb	500	Phillips				5 × klystron •
• 530	566 μm	InSb		ESA/ESTEC				2 × carcinotron •
693	433 μm	GaAs S.D.	4200	Lincoln Lab	~10 mW	1.48 GHz		OP laser, T_{IF} = 100°K
• 693	433 μm	GaAs S.D.	3800	Lincoln Lab	~10 mW	1.48 GHz	10.5 dB	Diode cooled to 40°K •
1630	184 μm	GaAs S.D.	19,000	Lincoln Lab	~60 mW	1.48 GHz	12 dB	OP laser LO
2521	119 μm	GaAs S.D.	32,000	Lincoln Lab	~30 mW	1.48 GHz		OP laser LO

*Also personal communication.

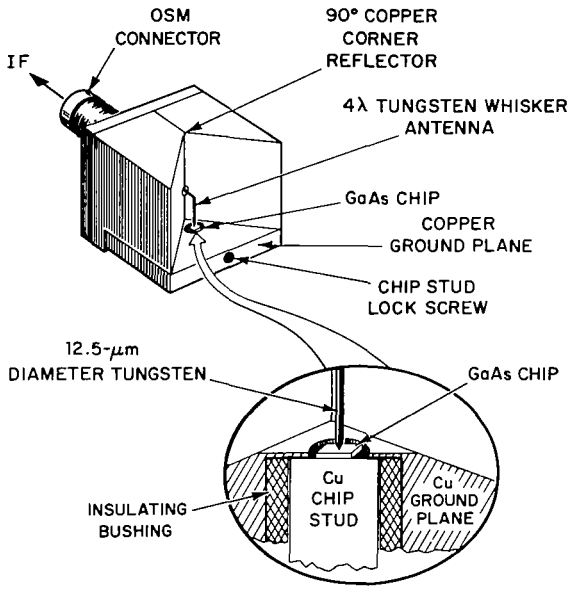

Figure 1.- Quasi-optical 90°-corner reflector diode mount.

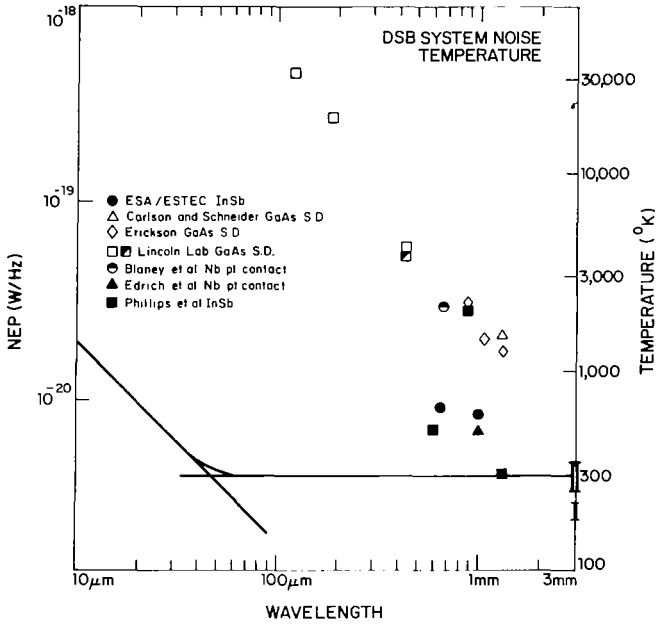

Figure 2.- Performance of operational heterodyne receiver/radiometer systems above 230 GHz. The solid (●) or half-solid (◓,◪) points represent low temperature results. The ranges of the best 100 GHz room temperature (II) and low temperature receivers (I) are also shown.

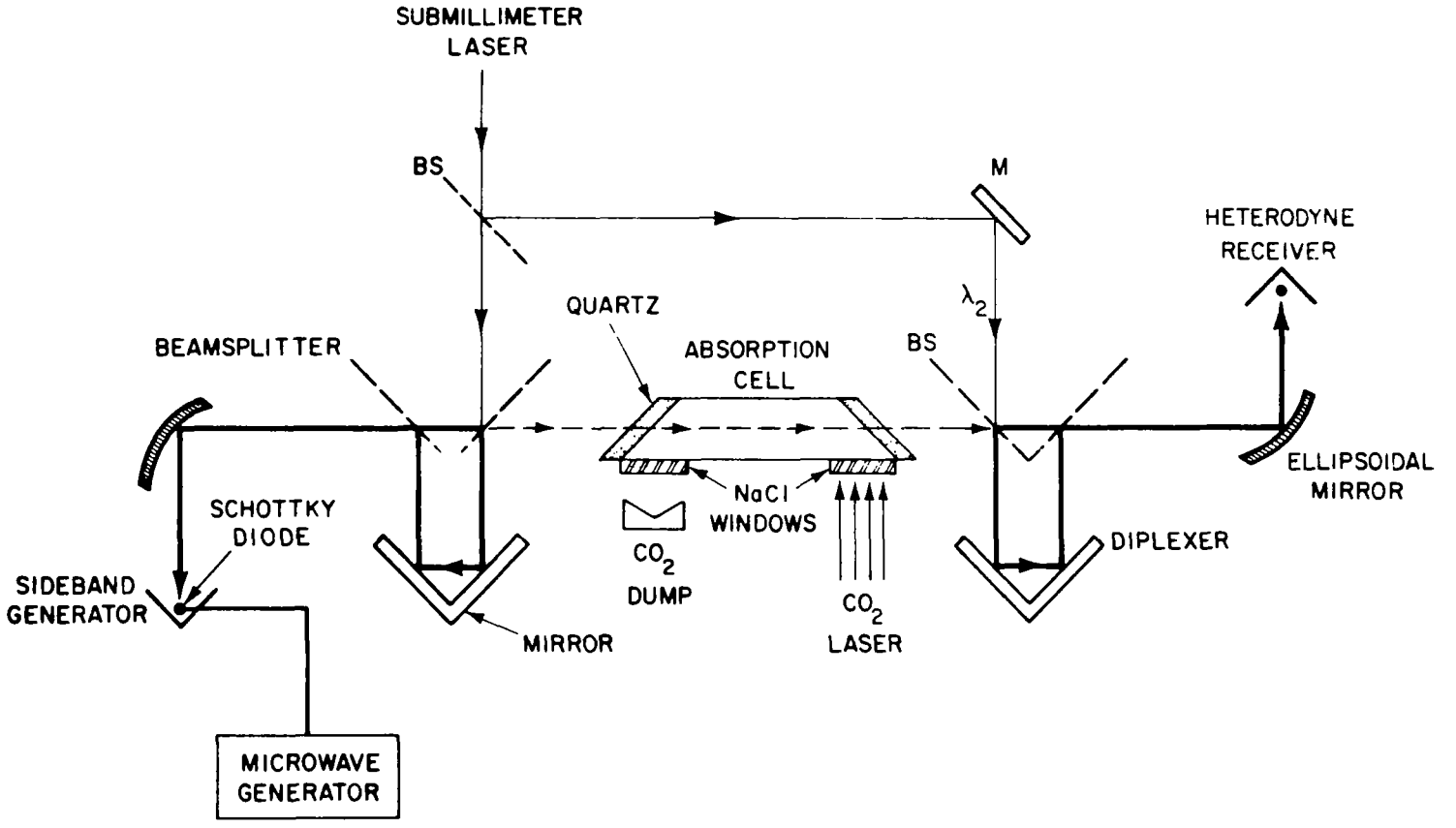

Figure 3.- Sketch of tunable sideband submillimeter spectrometer. Sideband generator and heterodyne receiver each use a Schottky diode mixer. In the particular example shown, CO_2 laser excites molecules under study in absorption cell while tunable submillimeter radiation provides high resolution spectrum of excited state.

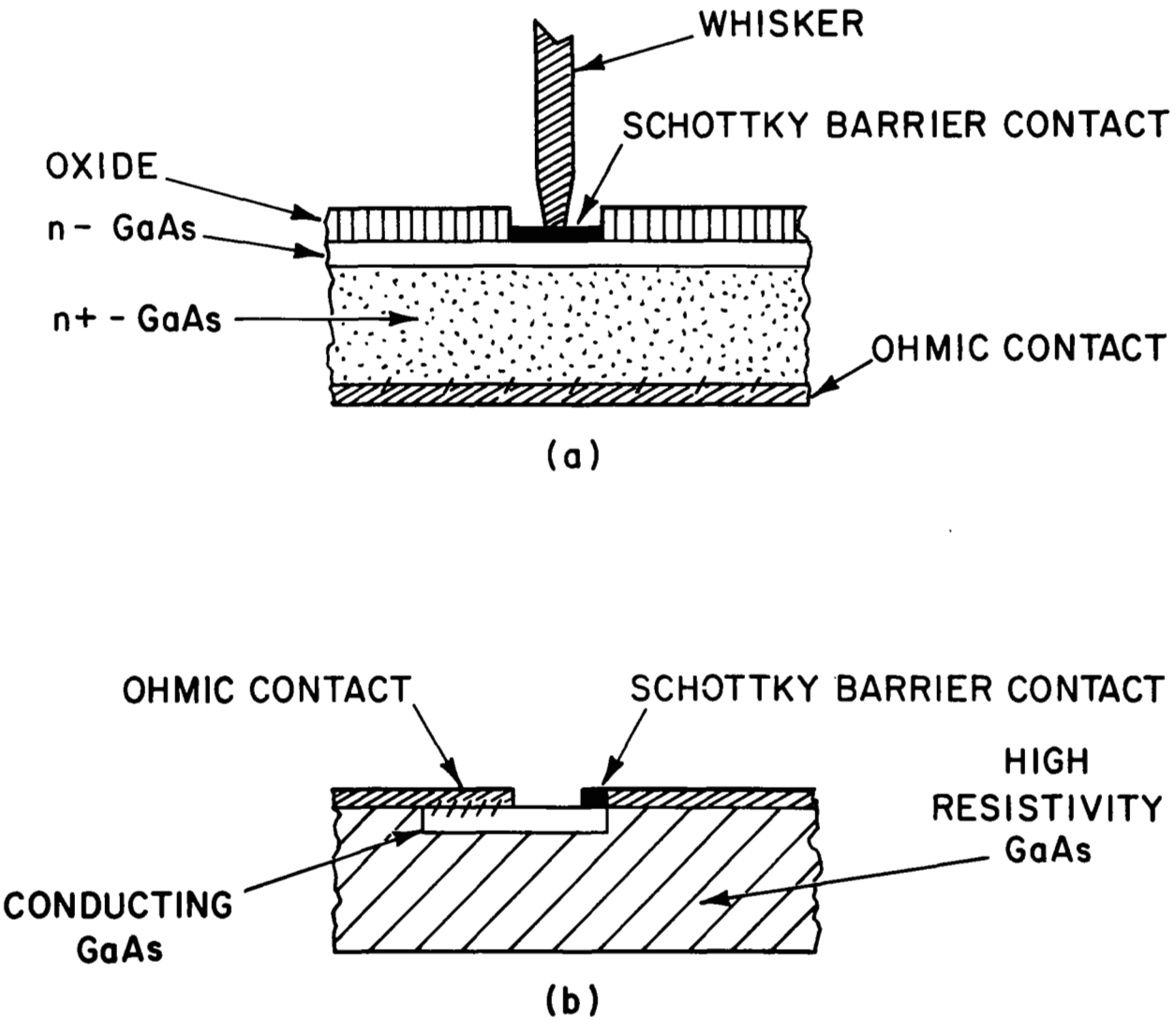

Figure 4.- Sketch of whisker contact diode (a) and planar diode (b). In planar diode both ohmic contacts are brought out in same surface plane.

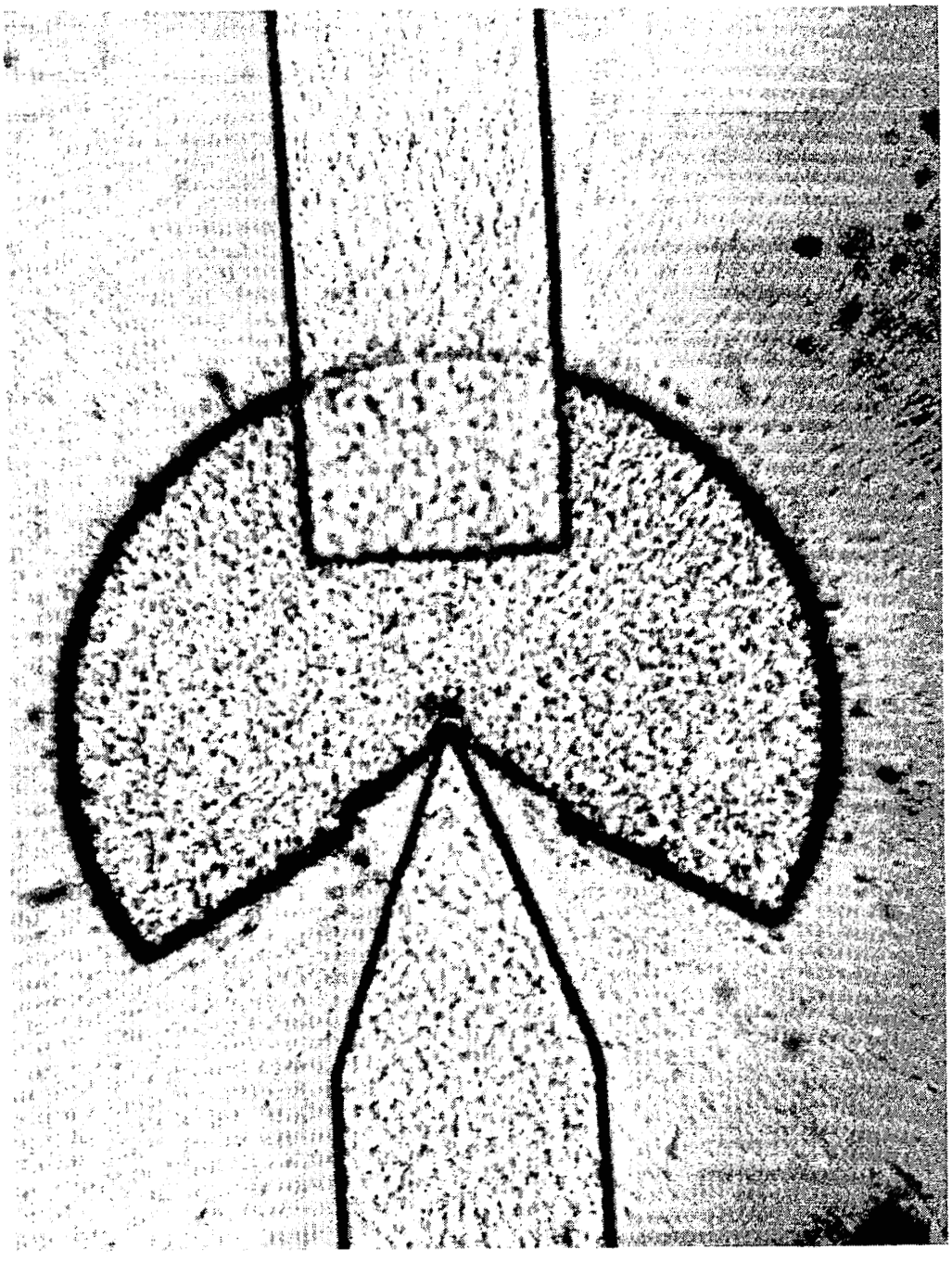

Figure 5.- Photomicrograph of a planar, surface-oriented diode.

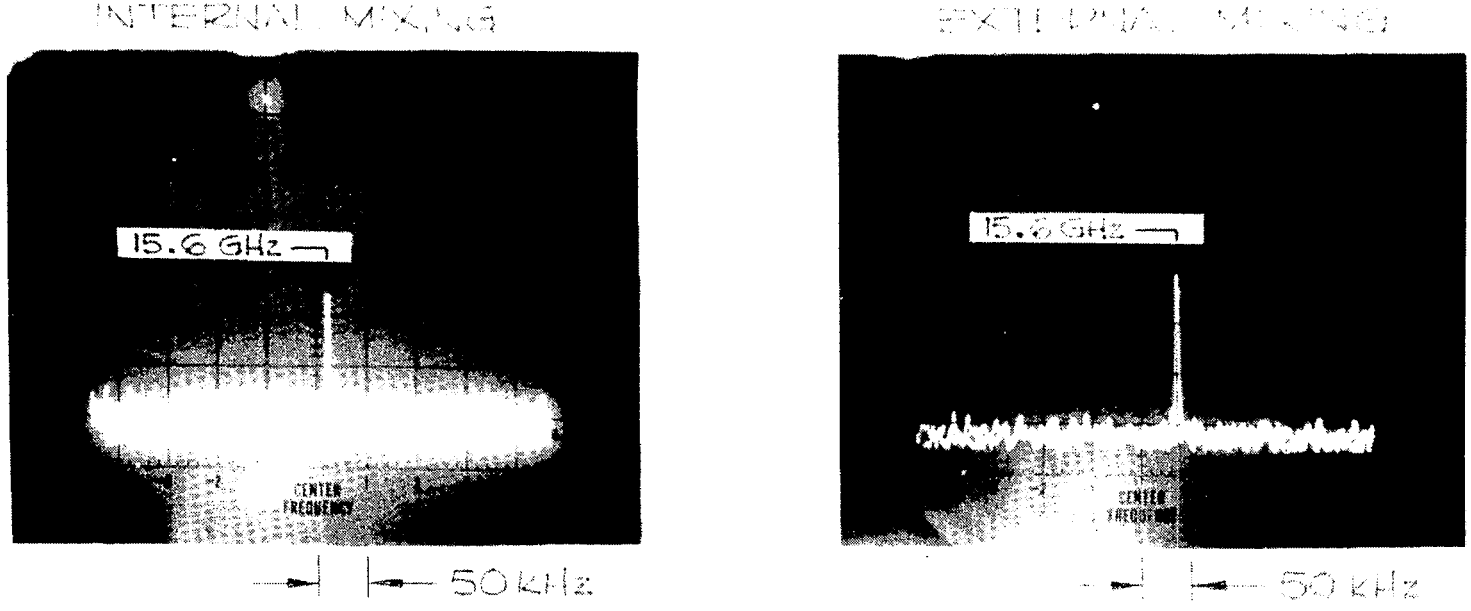

SPECTRUM ANALYZER DISPLAYS OF 15.6 GHz BEAT NOTE
HORIZONTAL SCAN: 50 kHz/cm ; I.F. BANDWIDTH: 1 kHz ; VERTICAL SCALE: LINEAR

Figure 6.- Beats between two CO_2 lasers in the 10 μm regime obtained with a GaAs Schottky diode. Second down-conversion to a 50 MHz IF is produced either in the Schottky diode itself or in an external microwave diode.

BULK SUBMILLIMETER-WAVE MIXERS: STRAIN AND SUPERLATTICES

M. M. Litvak and H. M. Pickett
Jet Propulsion Laboratory
California Institute of Technology
Pasadena, California 91103

SUMMARY

Strained germanium crystals, doped with gallium, are used as heterodyne mixers at THz frequencies, with IF bandwidths approaching a GHz. The mixer performance (conversion loss and mixer noise) is analyzed in terms of nonlinearities associated with acceptor levels and with relaxation rates of free holes. Comparison is made with similar mixers employing low-lying donor levels in high-purity GaAs and with hot-electron InSb mixers.

INTRODUCTION

Stress has been used to tune the photoconductive response of lightly Ga-doped Ge bolometers in the far infrared over the range 50 to 100 cm^{-1} (100 to 200 μm)(ref. 1).

The degeneracy of the valence band edge (fig. 1) and of the acceptor ground levels is lifted by the strain (ref. 2). The acceptor binding energy decreases with compressive strain (ref. 3). The split-off component of the band edge that is higher in the gap dominates the character of the hole motion. That is, for large strains the acceptor ground level wave function is a superposition of wave functions for the energy-raised part of the valence band. The effect of the wave functions of the energy-lowered part is small for stresses approaching 10^4 kg/cm^2. For somewhat weaker stress, the binding energy is given by $\varepsilon(S) = \varepsilon_o + \varepsilon_1/S$, where ε_o = 4.9 meV, ε_1 = 8.64 eV-kg/cm^2 and S is the stress in kg/cm^2.

The mechanism for mixing in n-InSb is the power dependence of the mobility (ref. 4). The mobility is temperature dependent, mainly due to momentum-changing collisions of electrons with ionized impurities. The temperature increases with the absorbed power. This power contains the usual contribution that oscillates at the beat frequency between the signal and local-oscillator frequencies. The response time is the energy relaxation time of hot electron energy to the lattice, which time is 10^{-7}s. This corresponds to an IF bandwidth of ~3 MHz (FWHM).

Extensive far-infrared spectroscopy (ref. 5) and mixing experiments (ref. 6) have been done in high-purity n-GaAs. The main mechanism for mixing has been via the modulation of the density of conducting electrons upon

photoionization of the low-lying donor levels. This photoionization might arise from a two-step process of photoexcitation to an excited, bound level of the donor, followed by rapid thermal (or near thermal) ionization by acoustic phonons at 4K, with little carrier heating. The time response is the capture relaxation time of the conduction electrons by the ionized donors, which time is 10^{-8}s (about ten times shorter than for InSb). This corresponds to an IF bandwidth of 30 MHz (FWHM). This time and bandwidth depend upon the density of capture centers, as determined by the doping, the degree of compensation, the temperature, and the amount of photoionization.

Heterodyne mixing between the signal and local oscillator (LO) at THz (10^{12} Hz) frequencies is detected in the photocurrent collected with an applied bias voltage. The mixing is accomplished mainly through modulation of the free-carrier density. The free carriers appear from the photoionization of the impurity ground level. For acceptors (Ga), the bound holes are excited to the valence band by absorption of the combined signal to be measured and the LO. See fig. 2. The modulation has a frequency (IF) equal to the difference of frequencies of these two sources.

The depth of modulation rapidly decreases when the IF (in s^{-1}) exceeds the inverse-response time of the carrier density. This response time is mainly the hole capture (recombination) time owing to ionized acceptors. The Coulomb-like capture cross sections are very large at low temperatures. Compensation by donors assures the presence of ionized acceptors despite the tendency for carrier freezeout. Higher degrees of compensation and higher LO power increase the number of capture centers and, thus, the inverse-response time, which is the FWHM IF bandwidth (divided by π).

MIXING MECHANISM

The photocurrent waveform in the crystal is the current density, $\underline{j}(t)$, integrated over the cross-sectional area. Assuming carriers of only one type for simplicity, $\underline{j}(t) = e\, n(t)\, \underline{v}(t)$, where n and $\underline{v}$ are the number density and velocity of the carriers. Then, in the small-signal limit, the current can be modulated at the IF under three circumstances, i.e., the density can be modulated at the IF, the velocity can be modulated at the IF, or one is modulated at the LO frequency and the other at the signal frequency. A dc bias current is also present. Modulation of the density, the first case, is mainly caused by the square-law dependence on total incident electric field E(t), i.e., LO plus signal, $\underline{E}(t) = 1/2\, [\underline{E}_L \exp(-i\omega_L t) + \underline{E}_1 \exp(-i\omega_1 t)]$ + complex conjugate, through the rate of photoionization in p-Ge (Ga), or photo-excitation/ionization in n-GaAs, or free-carrier absorption in n-InSb. Modulation of the velocity, the second case, can occur through temperature dependence of the mobility or through nonparabolic-band effects. The third case, modulating density and velocity each at high frequency, really coresponds to a displacement current density. Only the first case, modulation of the carrier density, appears capable of both good sensitivity and large bandwidth. Modulation of the velocity through the mobility is the hot electron mechanism of n-InSb, while the other mechanisms appear too weak (ref. 7).

The equation for the carrier density n in excess over dark conditions is

$$\frac{\partial n}{\partial t} + \underline{\nabla} \cdot n\underline{v} = \dot{n} - \frac{n}{\tau}$$

where $\dot{n}$ is the volume rate for carrier photogeneration and τ is the carrier recombination time. The dominant component at the IF for the current density is given by

$$\underline{j}_o = \frac{e\,\underline{\underline{\mu}} \cdot \underline{E}_{dc}\,\tau}{1 - i\omega_o \tau} \quad \frac{\alpha\,\underline{E}_L \cdot \underline{E}_1 c}{4\pi\hbar\,|\omega_L \omega_1|^{1/2}}$$

where $\underline{\underline{\mu}}$ denotes the mobility tensor in the presence of uniaxial strain, $\underline{E}_{dc}$ is the bias field and α is the absorption coefficient (cm^{-1}) at the LO or signal frequency, the distinction being neglected. Quantities associated with the IF, LO, and signal frequencies are denoted by subscript o, L, and 1, respectively.

Conversion Loss

The intrinsic conversion loss L' is the ratio of the absorbed signal power to the IF power associated with the above current density, i.e.,

$$L' = \int d^3r\ \alpha |\underline{E}_1|^2 \frac{c}{8\pi} \Big/ \int d^3r\ |j_o|^2 / 2\sigma_o$$

where σ_o is the IF conductivity and the integrals are over the crystal volume. See fig. 3 for the geometry being used. Thus,

$$L' = \frac{\left(1 + \omega_o^2 \tau^2\right) R_o}{2\, P_L \mathscr{R}^2 \eta} \tag{1}$$

where the responsivity $\mathscr{R} = GeR_o/\hbar|\omega_L\omega_1|^{1/2}$ (volts/watt) and the photoconductive gain $G = \tau/\tau_d$, where $\tau_d = \ell/\mu E_{dc}$, is the drift time along the crystal length ℓ. The power $P_L = E_L^2\, c\ell w/8\pi$, where w is the width (see fig. 3). The efficiency factor η accounts for absorption and surface impedance-mismatch. The conversion loss L based on power delivered to an IF load resistance $R_{o,e}$ is obtained by multiplying L' by $(R_o + R_{o,e})^2/R_o R_{o,e}$ (ref. 4).

The conversion loss for InSb is a similar expression as for L', when the responsivity, $\mathscr{R}$, is set equal to the following (ref. 4): $\mathscr{R} = [GeR_o/(3kT_e/2)]$ $(d\ \ell n\ R_o/d\ \ell n\ T_e)$ and when τ is replaced everywhere by τ_ε, the hot electron-temperature (T_e) relaxation time. With the same absorption efficiencies η

for the Ge- and InSb-cases, the conversion losses will be in the inverse square of the ratio of the responsivities. Since this responsivity ratio is $(\tau/\tau_\varepsilon)(3kT_e/2\hbar\omega_L)/(d\ \ell nR_o/d\ \ell nT_e)$ and since the first two factors are considerably smaller than unity, and the third factor is approximately unity, the higher conversion loss for Ge is evident. Note that the product GR_o in the formula for either responsivity is independent of the mobility and the crystal length. However, L' is proportional to R_o, in equation (1), which makes L' vary inversely with the mobility. The responsivity for $Hg_{0.8}\ Cd_{0.2}\ Te$ is reported (ref. 8) to be 15 times higher than InSb, owing to a larger logarithmic derivative of the resistance when a magnetic field induces a transport anomaly at low temperature. As seen in equation (1), the IF response has a half-width at half-maximum equal to τ^{-1}, where τ is the effective recombination time. As the LO power is increased, this bandwidth is also increased, owing to the appearance of additional ionized acceptors which have large capture cross-sections.

Polarization Dependence

The ground acceptor level and the uppermost valence band edge have J = 3/2, $M_J = \pm 1/2$ for angular momentum quantum numbers. The electric dipole line-strengths for the two orthogonal senses of linear polarization (parallel and perpendicular to the uniaxial stress) are proportional to:

$$S_K = (2J + 1)^2 \begin{pmatrix} J & 1 & J \\ -M_J & K & M_J - K \end{pmatrix}^2 \varepsilon_K$$

where, in the Wigner 3-J symbol (ref. 9) K = 0 for parallel polarization, K = 1 for perpendicular linear polarization, $\varepsilon_o = 1$ and $\varepsilon_1 = 1/2$. Then $S_o = 4/15$ and $S_1 = 16/15 = 4S_o$. Thus, polarization perpendicular to the stress is preferred by the relative line strengths by a factor of four. The electric dipole moment squared for absorption along either direction is also proportional to the square of the inverse-mass component for that direction. Since the ratio of perpendicular-to-parallel mass (ref. 3) is 2.5 for stress in the [100] direction (and 3.2 for a [111] stress direction), the mass dependence more than offsets the above line-strength preference.

Noise Characteristics

Mixer IF noise consists mainly of thermal noise associated with dissipative processes, shot noise associated with the current produced by the LO, and generation-recombination noise associated with ionization of impurities and capture of carriers.

The thermal noise is mainly caused by carrier-velocity fluctuations $\langle \delta v^2 \rangle = kT/m$, so that the spectral density of current fluctuations in a bandwidth $\Delta\nu$ is given by (ref. 10)

$$\langle \delta I^2_{\omega_n} \rangle / \Delta\nu = \hbar\omega_n \coth\left(\frac{\hbar\omega_n}{2kT}\right) \text{ Re } Y_{nn} ,$$

where Y_{nn} is the total admittance for mixer and external load or terminations. The coth factor includes the zero-point quantum fluctuations. The frequency (s^{-1}) $\omega_n = \omega_o + n\omega_L$, is for the n-th sideband for an LO frequency ω_L and an IF, ω_o.

In general, Y_{mn} is the matrix element of admittance that multiplies the small-signal voltage at frequency ω_n to give the small-signal current at frequency ω_m. Thus,

$$Y_{mn} = G_{m-n} - i\,(\omega_o + m\omega_L)\, C_{m-n}$$

where G_k and C_k are the time-Fourier components of total conductance and capacitance in the presence of the large-signal, periodic, LO electric field (ref. 11) at the frequency ω_L.

Shot noise consists of charge-density fluctuations owing to the discrete particle nature of the carriers. The corresponding noise-Fourier correlation matrix elements are given by

$$\langle \delta I_m \, \delta I_n^* \rangle / \Delta\nu = 2e\, I_{m-n}$$

where I_{m-n} is the (m-n)-th Fourier component of the large-amplitude current waveform i(t) in the presence alone of the LO electric field at ω_L, i.e.,

$$i(t) = \sum_{k=-\infty}^{\infty} I_k \, e^{-ik\omega_L t}$$

The off-diagonal elements represent anomalous noise owing to correlations among the up- and down-converted components of the modulated shot noise, which is proportional to the instantaneous current i(t).

The noise temperature T_M of the mixer is determined by the apparent noise current, acting in the signal sideband alone at the mixer input, that would result in the observed IF noise voltage. This IF noise voltage is mainly the result of thermal noise, LO shot-noise, and generation-recombination (g-r) noise at all sidebands.

If the impedance Z_{ij} is the ij-th matrix element of the inverse of the admittance matrix, then the apparent signal noise current in the bandwidth $\Delta\nu$ is given by

$$\langle \delta I^2_{\omega_1} \rangle / \Delta\nu = \hbar\omega_1 \coth\left(\frac{\hbar\omega_1}{2kT_M}\right) \text{ Re } Y_{11}$$

$$= \text{Re}\left(\sum_{i,j} Z_{oi}\, Z^*_{oj} \langle \delta I_i\, \delta I^*_j \rangle / \Delta\nu\right) / |Z_{01}|^2 \qquad (2)$$

where $\text{Re} \langle \delta I_i\, \delta I^*_j \rangle / \Delta\nu = \delta_{ij}\, \hbar\omega_i \coth\left(\frac{\hbar\omega_i}{2kT}\right) \text{ Re } Y_{ii} + 2eI_{i-j} + (g\text{-}r) \text{ noise}$

$$Y_{00} \simeq R_o^{-1} + R_{o,e}^{-1}$$

$$Y_{11} \simeq \frac{c}{4\pi}\, \eta\, \frac{\ell}{w} + Y_{1,e}$$

$$Y_{01} \simeq \frac{c}{4\pi}\, \eta\, \frac{eE_L\, \ell}{\hbar |\omega_L \omega_1|^{1/2}}\, \frac{G}{1 - i\omega_o \tau}$$

and

$$Y_{10} \simeq \frac{c}{4\pi}\, \eta\, \frac{eE_L\, \ell}{\hbar |\omega_L \omega_o|^{1/2}}\, \frac{G}{1 - i\omega_1 \tau}$$

The subscripts 0, 1 and L refer to the IF, the signal and the LO, respectively. The admittances with subscript e refer to external loads or terminations, which may be suitably matching. Admittances are in Gaussian units. For practical units, replace $c/4\pi$ by $1/Z_o$, where Z_o is the wave impedance of free space. The factor η is the overall efficiency factor for absorption of the incident radiation, including the factor correcting for surface reflectance.

For no surface reflection and a thin crystal width, $\eta \simeq \alpha w$, where α is the absorption coefficient for acceptor photoionization and w is the width. Equation (2) may be solved then for T_M.

With this admittance formalism, the conversion loss L can be rewritten more generally (ref. 11) as

$$L_{01} = \text{Re}(Z_{00})\, \text{Re}(Z_{11}) / |Z_{01}|^2$$

where the impedance matrix elements are obtained from the inverse admittance matrix, which includes all sidebands together. The image sideband, for example, at ω_{-1} can be expected to have some influence.

The photoconductor density fluctuations due to generation-recombination (g-r) of the carriers is given by $\langle \delta n_h^2 \rangle = \eta P_L \tau/(\text{vol.}^2 \hbar\omega_L)$, where vol. is the crystal volume being illuminated. The g-r noise current is then

$$\langle \delta I_o \, \delta I_o^* \rangle / \Delta\nu = \frac{4e^2 P_L}{\hbar\omega_L} \frac{\eta G^2}{1 + \omega_o^2 \tau^2}$$

This spectral shape (with respect to ω_o) arises from the exponential decay in time, with correlation time τ, of the density fluctuations. This noise source is to be incorporated into the right-hand side of the equation for the mixer temperature, equation (2). Space-charge effects can influence this spectral shape (ref. 10). A particular concern is the plasma resonance near the hole plasma frequency, $\omega_p = (4\pi n_h e^2/m\varepsilon)^{1/2}$. Spatial fluctuations cause charge separation fields between holes and ionized acceptors. The divergence of this field causes a $\nabla \cdot \underline{v}$ - contribution in the equation for the carrier density, resulting in an enhancement of the above fluctuations by a factor $|\varepsilon(\omega_o)|^{-2}$ where

$$\varepsilon(\omega_o) \simeq 1 + \omega_p^2 \Big/ \left(-i\omega_o + \frac{1}{\tau}\right)\left(-i\omega_o + \frac{1}{\tau_p}\right)$$

and τ_p is the mobility relaxation time. These expressions ignore the shielding effects by electrons and the wavevector dependence, involving the Debye lengths. The thermal noise will be enhanced through modification of the IF admittances. Note that the plasma frequency is ~ 1 GHz for $n_h = 10^{11}$ holes/cm^3.

HETEROJUNCTION — SUPERLATTICES

Spatially periodic heterojunctions (e.g., Ge/GaAs) establish walls of adjacent one-dimensional potential wells and barriers. These can favorably affect the hole density of states and collision/capture times in the valence band (refs. 12 and 13). Improved mixer performance results from an increased photoabsorption with a greater density of final states and from decreased thermal noise with decreased dissipation in the IF sideband.

Major improvement would occur with an increased steepness of photocurrent dependence on modulated power. Tunneling through the potential barriers allows an exponential dependence. One means of introducing this dependence is to consider that the power modulation causes a carrier density modulation $\Delta n(t)$ in the Ge doped with Ga. Note that the superlattice acts to lift the degeneracy of the valence band edge much as strain would. The density modulation causes

an electrostatic potential energy $e\phi = 4\pi e^2 a^2 \Delta n(t)/\varepsilon$, where ε is the Ge dielectric constant, and a is the radius of curvature of the band bending (in the Ge potential wells) owing to excess holes near the walls to the adjacent barriers. See figure 4. This potential energy oscillates at the IF, i.e., $\phi = \phi_o \cos \omega_o t$.

This time dependence affects the hole quantum wave functions for the potential wells. The resulting tunneling current ΔI_o at the IF involves the overlap of wave functions for modulated energy levels in the wells, whose energies consistently differ by $\hbar\omega_o$. Thus, in terms given (ref. 14) by the Bessel functions J_n,

$$\Delta I_o \simeq \sum_{n=-\infty}^{\infty} J_n(X) \left[J_{n+1}(X) + J_{n-1}(X) \right] I_{dc}(eV_{dc} + n\hbar\omega_o)$$

where $X = e\phi_o/\hbar\omega_o$ and I_{dc} is the dc current as a function of bias voltage. This function can be an approximate exponential function of bias voltage, which is effectively $(V_{dc} + n\hbar\omega_o/e)$ for the n-photon contribution.

By appropriate spatial modulation of the doping and compensation in the superlattice the carrier lifetime can be shortened to increase the bandwidth, yet the mobility can be increased to reduce the noise and conversion loss. This requires the trapping in the Ge wells to increase capture by the local acceptors but the scatter of the two-dimensional hole gas, especially by impurities in the GaAs barrier regions, to be reduced.

CONCLUSIONS

The mixing mechanism in stressed Ge is similar to that in high-purity GaAs, and leads to larger bandwidths than for hot-electron InSb. Stress allows tunability of the Ge (doped with Ga) in a wavelength range inaccessible to n-GaAs even with magnetic fields.

Superlattices can provide exponential-type IF current-voltage characteristics for greater sensitivity. Spatial modulation of the doping and compensation can increase the bandwidth and the mobility for better performance, i.e., less conversion loss and less noise.

REFERENCES

1. Kazanskii, A. G.; Richards, P. L.; and Haller, E. E.: Far-Infrared Photoconductivity of Uniaxially Stressed Germanium. Appl. Phys. Lett., Vol. 31, 1977, pp. 496-497.

2. Hensel, J. C.; and Feher, G.: Cyclotron Resonance Experiments in Uniaxially Stressed Silicon. Phys. Rev., Vol. 129, 1963, pp. 1041-1062.

3. Hall, J.J.: Large-Strain Dependence of the Acceptor Binding Energy in Germanium, Phys. Rev., Vol. 128, 1962, pp. 68-75.

4. Whalen, J.J.; and Westgate, C.R.: Temperature Dependence of the Conversion Loss and Response Time of InSb Mixers. IEEE Trans. Electron Devices, Vol. ED-17, 1970, pp. 310-319.

5. Stillman, G. E.; Wolfe, C. M.; and Dimmock, J. O.: Detection and Generation of Far Infrared Radiation in High Purity Epitaxial GaAs. Symposium on Submillimeter Waves, Polytechnic Institute of Brooklyn, 1970, pp. 345-359.

6. Fetterman, H.; Tannenwald, P. E.; and Parker, C. D.: Millimeter and Far Infrared Frequency Mixing in GaAs. Symposium on Submillimeter Waves, Polytechnic Institute of Brooklyn, 1970, pp. 591-594.

7. Lao, B. Y.; and Litvak, M. M.: Far-Infrared Mixing in High-Purity GaAs. Journ. Appl. Phys., Vol. 42, 1971, pp. 3357-3360.

8. Nimtz, G.; Schlicht, B.; Lehmann, H.; and Tyssen, E.: A New Sensitive Microwave Bolometer Heterodyne Receiver. Appl. Phys. Lett., Vol. 35, 1979, pp. 640-641.

9. Edmonds, A. R.: Angular Momentum in Quantum Mechanics. (Princeton U, Princeton, 1960) 2nd ed., pp. 45-52.

10. Van Vliet, K. M.; and Fassett, J. R.; Fluctuations due to Electronic Transitions and Transport in Solids. Fluctuation Phenomena in Solids, R. E. Burgess, ed. (Academic: New York, 1965), pp. 267-354.

11. Held, D. N.; and Kerr, A. R.: Conversion Loss and Noise of Microwave and Millimeter-Wave Mixers: Part 1 - Theory. IEEE Trans. Microwave Theory and Techn., Vol. MTT-26, 1978, pp. 49-55.

12. R. Dingle: Confined Carrier Quantum States in Ultrathin Semiconductors in Heterostructures. Festkorperproblem XV, Advances in Solid State physics, H.J. Queisser, ed. (Pergamon-Vieweg: Braunschweig), 1975, pp. 21-48.

13. Hess, K: Impurity and Phonon Scattering in Layered Structures, Appl. Phys. Lett., Vol. 35, 1979, pp. 484-486.

14. Tucker, J. R.; and Millea, M. F., Photon Detection in Nonlinear Tunneling Devices. Appl. Phys. Lett., Vol. 33, 1978, pp. 611-613.

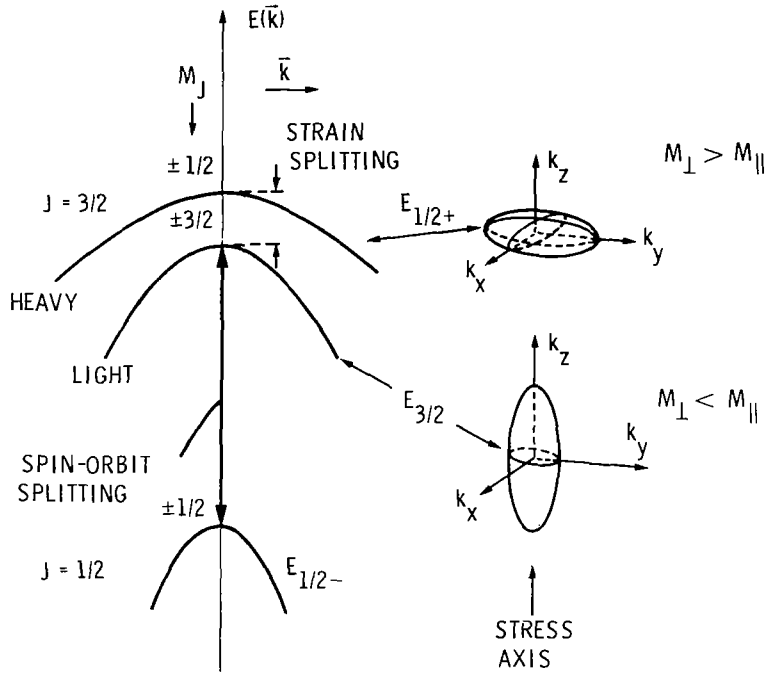

Figure 1.- Split valence bands of uniaxially compressed germanium. Uppermost valence band is heavy hole (J = 3/2, $M_J = \pm 1/2$) band with perpendicular mass greater than parallel mass.

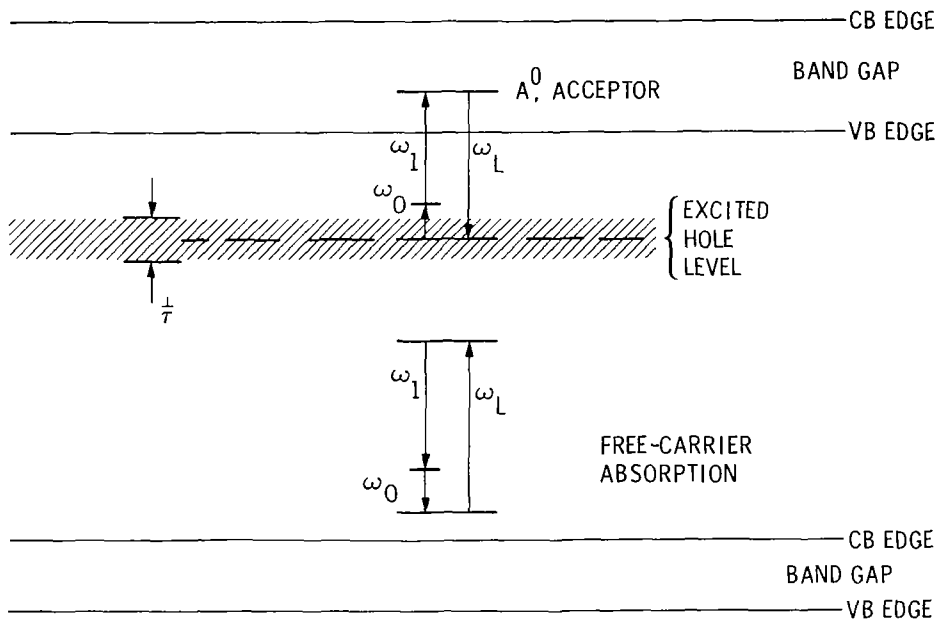

Figure 2.- Nonlinear photoionization process for mixing. Width of individual hole level within valence band (VB) is shown as $1/\tau$, where τ is effective carrier lifetime. Local oscillator (LO) frequency, signal frequency, and intermediate frequency (IF) are ω_L, ω_1, and ω_o, respectively, where $\omega_o = \omega_L - \omega_1$.

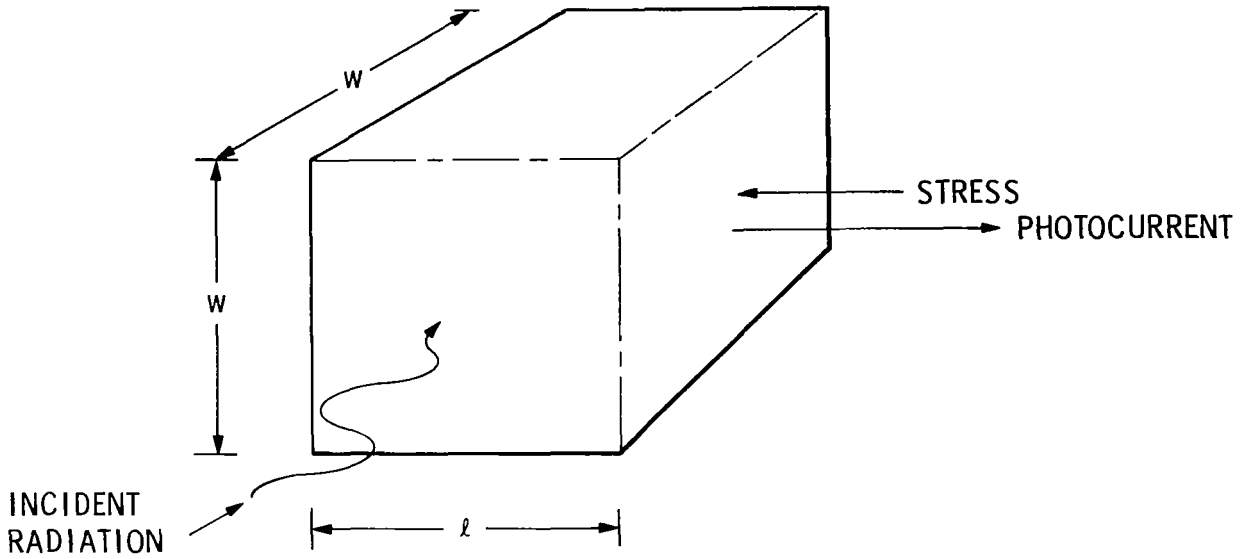

Figure 3.- Crystal geometry and directions for illumination, photocurrent, and uniaxial stress.

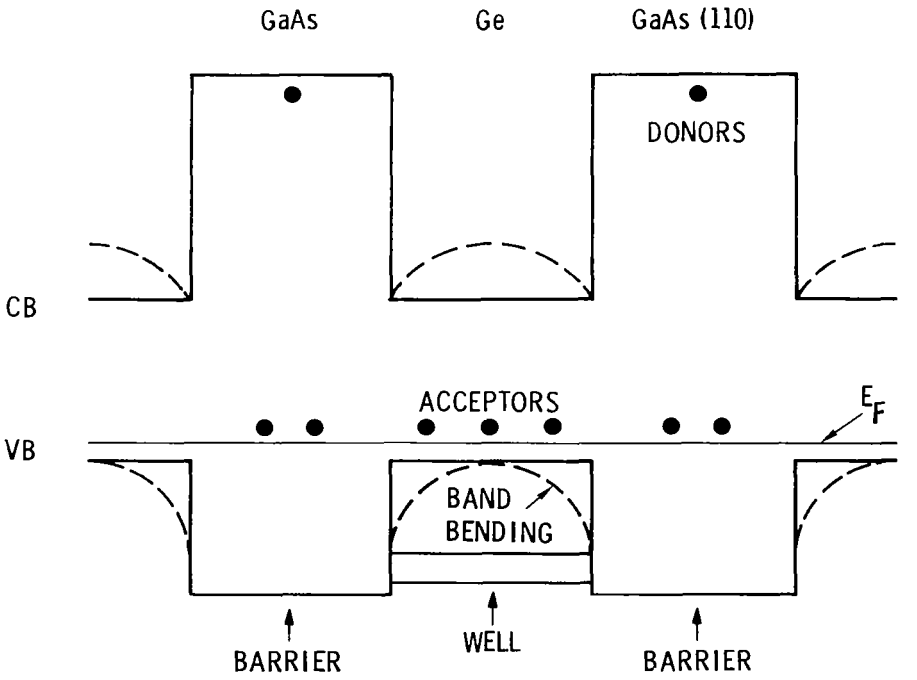

Figure 4.- Energy band diagram for p-Ge/GaAs (110) superlattice.

OPTICAL CONSIDERATIONS IN INFRARED HETERODYNE SPECTROMETER DESIGN

T. Kostiuk and M.J. Mumma
Infrared and Radio Astronomy Branch
NASA/Goddard Space Flight Center
Greenbelt, MD. 20771

and

D. Zipoy
Department of Physics and Astronomy
University of Maryland
College Park, MD.

ABSTRACT

The optical design considerations for optimization of sensitivity, tuneability and versatility of an infrared heterodyne spectrometer will be discussed using the GSFC CO_2 laser heterodyne spectrometer optical front end as an example. Problems related to the coherent nature of the laser local oscillator beam (e.g. interference effects at edges of optical elements and at the beam combining beamsplitter) will be described and proper beamsplitter design discussed. Optimum matching to the telescope will be discussed. The severe effects of large central obscuration on the coherent telescope efficiency will be described and steps to partially recover the lost system sensitivity will be proposed. Measurements made with the GSFC 48-inch telescope (linear obscuration ratio = 0.5) and the KPNO McMath telescope (no obscuration) will be given as examples.

DISCUSSION

Sensitivity of infrared heterodyne spectrometers can be expressed by the instrumental noise equivalent flux

$$(NEF) = \frac{\Delta}{\sqrt{B\tau}} \quad \text{photons/sec Hz}$$

The degradation of performance from ideal, Δ, is a total degradation factor - due to effects of chopping, polarization, detector-preamplifier efficiency, phase front misalignment, beam filling factor, line shape distribution, and optical losses (refs. 1,2).

In an operating system the optical degradation factor consists mainly of two components - losses due to the telescope and the system-telescope matching, and losses in the optical front end. Careful optical design can limit both losses to essentially those due to optical transmission of the components ($\Delta \sim 1.2$). However, highly obscured telescopes and improper front end design can introduce significant degradation in heterodyne

efficiency. In this paper we will describe a representative heterodyne system design and discuss several of the many optical problems arising on the optical table as well as in coupling the system with a field telescope.

Let us consider the optical design of the Goddard Space Flight Center CO_2 laser-infrared heterodyne spectrometer (Figure 1). The design goals were to optimize system sensitivity while maintaining maximum spectral tuning range, permit easy tuning and absolute calibration, and in general maintain system versatility for field or laboratory use.

In Figure 1 the signal beam S (source) from the telescope is chopped against a reference beam R (sky). A dichroic mirror D_1 permits a portion of the visible beam to enter a guiding eyepiece. It also can be moved to, in effect, interchange the S and R beams. The telescope beam, ν_{IR}, is collimated by an off-axis parabola. The output beam, ν_{LO}, of an in-house built grating tuned, line center stabilized CO_2 laser is attenuated, expanded, collimated and combined at a ZnSe beamsplitter with the telescope beam. The two matched collimated beams are then focussed onto a HgCdTe photomixer (supplied by Dr. David Spears, MIT Lincoln Laboratories). A portion of the visible signal is again transmitted to a guiding eyepiece by dichroic D_2. The difference frequency $|\nu_{lo}-\nu_{ir}|$ generated in the photomixer over a bandwidth of $\sim$2 GHz is then fed into our R.F. spectral line receiver (ref. 3). System calibration can be done by inserting a kinematic mirror M_1 and measuring a calibrated black body reference. This arrangement can also be used for laboratory spectroscopy of target field molecules (refs. 4,5).

Minimum optical transmission losses and elimination of chromatic effects were achieved by the use of all reflecting optics (except beamsplitter and dewar window). Thus, all focal points and all major component positions (e.g. off axis parabolas, pinholes, photomixer) are independent of the operating wavelength and no adjustments are necessary as one tunes the local oscillator. This concept is even more important for more broadly tuneable systems such as diode laser heterodyne spectrometers.

Even with the basic design goals met, many problems can arise to further degrade heterodyne performance, such as optical feedback into the laser cavity, optical standing waves, internal reflections and interference. These problems can be minimized by tilting and wedging various system components.

Let us look at two specific problems, both of which are consequences of the coherent nature of the CO_2 laser local oscillator. The first problem is illustrated in Figure 2. Displayed are scans of the expanded laser beam cross section. The upper plot shows a nearly Gaussian cross section of the laser beam which is ultimately combined with the signal beam. If the optical elements in the beam path (e.g. mirrors, apertures, beamsplitter) are smaller than the beam diameter ($\sim$distance between $1/e^2$ power points) Fresnel fringes related to edge diffraction patterns are formed (lower plot). Focussing such a local oscillator intensity distribution on the photomixer can introduce phase cancellation and noise,

and can degrade the heterodyne signal to noise.

A second problem is related to the design of the combining beamsplitter. If sufficient laser power exists, proper dielectric coating (or substrate) will enable maximum coupling of the signal beam $\geq$ 95% of signal) with sufficient local oscillator signal ($\leq$ 1 mW) for shot noise limited operation. The beamsplitter is designed to reflect the LO beam, the front surface being the beam combining plane. The back surface will also reflect a portion of the LO beam. Interference fringes will thus be generated with their separation dependent on the wavelength and the path difference between the reflected beams (i.e. wedge angle between the two surfaces). Figure 3 illustrates this problem for a 30 arc-second wedged ZnSe beamsplitter. Fringes due to the reflected CO_2 laser beam were measured by scanning a detector across the beam. The fringe spacing was consistent with the measured wedge angle. The intensity distributions and positions of the principal and second surface reflected beams yielding such fringes are plotted below. If the usable, matched beam diameter is about 2.54 centimeters (1 inch) centered on the optic axis (center of principal beam), the laser beam profile incident on the mixer is reduced in power and is far from Gaussian. It is obvious this can introduce significant degradation in the resultant heterodyne signal. The worst case would be if the intensity minimum occurs on the optic axis. This problem can be solved by designing sufficiently wedged beamsplitters so that the back surface reflection is deflected out of the optical acceptance angle of the system.

Let us now look at the degradation associated with telescope - system interface and matching. Ideally, the optics are matched to the diffraction limit of the telescope aperture and the only loss is the optical transmission of the telescope. Telescopes with a central obscuration can, however, introduce greater losses in heterodyne signal. Such effects are illustrated in Figure 4. Assuming a plane wave incident on the telescope at first glance the losses expected would be due to area blockage by the obscuration and a relative measured signal, heterodyne or direct, can be represented by the equation

$$I_{Het} = \left[1 - \left(\frac{D_{obs}}{D_A}\right)^2\right]$$

where D_{obs} and D_A are the obscuration and aperture diameters. This parabolic curve is plotted in Figure 4 (upper solid curve).

For a point source, the intensity and phase distributions at the telescope aperture are both uniform (neglecting seeing). The local oscillator beam has a Gaussian cross section and is matched to the Airy pattern of a fixed size aperture. As the central obscuration increases, the Airy pattern becomes narrower and less power is concentrated in the central maximum and more in the secondary maxima (ref. 6). For a matched fixed area detector this leads to lower incident power and signal cancellation due to the out of phase components of the electric field in the secondary maxima, which are now within the detector area. These effects on the

heterodyne signal were calculated by Degnan and Klein (ref. 7) and are plotted in Fig. 4 (crosses). These losses are seen to be greater than areal.

For an extended source (planets, Moon, Sun) the intensity pattern at the telescope aperture is a planar distribution. Assuming a detector size matched to the first Airy maximum (i.e. $2.4\,\lambda/D$), then the measure of source coherence, the mutual coherence function (MCF), takes the form of an Airy pattern with first minima occurring at the edges of the telescope aperture (ref. 8). Since heterodyne detection is a coherent technique, one would expect any obscuration of the mutual coherence function to introduce additional losses. To demonstrate this on the optical table, a variable obscuration telescope and source were simulated with an extended black-body reference source and several annular apertures inserted in the source beam. The resulting heterodyne signals (circles in Fig. 4) show even greater losses than the point source case, at large obscuration ratios. Similar measurements on the Sun increasing the 0.45 linear obscuration of the 48 inch GSFC telescope (triangles) show a similar trend.

The extent of this "coherence" loss can be estimated for a given obscuration by integrating the unobscured annulus of the mutual coherence function. Assuming a direct relationship between this integral and the heterodyne signal one can compare the results to our measurements. The Airy-like curve in Fig. 4 represents these calculations and indeed is in good agreement with measured points.

Varying the central obscuration in a 10 inch off-axis aperture in the 48-inch primary shows a heterodyne signal dependence more like the simple area blockage case. This is consistent with the present arguments since the system optics are matched to the f/no. and aperture of the 48-inch telescope. The IR mixer thus "sees" the whole aperture and the full mutual coherence function. A 10 inch slice of the 48-inch wide MCF will not vary significantly and blocking this more uniform function is similar to the simple plane wave case. The intensity distribution on the fixed area detector will also not change appreciably, since the detector intercepts only $\sim$ 1/5 of the Airy intensity pattern of the 10 inch aperture. Thus, as the obscuration is modestly increased, the active intensity on the detector is not severely altered.

We attempted to improve the heterodyne efficiency on extended sources at a highly obscured telescope by varying and matching the intensity pattern from the local oscillator to that of the telescope. We were able to recover $\sim$ 50% of the signal (star in Fig. 4) by introducing a matched central obscuration in the L.O. beam. However, this results in a great reduction of laser power on the photomixer and it may not always be possible to recover the necessary power from weak lasers to obtain optimum heterodyne efficiency at the mixer (shot noise limited operation). This may be impossible with present diode laser local oscillators, implying that central obscurations should be avoided in diode laser heterodyne

spectrometers. Theoretical treatment of the obscuration effect for extended sources by Degnan (ref. 9) suggests that it may be possible to recover all but the areal losses; however this was not found to be true on our measurements, possibly because not all the Airy lobes fall onto our photomixer.

Measurements on the Sun, identical to those taken at the 48 inch Goddard telescope, were made with our heterodyne spectrometer matched to the 55 inch McMath telescope at Kitt Peak National Observatory. Under matched conditions, and after accounting for the differences in the transmission between the two telescopes, the Sun signal measured at the unobscured McMath telescope was a factor of 2 to 3 greater than at GSFC. A degradation factor $\Delta_A \sim 1.3$ is due to area blockage alone. An additional "coherence" component Δ_{coh} of up to 2.2 was thus observed at the 48-inch telescope ($D_{obs}/D_A \sim 0.5$).

It is thus clear that coherence effects in infrared heterodyne system optical design and use have to be carefully considered in order to obtain optimum heterodyne performance. In particular, highly obscuring telescopes are inappropriate for sensitive heterodyne measurements, particularly when using diode laser local oscillators.

References

1. Kostiuk, T., M.J. Mumma, M.M. Abbas, and D. Buhl, Infrared Physics, 16, 61-64 (1976).

2. Abbas, M.M., M.J. Mumma, T. Kostiuk, and D. Buhl, Applied Optics, 15, 427 (1976).

3. Mumma, M., T. Kostiuk, and D. Buhl, Optical Engineering, 17, 50 (1978).

4. Hillman, J.J., T. Kostiuk, D. Buhl, J.L. Faris, J.C. Novaco, and M.J. Mumma, Optical Letters, 1, 81 (1977).

5. Kostiuk, T., M.J. Mumma, J.J. Hillman, D. Buhl, L.W. Brown, J.L. Faris, and D.L. Spears, Infrared Physics, 17, 431-439 (1977).

6. Tschunko, H.F.A., Applied Optics, 13, 1820 (1974).

7. Degnan, J.J., B.J. Klein, Applied Optics, 13, 2397 (1974).

8. Born, M., and E. Wolf, "Principles of Optics," p. 511, Pergamon Press, Oxford, 1975.

9. Degnan, W., Heterodyne Systems and Technology, NASA CP-2138, 1980. (Paper 33 of this compilation.)

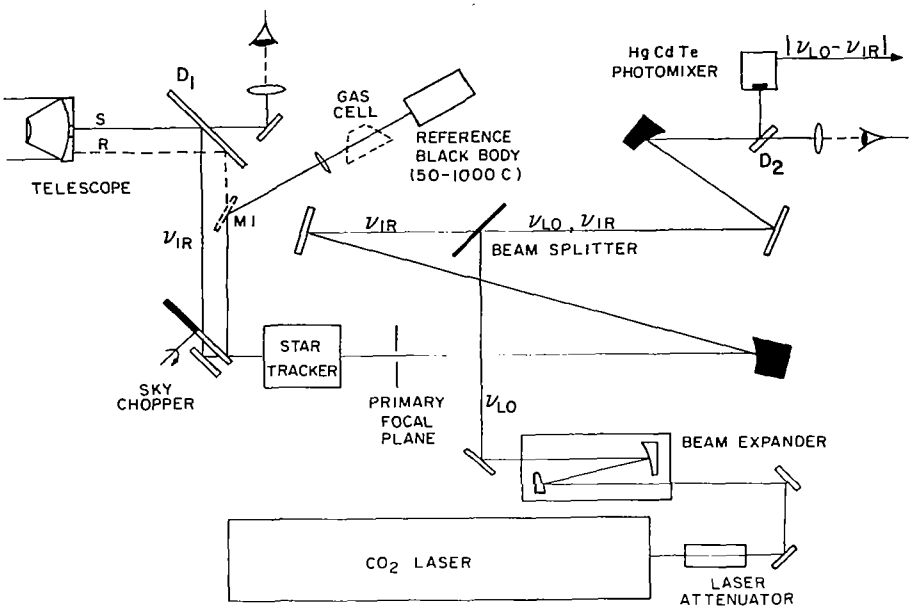

Figure 1.- GSFC CO_2 laser-infrared heterodyne spectrometer.

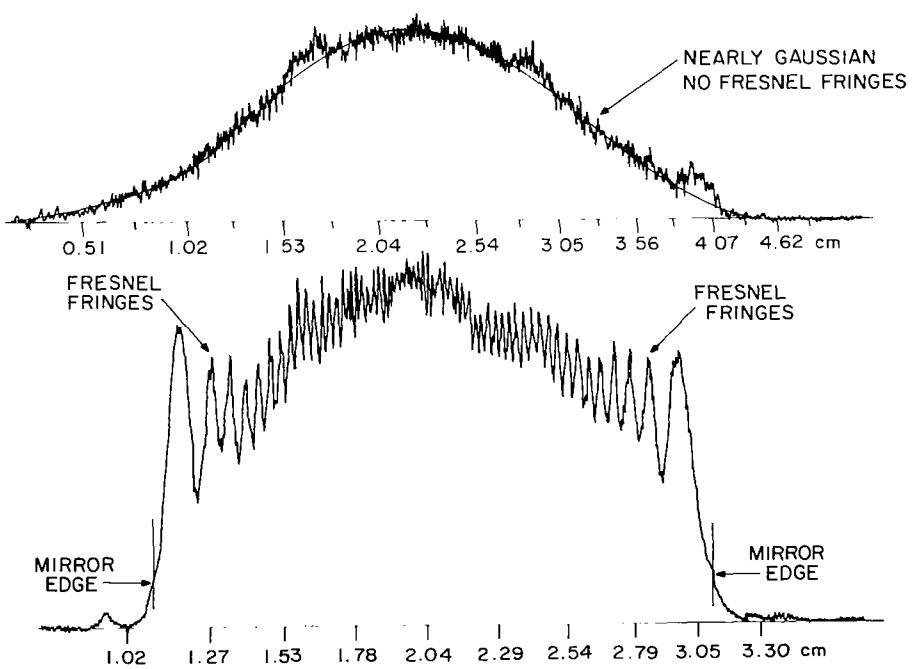

Figure 2.- CO_2 laser beam cross section. Upper plot shows nearly Gaussian output beam. Lower plot shows edge diffraction of beam by undersize mirror resulting in Fresnel interference fringes on laser beam profile.

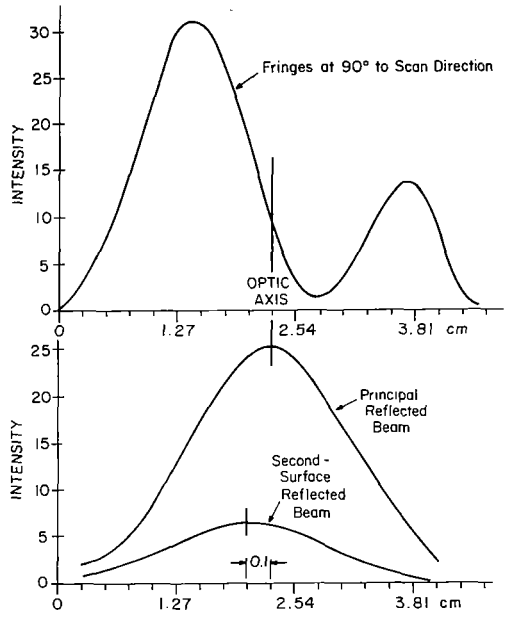

Figure 3.- Beam splitter interference fringe. The upper trace is the intensity distribution of the local oscillator measured after the beam splitter. The front and back surface reflected beams which interfere to give this pattern are indicated in the lower half of this figure. A sufficiently large wedge angle will cause the convented beam to miss the focussing parabolic mirror, eliminating heterodyne efficiency losses. Wedge angle = 30 arc-seconds.

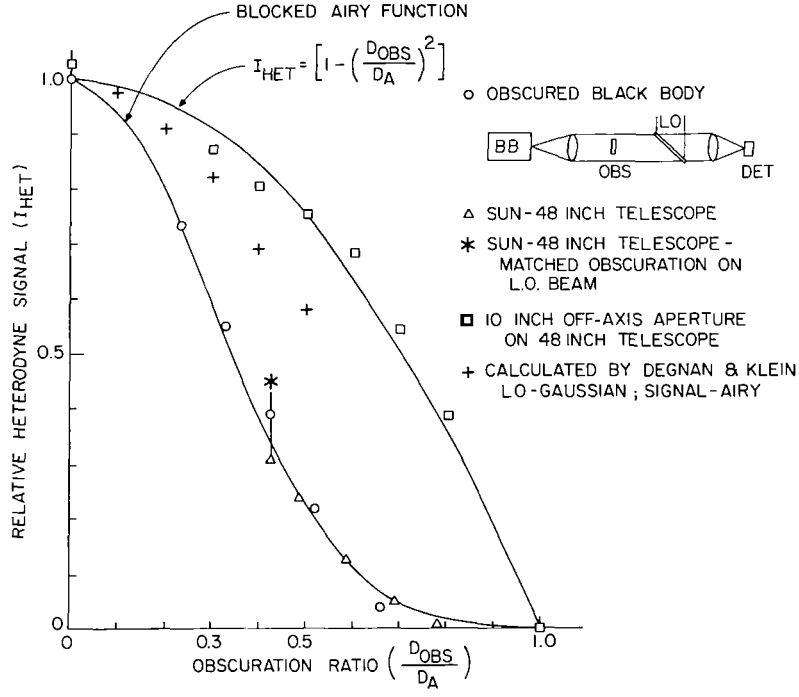

Figure 4.- Heterodyne signal losses due to central obscuration of the signal beam.

RF SPECTROMETERS FOR HETERODYNE RECEIVERS

D. Buhl and M.J. Mumma
Infrared and Radio Astronomy Branch
NASA Goddard Space Flight Center
Greenbelt, MD. 20771

Spectral line receivers require a spectrometer to divide the detected signal into a number of high resolution channels for display and analysis of a molecular line profile. Several types of spectrometers have been developed for radio astronomy receivers which utilize RF filters, multiple oscillators and mixers, digital auto-correlators and acousto/optic devices. In the infrared the heterodyne receiver places severe requirements on the spectrometer, particularly if it is to be used with a balloon or space flight receiver.

Heterodyne spectroscopy began 30 years ago with the discovery of lines due to hydrogen (HI) and then hydroxyl (OH) in various galactic gas clouds. These early receivers operated at L-band (1-2 GHz) and used maser and parametric amplifiers to achieve high sensitivity. Subsequent higher frequency receivers revealed a number of galactic molecular species (figure 1). Activity was particularly intense in the mm spectrum, leading to the discovery of over 50 interstellar molecules. The spectral lines of these molecules continue into the far infrared (FIR) where line intensities should increase. In addition to the rotational lines shown in figure 1 there are vibrational lines of molecules in the infrared. This is illustrated in the energy level diagram in figure 2. Rotational lines of SiO are shown as bars while vibrational lines are shown as arrows marked 8 and 4 μ. The rotational level separations are exaggerated, being approximately 1000 times weaker than the vibrational levels. The molecular spectrum for Orion (Figure 2) shows a width of 50 km/s with a spectral detail requiring a resolution of < 1 km/s. Hence the spectrometer must be capable of providing several hundred channels with a total bandwidth approaching 100 km/s.

A block diagram of a typical heterodyne receiver is shown in figure 3. For most receivers in the infrared the phaselock system is generally a frequency stabilizer. IF amplifiers vary from bandwidths of 100 MHz to several GHz depending on the line widths expected. Generally there is a trade off between low noise and wide bandwidth. The GaAs FET amplifier is now widely used because of its low noise, power and weight.

The RF spectrometer has been developed at GSFC to provide wide bandwidths (> 1 GHz) as well as high resolution (5 MHz). This is accomplished by dividing the 128 channel filter bank into high and low resolution sections. The high resolution section is tuneable by providing a second mixer ahead of the filter bank. This is necessary because infrared receivers which use gas lasers as local oscillators are only

tuneable to specific laser frequencies. To compensate for astronomical doppler shifts and molecule frequency differences a second local oscillator and mixer is needed. A diagram of the RF section of the filter bank is shown in figure 4.

This RF spectrometer was designed for a 10μ CO_2 laser receiver. The mixer is a HgCdTe diode made by D. Spears (Lincoln Lab). Output of the mixer is useable to 1.5 GHz and so the low resolution section of the filter bank has a bandwidth of 1.6 GHz and a resolution of 25 MHz. The high resolution section has a bandwidth of 320 MHz and a resolution of 5 MHz. Tuneability is provided by a balanced mixer and oscillators which tune from 1.6 to 3.2 GHz. This allows the high resolution section to be set at any point within the low resolution section where the spectral feature is located. This is illustrated in figure 5 which shows an atmospheric absorption line of Ozone as seen against the solar continuum. The left hand spectrum is the low resolution section running from 0 to 1.6 GHz with respect to the CO_2 laser frequency. The high resolution section on the right is set on the wings of the line profile and shows a 320 MHz detail of the wing shape. In terms of velocity for an astronomical source, 1 km/s is equal to 100 MHz at a wavelength of 10μ. Hence the filter bank bandwidth corresponds to $\pm$16 km/s and $\pm$3.2 km/s and the resolution to 0.25 km/s and 0.05 km/s for the two sections.

The RF diagram in figure 4 starts at the output of the HgCdTe mixer where the RF signal goes thru a bias T and a low noise preamp located close to the mixer dewar. A variable attenuator is at the input to the filter bank rack and provides a level set as well as a remotely control zero function for recording the DC channel offsets. The signal is then split in half for the 0-1 and 1-2 GHz amplifier chains. After boosting the signal level to 100 mw it is split by power dividers and fed to the individual filter trays which contain 8 filters each. In addition the 0.1-2 GHz signal is split to drive the balanced mixer and the high resolution amplifier chains. Various bandpass filters are present in the high resolution section to prevent amplifier saturation. The RF signal from each filter is passed through a square law detector so that the voltage output is proportional to the power input. A variable gain op amp boosts the signal level and then the individual channel outputs are sent to an integrator/multiplexer which integrates and converts the signals to 12 bit numbers which are accumulated separately as signal and reference in a 32 bit memory. Further synchronous detection and spectral processing are done by an LSI-11 computer or HP 9830 calculator connected to a Tektronix terminal. This provides on line spectral analysis capability for immediate retrieval of molecular line profiles.

A 64 channel filterbank was developed for use with 10μ and 500μ receivers. The 10μ configuration is similar to the filterbank described previously. The 500μ system requires narrower bandwidths since the doppler shift is 2 MHz for 1 km/s. The bank contains a 5 MHz low resolution section and a 1 MHz high resolution section which are both tuneable. The RF section of the spectrometer is shown in figure 6. At the input to the filter bank is a mixer driven by two transistor oscillators which can be selected to acquire any RF frequency up to 5 GHz. Following this there is

an optional amplifier and a variable attenuator to provide the correct gain or attenuation to set the level in the filter channels. Two amplifiers and a filter boost and bandlimit the signal before it is split into the high and low resolution paths. At this point the high resolution signal is sent thru another mixer to down convert it to 165 MHz. Final power amplifiers then drive the individual filter trays through a power splitter. The rest of the system is similar to the 128 channel filter bank. The 64 channel spectrometer has been used with a 10μ diode laser receiver (ref. 1). Figure 7 shows some 32 channel spectra of excess noise in the mixer caused by noise sidebands and multiple modes in the diode laser local oscillator. The first three (a,b and c) show broadband noise with different spectral shapes. The next two (d and e) show beats between different modes of the laser. The numbers inside the figures indicate the reduction factors which were used on the spectra (a,d and e). The last spectra shows the noise of the preamp which has been subtracted from the other spectra. These figures illustrate the problem of designing a spectrometer which is able to cope with the large dynamic range in the noise and its change in spectral shape, which is determined by the mixer RF response and the noise profile of the local oscillator.

The 5/1 MHz configuration of the filterbank is scheduled to be used with a 500μ receiver (ref. 2, 3 and 4). For an astronomical spectroscopy experiment at the NASA 3m telescope on Mauna Kea in May, 1980. Despite the large atmospheric absorption (> 10 db) several interstellar or planetary molecules should be detected. This is the first major astronomical spectroscopy experiment in the 500 micron region an should give an indication of the intensity, width and complexity of far infrared molecular profiles on which to base future spectrometer designs.

The RF spectrometer will continue to provide the best means of achieving ultra-wide bandwidths for infrared heterodyne receivers. For high resolution with a large number of channels, the acousto/optical spectrometer will be the principle instrument, particularly for balloon or space flight applications (ref. 5).

REFERENCES

1. Glenar, D.; Kostiuk, T.; Jennings, D. E.; and Mumma, M. J.: Development and Performance of a Laser Heterodyne Spectrometer Using Tunable Semiconductor Lasers as Local Oscillators. Heterodyne Systems and Technology, NASA CP-2138, 1980. (Paper 15 of this compilation.)

2. Tannenwald, P. E.: Far Infrared Heterodyne Systems. Heterodyne Systems and Technology, NASA CP-2138, 1980. (Paper 25 of this compilation.)

3. Koepf, Gerhard A.: Sub mm Laser Local Oscillators: Design Criteria and Results. Heterodyne Systems and Technology, NASA CP-2138, 1980. (Paper 32 of this compilation.)

4. McAvoy, N.: Submillimeter Wave Heterodyne Radiometry. NASA paper presented at the Heterodyne Systems and Technology Conference (Williamsburg, Va.), Mar. 25-27, 1980.

5. Chin, Gordon; Buhl, David; and Florez, Jose M.: Acousto-Optic Spectrometer for Radio Astronomy. Heterodyne Systems and Technology, NASA CP-2138, 1980. (Paper 29 of this compilation.)

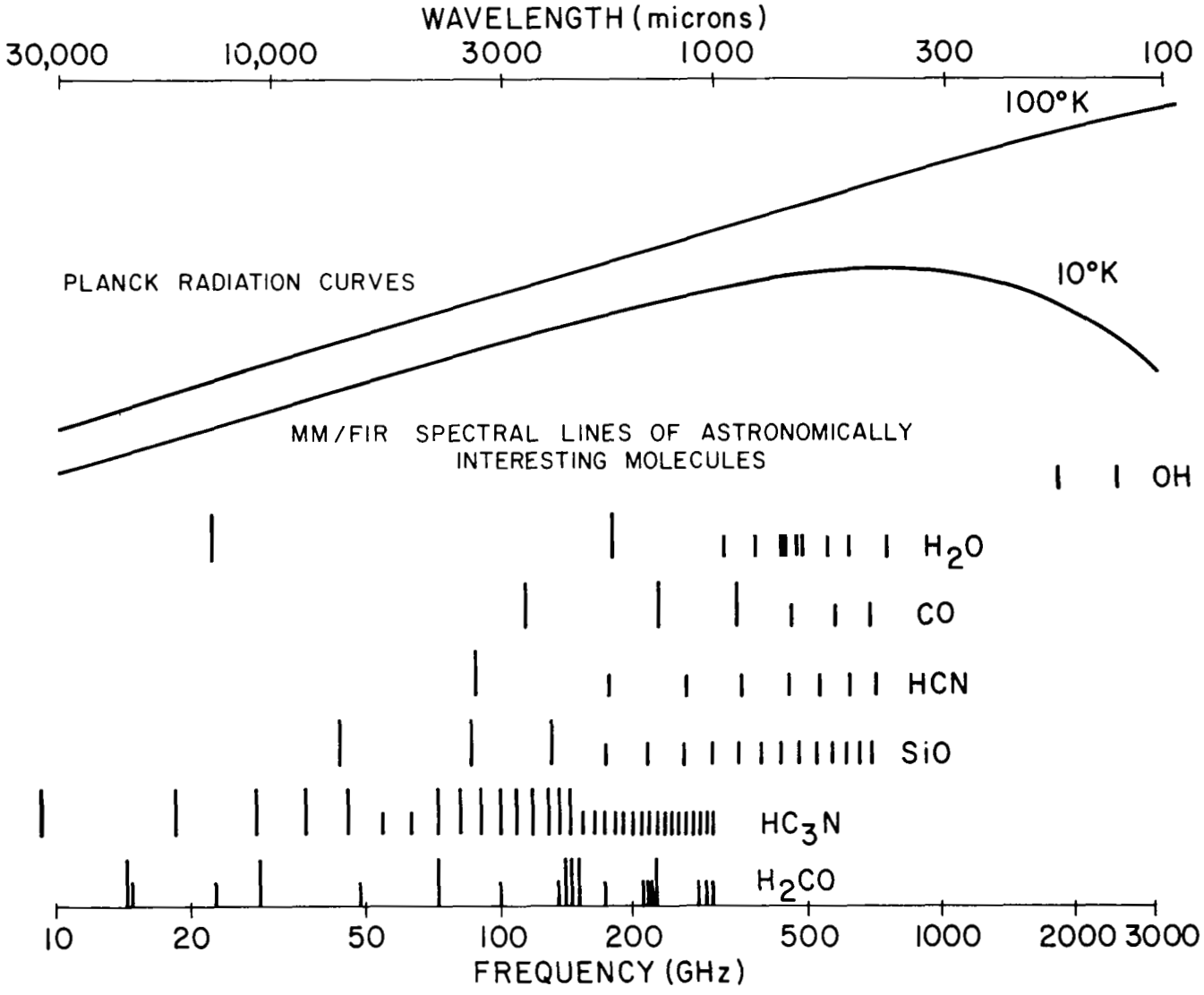

Figure 1.- Molecular lines in the radio and far infrared spectrum. The taller bars represent presently detected interstellar lines.

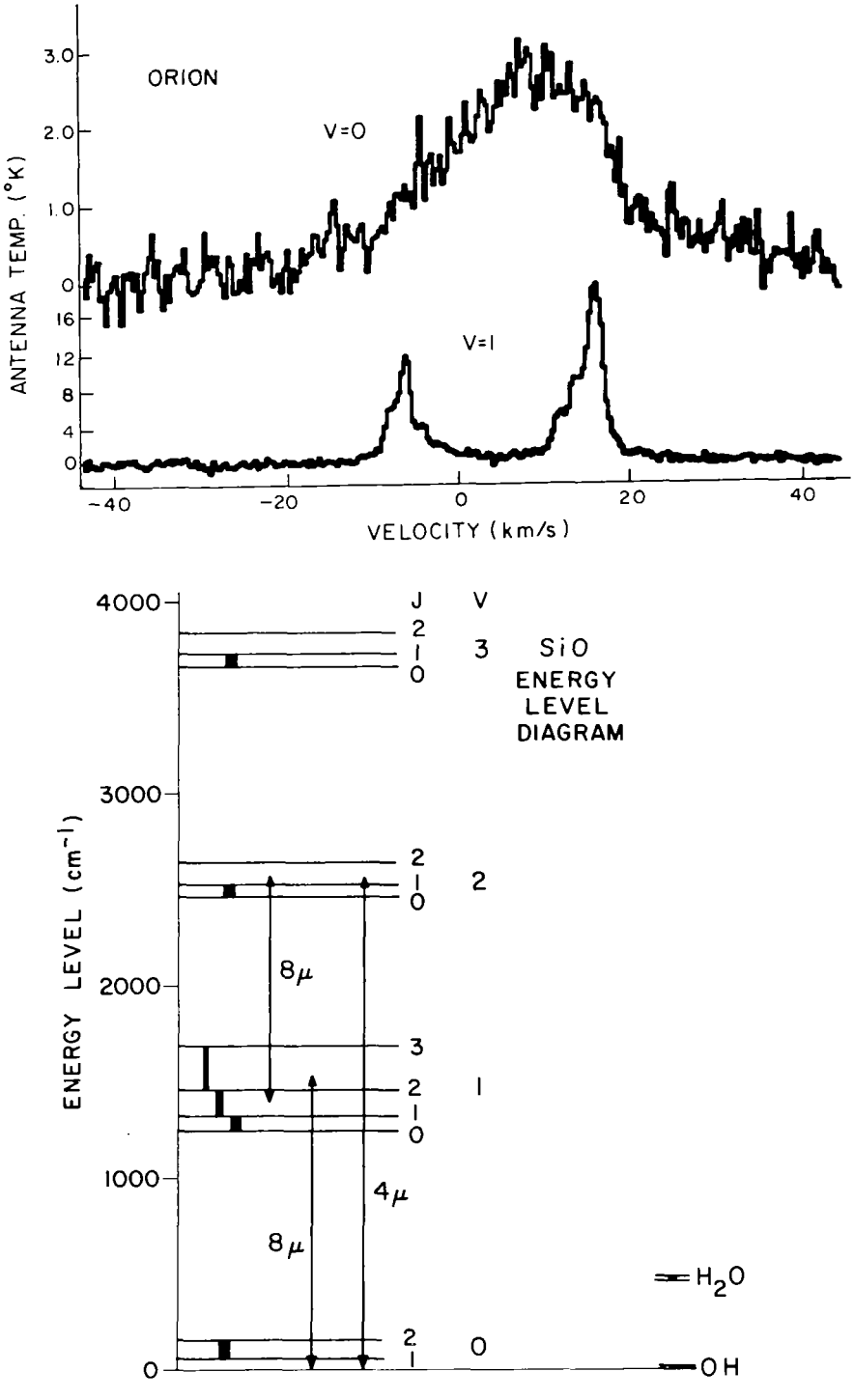

Figure 2.- The spectrum and energy level diagram for the SiO molecule illustrating the dramatic difference between the ground state (v=o) and first vibrational state (v=1) of the molecule.

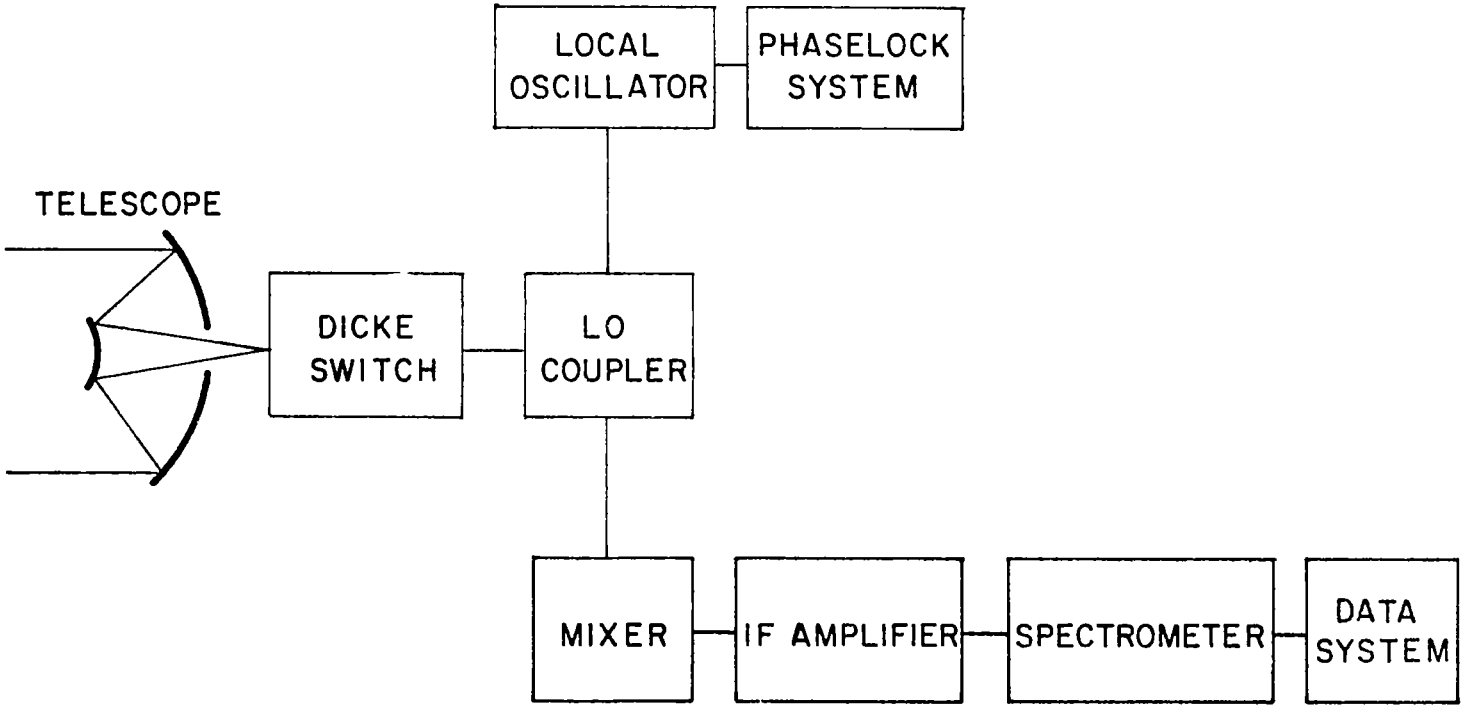

Figure 3.- Block diagram of a heterodyne receiver.

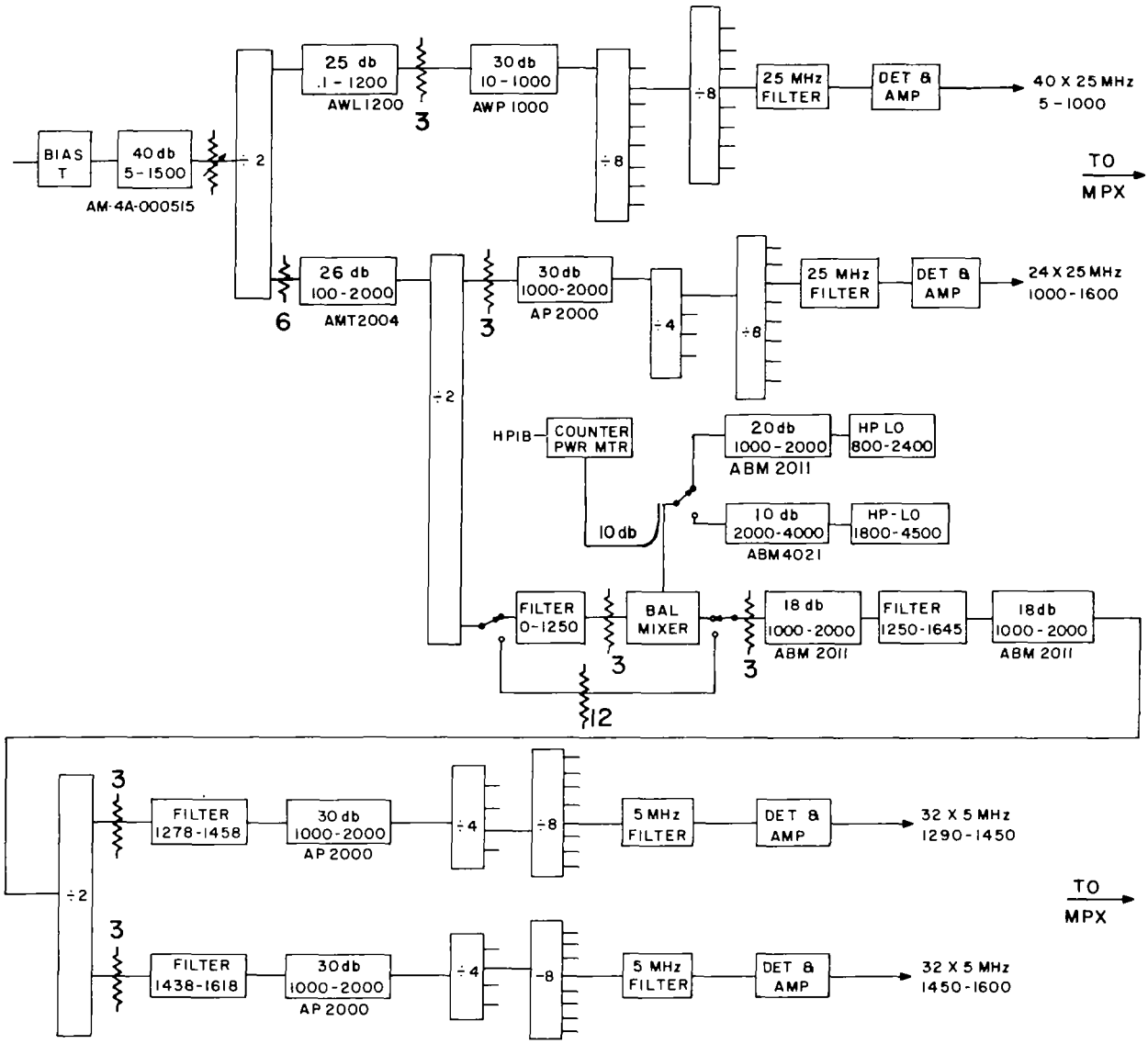

Figure 4.- 128 channel filter bank RF section: attenuation of pads between amplifiers is indicated in db, gain and bandwidth of amplifiers is shown inside boxes, filter bandwidths are also shown and power dividers are indicated as ÷2, ÷4 and ÷8. Numbers underneath amplifier boxes are Avantek model nos.

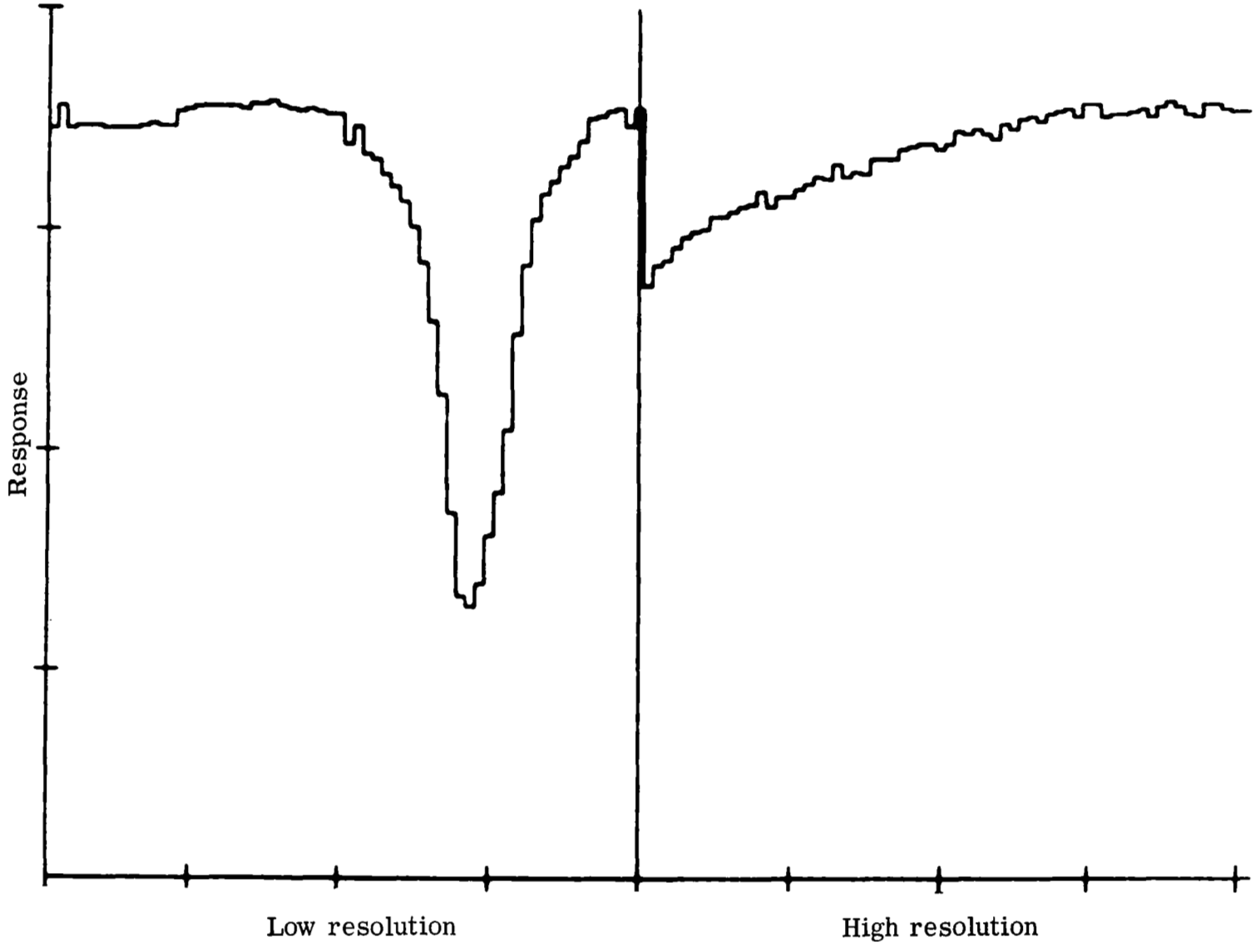

Figure 5.- Solar absorption spectrum of ozone. Low resolution section is 1.6 GHz wide and high resolution section is 320 MHz wide.

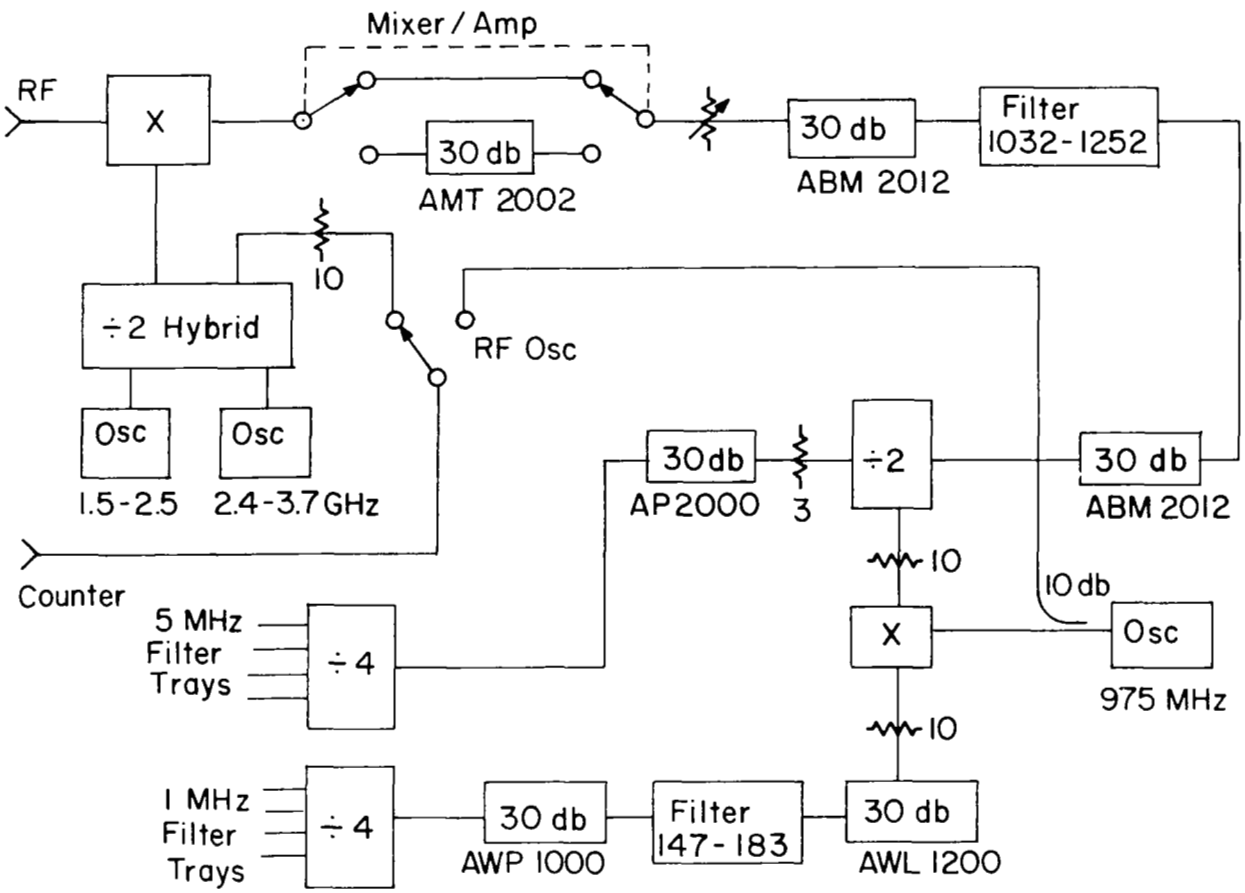

Figure 6.- 64 channel filter bank RF section showing wideband tunability of the spectrometer using a mixer and transitor oscillator.

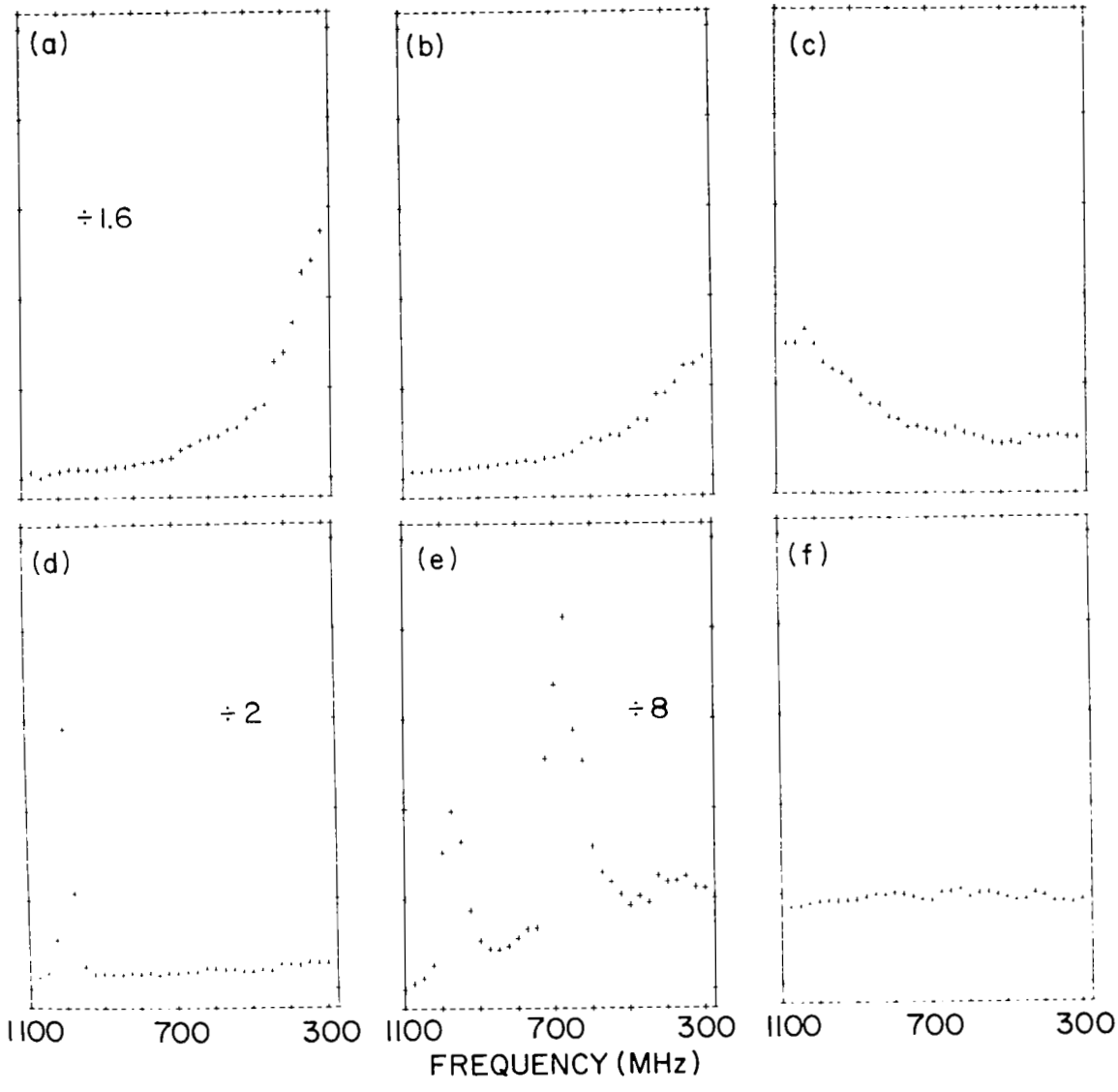

Figure 7.- 32 channel spectra of a 10μ laser diode receiver. The preamp spectrum (f) has been subtracted from the other spectra so that they show only the excess noise due to the laser. (d) and (e) illustrate multiple mode beats from the laser. Numbers inside boxes indicated reduction factors for that spectrum.

ACOUSTO-OPTIC SPECTROMETER FOR RADIO ASTRONOMY*

Gordon Chin and David Buhl
Code 693, Infrared and Radio Astronomy Branch
NASA/Goddard Space Flight Center, Greenbelt, MD 20771

Jose M. Florez
Code 728, Instrument Data Management Branch
NASA/Goddard Space Flight Center, Greenbelt, MD 20771

ABSTRACT

One of the most significant developments in radio astronomy has been the recent discovery of over 50 different molecules in the interstellar medium. These observations have changed our picture of the distribution of mass in the galaxy, altered our understanding of the process of star formation, and has also opened up a new and lively field of interstellar chemistry. This achievement was made possible not only by the development of sensitive heterodyne receivers (front-end) in the centimeter and millimeter range, but also by the construction of sensitive RF spectrometers (back-end) which enabled the spectral lines of molecules to be detected and identified. Traditionally spectrometers have been constructed as banks of discrete adjacently tuned RF filters or as digital auto-correlators. However, a new technique combining acoustic bending of a collimated coherent light beam by a Bragg cell followed by detection by a sensitive array of photodetectors (thus forming an RF acousto-optic spectrometer (AOS)) promises to have distinct advantages over older spectrometer technology. An AOS has wide bandwidth, large number of channels, high resolution, and is compact, lightweight, and energy efficient. These factors become very important as heterodyne receivers are developed into the submillimeter, far infrared, and 10 micron spectral ranges and as more observations are performed from remote, airborne, or spaceborne platforms.

We give a short description and report of existing AOS back-ends in Australia and Japan but will concentrate on our recent construction of a proto-type AOS at Goddard Space Flight Center. The GSFC AOS uses a discrete bulk acoustic wave Itek Bragg cell, 5 mW Helium-Neon laser, and a 1024 element Reticon CCPD array. The analog signals from the photodiode array are digitized, added and stored in a very high-speed custom built multiplexer board which allows us to perform synchronous detection of weak signals. The experiment is controlled and the data is displayed and stored with an LSI-II microcomputer system with dual floppy disks. We will report the performance of the GSFC AOS obtained from our initial tests.

We also will give a description of an integrated SAW Bragg cell which will miniaturize a complete AOS system into a 2.5 X 7.6-cm (1 X 3-in) package.

*This work is sponsored by Goddard Space Flight Center Director's Discretionary Fund for FY1979 and FY1980.

INTRODUCTION

A recent compilation of observed interstellar molecules[1] lists forty-six molecular species with close to 600 different observed transitions. The actual number of observed molecules is now over fifty with this figure constantly increasing. Observed molecular lines range in frequency from 1 to ~ 345 GHz. A variety of receiver front-ends are needed to cover this extremely broad frequency spectrum[2]. Below 20 GHz the signals may be amplified directly by transistor, parametric, or maser amplifiers. These receiver systems range in system temperature from 50K for the 20 GHz ruby-maser receiver to ~400K for the 50 MHz transistor receivers. Above 20 GHz, the lack of suitable pre-amplifiers forces the signal to be mixed (heterodyne) with a local oscillator (LO) and the intermediate frequency (IF) amplified by a low noise system. Heterodyne receivers in the 80-120 GHz range have achieved system temperatures of 500-1000K single side band (SSB) per channel by efficiently coupling signal and LO into cooled Schottky diode mixers followed by cooled parametric amplifiers. A room temperature heterodyne mixer receiver in the 130-170 GHz range has a system temperature of 2000K SSB while a bolometer receiver operating in the 250 GHz range has a system temperature of 30000K. Recently heterodyne techniques have been employed in the 10μm infrared band, i.e. 3×10^{13} Hz, using broad band infrared detectors as photo-mixer and 10μm CO_2 laser as local oscillator[3]. Work has been done on Josephson mixer receivers for 115 GHz and for higher frequencies[4].

The thrust of receiver development is towards high frequency heterodyne systems particularly in the millimeter, submillimeter, far infrared, and 10μm spectral ranges. The motivation for this development comes from the need to determine the chemical composition of the interstellar medium and to achieve a thorough understanding of the excitation of interstellar molecules. The most important constituent of the interstellar medium after molecular hydrogen is carbon monoxide (CO) which has its rotational transitions at 115.3, 230.5, 345.8 GHz, etc., while hydroxyl (OH), an equally important constituent, has its ground-state rotational transition at 2508 GHz. In general, the lighter the molecule, the higher its ground-state transitions which fall often above currently accessible receiver ranges.

The LO, LO coupler, and mixer present difficult challenges as the range of the receiver is extended towards higher frequencies. Klystrons which are already expensive and short-lived in the 3 millimeter range become impractical at shorter wavelengths forcing development of frequency doubling or tripling mixers utilizing cheaper and more robust lower frequency LOs. In the 10μm band CO_2 gas laser-heterodyne systems, with its various isotopic mixtures, can cover only about 10% of the spectral band due to the limited tunability of the gas laser transition and limited bandwidth response of mixers. Work is presently underway in this laboratory to construct a diode heterodyne system which will have a 2μm continuously tunable range. RF tuned cavity LO couplers which work well in the 3 millimeter wavelength become highly lossy in the millimeter range forcing development of quasi-optical techniques to combine signal and LO efficiently

to the mixer. Mixer development is also continuing to extend usable range of mixers into the far infrared and 10μm bands.

Common to all heterodyne systems is a RF spectrometer (back-end) which recovers the power spectrum of the signal from the IF. Traditionally the spectrometer is a bank of discrete adjacently tuned RF filters or a digital auto-correlator. Most radio telescopes have 256 or 512 channels at 1 MHz or 0.25 MHz resolution. Heterodyne receivers in the millimeter, submillimeter, or far infrared will be operated from remote mountain, airborne, balloon-borne, or spaceborne platforms to avoid the severe atmospheric attenuation in the 20μm to 1 mm range. This will place severe demands of size, weight, and energy usage on the back-end which RF filters may not be able to satisfy. A feasibility study of placing a submillimeter telescope on the space shuttle has been made at JPL[5]. A recent study of a 10μm heterodyne receiver on the Upper Atmospheric Research (UARS)[6] satellite shows that a 20-channel filter bank requires ~25% of the volume, ~33% of the weight, and ~30% of the power of the total instrument. A back-end using RF filters which can provide bandwidth and resolution coverage comparable to ground-based installations will prove prohibitive with respect to volume, weight, and power requirements in any free flying spaceborne experiment.

ACOUSTO-OPTIC SPECTROMETER (AOS)

Recent developments in acousto-optic techniques and in photodetector arrays have made feasible a new type of RF spectrometer [7,8] offering the advantages of wide bandwidth, high resolution, large number of channels in compact, lightweight, energy efficient, and relatively low cost systems. Such a system employs an acousto-optic diffraction cell which serves the key role of converting RF signals to ultrasonic traveling-waves modulating the optical index of the cell. The cell is illuminated across its aperture by a monochromatic laser beam. A fraction of the light is diffracted by the acoustic waves; the angle of diffraction is determined by the frequency while the intensity of the diffracted light is proportional to the power of the input RF signal. (The major portion of the laser beam at zero order passes through the cell undeflected.) A focusing lens follows the cell and essentially performs a Fourier transform of the RF signal into a far-field intensity pattern. The output intensity distribution is typically received by a linear array of photodetectors whose output is the RF power spectrum we seek. The advantages of an AOS are due to the simplicity arising from the small number of components needed to build up the system.

Currently there is intense commercial interest in applying acousto-optic techniques to electronic warfare (EW), electronic countermeasures (ECM) and electronic support systems (ESM)[9,10] which is spurring rapid technical advancements in the field. The Air Force and Navy, in a joint effort, are funding research at GTE-Sylvania, ATI-Itek, ESL, Teledyne-MEC, and Rockwell International in bulk Bragg cell AOS components. One benefit from this research is the commercial availability of 1 GHz bandwidth, 1 MHz resolution Bragg cells. The Air Force and the Navy have also funded Hughes Research and Westinghouse in an effort to further miniaturize an acousto-optic system by integrating all its components on a single

substrate. These recent developments have made acousto-optic techniques increasingly attractive for use in astronomical applications.

Radio Astronomy

Commonwealth Science and Industry Research Organization (CSIRO) in Australia and the Tokyo Astronomical Observatory in Japan have taken the lead in using acousto-optic techniques in astronomical applications. The first practical device was successfully made at CSIRO for obtaining dynamical spectrographs of solar radio emission[11,12] using a Data Light SLM 100 quartz modulator with $LiNbO_3$ transducer. This instrument has a bandwidth of 100 MHz centered on 150 MHz although the performance of the modulator was actually less. The output of the modulator is detected by a 512 element Reticon array (RL512C/12), corrected by a minicomputer, and subsequently stored on photographic film. The instrument provided time resolution of 0.06 sec.

CSIRO has also constructed prototype AO back-ends for spectral line observations on the Parkes radio telescope[13,14]. Typical galactic molecular lines are very weak compared to receiver noise figures; e.g. 1 K signals on top of ~1000K receiver noise. The standard approach to recover the weak spectral line signal from the receiver noise is to subtract a background when the telescope is pointed off source from the receiver output when the telescope is pointed on source (or some other form of Dicke switching). The CSIRO backends used both a quartz and a water-medium modulator to recover the galactic OH maser spectra on the Parkes telescope. The quartz modulator system obtained 80 MHz bandwidth at 200 kHz resolution, while the water modulator achieved an effective resolution of 20 kHz and a bandwidth of 1.5 MHz. The background subtraction was performed by a minicomputer system with gain variations removed by observation of a broadband noise source.

The radio astronomy group in Japan has chosen to bypass the traditional RF filter and auto-correlator backends in favor of the acousto-optic techniques for the 6-m millimeter wave telescope at the Tokyo Astronomical Observatory[15]. They have constructed their own Bragg modulators from bonding a cross-cut $LiNbO_3$ transducer on a TeO_2 crystal (2-cm length) with a Pb acoustic attenuator bonded on the other end. The Bragg cell is illuminated by a 5 mW HeNe laser and the output is detected by a 256-element Reticon photodetector array (RL256C/17). The achieved RF bandwidth was 10.4 MHz at 40.7 kHz resolution. The image is integrated on the Reticon for 40 ms in conjunction with 2 sec cycle chopping wheel. The output is digitized, stored, and calibrated by a minicomputer system. Their reported spectra showed 5K SiO maser emission at 86.2 GHz ($v=1$, $J=2 \rightarrow 1$) from the evolved variable star Mira (o Ceti) after 5-6 hours integration with a SSB receiver temperature of 3500K.

Prototype AOS at GSFC

Although there is extensive commercial development in AO techniques in this country, all of the applications are geared towards military needs. A thorough evaluation of AO techniques for astronomical use is in order, especially since the thrust in receiver developments is to higher frequency

and wider bandwidth and because of encouraging reports of successful AO back-ends in Australia and Japan.

The GSFC prototype AOS uses a discrete bulk acoustic wave Itek/Applied Technology Bragg cell with 300 MHz bandwidth (specified) 0.67 MHz resolution (~500 resolution elements), 5 mW Spectrophysics Model 120 helium-neon laser, and a 1024-element Reticon CCPD array. The system is mounted on stainless steel and anodized aluminum optical assembled bench components from Klinger Scientific (see figure 1).

The length of the stainless-steel rods is 1 meter, and although the optical layout is fairly compact, no attempt was made to optimize the unit for size. The laser is located on the bottom of a two tier construction, with the beam directed to the upper level by guiding mirrors. A beam expander (16X) is placed in front of the Itek Bragg cell with the cell mounted on X-Z position translators. An aberration-minimized bi-convex lens 80 mm diameter with a 47 cm focal length follows the Bragg cell. The diffracted light is then guided downward by a flat mirror, and the output light is detected by a 1024 element CCPD Reticon array mounted on precision rotation and translation stages. The interlocking construction of the Klinger assembly gives the system very good rigidity, and once the optical path has been aligned retains its alignment even after movement of the assembly as a unit. Although no attempt has been made to temperature control the assembly, the AOS appear to drift less than 1 channel over a 24-hour period.

The Itek/Applied Technology Bragg cell is made from a 1 cm optical aperture $LiNbO_3$ crystal with a specified 300 MHz bandwidth centered at 450 MHz. The interaction time is ~1.5μs with a time-bandwidth factor of ~450. The diffraction efficiency of the cell is reported to be 7%/watt of RF power. The deflection angle as a function of frequency is given by

$$\frac{\Delta\theta}{\Delta f} = \frac{\lambda}{v_s} \frac{.6328\times10^{-4}\,(\text{cm})}{6.57\times10^{5}\,(\text{cm/s})} \simeq 9.6\times10^{-5}\ \text{rad/MHz} \qquad (1)$$

where v_s the speed of sound in $LiNbO_3$. The resolution is given by

$$\delta\theta \simeq \frac{\lambda}{D} \simeq \frac{.6328\times10^{-4}\,(\text{cm})}{1\ (\text{cm})} \simeq 6.328\times10^{-5}\ \text{rad} \qquad (2)$$

and

$$\delta f = \frac{\delta f}{\Delta\theta}\ \delta\theta \simeq 657\ \text{kHz} \qquad (3)$$

This is consistent with the time bandwidth product:

$$\delta f = \frac{\Delta f}{N} = \frac{300\ \text{MHz}}{\sim 450} = 667\ \text{kHz} \qquad (4)$$

The 1024-element Reticon CCPD array has 15μm center to center. In order to match the detector element to the frequency resolved light spot (using 2 detector elements/resolution unit),

$$F = \frac{\Delta}{\delta\theta} = \frac{30 \times 10^{-6}\ \text{m}}{6.328 \times 10^{-5}} \simeq 0.47\ \text{m} \qquad (5)$$

where F is the focal length of the Fourier transform lens, and Δ is the 2 element spacing of the Reticon array. We will see that the actual deflection for the Bragg cell appears larger and that the Reticon array is over illuminated with a 47-cm focal length lens.

A custom-built multiplexer unit controls the operation of the AOS by controlling the readout, digitization, and storage of the integrated spectrum (see figure 2). Two 1024x32 bit buffer memories are necessary so that signal and reference can be subtracted to retrieve small signals by synchronous detection. The multiplexer is interfaced to a LSI-11 microcomputer system where scans are calibrated and displayed on Tektronix terminal and stored on dual-density floppy disks.

The Reticon array is read out every 15 ms with each 1024 photodetector element transferred in parallel to on-chip buffers then read out sequentially. The analog signals from the array are digitized to 10-bit accuracy and added to 32-bit memory. The standard CCPD evaluation board was used to provide the four-phase clocking to the detector chip with a primary clock signal from the multiplexer unit. The multiplexer is designed to run at a maximum rate of 1 MHz, i.e. 1 μsec to digitize and to add to memory, providing ~1msec integration on the detector chip. We hope to run experiments varying the photodetector integration period from 1 to 20 msec to evaluate the performance of the detector chip at different read out rates. A balanced set of signal and reference must be obtained and usually a multiple of ~40 secs total integration time, 20 sec on signal, 20 sec on reference, is used in conjunction with 15 msec Reticon integration and readout.

Bandwidth and Frequency Linearity

Figure 3 shows the direct readout of the 1024-element Reticon array. The AOS was operated without a light box at ordinary room illumination. The lower trace shows the detector readout after 20 sec integration at ambient light level. The two spikes are defects on the glass covering the detectors. The upper curve shows the spectrometer response to broadband noise (300K/ 50Ω terminator after ~ 120 dB gain) and is the response of the Reticon array to the diffracted laser beam. The horizontal tic marks indicate 256 channel divisions and the 450 MHz mark is at the center position of this scan. A frequency comb with signals starting at 300 MHz separated by 25 MHz each (we could not cover the full 300 MHz range of the cell due to frequency limitation of our signal generator and the over illumination of the Reticon array) was used to produce Figure 4, which graphically displays the frequency as a function of channel number (the uncertainty in both channel number and frequency are smaller than the size of the dots). Figure 4 shows that the

AOS is very linear with frequency although the deflection is greater than what is calculated by equation 1. The Reticon array covers ~235 MHz range rather than the 300 MHz implied by using a lens with a focal length given by equation 5. We also see from Figure 3 that the 3 dB bandwidth for this Itek Bragg cell is closer to 150 MHz than the reported 300 MHz. The response of the spectrometer at 300 MHz bandwidth appears to be down by at least 8 dB.

Sensitivity

The AO spectrometer is a very sensitive device in detecting weak signals. We simulated observation of a spectral line by using the chopper square wave drive from the multiplexer to amplitude modulate a 450 MHz -30 dBm signal to the Bragg cell from the signal generator (we achieved ~70% AM). The unmodulated signal is stored in the signal memory while the modulated signal is stored in the reference memory. Figure 5 shows the difference between signal and reference after 40 sec. total integration (20 sec on signal plus 20 sec on reference). We get a signal to noise of better than 50:1, but more importantly the noise spectrum away from the signal is flat without any systematic pattern. We have used the AOS to detect a -40 dBm signal to the Bragg cell by integrating over 24 hrs achieving better than 30:1 signal to noise, and again with no systematic errors over the 1024 channels. Using this synchronous detection mode the dynamic range of the AOS is better than ~40 dB.

The response of the AOS to a given RF signal is given by

$$v_i = G_i I_i + Z_i \tag{6}$$

where v_i is the output voltage at the i-th channel, G_i is the i-th channel gain of the system (Bragg cell, amplifier, and detector array gains), I_i is the RF input signal, and Z_i is the zero offset of the i-th channel (Reticon zero-th level, ambient light, and laser scattered light). The systematic gains of the AOS may be removed by forming the ratio

$$\frac{S_i - R_i}{R_k - Z_i} \tag{7}$$

where

$$\begin{aligned} S_i &= G_i I_i \text{ (signal)} + Z_i \\ R_i &= G_i I_i \text{ (reference)} + Z_i \end{aligned} \tag{8}$$

The difference between the upper and lower curves in Figure 3 gives essentially the result for $R_i - Z_i$ over the 1024 channels. The RMS noise of equation 7 should give us

$$\Delta \frac{S-R}{R-Z}_{RMS} = \frac{1}{(B\tau)^{1/2}} \tag{9}$$

where B is the bandwidth of the measurements and τ is the integration time. Figure 6 displays graphically the expected $1/(B\tau)^{1/2}$ for B = 333 kHz at 40 sec τ increments for the upper solid curve and for the lower solid curve, B = 3.3 MHz at 40 sec τ increments. Measured values at 40 sec integration time increments are given by points surrounded by boxes. We see that the measured noise of the AOS follows the $1/\tau^{1/2}$ law very well for over the 2000 sec (33 minute) period of the measurement. This indicates that there is no correlated noise source associated with the instrument. The AOS noise should follow the upper curve, which it does not. But this is not to say that the frequency resolution of the AOS is 3 MHz. The lower scale of measured points is due to uncertainty in measuring R-Z, and is caused by fluctuating ambient light levels and slow drifts in Reticon zero levels. The important result of this measurement is that the prototype system has no indication of correlated noise which limits the length of integration. However, we have not yet established the scale of the noise level.

SUMMARY

The preliminary results of tests with the GSFC AOS are encouraging. We have determined that the instrument is linear in frequency, has high dynamic range, is sensitive in retrieving weak signals, and has no correlated noise which limits integration time. However, we note that the bandwidth of the Itek Bragg cell is not as wide as advertised ($\sim$ 1/2 to 2/3 of the 300 MHz specified width), but this is not an intrinsic limitation to this technique since, hopefully, there are Bragg cells which do meet their specification. At this point we are ready to move the instrument to an existing radio telescope to perform actual observations.

Future Developments

We are planning to test a 1 GHz bandwidth 1 MHz resolution Itek Bragg cell on the existing optical setup. The only change necessary is to obtain a Fourier transform lens which will match the 1 MHz resolution light spot to the 15μm Reticon detector elements.

A more exciting development is the possibility of using integrated optics to miniaturize a complete AOS system on a single substrate of $LiNbO_3$ with dimensions of 1 in x 3 in. This concept involves using surface acoustic waves (SAW) to diffract a laser beam traveling in a single-mode wave guide formed by indiffusing Ti on a $LiNbO_3$ substrate[16]. The laser source is a GaAs diode laser in the near infrared butt coupled to one end of the substrate, while the photodetectors would be butt-coupled to the other end. Two geodesic lenses form concave aspheric surfaces which are diffraction limited lenses to collimate and focus the laser beam. We hope to acquire a hybrid integration AOS in the near future for evaluation from Westinghouse Baltimore. In place of the GasAs diode laser we will end-fire couple an HeNe laser as a first phase project. We will evaluate and test a completely integrated unit for the second phase. The integrated AOS will have 400 MHz bandwidth with 100 channels at 4 MHz resolution.

REFERENCES

1. Lovas, F.J., Snyder, L.E., and Johnson, D.R.: Recommended Rest Frequencies for Observed Interstellar Molecular Transitions. Ap. J. Supplement Series, Vol. 41, pp. 451-480, November 1979.

2. NRAO Front-end Box Status, Technical Data Sheet No. 12, National Radio Astronomy Observatory, May 1977.

3. Mumma, M.J., Kostiuk, T., Buhl, D.: A 10μm Laser Heterodyne Spectrometer for Remote Detection of Trace Gases. Optical Engineering, Vol. 17, No. 1, pp. 50-55, January-February 1978 and references within.

4. Taur, Y., Kerr, A.R.: Low Noise Josephson Mixers at 115 GHz Using Recyclable Point Contacts. Applied Physics Letters, Vol. 32, p. 775, 1978.

5. Gulkis, S., Kuiper, T.B.H., Swanson, P.N.: Scientific and Technical Prospects for Submillimeter Wavelength Radio Astronomy from Space, Jet Propulsion Laboratory, report 750-90, February 1977.

6. Mumma, M.J., et al.: Determination of Global, Absolute, Vertical Concentration Profiles of $C\ell O$ in the Earth's Stratosphere, A Proposal Submitted in Response to AO-OOS-3-78, for Upper Atmospheric Research Satellite (UARS) 1978.

7. Lambert, L.B.: Wideband Instantaneous Spectrum Analyzers Employing Delay Line Modulators. IRE National Convention Record Vol. 10, Part 6, pp. 69-78, March 1962.

8. Hecht, D.L.: Spectrum Analysis Using Acousto-Optic Devices. Optical Engineering, Vol. 10, No. 5, pp. 461-466, September-October 1977.

9. Peliotis, S.: Acousto-optics Light the Path to Broadband ESM Receiver Design. Microwaves, pp. 54-58, September 1977.

10. Oakley, W.S.: Acousto-optical Processing Open New Vistas in Surveillance and Warning Receivers. Defense Electronics, pp. 91-101, October 1979.

11. Cole, T.W.: An Electro-Optical Radio Spectrograph. IEEE Proc. Vol. 61, No. 9, pp. 1321-1323, September 1973.

12. Cole, T.W., Stewart, R.T., Milne, D.K.: An Acousto-Optical Solar Radio Spectrograph. Astron. Astrophys. 67, pp. 277-279, 1978.

13. Cole, T.W., Ables, J.G.: An Electro-Optical Spectrograph for Weak Signals. Astron. Astrophys. 34, p. 149, 1974.

14. Milne, D.K., Cole, T.W.: An Acousto-Optical Spectrometer for Radio Astronomy. Digest for Inst. Radio Eng. Aust. 16th Intl. Conf., Melbourne, p. 295, August 1977.

15. Kaifu, N., Ukita, N., Chikada, Y., Miyaji, T.: A High Resolution Acousto-Optical Radio Spectrometer for Millimeter-Wave Astronomy. Publ. Astron. Soc. Japan, Vol. 29, pp. 429-435, 1977.

16. Hamilton, M.C., Wille, D.A., Miceli, W.J.: An Integrated Optical RF Spectrum Analyzer. Optical Engineering, Vol. 16, No. 5, pp. 475-478, Spetember-October 1977.

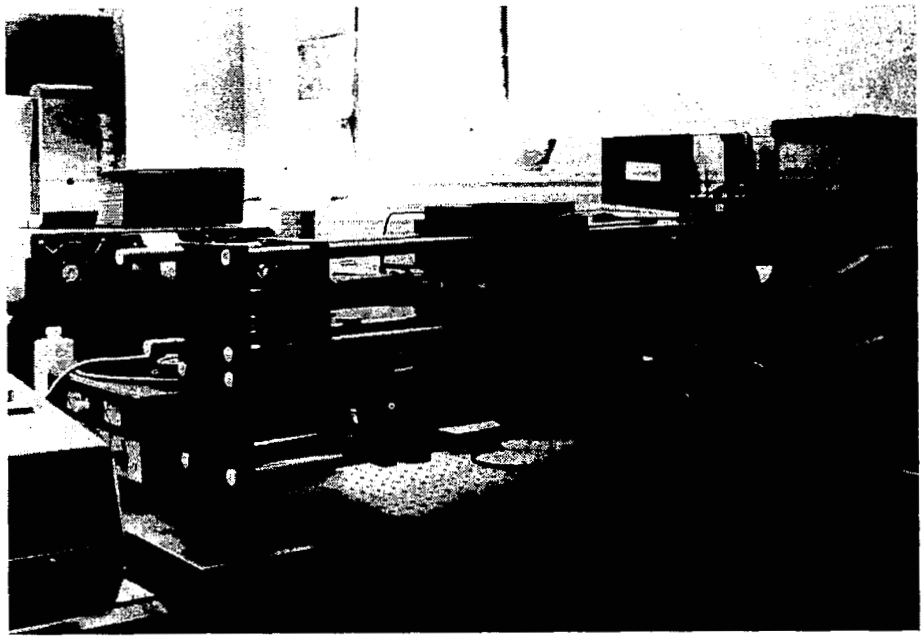

Figure 1.- GSFC acousto-optic spectrometer mounted on stainless steel and anodized aluminum optical bench. HeNe laser is located on lower level and beam is directed to upper level where Itek Bragg cell is located. The 1024 CCPD Reticon array is mounted on right.

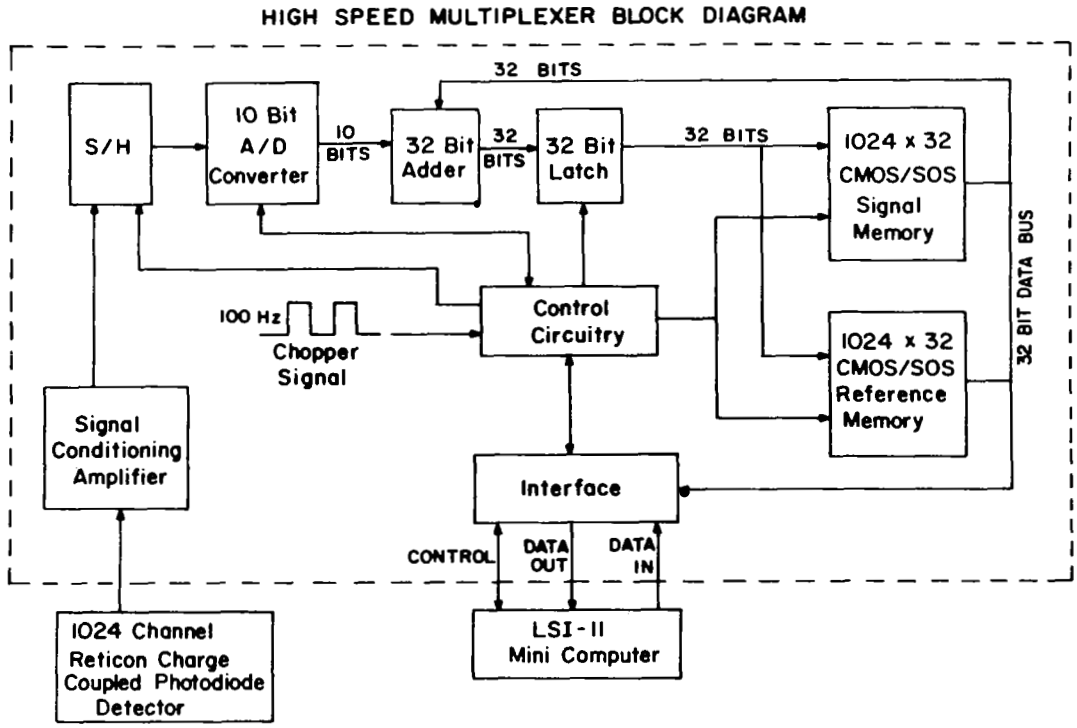

Figure 2.- Block diagram for the high speed AOS multiplexer.

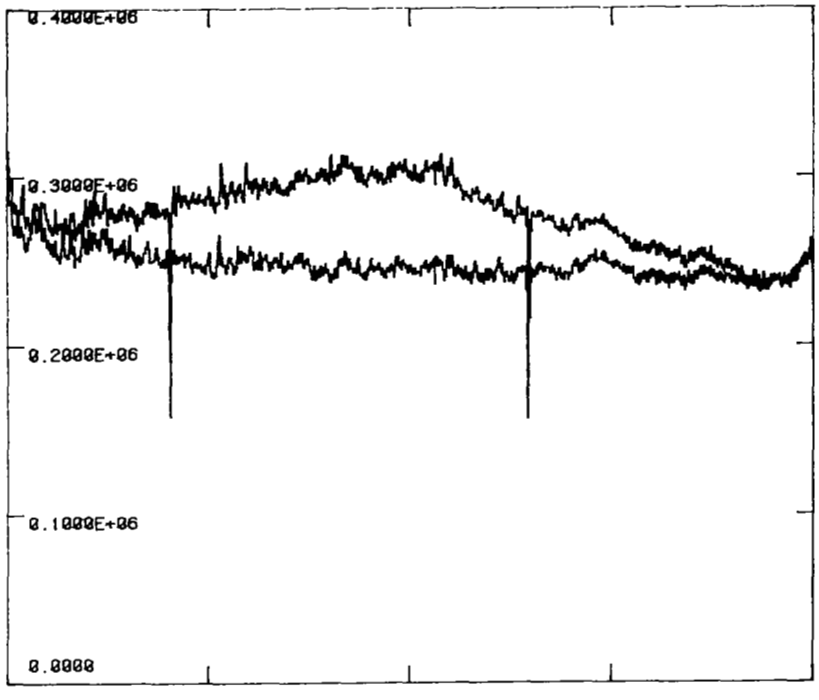

Figure 3.- Output of the 1024 channel AOS. Vertical scale in arbitrary units; horizontal scale indicates channel. Lower curve is output with broadband noise off while upper curve shows the bandpass of the AOS. Spikes are faults on the glass cover of the photodetectors.

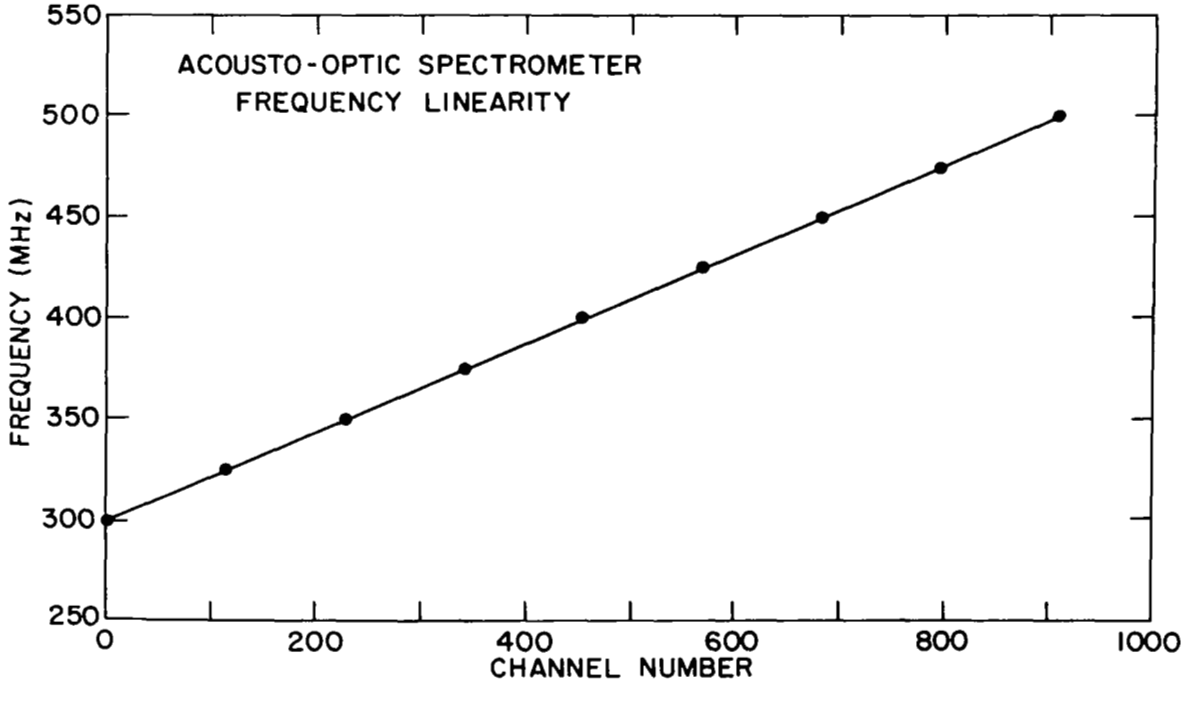

Figure 4.- Frequency linearity of the AOS.

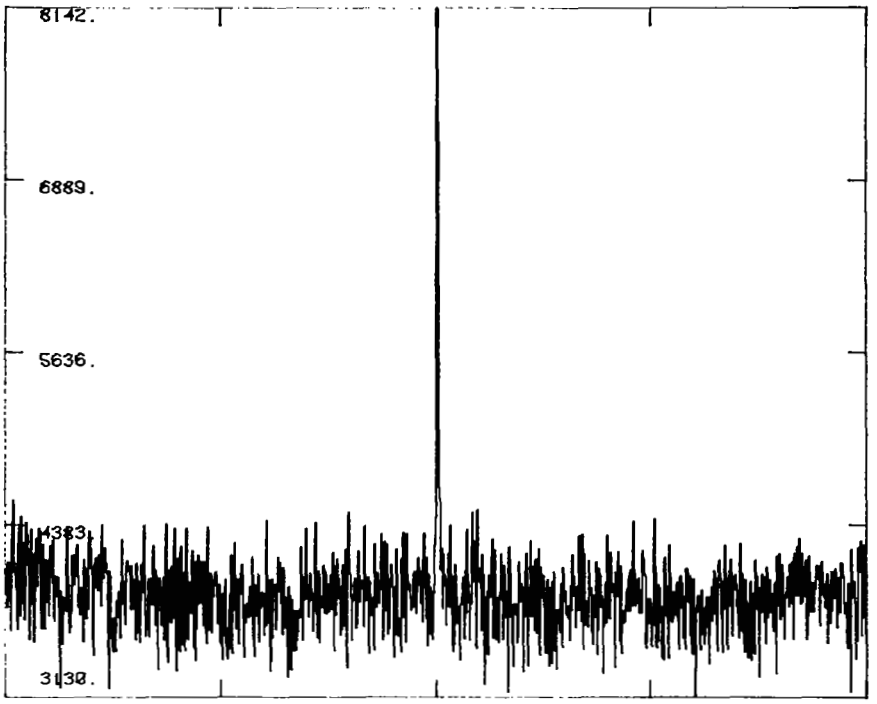

Figure 5.- Simulated observations of 450 MHz spectral line with the AOS. The -30 dBm signal was observed after 40 sec integration. Vertical scale in arbitrary units; horizontal scale indicates channel.

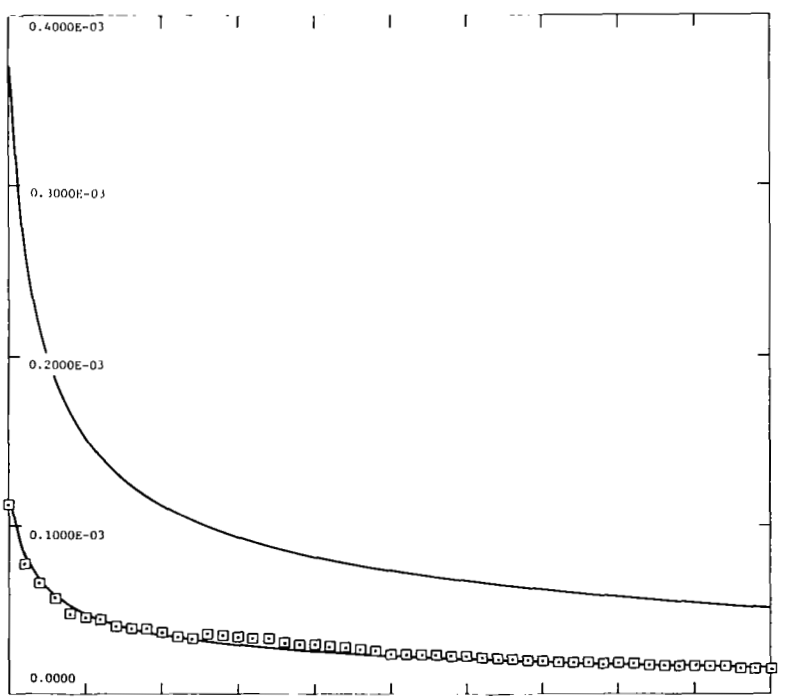

Figure 6.- RMS noise of the AOS falling as $1/\tau^{1/2}$ (τ = 40 sec increments). Solid curves correspond to B = 333 kHz (upper), and B = 3.3 MHz (lower). Observed values are points surrounded by boxes. Vertical scale in arbitrary units; horizontal scale indicates channel.

MICROWAVE TUNABLE LASER SOURCE: A STABLE, PRECISION TUNABLE HETERODYNE LOCAL OSCILLATOR

Glen W. Sachse
NASA Langley Research Center

SUMMARY

A tunable laser source utilizing a wideband electro-optic modulator and a CO_2 laser has been developed. Its precision tunability and high stability are demonstrated with examples of laboratory spectroscopy. Heterodyne measurements are also presented to demonstrate the performance of the laser source as a heterodyne local oscillator.

INTRODUCTION

A stable, precision-tunable laser source for the intermediate infrared (IR) would have numerous applications including: remote sensing of the earth, planetary, and stellar atmospheres, injection locking of high-pressure laser amplifiers, ultra-high resolution spectroscopy, isotope separation, etc. Diode lasers possess wide tunability in this region and have found wide usage in laboratory spectroscopy. However, operational difficulties primarily associated with cryogenic requirements and lack of built-in wavelength information have hampered the application of diode lasers outside the laboratory. Although several heterodyne measurements using the diode laser have been reported (refs. 1 to 3), mode competition problems (ref. 4) present additional difficulties in their use as heterodyne local oscillators. On the other hand, several line-tunable gas lasers, including the CO_2, CO, and N_2O lasers, also exist in the intermediate IR. These lasers generally possess high-frequency stability and accuracy, possess good mode quality, and operate at or near room temperature. The CO_2 laser and, to a limited extent, the CO laser have been used successfully as heterodyne local oscillators in several instruments. (See refs. 5 to 7.) However, their discrete tunability restricts their use to chance coincidences with frequencies of interest (i.e., specific absorption-line or window frequencies).

An alternative approach for providing tunability in the intermediate infrared is to utilize wideband electro-optic modulators to generate tunable optical sidebands on gas-laser carriers. This approach has the potential for providing some of the attractive features of gas lasers along with piecewise continuous tunability over significant portions of the infrared where line-tunable gas lasers of moderate power output ($\geq$ 1 W) exist. Absolute wavelength accuracy and stability of such a laser source is limited only by the gas laser. Its room-temperature operating capability may also make it more readily applicable to in-the-field operation.

Several infrared modulators (refs. 8 to 10) have been developed; however, only the GaAs waveguide modulator (ref. 11) developed by Peter Cheo of United

Technologies Research Center is discussed in this paper. The Microwave Tunable Laser Source (MTLS) is an optical/microwave system which was developed utilizing the GaAs modulator (ref. 12). In this paper the MTLS is briefly described and examples of laboratory spectroscopy and a characterization of its heterodyne properties are presented.

MTLS DESCRIPTION

The key component of the MTLS is the GaAs waveguide modulator. The modulator utilizes the linear electro-optic effect (ref. 13) to generate optical sidebands on an incident CO_2 laser carrier. The sidebands are located at the sum and difference frequencies and may be tuned by simply varying the microwave frequency within the modulator bandpass. The modulator was originally reported to have a nominal 3-dB bandpass of 5 GHz. (See ref. 11.) Since then the sideband tunability of this same modulator has been improved to $\approx$ 10 GHz. (See ref. 12.) This bandpass (see fig. 1) is located between the offset frequencies of 8 and 18 GHz. The conversion efficiency (ratio of output sideband to carrier power) reaches a maximum at 10 GHz, where it equals 0.7 percent for 20 watts of microwave power. The optical throughput of the modulator is 20 percent, and the output beam is a slowly diverging ellipse with a major to minor axis ratio of 3. After more than a year of use in our laboratory, no significant changes in the modulator performance have been observed.

The MTLS transforms the multifrequency output of the modulator into a precisely tunable monochromatic output. The carrier, which is typically 150 to 300 times more intense than either sideband, is suppressed by passing the modulator output through a heated ($\approx$ 60°C), 0.375-m long white cell with an internal 22-m path and containing low-pressure CO_2. Figure 2 contains Fabry-Perot scans of the white-cell output which indicate that, with the aforementioned white-cell parameters, the carrier is suppressed to a level equal to or less than the sidebands for the lasing transitions P(10) to P(30). Single-frequency operation is achieved by dither stabilizing a tunable Fabry-Perot etalon on the desired sideband, thereby rejecting the remaining carrier and extra sideband. A small desk-top calculator presently controls the microwave sweeper, power meter, and frequency counter. The controller can accurately place the microwave frequency anywhere between 8 and 18 GHz, or can perform high-precision scans with microwave frequency resolution well below 0.1 MHz. For a perspective of the optical and microwave powers involved, the single frequency MTLS output is typically 0.5 mW for an incident CO_2 laser power of 3 W and 20 W of microwave power. At least a 50-percent improvement in MTLS output is realizable through straightforward increases in the system optical throughput.

By utilizing the line tunability of CO_2 lasers, significant spectral coverage over the 9- to 12-μm region is achievable. Since the average CO_2 line separation is about 50 GHz, approximately 40-percent spectral coverage is achieved within the lasing region of a single CO_2 isotope laser. Figure 3 shows the calculated MTLS spectral coverage that results with five different CO_2 isotope lasers ($C^{12}O_2^{16}$, $C^{12}O_2^{18}$, $C^{13}O_2^{16}$, $C^{13}O_2^{18}$, and $C^{14}O_2^{16}$). This bar graph was generated by dividing the 9- to 12-μm region into bins each 2 cm^{-1}

(60 GHz) wide and calculating the percentage spectral coverage within each bin. Laser tunability was assumed to be P(10) to P(30) and R(10) to R(30) in each band. The calculations indicate that the spectral coverage approaches 100 percent in regions of high isotope overlap, and exceeds 50 percent when averaged across the entire 9- to 12-μm region. The N_2O laser tunability should add significantly to the spectral coverage, particularly in the 10- to 11-μm region. However, its tunability was not included in the preceding calculation.

SPECTROSCOPIC MEASUREMENTS

To illustrate the precision tunability of the system, laboratory spectroscopy of SF_6 and NH_3 was performed. The $C^{12}O_2^{16}$ laser used in these measurements was not grating-tunable; consequently, laser operation was confined to a few lines in the 10.6-μm band. The single-frequency sideband output was digitally stepped in intervals of 0.6 MHz by command from the calculator. A scan rate of 6 MHz/sec was used in these measurements. A beam splitter diverted approximately 50 percent of the optical beam to a pyroelectric detector, which served to monitor power changes during the frequency sweep. The remaining optical power passed through the 12.5-cm-long sample cell and was focused on a second pyroelectric detector. The two detector outputs were analog ratioed to provide the normalized spectra shown in figures 4 and 5.

In figure 4(a), the upper sideband of the P(20) line was stepped 10 000 times between 12 and 18 GHz, which revealed the complicated absorption spectrum of low-pressure SF_6. In figure 4(b), the same sideband was scanned across a narrower frequency interval to illustrate that the narrow 38-MHz FWHM absorption lines are easily resolved by the MTLS. In figure 5, the MTLS was scanned across two NH_3 lines - one located within the tuning range of the lower sideband, and the other within the range of the upper sideband of the P(18) CO_2 line. The determination of the line positions differed significantly from Taylor (ref. 14), but agreed to within 250 MHz with the positions reported by Curtis (ref. 15). When these measurements were performed, the microwave counter, which provides frequency accuracy to better than 1 kHz, was not in use and the CO_2 laser was not actively stabilized. The frequency accuracy of the sweep oscillator, independent of the frequency counter, is specified by the manufacturer as ±20 MHz, and the stability of the CO_2 laser during the measurement period was estimated to be better than ±5 MHz. Through stabilization of the CO_2 laser, spectroscopic measurements with frequency resolution better than 1 MHz (0.000033 cm^{-1}) should be readily achievable.

HETERODYNE CHARACTERIZATION

Before heterodyne measurements were performed, the noise characteristics of the sidebands between 0.1 and 100 MHz were investigated. This frequency range corresponded to the approximate bandpass of the heterodyne photomixer, IF amplifier, and filter. A qualitative look at the integrated noise within this bandpass was accomplished by monitoring the rectified RF photomixer output while the Fabry-Perot was spectrally scanned across the carrier and sidebands. The upper right photograph in figure 6 shows that sizable rectified noise is present at the sideband frequencies but is barely discernible at the carrier

frequency. For this particular measurement, the carrier and sideband power levels were equal as shown by the Fabry-Perot scan of the quasi-dc photomixer output (upper left photograph). The carrier power was made to equal the sideband power by fine tuning the white-cell temperature. It was found that the sideband noise was a function of the traveling-wave-tube (TWT) amplifier drive power and that a dip in the noise was achieved by operating the amplifier beyond the saturation point at a microwave output power of 15.6 W. (The output power at the saturation point was about 20 W.) Interestingly, as the drive was decreased, the sideband noise grew rapidly and reached a maximum when the microwave output was 7.2 W, which is below saturation. The dc sideband power (lower left photograph) responded proportionally to the microwave power as expected, but the noise peaks (lower right photograph) increased approximately 12 dB. Since the RF detector output was proportional to the product of the dc sideband power and the sideband noise power, the actual increase in sideband noise was approximately 15 dB. Further reduction of the drive power resulted in the noise peaks decreasing at the same rate, which implied a constant sideband noise power. The oscilloscope scale was the same for each photograph. The quasi-dc photomixer output was not preamplified; however, the RF output was amplified 60 dB.

The interpretation of these data is as follows: The broadband noise output P_N of an amplifier consists of amplified Johnson noise and internally generated noise. These noise contributions are independent of the drive power, provided the amplifier is operating in the linear region. For a matched input,

$$P_N = kTGN$$

where k is Boltzmann's constant, T is room temperature, G is the TWT gain, and N is the noise factor. The noise figure (the dB equivalent of the noise factor) is the measure of the internally generated noise and was manufactured specified to be 35 dB. The small signal gain was measured to be 62 dB at the operating frequency. Since the sweep oscillator is capable of delivering 10 dBm, only 33-dB TWT gain is necessary to reach the desired 20 watts microwave output. Because the drive signal was by necessity strongly attenuated, this excess TWT gain in effect contributed nearly the same signal-to-noise (S/N) degradation as did the noise figure when the TWT was operated in the small signal region. The large reduction in sideband noise observed when the TWT was operated well into saturation was simply due to a 15-dB gain compression which reduced P_N according to the preceding equation.

The properties of the sideband noise were further analyzed by monitoring the photomixer amplifier output with a spectrum analyzer. Three conditions of photomixer illumination were investigated. In the bottom spectrum of figure 7(a), the photomixer was not illuminated, which resulted in a noise spectrum associated with the photomixer and the IF amplifier. Next, the etalon bandpass was tuned so that only the carrier illuminated the photomixer. This resulted in a broadband noise increase of $\approx$ 3 dB associated with the carrier shot noise. When the etalon was tuned to the sideband frequency, the expected large increase in noise was observed. The increase above the carrier noise amounted to $\simeq$ 16 dB at the low-frequency end and $\approx$ 12 dB near 100 MHz. The sideband and carrier power were roughly equal at 140 μW, and the TWT was operated well into saturation to yield the minimum sideband noise.

With the TWT used in the aforementioned measurements, the minimum sideband noise was achieved with the TWT gain compressed to 47 dB and an output power of 15.6 W. Under these conditions, the drive signal had to be attenuated ≈ 15 dB, which resulted in a corresponding microwave S/N degradation. Since the sideband noise was 12 to 16 dB greater than the carrier shot noise, a lower-gain TWT amplifier not requiring attenuation of the input drive signal might be expected to introduce a noise level comparable to the shot noise. A lower-power (10 W) TWT amplifier with low gain and a manufacturer-specified noise figure of 35 dB was located and its noise spectral characteristics were investigated in figure 7(b). With no input attenuation, the amplifier was driven to 9.6 W output. The carrier power was again made to equal sideband power. At a reduced carrier power of 100 μW, a shot noise of 1.5 to 2 dB above the "photomixer" noise was observed. As expected, the broadband component of the sideband noise decreased sharply to a level 3 to 4.5 dB above the shot noise. Narrow-band noise at 5 and 15 MHz is probably due to coherent oscillations (ref. 16) in the traveling wave tube, and is not generally found in a well-designed tube that is operating properly. Further reductions in the sideband noise can be achieved by lowering the noise figure. Low-gain TWT amplifiers are commercially available with noise figures on the order of 30 dB. An alternative method of lowering the overall noise figure would be to include an intermediate amplifier of low noise figure.

A heterodyne measurement of the thermal radiation from a 1273 K blackbody was performed to compare the S/N achieved using the carrier and the sideband as local oscillators. The collimated blackbody beam was passed through a long-wave pass filter (8.9 μm cut-on wavelength) in order to minimize the contribution of the chopped thermal shot noise to the heterodyne IF output. A 50-percent beam splitter was used to bring the local oscillator and blackbody beams into coincidence. During the experiment the MTLS delivered 220 μW after the beamsplitter, but generated a detector photo-current the equivalent of only 100 μW. The excessive detector overfill occurred since no attempt was made to optically match the elliptical modulator output with the circular detector. A 10-MHz high-pass filter was added to the heterodyne IF stage in order to reject the strong TWT-generated noise peak at 5 MHz. Thus, the total heterodyne bandpass was 90 MHz.

The results of the heterodyne measurements are shown in figure 8. The rectified outputs of the heterodyne IF state are plotted against time for three local oscillator cases - carrier, no local oscillator, and sideband. In each case a measurement period of 30 sec is plotted. The RC time constant of the lock-in amplifier filter was 1.25 sec, which is equivalent to an effective bandpass of 0.1 Hz for a 12 dB/octave filter. As expected, the heterodyne signal magnitudes were very nearly equal and the sideband local oscillator exhibited somewhat poorer S/N than the carrier. The non-zero output registered with no local oscillator was due to the chopped thermal shot noise.

CONCLUDING REMARKS

A stable precision tunable laser source has been developed using a wide-band electro-optic modulator and a CO_2 laser. With the use of five CO_2 isotope

lasers and the 8 to 18 GHz sideband offset tunability of the modulator, calculations indicate that > 50 percent spectral coverage in the 9- to 12-μm region is achievable. This wavelength region is especially important for the development of optical atmospheric sensing instrumentation, since it coincides with an atmospheric window and a region where high technology infrared components exist. The wavelength accuracy and stability of this laser source is limited by the CO_2 laser and is more than adequate for the measurement of narrow Doppler-broadened line profiles. This was demonstrated with the spectroscopic measurements of SF_6. The room-temperature operating capability and the programmability of the MTLS are attractive features for its in-the-field implementation. Although heterodyne measurements indicated some S/N degradation when using the MTLS as a local oscillator, there does not appear to be any fundamental limitation to the heterodyne efficiency of this laser source. Through the use of a lower noise-figure TWT amplifier and optical matching of the MTLS output beam with the photomixer, a substantial increase in the heterodyne S/N is expected.

REFERENCES

1. Harward, C. N.; and Hoell, J. M.: Atmospheric Solar Absorption Measurements in the 9-11 Micron Region Using a Diode Laser Heterodyne Spectrometer. Heterodyne Systems and Technology, NASA CP-2138, 1980. (Paper 16 of this compilation.)

2. Ku, R. T.; and Spears, D. L.: High Sensitivity Infrared Heterodyne Radiometer Using a Tunable Diode Laser Local Oscillator. Optics Letters, Vol. 1, No. 3, Sept. 1977, pp. 84-86.

3. Frerking, M. A.; and Muehlner, D. J.: Infrared Heterodyne Spectroscopy of Atmospheric Ozone. Applied Optics, Vol. 16, No. 3, March 1977, pp. 526-528.

4. Harward, C. N.; and Sidney, B. D.: Excess Noise in $Pb_{1-x}Sn_xSe$ Semiconductor Lasers. Heterodyne Systems and Technology, NASA CP-2138, 1980. (Paper 10 of this compilation.)

5. Hoell, J. M.; Harward, C. N.; and Williams, B. S.: Remote Infrared Heterodyne Radiometer Measurements of Atmospheric Ammonia Profiles. Geophysical Research Letters, Vol. 7, No. 5, May 1980, pp. 313-316.

6. Menzies, R. T.: Remote Measurement of CℓO in the Stratosphere. Geophysical Research Letters, Vol. 6, No. 3, March 1979, pp. 151-154.

7. Menzies, R. T.: Use of CO and CO_2 Lasers to Detect Pollutants in the Atmosphere. Applied Optics, Vol. 10, No. 7, July 1971, pp. 1532-1538.

8. Magerl, G.; and Bonek, E.: Broadband Electronically Tunable Resonant Microwave Modulators for CO_2 Lasers. Applied Physics Letters, Vol. 34, No. 7, April 1, 1979, pp. 452-454.

9. Carter, G. M.; and Haus, H. A.: Optical Single Sideband Generation at 10.6 μm. IEEE Journal of Quantum Electronics, Vol. QE-15, No. 4, April 1979, pp. 217-224.

10. Spears, D. L.; and Strauss, A. J.: CdTe Optical Waveguide Modulators. Revue de Physique Appliquee, Vol. 12, Feb. 1977, pp. 401-404.

11. Cheo, P. K.: Generation and Applications of 16 GHz Tunable Sidebands from a CO_2 Laser. Proceedings of the Third International Conference on Laser Spectroscopy, Jackson Lake, WY, July 4-8, 1977.

12. Sachse, G. W.; and Cheo, P. K.: Microwave Tunable Laser Source for the Infrared. Proceedings of the Conference on Laser and Electro-Optical Systems, San Diego, CA, Feb. 26-28, 1980.

13. Kaminow, I. P.; and Turner, E. H.: Electro-optic Light Modulators. Applied Optics, Vol. 5, No. 10, Oct. 1966, pp. 1612-1628.

14. Taylor, F. W.: Spectral Data for the ν_2 Band of Ammonia with Application to Radiative Transfer in the Atmosphere of Jupiter. Journal of Quantitative Spectroscopy and Radiative Transfer, Vol. 13, No. 1973, pp. 1181-1217.

15. Curtis, J. B.: The Vibration-Rotation Bands of NH_3 in the Region 670 cm^{-1} to 1860 cm^{-1}. Ph.D. Thesis, Ohio State University, 1974.

16. Gittins, J. F.: Power Traveling Wave Tubes. American Elsevier Publishing Company, Inc., New York, 1965.

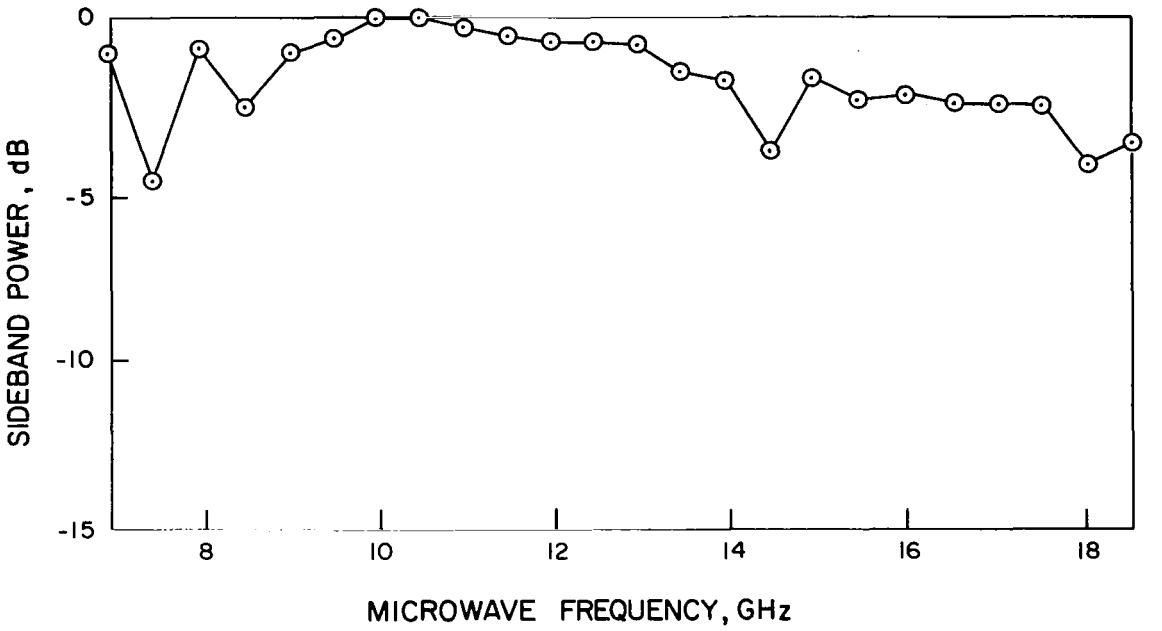

Figure 1.- Microwave bandpass of the GaAs waveguide modulator.

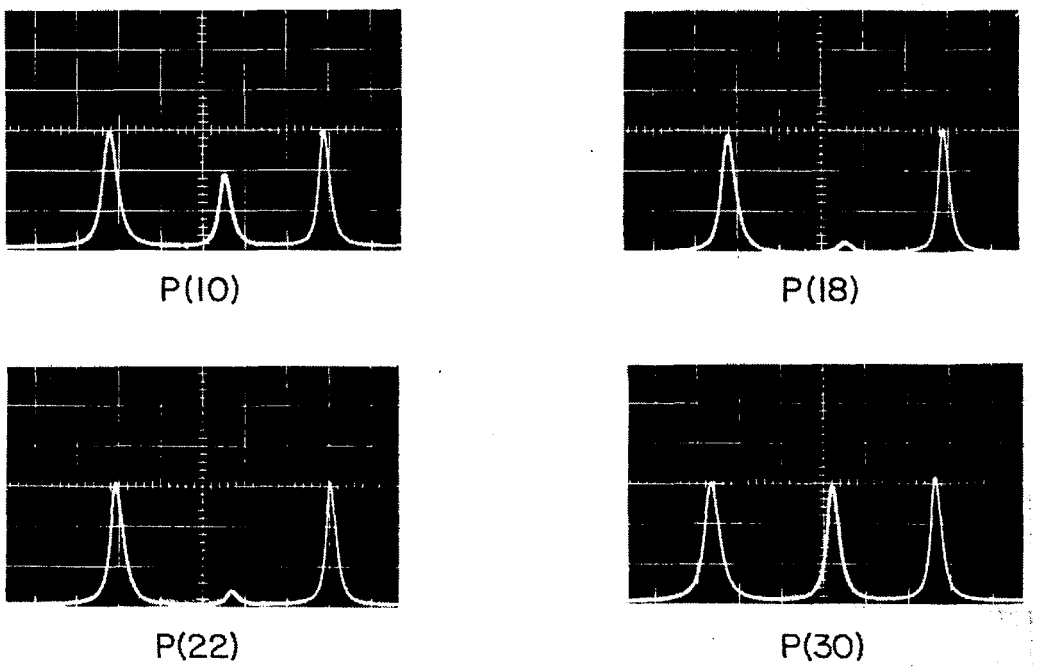

Figure 2.- Fabry-Perot scans of white-cell output as a function of CO_2 laser transition.

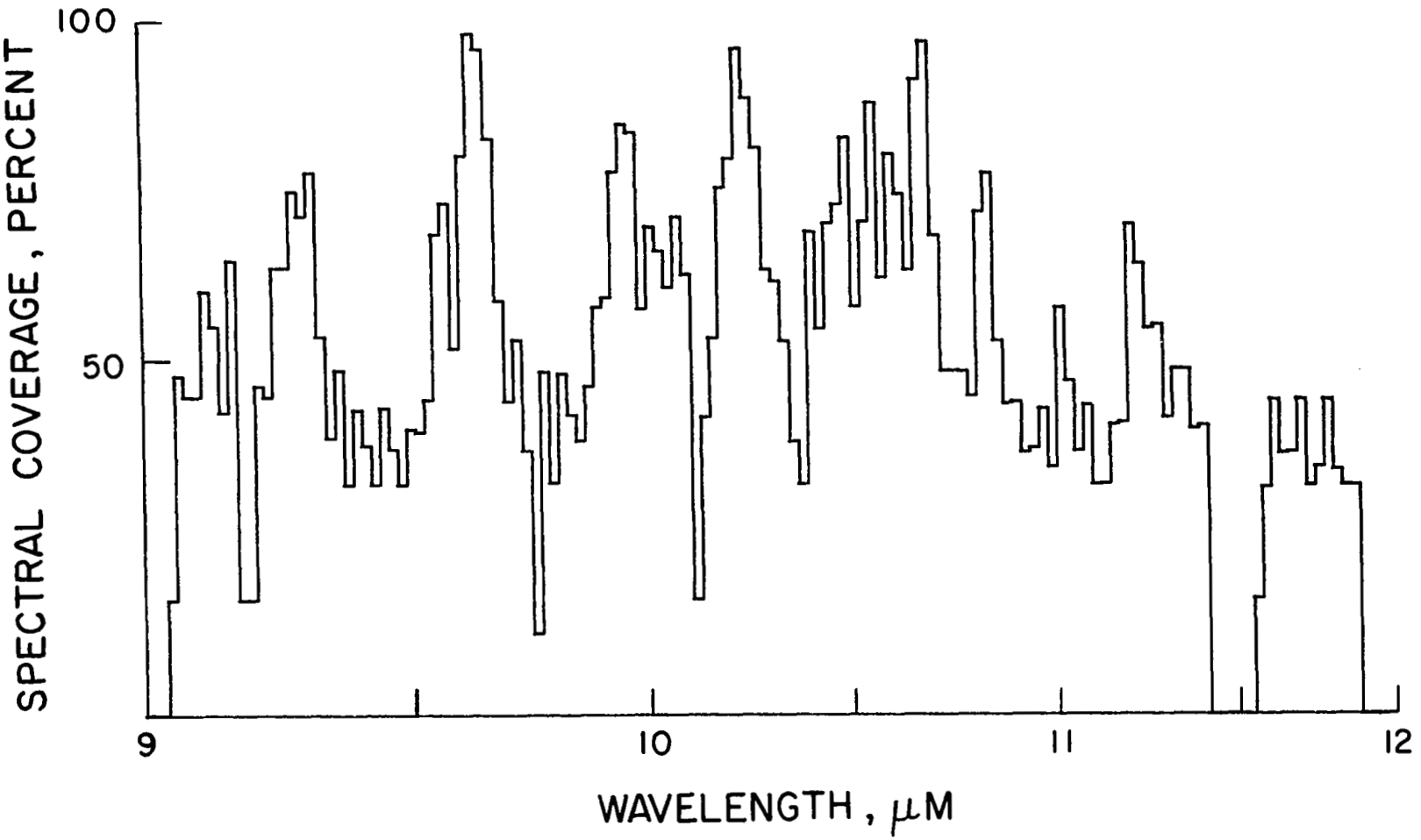

Figure 3.- Calculated spectral coverage of MTLS.

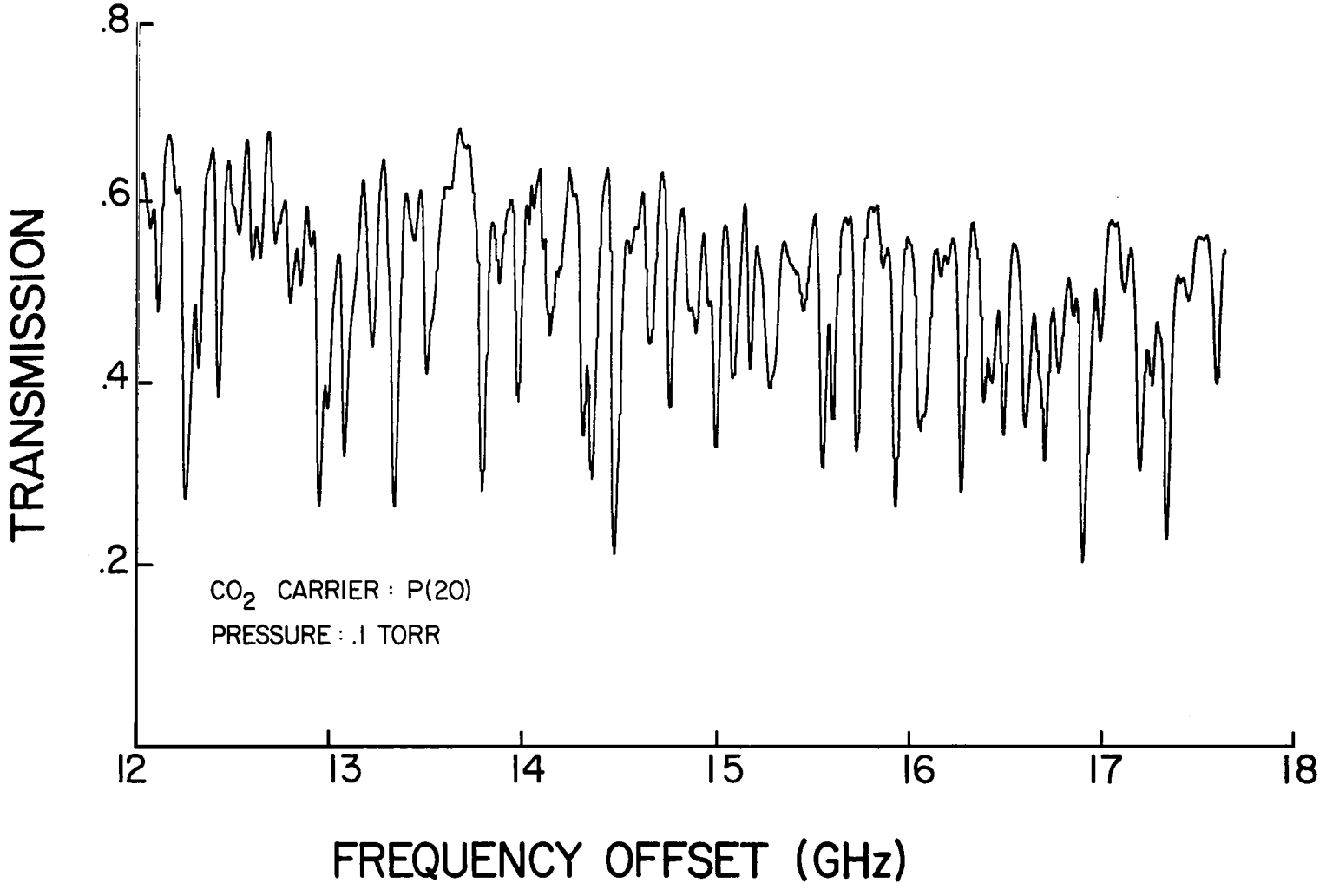

(a) Microwave frequency 12 to 18 GHz.

Figure 4.- SF_6 absorption spectrum resulting from high-resolution scans of upper sideband of P(20) $C^{12}O_2^{16}$ line.

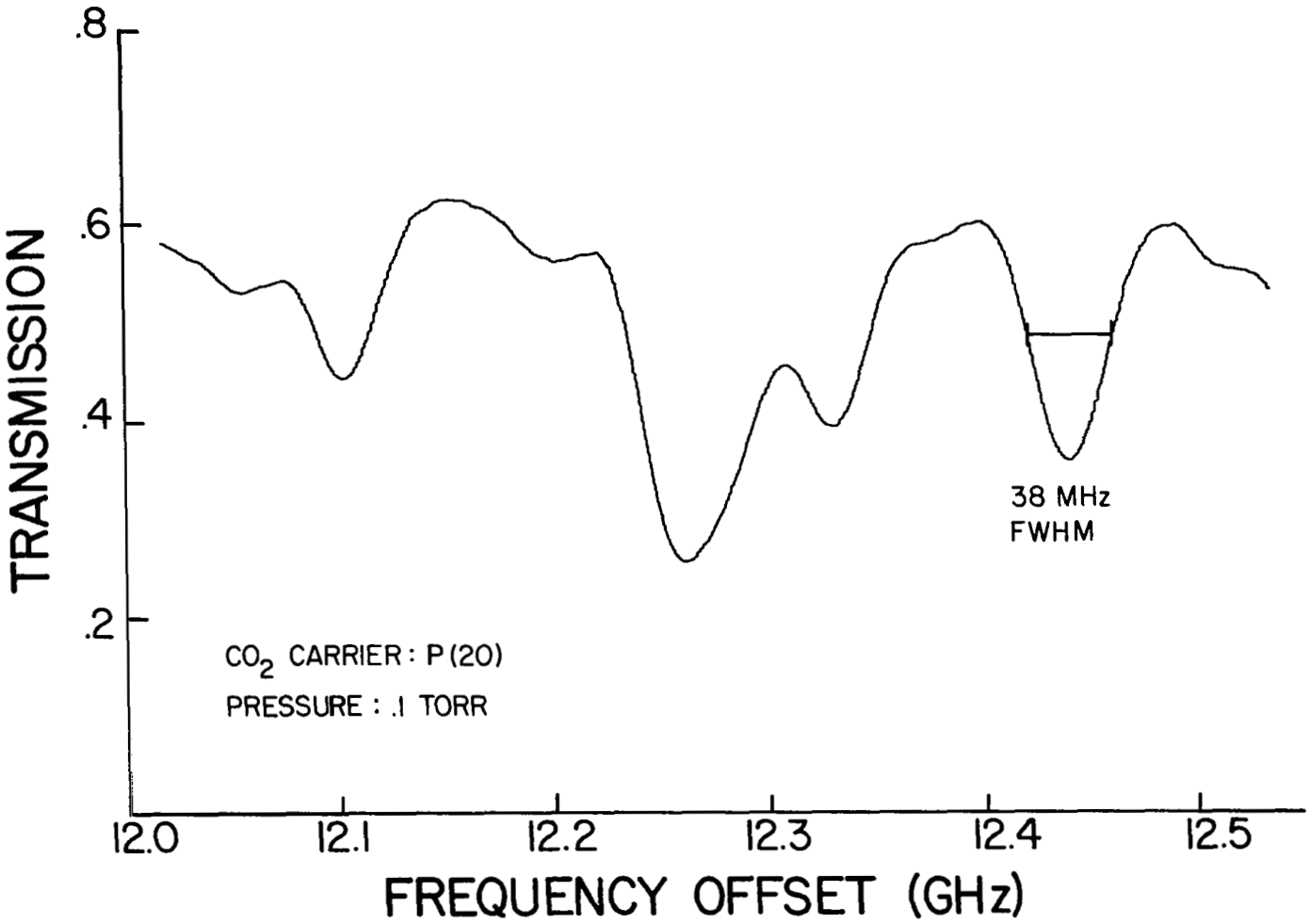

(b) Microwave frequency 12 to 12.5 GHz.

Figure 4.- Concluded.

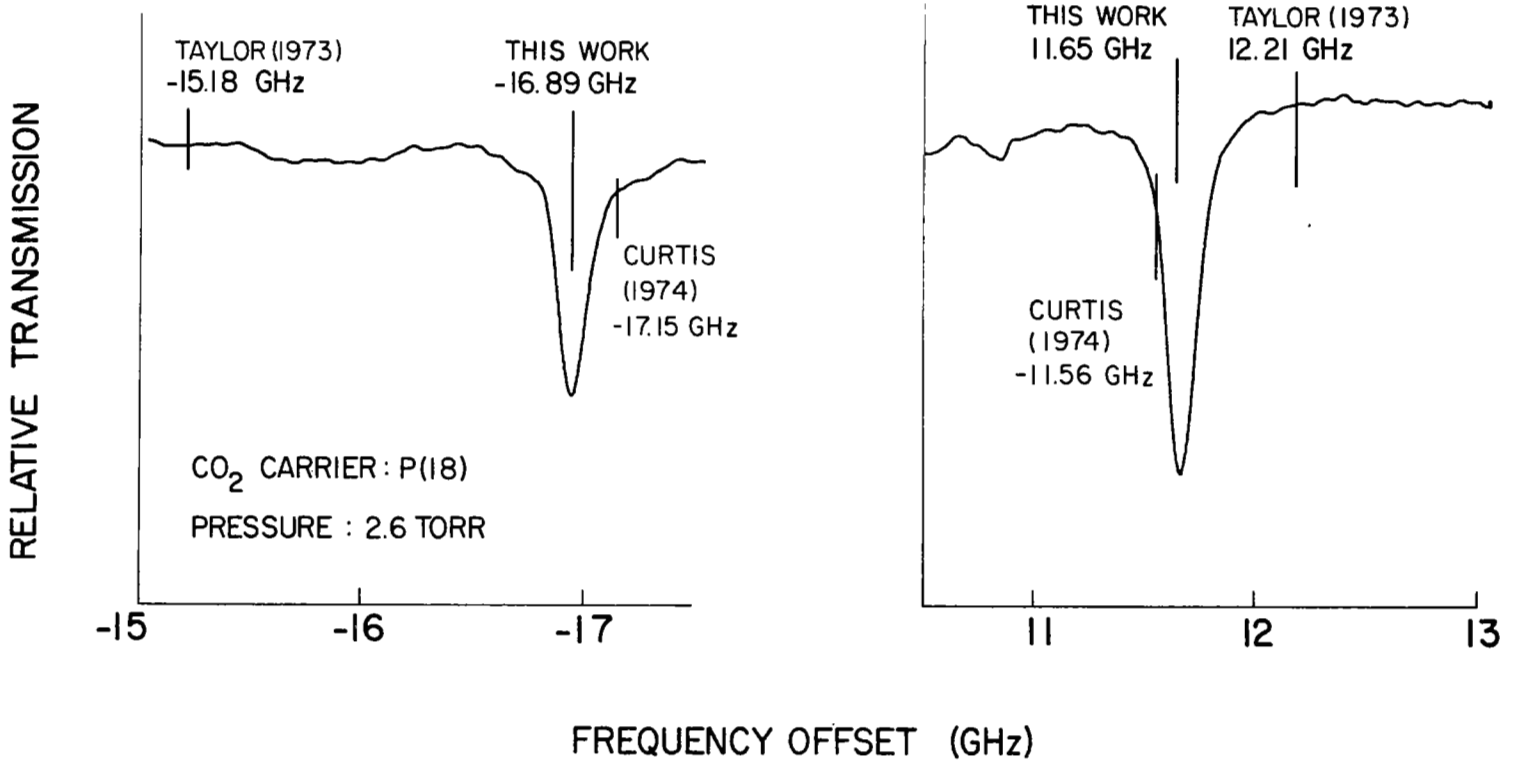

Figure 5.- High-resolution absorption spectra of NH_3.

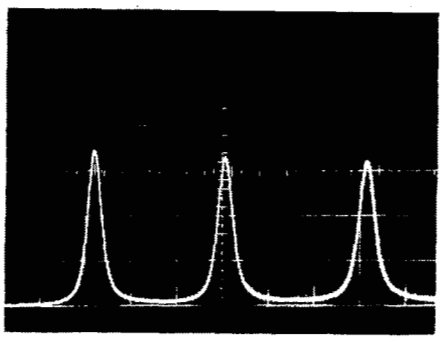

DC PHOTOMIXER OUTPUT
15.5 W MICROWAVE SATURATION

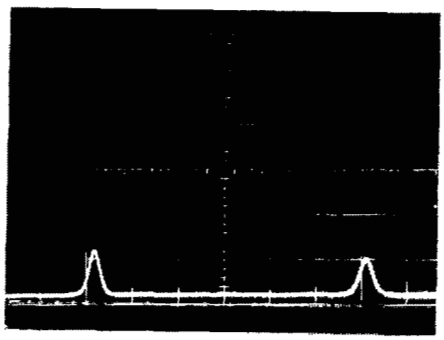

RECTIFIED PHOTOMIXER OUTPUT
100 MHz LOW PASS FILTER
15.5 W MICROWAVE SATURATION

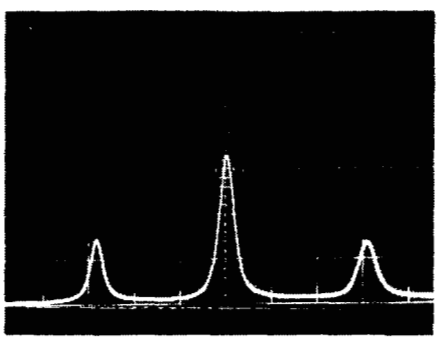

DC PHOTOMIXER OUTPUT
7.2 W MICROWAVE

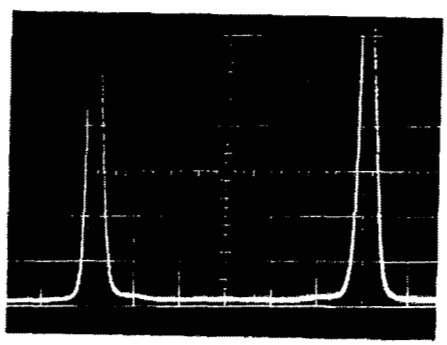

RECTIFIED PHOTOMIXER OUTPUT
100 MHz LOW PASS FILTER
7.2 W MICROWAVE

Figure 6.- Fabry-Perot scans of quasi-dc and rectified RF (100 MHz bandpass) output of photomixer.

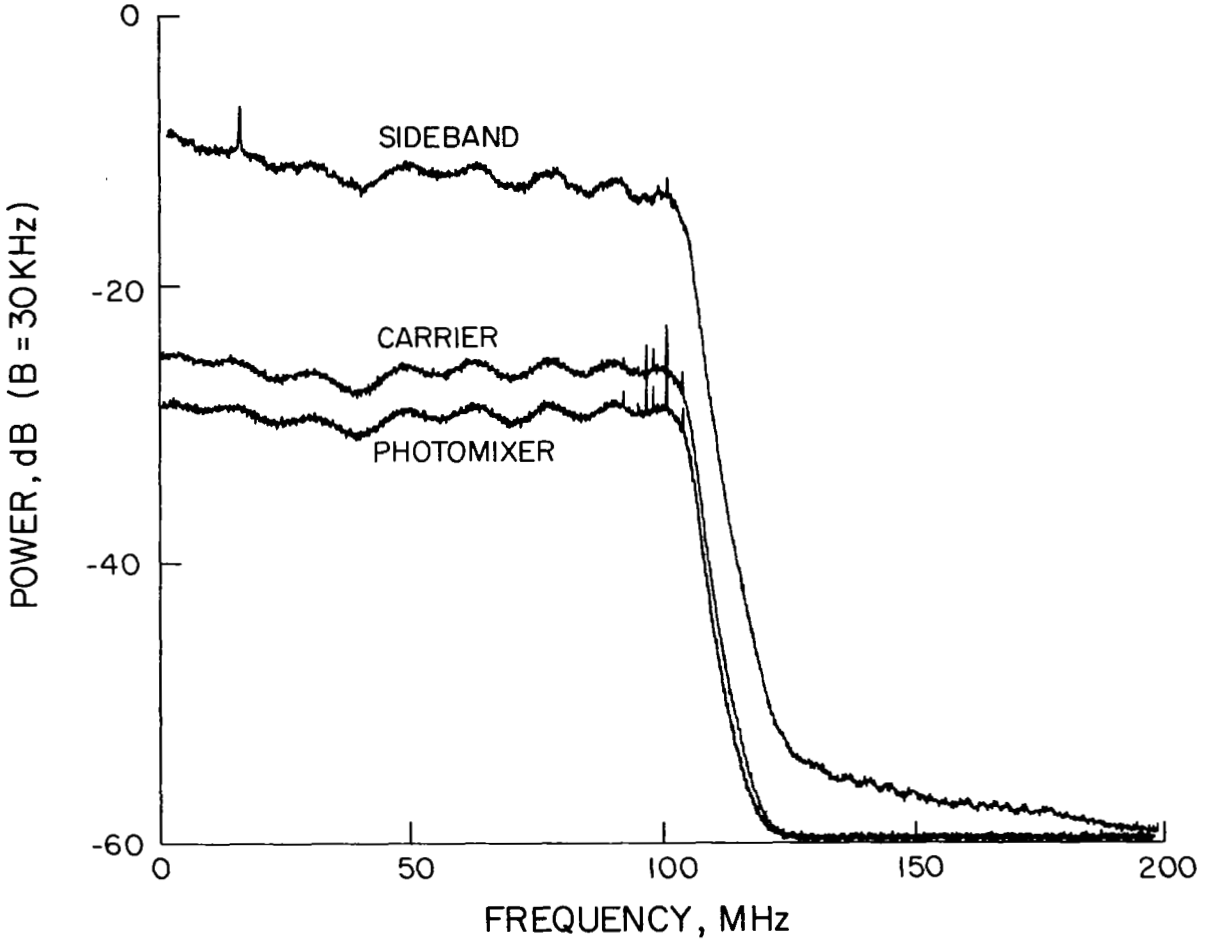

(a) Excess TWT gain introduced substantial noise on optical sideband.

Figure 7.- Spectrum-analyzer displays of photomixer RF output under three conditions of illumination: sideband, carrier, and no illumination.

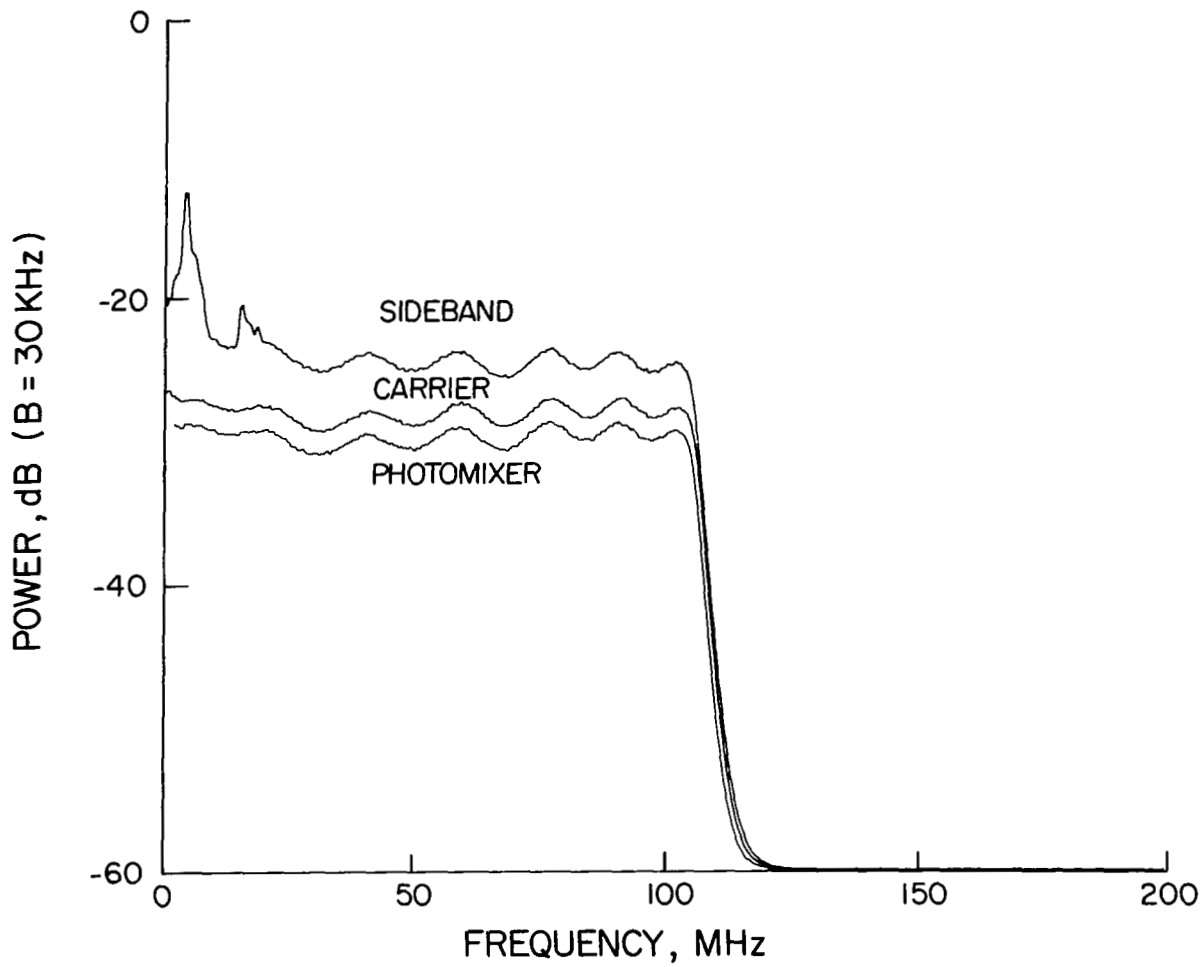

(b) A different TWT exhibiting no excess gain substantially improved the sideband S/N.

Figure 7.- Concluded.

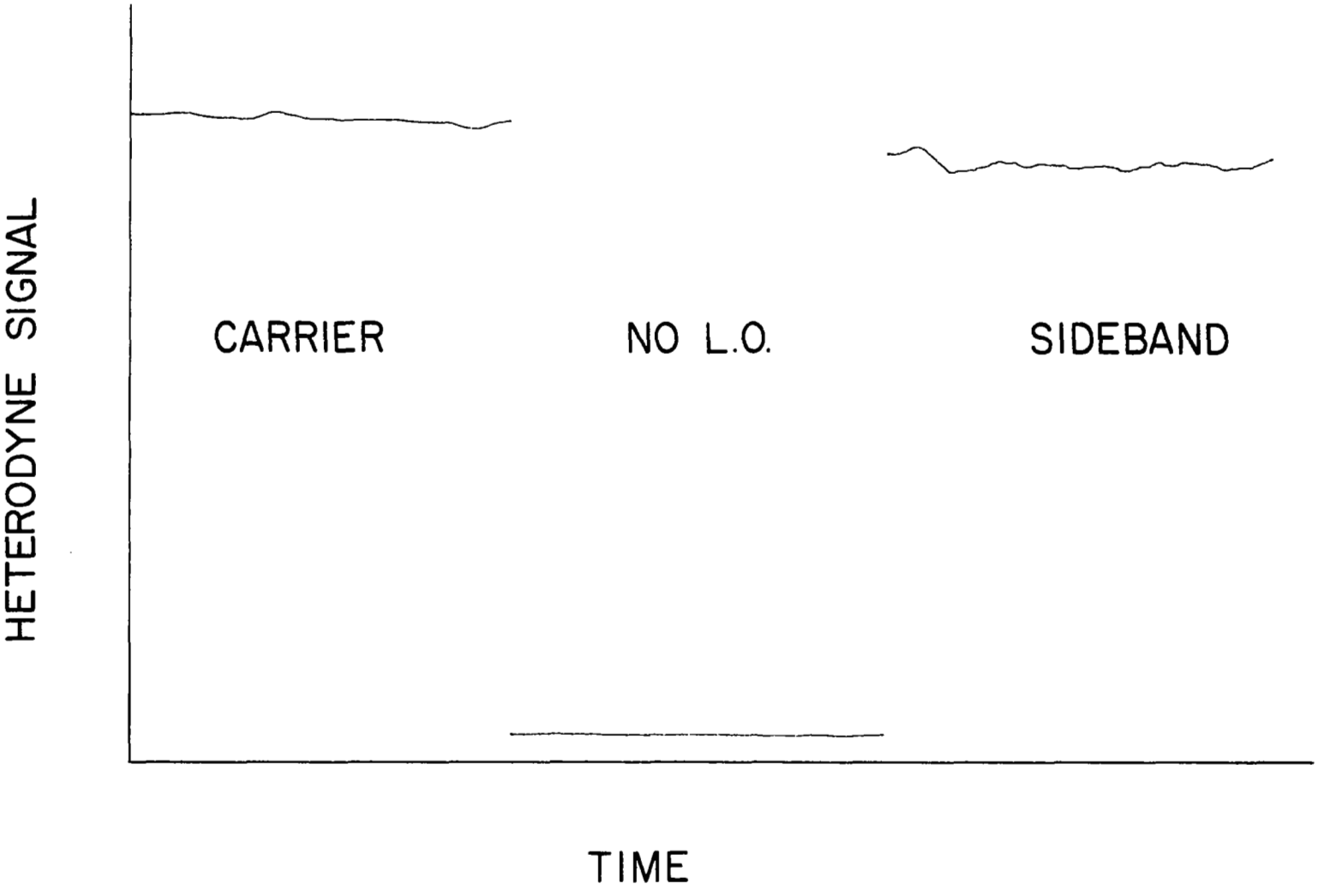

Figure 8.- Heterodyne measurements of a 1273 K blackbody for three cases of local-oscillator illumination: carrier, no local oscillator, and sideband.

SUBMILLIMETER LOCAL OSCILLATORS FOR HETERODYNE SPECTROSCOPY*

Edward J. Danielewicz, Jr.
Electronics Research Laboratory
The Aerospace Corporation
P.O. Box 92957
Los Angeles, CA 90009

SUMMARY

The far infrared or submillimeter portion of the electromagnetic spectrum, which spans the range of wavelengths between roughly 50 μm and 1.0 mm, is experiencing a tremendous growth in activity due to rapidly emerging source technologies. This paper reviews the major technological innovations in continuous wave (CW) submillimeter sources which are specifically suitable for application as local oscillators in heterodyne systems. A description of the various sources is given which underscores the general principles and operating features for each type of device. Particular emphasis is placed on CW optically pumped lasers, which have had a dramatic impact as widely available sources of narrow linewidth coherent radiation. The state-of-the-art is summarized for these lasers and performance data are presented for a compact and reliable local oscillator package recently developed at the Aerospace Corporation and for several different designs from other laboratories. Optically pumped lasers are then compared and contrasted with other competing sources such as backward wave oscillators, IMPATT diodes, and Josephson junctions. By comparing their advantages and limitations for use as local oscillators, the potential applications of these different sources are projected. The prospects for increased tunability, reliability and scalability are briefly considered, and several novel techniques for generating partially tunable radiation using Schottky diode mixers or CW Raman lasers are highlighted.

I. INTRODUCTION

The submillimeter wave (SMMW) portion of the electromagnetic spectrum between the infrared and millimeter regions corresponding to wavelengths between 50 μm and 1.0 mm is experiencing tremendous growth due to rapidly developing source technologies. In spite of absorption by atmospheric water vapor in the SMMW region, there is an enormous wealth of information to be somehow obtained within this large segment of the spectrum that covers nearly two decades in frequency. This potential provides strong motivation for attempts to exploit the recent progress in source availability.

*This work supported by the Division of Magnetic Fusion of the U. S. Department of Energy

Many practical applications of SMMW technology in areas such as high-resolution astronomy [1], plasma diagnostics [2], remote sensing of upper atmosphere constituents [3], molecular spectroscopy [4], imaging and non-destructive testing [5], and all-weather radar and communication [6] will require the advantages of high spectral resolution and sensitivity provided by heterodyne systems. Coherent sources are essential as local oscillators in any heterodyne system, and several excellent general review articles on SMMW sources are available [7], [8]. The aim of this paper is to review the present state-of-the-art of the most promising continuous wave (CW) SMMW sources suitable for local oscillator applications. Strictly speaking this paper should only assess the relevant properties of SMMW sources. However, it is useful to preface the detailed description of the various sources with some general remarks about SMMW heterodyne receivers.

In contrast to other spectral regions, the performance of a SMMW heterodyne receiver is so intimately coupled to the performance of both the local oscillator and the mixing element that an understanding of these receivers requires some discussion of the complete "front end". There are two possibilities for a heterodyne receiver: one chooses either a tunable oscillator and a narrow band detector or a fixed frequency oscillator and a broad band detector. Both approaches have been successfully demonstrated in the SMMW range. A very important consideration in both cases is the minimum local oscillator power for which maximum sensitivity can be obtained from the mixer. This requirement is a strong function of the selected mixer element.

The most widely used mixer element at microwave and millimeter wave frequencies is the Schottky diode. It is a room temperature, wide bandwidth device having high sensitivity and good mechanical stability. A basic property of a Schottky diode is that substantial local oscillator power is needed to minimize its conversion loss. On the order of a few milliwatts is typically required at lower frequencies near $\lambda \approx 1$ mm, and this increases to tens of milliwatts as one goes toward higher frequencies. Such SMMW power has been difficult and expensive to obtain in the past, and this was the primary limitation in the development of SMMW technology. However, recent innovations in SMMW sources, particularly the optically pumped lasers, have provided the necessary local oscillator power needed for efficient Schottky diode receivers. If one can accommodate cryogenic mixers such as photoconductors or Josephson junctions, the requirements on local oscillator power are significantly relaxed at the expense of the added complications with helium cooled operation. In addition, the photoconductors have fundamental bandwidth limitations of $\leq$100 MHz. Besides the threshold requirements on output power, there are a number of other criteria listed in Table I which also must be considered when comparing the choices for a local oscillator. In the next section these criteria will be used to compare the competing sources in an attempt to evaluate the potential of each type for local oscillator applications.

II. CW SUBMILLIMETER SOURCES

SMMW source development is being pursued from both of the bounding spectral regions. From the low frequency side efforts are underway to extend millimeter wave technology toward higher frequencies. Others are trying to transfer optical or laser techniques from the high frequency end, so that one often finds a blend of these two technologies in the SMMW transition region. The overlapping and intermingling of technologies are reflected in Table II which lists the possible CW sources to be considered.

Heading the list are the optically pumped lasers, which have had a revolutionizing impact on SMMW technology since their inception in 1970 [9]. Particular emphasis will be placed on describing the latest developments in these rapidly maturing sources.

Backward wave oscillators are a considerably older vacuum tube technology which has enjoyed renewed interest in the SMMW region because of their highly desirable tunability.

Josephson junctions are more esoteric devices which offer the potential of acting simultaneously as both the mixing element and the local oscillator. LO power can be derived from the internal Josephson oscillation in the junction itself, with the frequency of this internal oscillation proportional to the voltage bias across the device. In principle, a readily tunable receiver is then possible. The main source of difficulty with the internal LO mode of operation is the broad linewidth on the order of 1 GHz, which is characteristic of such Josephson oscillations. Promising results have been reported at short MMW frequencies [10], however, so this type of system cannot be ruled out for wide bandwidth heterodyne systems in the future. Unless arrays of junctions can be developed, Josephson devices do not appear to be the best prospect for tunable coherent SMMW sources with milliwatt level output powers. However, Josephson devices will continue to be of importance as heterodyne mixers in conjunction with external LO sources because they are highly nonlinear, extremely fast, and have very low LO power requirements on the order of 1-10 μW in the SMMW region [11].

IMPATT diodes are solid state sources which have been operated into the SMMW region, and combined with harmonic generators offer some hope of achieving compact solid state local oscillators in the near future. Progress in these two areas will also be covered in the following sections.

Electric discharge lasers can provide large amounts of power up to about 300 mW, but only at a very few fixed frequencies at short SMMW wavelengths. This limits their utility in heterodyne applications [12].

Gyrotrons are receiving considerable attention lately as sources of exceedingly high power and efficiency [13]. CW output power on the order of 1.5 kW has been reported at a wavelength of 0.9 mm [14], but the main emphasis is on achieving high power and these are large devices at present. Gyrotron oscillators have poor temporal coherence and it appears

that these devices cannot be scaled down in size and power for LO applications without significant loss in efficiency.

In the following sections, advantages and limitations will be discussed in more detail for a few selected sources which have been most successfully utilized in practical heterodyne applications.

III. BACKWARD WAVE OSCILLATORS

The operating features of a backward wave oscillator (BWO) or carcinotron can be very briefly described in a highly simplified manner with the help of the cross-sectional diagram given in Fig. 1. An electron beam is emitted from a cathode (1) and is focused through an interaction region (4) by a magnetic field $\vec{B}$ (3) and is collected at the collector (6). The electron beam moving in a vacuum interacts with a periodic structure (4) which supports the generated electromagnetic wave. The interaction is phase-matched for the wave in the reverse direction to the electron beam (hence the name backward wave oscillator) and is coupled out through the output port (5). The BWO is essentially a voltage tunable oscillator whose tuning characteristics are strongly dependent on the characteristics of the periodic slow wave structure. The advantages and limitations are summarized in Table III for these devices.

The primary advantage of the BWO is the continuous electrical frequency tuning which can be done rapidly without mechanical adjustments. The typical tuning range for a wideband BWO is about 20% of the center frequency. Thomson CSF, Paris, offers the highest frequency commercially available carcinotrons (up to 400 GHz) and they are presently developing tubes which would have output powers > 10mW in the 400-600 GHz range [15]. Frequencies of up to 1,300 GHz have been reported for laboratory models [16], but above 300 GHz the efficiency of operation falls off rapidly. Table IV shows that at λ = 0.4 mm the efficiency has fallen to less than 2 x 10^{-3}%, compared with 11% for a tube designed for λ = 4.0 mm. Unless there is a considerable advance in the technology of cathode emitters, there seems to be little hope of pushing the efficient performance to higher frequencies.

State-of-the-art in performance for SMMW BWO's is illustrated in Fig. 2 which shows the operating characteristics of an extended bandwidth BWO intended for use as a local oscillator in a heterodyne receiver [17]. Continuous spectral coverage from 320-390 GHz with greater than 10 mW output power is achieved at rather low power consumption. One obvious technical weakness of the BWO is the strong variation in the output power as the frequency is changed (Fig. 2) due to the unintended resonances in the guiding structure and the output couplers.

A relatively high sensitivity of the output frequency to the beam voltage of 10-30 MHz/V for these tubes would seem to preclude their use in heterodyne systems when a stable frequency is necessary. However, recent studies [18] designed to evaluate the potential of using BWO's as local

oscillators for heterodyne spectroscopy have shown that they can be readily phase-locked to an external stable reference source of lower frequency. Linewidths as narrow as 750 kHz at 40 db below the peak value at 244 GHz were achieved. These same studies measured the noise properties in the 230-380 GHz range of three different tubes. Noise temperatures were in the 1000-3000°K range at an IF frequency of 1.4 GHz, which corresponds to a signal to noise ratio approximately equal to 120 db/MHz. This resulted in the conclusion that the BWO has all of the required qualities of a tunable oscillator for wavelengths near $\lambda \approx 1$ mm and several successful heterodyne experiments have already been performed [19], [20], [21].

A fine example of a practical application of a BWO in a SMMW heterodyne receiver is the recent observation of the carbon monoxide molecule in interstellar clouds by Erickson [22], who was able to achieve system noise temperatures as low as 3400°K (SSB) at 345 GHz. The requirements for high voltages and magnetic fields make carcinotrons relatively large and heavy (10-30 kg), but this situation may be improved with the development of new advanced magnetic materials.

The BWO performance at long SMMW wavelengths is satisfactory, but there are, however, basic fundamental limitations to extending the efficient operation of BWO's to higher frequencies. Serious fabrication difficulties arise, because extremely high precision of machining and alignment is demanded for SMMW operation. The slow wave structure has to be machined to tolerances within 1μm and the dimensions of the structure are on the order of a fraction of a free space wavelength. As the size of the device decreases, a difficulty arises in avoiding serious heat dissipation due to unwanted interception of the electron beam by the structure. Along with these problems are additional circuit losses which increase at least as the square root of the frequency due to the decrease in the skin depth and even more rapidly increasing losses caused by surface machining imperfections. All of these loss mechanisms contribute to the rapid power falloff with increasing frequency, and impose severe requirements on the electron beam quality, particularly with respect to the high values of beam current density and magnetic focusing field required. To offset the increasing losses, the beam current must be increased to densities of 10-20 A/cm^2, which can only be obtained at cathode temperatures exceeding the values usually recommended for long life. Lifetimes of 1000-2000 hours are typical for tubes operating near 300 GHz and decrease at higher frequencies. These rather short lifetimes, the high cost of approximately $80,000 for the tube and its stabilized high voltage power supply, and the limited availability of these devices, especially for frequencies above abut 400 GHz, diminish the prospect of near term widespread application of the BWO as a local oscillator for the SMMW region.

A very promising alternative electron beam oscillator design, the ledatron [23], offers the possibility of overcoming or reducing the deficiencies of the BWO. Oscillation at $\lambda \approx 1$ mm has been observed with a peak power of about 300 mW and a tuning range of 40%, but these tubes are

still in an early stage of development and more work is needed to establish the potential for efficient SMMW operation.

IV. IMPATT DIODE OSCILLATORS

Over the past several years, significant progress in increasing output power and efficiency has been achieved with silicon IMPATT diode oscillators operating at frequencies up to about 300 GHz [24]. These results clearly place IMPATT diodes as the premier solid state device for the generation of millimeter wave power. Therefore, their potential for extension into the SMMW region must be examined.

The operating principle of IMPATT (impact avalanche and transit time) diodes is based on the injection of carriers, generated in a reverse-biased p-n junction by avalanche breakdown, into an intrinsic drift region. The electric field across the drift region is high enough so that the velocity of the electrons is constant and independent of the electric field. When an alternating voltage is applied, a phase delay occurs between the current and the voltage waveforms due to the transit time effect. This results in a frequency dependent negative resistance that can be used to give oscillation when the crystal is incorporated in a microwave circuit as in Fig. 3. Variation of the external circuit impedance allows the frequency of oscillation to be tuned over a broad range since the negative conductance covers a wide frequency bandwidth of 10-20%. Bias current tuning is the most effective way of producing broadband swept frequency generation, and high frequency modulation rates ($\geq$100 MHz) can be achieved. Mechanical tuning is necessary for optimum performance at a specific frequency and this is achieved by varying the position of the movable short in the oscillator circuit.

A comparison of the properties of IMPATT devices is given in Table V. Besides tunability, there are many other attractive features of such a solid-state generator like compact size and ruggedness, low power consumption, and reliable operation with long lifetimes. These advantages would make IMPATT devices highly desirable as local oscillators in the SMMW region if the high efficiency operation can be extended to higher frequencies.

Unfortunately, there are some fundamental limitations which have hindered the scaling of IMPATT's to higher frequencies. The current state-of-the-art is shown in Figure 4 where the steep falloff in output power with frequency above the demarcation point at about 100 GHz can be clearly seen. The output power is ultimately limited by the realizable circuit impedance which causes the mismatch between the device and the circuit to become increasely difficult to overcome at higher frequencies. The power falloff is mainly due to the adverse effects of the diode package and mounting parasitics. Limitations other than transit time effects have also been considered. There are problems with diffusion aided spreading and buildup of the injected current, and with the frequency response of the avalanche process itself [25].

As one attempts to extend IMPATT operation to higher frequencies, the diode dimensions must be reduced to reduce the parasitic capacitance effects. Unfortunately, thermal problems associated with dissipation of the power increase as the size of the device decreases. Since the parameters of the junction are strongly dependent on temperature, the minimization of thermal resistance in device packaging plays an important role in performance [26]. The physical dimensions of the device also become inconveniently small and severe demands are placed on processing and fabrication techniques. Recent improvements in output power from the MMW devices are primarily due to diamond heat-sinking and improved packaging techniques. Commerically available CW IMPATT oscillators can now produce single device outputs of 700 mW at 94 GHz, 100 mW at 140 GHz, and 25 mW at 220 GHz. Recently, liquid nitrogen cooled Si IMPATT's have produced output powers of 2.2 mW and 4.5 mW at frequencies of 412 and 295 GHz respectively with a tuning range of 10% [27]. With such output powers these devices are on the verge of being useful as LO sources and hopefully developments in this area will continue.

Another serious problem with IMPATT oscillators is the very high noise level, which is attributable to the random way in which the avalanche grows from a few initial ionizing events. The noise exceeds that of a klystron or Gunn diode MMW oscillator and for this reason they are difficult to use as LO's in low noise receivers. Recent results have shown that they can be phase-locked at harmonic frequencies through injection-locking with a fundamental mode reference source of high frequency stability and low noise [28]. But as yet it is difficult to assess the extent to which this technique will be effective in the SMMW region.

The catastrophic fall in efficiency as the frequency approaches the SMMW region is reasonably well understood and it is unlikely that efficient operation will be extended beyond 400 GHz with conventional techniques. Perhaps a quasioptical approach to diode packaging may be the only way to extend the frequency coverage further into the SMMW range. There is no doubt about IMPATT utility at the long wavelength end of the SMMW spectrum, and, as shown in the following section, harmonic generators can provide useful extension of the frequency coverage.

In addition to avalanching, electron tunneling can occur in a sufficiently thin p-n junction and this leads to a tunnel transit time or TUNNETT mode of oscillation [25]. Since tunneling is a very fast process (10^{-16} sec), the idea of using a tunnel transit time mode offers promise of enabling one to extend the frequency limit well beyond 300 GHz, assuming the appropriate quasioptical circuit can be devised. Further experimental work on TUNNETT's should enhance their value for SMMW systems.

V. HARMONIC GENERATORS

The long-standing method of harmonic generation in nonlinear junctions pumped by tunable sources offers the possibility of extending the range of tunable MMW oscillators into the SMMW region. The formidable

problems of pushing existing MMW sources to higher frequencies, combined with recent advances in the fabrication of Schottky diodes have caused renewed interest in these harmonic generation techniques.

A harmonic generator is simply a frequency converter in which power is generated at a higher frequency by exploiting a nonlinearity in the current-voltage characteristic. For example, the current through a Schottky diode will contain harmonics of the frequency of the driving field, and this harmonic power can be radiated into free space or into a waveguide in which the diode is mounted [29]. In principle harmonic power can be generated in proportion to $1/n^2$ at the nth harmonic of the applied field, but the useful range of frequencies is limited by junction capacitance and impedance matching to the external circuit [30]. Higher frequencies require special fabrication techniques that produce extremely small area contacts with diameters of 0.1-2.0 μm and very low values of junction capacitance [31]. These small contact areas create a limit on the amount of generated harmonic power, however, since they restrict the allowable fundamental pump power to about 100 mW. Above this power level the diode will usually burn out or suffer electrical breakdown.

The most successful device of this type has been a crossed waveguide harmonic generator (Figure 5), and conversion efficiencies of 2% giving 2 mW of output power at 228 GHz have been obtained [29]. The maximum second harmonic output was 3.5 mW at 226 GHz for the saturation limit of 200 mW of input power from the source klystron, and a frequency tunability of about 5% was retained. In the 200-300 GHz region more recent results have achieved second harmonic conversion efficiencies as high as 6-8% yielding 4 mW at 270 GHz, and 2-3 mW was produced at 305 GHz with ~1% conversion efficiency in a tripling mode [32]. This represents sufficient LO power for good conversion efficiency in a Schottky diode mixer at these frequencies, and has allowed system noise temperatures of 3100°K (SSB) to be reached at 270 GHz [32].

Further into the SMMW region, output powers of about 0.1 mW have been obtained at 447 GHz [30] which are thus far insufficient as sources of LO power for Schottky diode mixers. However, these power levels will suffice for He cooled InSb or Josephson mixers, and several heterodyne receivers have been realized for such applications as measuring the first SMMW molecular line in an astronomical source [33], and for airborne observation of atmospheric ozone in the 440-530 GHz region [34]. In molecular spectroscopy, more SMMW experiments have been performed using this technique than with any other [35]. Above about 500 GHz, however, harmonic generation has not proved a useful source of LO power even for the very sensitive cryogenic detectors.

Some improvement can be anticipated as new fabrication techniques are introduced, since these sources are as yet relatively undeveloped. If more power can be generated in the future, the favorable features of these devices will bring them into much more widespread use.

VI. OPTICALLY PUMPED MOLECULAR LASERS

All of the sources previously discussed are characterized by a drastic falloff in output power with increasing frequency. Transit time effects, unrealizable mechanical tolerances, and impedance matching problems severely limit their high frequency response. To circumvent these limitations a fresh approach was needed. The departure from attempts to extend conventional technology to higher frequencies was pioneered in 1970 by Chang and Bridges, who introduced the optically pumped molecular (OPM) laser [36]. The optical pumping technique has now succeeded in generating a rich spectrum of laser lines from $\lambda \approx 40$ to $2000\mu m$, thereby bridging the gap in source availability up to the infrared. A comparison of OPM lasers with other CW SMMW sources (Fig. 6) shows that for frequencies greater than 600 GHz they are clearly the dominant source technology [37]. A brief outline of the operating features of these lasers is worthwhile, since they have had such a dramatic impact on the SMMW region. Detailed descriptions are available in several excellent review articles [37], [38].

The basic operation of an OPM laser is illustrated in Figure 7. Transitions between specific rotational energy levels within the ground and first excited vibrational states of a polar molecular gas are utilized in both the absorption and emission processes. The pumping is achieved through an accidental near coincidence between a rotational-vibrational absorption line of the molecule and a suitable pump laser line. The intense and efficient CO_2 laser emission lines in the infrared near $\lambda = 10\mu m$ are almost exclusively used for this purpose. The pump photons selectively excite a particular rotational level in the excited vibrational state and produce population inversion between the unoccupied adjacent rotational states. In typical molecules like CH_3F and CH_3OH possessing a permanent dipole moment, the large rotational transition matrix elements lead to high gain, and laser emission can be achieved with a suitable optical cavity. The molecular kinetics are also very important for efficient CW operation of an OPM laser. In the steady state, vibrational relaxation through diffusion or V-T/R processes must be sufficiently fast to prevent destruction of the inversion by rotationally thermalizing collisions. Operating pressures are typically limited to the 100 mtorr region by the relatively slow rate of vibrational relaxation in diffusion dominated systems, such as CH_3F, and this adversely affects the rate of energy extraction by limiting the pump absorption. However, non-diffusion limited operation using molecules such as CH_2F_2 with very fast V-T/R relaxation rates has recently overcome this limitation, leading to increased CW power and operating efficiencies as high as 32% of the theoretical limit [39], [40].

The physical components which make up an actual OPM laser system are displayed in Figure 8. The setup consists of a grating tuned CW CO_2 laser with a single line output power in the range of 10-50 W. The pump radiation is normally injected into the SMMW resonator by focusing through a hole in one of the cavity end reflectors. The more common resonators and output coupling schemes have been well reviewed [41], [42], but in general

the best beam mode quality, linear polarization, and output powers have been obtained from hollow dielectric waveguide resonators [43]. The combination dielectric-metallic rectangular waveguide is another configuration [44] which has proven to be very useful for Stark tuning [45], high speed modulation [46], and phase-locking of the laser output [47]. Output coupling can be accomplished with a simple hole in the cavity end reflector, but for practical applications where output beam quality is important some type of hybrid output coupler either metal mesh-dielectric [48] or dielectric-hole coupler [43] is necessary.

The properties of OPM lasers are summarized in Table VI. A prime advantage of the OPM laser as a local oscillator is its inherently narrow linewidth, since molecular transitions in these low pressure gases yield gain linewidths of $\leq$ 10 MHz. OPM lasers are easily constructed and relatively inexpensive. Commercial systems complete with power supplies and associated electronics are available for under $40K from a number of suppliers, so that these sources are widely available to researchers. Another important advantage of these lasers is their versatility. A large number of emission lines (>1000) are available, so that there is almost complete coverage of the entire SMMW range with an average spacing on the order of a fraction of a wavenumber [49]. A single laser can also be made to operate over the entire SMMW on a variety of wavelengths by tuning the CO_2 pump. Molecules like CH_3OH [50] and CH_2F_2 [51] each have more than 50 laser lines spread throughout this region. For other wavelengths, it is often a relatively simple procedure to change the laser gas. These lasers operate sealed-off because there is no discharge to destroy the lasing molecules. This allows very high frequency stability, about three orders of magnitude better than for free running electric discharge SMMW lasers [52]. Phase-locking to a low frequency reference standard has also been demonstrated [53].

The major disadvantage of OPM lasers is their lack of tunability. Stark tuning offers the potential for increased range, but only up to about 100 MHz [54]. Recent advances in Schottky diode mixer technology have practically eliminated this problem, however since IF bandwidths as large as 20 GHz can be now obtained [55]. In conjunction with the available laser lines, this increased bandwidth will allow a heterodyne spectrometer to be built which provides almost complete coverage of the SMMW region [56]. Several novel techniques have also been recently demonstrated for increasing the tuning of OPM lasers and they will be described in the following section. Another limitation of OPM lasers is their inherent inefficiency. The optical pumping process at best cannot achieve power conversion exceeding about one-half of the Manly-Rowe limit [37]. Only a handful of lines actually operate with CW conversion efficiencies within an order of magnitude of this limit, but the proliferation of new source molecules such as CH_2F_2 has greatly added to the number of such strong SMMW laser lines. Relatively low efficiency imposes larger size and higher power requirements on the CO_2 pump laser system, and the need for two laser resonators increases the complexity of the overall system. Amplitude instability caused by coupling between the two laser cavities has been a

problem in the past, but recent design improvements have now essentially eliminated this problem. None of the limitations for OPM laser sources have proved insurmountable, and compact and well engineered systems have been built in several laboratories.

One such OPM laser system was constructed at the Aerospace Corporation for use in a transportable heterodyne receiver suitable for diagnostic experiments on large Tokamak plasma machines [57]. Several unique design features have been incorporated into this new self-contained OPM laser package. Because of the stringent requirements for reliable operation in hostile environments and remote field sites, this new design is much more complex than the laser normally used in the laboratory. For compactness and mobility, both the CO_2 pump laser and the FIR laser cavities were built into a single Invar frame with overall dimensions of 2.0 m x 0.4 m x 0.4 m. Figure 9 shows a view of the complete package with the CO_2 pump laser mounted above the SMMW waveguide resonator. The low temperature coefficient of expansion of Invar helps to ensure the long term temporal stability of the laser power and frequency. In addition, a temperature controller circulates constant temperature coolant throughout the structural components of the frame. Provisions have also been made for remote-tuning of the CO_2 and SMMW lasers for operation from remote control areas. The highest possible CW output power is required, as well as a small angular divergence for the output beam. To achieve these goals, the SMMW laser is equipped with a state-of-the-art hybrid output coupling mirror.

Preliminary performance measurements have been obtained with two prototype systems operating in our laboratory. Using CH_2F_2 as the lasing medium, true CW output power of typically 45 mW is obtained at a wavelength of 214.7 μm with long term amplitude stability of ±3% (Figure 10). It must be emphasized that this excellent amplitude stability has been achieved without actively stabilizing the CO_2 pump laser, and conceivably it can be improved with such a stabilization system. Another important feature of the package is that it can be operated in a sealed-off mode with a single fill of CH_2F_2 gas for extended periods of up to 2 weeks. This is very desirable for increased reliability and ease of day to day operation. A vapor trap has also been constructed that can be used to recapture and recycle the CH_2F_2 gas for a number of cycles, since the chemical reactivity of this molecule is quite low.

The noise spectrum and frequency stability of this SMMW laser package are critical performance characteristics. These parameters were measured by heterodyning two of these lasers together. The outputs from both lasers were mixed in a 0.25μm Schottky diode mixer fabricated in house and optimized for the high laser frequency [58]. The IF signal produced by offsetting one laser 3.9 MHz from the other in Figure 11 confirms single mode operation from both lasers, since only a single beat note is present on either side of the receiver center frequency. The free-running frequency stability of the beat signal in Figure 12 was better than 20 kHz, as measured from the half-width of the signal for a two minute

exposure. This excellent level of performance is well within the requirements for local oscillator applications in Tokamak diagnostic experiments, and plans to utilize this system for such measurements are now underway.

Another noteworthy design has been developed at the NASA Goddard Space Flight Center, where CO_2 pump laser radiation is injected off-axis into a novel four-fold degenerate Gaussian resonator within the SMMW waveguide [59]. This has the advantages of improved stability, through elimination of feedback effects and greater efficiency associated with better utilization of the pump power. The technique may prove especially useful for many of the more weakly absorbing gases other than CH_2F_2. Excellent amplitude and frequency stability has been obtained with this system, which is described in detail elsewhere in these proceedings [60].

A SMMW heterodyne receiver system has also been constructed at the Max Planck Institute for Radio Astronomy for the observation of interstellar molecules [61]. Figure 13 shows results for heterodyne mixer conversion loss indicating that values as low as 11.6 dB have been achieved at 761 GHz. This translates to a system noise temperature of only 3,670°K (DSB) [62]. From Figure 13 one can see that the conversion loss for this Schottky diode is not yet saturated up to the maximum available laser LO power of 10 mW. This establishes a lower limit on the amount of LO power necessary for efficient performance at these high frequencies, and implies that with increased LO power it will be possible to achieve still lower system noise temperatures.

OPM laser technology is now rapidly maturing, and several well-engineered systems have been designed and constructed for various purposes. Present levels of performance are sufficient for local oscillator applications in practical heterodyne systems well into the SMMW region. Novel techniques described in the following section for extending the tuning range of OPM lasers will contribute significantly to their utility, and the accelerating rate of advance in OPM laser technology should lead to additional practical applications during the next 1-3 years.

VII. NOVEL OPTICALLY PUMPED LASER TUNING TECHNIQUES

The techniques of sideband generation and CW stimulated Raman emission have recently been extended into the SMMW region. These advances show promise of eliminating the serious tuning problems now associated with OPM lasers.

The principle of generating tunable sidebands is illustrated in Figure 14. A quasi-optical Schottky diode mixer is fed coaxially with tunable microwave radiation and simulataneously irradiated with the output of an OPM laser. Tunable sidebands are generated at the SMMW frequency by nonlinear mixing in the Schottky diode and radiated by the long wire antenna of the corner cube mixer. Output powers of 10^{-7} W continuously

tunable from 2.5 to 18 GHz have been obtained in this way from the first SMMW experiments [63]. Initial laboratory experiments have used this tunable SMMW source in an infrared-submillimeter double resonance study of an excited vibrational state in CH_3F [64]. A Schottky diode heterodyne receiver easily detected the sideband radiation with signal to noise ratios of 40 dB, and since the time response is fast the kinetics of energy transfer processes could also be investigated. Thus, the introduction of these tunable sources combined with the sensitive heterodyne detectors has opened up the possibility for new types of high resolution SMMW spectroscopic studies.

The technique of CW stimulated Raman scattering in a three level molecular system is schematically illustrated in Fig. 15. An intense pump laser with frequency ν_p is nearly resonant with an infrared transition of frequency ν_{31} with an offset $\Delta\nu_p = \nu_p - \nu_{31}$. Using the nonlinear properties of the molecular gas itself, a signal is generated by the stimulated Raman effect near the rotational frequency ν_{32}. In contrast to the two step resonant absorption and re-emission process of a normal OPM laser, the CW Raman laser is a simultaneous two-photon process, and changing of the pump offset will tune the SMMW frequency by the same amount. The tuning in the Raman case is larger, since in the normal laser the change in the emission frequency is reduced by the ratio of the SMMW frequency to the pump frequency due to the Doppler effect. Experiments have been conducted with NH_3 ** and HCOOH [65] and interpreted as the first observations of stimulated SMMW Raman lasing using a CW pump laser. These results demonstrated that Raman effects can be observed at the power levels typical in a CW OPM laser, and that dramatic increases in tuning range can be achieved. A frequency tuning of 50 MHz, which is roughly the tuning range of the CO_2 pump laser, was observed using NH_3 at 67μm. This corresponds to about an order of magnitude increase in tunability. Raman emission has the additional advantage that the power scaling behavior will also be different from normal OPM lasers, and could eventually lead to higher achievable output powers. Although very promising, this technique is still in the preliminary stages of development and more work will be needed to fully assess its true potential.

VIII. CONCLUSION

This review has summarized the state-of-the-art performance of CW SMMW sources. Each source type was introduced with a brief description of its basic operating features. The advantages and limitation of the various devices were then compared in an attempt to assess their potential for application as local oscillators in low noise heterodyne receivers.

**Unpublished article by G. D. Willenberg, U. Huebner, and J. Heppner entitled "Far Infrared CW Raman Lasing in NH_3."

The assessment of the current situation leads to the following conclusions. The combination of a sealed-off, high power OPM laser and a room-temperature Schottky diode mixer is an extremely attractive package for heterodyne systems. Present levels of performance are sufficient for many practical applications. As a consequence of the new compact and reliable laser packages, immediate applications to scientific problems and feasibility studies can be expected. The near term outlook is that OPM lasers will be implemented, simply because of their availability, throughout the SMMW range. For frequencies above 500 GHz, they are the sole alternative. In the long wavelength portion of the SMMW spectrum, backward-wave oscillators have demonstrated satisfactory performance in heterodyne systems. However, high cost, limited availability, and a reputation of short lifetime have prevented widespread applications. In spite of these limitations, backward-wave oscillators are currently the only sources of widely tunable coherent SMMW radiation. At present, solid state sources such as the IMPATT diode have not yet reached a stage of development to be useful in the SMMW region. The long range prospects are good that further efforts will lead to compact tunable solid state SMMW sources. In the near future, harmonic generators will extend the useful range of both the BWO and IMPATT devices to higher frequencies, but probably not much beyond 600 GHz.

A solid foundation now exists for continued development of SMMW sources, but SMMW technology is still in its infancy and significant work remains. As in the past, progress will depend on the synergistic relationship between practical applications and viable sources. The necessity to exploit the unique properties of SMMW radiation in important applications will accelerate the advancement of SMMW sources. Improved source performance, in turn, will multiply the number of potential applications. This cycle can be expected to continue, and significant results can be anticipated from SMMW heterodyne systems in the near future.

The assistance of my colleagues, D. T. Hodges and J. R. Tucker, in critically reviewing the manuscript is gratefully acknowledged.

REFERENCES

[1] C. B. Cosmovici, M. Inguscio, F. Strafella, and F. Strumia," On the Possibility of Submillimetric Interstellar Lines Detection by Means of Laser Heterodyne Techniques," Astrophysics and Space Sciences, 60, 475 (1979).

[2] N. C. Luhmann Jr., "Instrumentation and Techniques for Plasma Diagnostics: An Overview," in Infrared and Millimeter Waves, Vol. 2, K. J. Button, ed, Academic Press: New York (1980).

[3] H. M. Pickett, and T. L. Boyd, "A 163 Micron Laser Heterodyne Radiometer for OH: Progress Report," in Heterodyne Systems and Technology, NASA CP-2138, 1980. (Paper 21 of this compilation.)

[4] A. F. Krupnov, and A. V. Burenin, "New Methods in Submillimeter Microwave Spectroscopy," in Molecular Spectroscopy: Modern Research, Vol. II, K. N. Rao, ed., Academic Press: New York (1976).

[5] D. T. Hodges, F. B. Foote, E. E. Reber, and R. L. Schellenbaum, "Near Millimeter Wave Radiometric Imaging," Fourth International Conference on Infrared and Millimeter Waves and Their Applications, Miami, Florida, Dec. 10 - 15, (1979).

[6] H. R. Fetterman, and H. R. Schlossberg, "Submillimeter-Wave Optically-Pumped Molecular Lasers," Microwave J., 17, 35-39 (1974).

[7] D. H. Martin, and K. Mizuno, "The Generation of Coherent Submillimeter Waves," Adv. in Phys., 25, 211 - 246 (1976).

[8] B. D. Guenther, and R. T. Carruth, "Millimeter and Submillimeter Wave Sources for Radar Applications," U.S. Army Missile Research and Development Command, Technical Report H-78-6 (1978).

[9] T. Y. Chang, "Optically Pumped Submillimeter Wave Sources," IEEE Trans. Microwave Theory Tech., MTT-22, 983 - 988 (1974).

[10] B. T. Ulrich, "Josephson Effect Heterodyne Receivers," Inf. Phys., 17, 467 - 474 (1977).

[11] T. G. Blaney, "Radiation Detection at Submillimeter Wavelengths," J. Phys. E: Sci. Instrum., 11, 856 - 881 (1978).

[12] B. F. J. Zuidberg, and A. Dymanus, "Submillimeter Heterodyne Detection with a Laser Local Oscillator," Appl. Phys., 16, 375 - 379 (1978).

[13] J. L. Hirshfield, "Gyrotrons," in Infrared and Millimeter Waves, Vol 1, K. J. Button, ed., Academic Press: New York (1979).

[14] A. A. Andronov, V. A. Flyagin, A. V. Gaponov, A.L. Gol'Denberg, M. I. Petelin, V. G. Usov, and V. K. Yulpatov, "The Gyrotron: High-Power Source of Millimeter and Submillimeter Waves," Inf. Phys., 18, 385 - 393 (1978).

[15] G. Kantorowicz and P. Palluel, "Backward Wave Oscillators," in Infrared and Millimeter Waves, Vol. 1, K. J. Button, ed., Academic Press: New York (1979).

[16] M. B. Golant, Z. T. Elekceenko, Z. S. Korotkova, L. A. Lunkind, L. A. Negerev, O. P. Petrova, T. B. Rebrova, and V. S. Savelena, "Wide Range Oscillators for the Submillimeter Wavelengths," Prib. Tekh. EksP., 3, 231 - 237 (1969).

[17] B. Epsztein, "Recent Progress and Future Performances of Millimeter-Wave BWO's," Proceedings of AGARD Conference on Millimeter and Submillimeter Wave Propagation and Circuits, Munich, Germany, Sept. 4-8, (1978).

[18] Th. de Graauw, M. Anderegg, B. Fitton, R. Bonnefoy, and J. J. Gustincic, "Properties of O-Type Carcinotron Oscillators for Submm Heterodyne Spectroscopy," Third International Conference on Submillimeter Waves, Guildford, U. K., March 29 - April 1, (1978).

[19] S. Lidholm, and Th. de Graauw "A Heterodyne Receiver for Submillimeter-Wave Astronomy," Fourth International Conference on Infrared and Millimeter Waves, Miami, Florida, Dec. 10-15, (1979).

[20] A. H. F. Van Vliet, Th. de Graauw, and H. J. Schotzau, "Sub-mm Heterodyne Detection Using Carcinotron Local Oscillators and InSb Bolometer Mixers, Third International Conference on Submillimeter Waves and Their Applications," Guildford, U. K., March 29 - April 1, (1978).

[21] A. H. F. Van Vliet, and Th. de Graauw "A Heterodyne Receiver for Submillimeter Wave Astronomy", Fourth International Conference on Infrared and Millimeter Waves and Their Applications, Miami, Florida, Dec. 10-15, (1979).

[22] N. Erickson, "A 346 GHz Heterodyne Receiver and Its Use in Observations of Carbon Monoxide in Interstellar Clouds," Ph. D. Thesis, University of California, Berkeley, CA., August (1979).

[23] K. Mizuno, and S. Ono, "The Ledatron," in Infrared and Millimeter Waves, Vol. 1, K. J. Button, ed., Academic Press: New York (1979).

[24] H. J. Kuno, "IMPATT Devices for Generation of Millimeter Waves," in Infrared and Millimeter Waves, Vol. 1, K. J. Button, ed., Academic Press: New York (1979).

[25] M. E. Elta and G. I. Haddad, "High-Frequency Limitations of IMPATT, MITTAT, and TUNNETT Mode Devices," IEEE Trans. Microwave Theory Tech., MTT-27, 442 - 449 (1979).

[26] T. A. Midford and R. L. Bernick "Millimeter-Wave CW IMPATT Diodes and Oscillators," IEEE Trans. Microwave Theory Tech., MTT-27, 483 - 492 (1979).

[27] T. Ishibashi, M. Ino, T. Makimura, and M. Ohmori, Electron. Lett., 13, 299 - 300 (1977).

[28] K. Mizuno, M. Ohmori, K. Miyazawa, M. Morimoto, S. Kodaira, and S. Ono, "Frequency Stabilization of IMPATT Diodes in the Submillimeter Wave Region," Inf. Phys., 18, 401 - 403 (1978).

[29] N. J. Cronin, D. H. Martin, G. A. Ediss, and G. T. Wrixon, "Generation of Millimeter and Submillimeter Waves by Frequency Multiplication," Inf. Phys., 18, 731 - 734 (1978).

[30] T. Takada, and M. Ohmori, "Frequency Triplers and Quadruplers with GaAs Schottky-Barrier Diodes at 450 and 600 GHz", IEEE Microwave Theory Tech., MTT-27, 519 - 523 (1979).

[31] M. McColl, "Review of Submillimeter Mixers," S.P.I.E. Seminar on Far Infrared/Submillimeter Wave Tech. and Appl., Vol. 105, 24 - 34 (1977).

[32] N. R. Erickson, "A 200 - 300 GHz Heterodyne Receiver," The IEEE/MTT-S International Microwave Symposium, Washington, D. C., May 26 - 30, (1980).

[33] T. G. Phillips, P. J. Huggins, G. Neugebauer, and M. W. Werner, "Detection of Submillimeter (870 μm) CO Emission from the Orion Molecular Cloud," Astrophys. J., 217, L161 - L164 (1977).

[34] A. H. F. Van Vliet, Th. de Graauw, S. Lidholm and H. V. d. Stadt," An InSb Mixer Receiver Operating Between 440 and 530 GHz," Fourth International Conference on Infrared and Millimeter Waves, and Their Applications, Miami, Florida, Dec. 10-15, (1979).

[35] F. C. Delucia, "Millimeter-and Submillimeter-Wave Spectroscopy," in Molecular Spectroscopy: Modern Researh, Vol. II, K. N. Rao, ed., Academic Press: New York (1976).

[36] T. Y. Chang and T. J. Bridges, "Laser Action at 452, 496, and 541 μm in Optically Pumped CH_3F", Opt. Commun., 1, 423 - 426, (1970).

[37] D. T. Hodges, "A Review of Advances in Optically Pumped Far-Infrared Lasers," Inf. Phys., 18, 375 - 384 (1978)

[38] T. Y Chang, "Optical Pumping in Gases," in Topics in Appl. Phy., 16, Y. T. Shen, ed., Berlin: Springer Verlag (1977).

[39] T. A. Galantowicz, E. J. Danielewicz, F. B. Foote, and D. T. Hodges, "Characteristics of Non-Diffusion Limited Optically Pumped CW Lasers - Experimental Results for CH_2F_2," in Proceedings of the International Conf. on Lasers '78, V. J. Corcoran, ed., STS Press: McLean, VA. (1979).

[40] E. J. Danielewicz, T. A. Galantowicz, F. B. Foote, R. D. Reel and D. T. Hodges," High Performance at New FIR Wavelengths from Optically Pumped CH_2F_2," Opt. Lett., 4, 280 - 282 (1979).

[41] M. Yamanaka, "Optically Pumped Waveguide Lasers," J. Opt. Soc. Amer., 67, 7, 952 - 958 (1977).

[42] F. Kneubühl and E. Affolter," Infrared and Submillimeter-Wave Waveguides," in Infrared and Millimeter Waves, Vol. 1, K. J. Button, ed., Academic Press: New York (1979).

[43] D. T. Hodges, F. B. Foote, and R. D. Reel, "High-Power Operation and Scaling Behavior of CW Optically Pumped FIR Waveguide Lasers," IEEE J. Quantum Electron., QE-13, 491 - 494 (1977).

[44] M. S. Tobin, and R. E. Jensen, "Far IR Laser with Metal-Dielectric Waveguide To Observe the Stark Effect," Appl. Opt., 15, 2023-2024 (1976).

[45] M. Inguscio, P. Minguzzi, A. Moretti, F. Strumia, and M. Tonelli," Stark Effect on CH_3OH and CH_3F FIR Lasers: Large Frequency Tuning and Resolved Structures," Appl. Phys., 18, 261 (1979).

[46] S. R. Stein, A. S. Risley, H. Van de Stadt, and F. Strumia, "High Speed Frequency Modulation of Far Infrared Lasers Using the Stark Effect, " Appl. Opt., 16, 1893 - 1896 (1977).

[47] S. R. Stein, and H. Van de Stadt, "Electronic Tuning and Phase-Lock Technique for Optically Pumped Far-Infrared Lasers," Freq. Contr., 31 601 (1977).

[48] M. R. Schubert, M. Durschlag and T. A. De Temple, "Diffraction Limited CW Optically-Pumped Lasers," IEEE J. Quantun Electron., QE-13, 455 - 459 (1977).

[49] M. Yamanaka, "Optically Pumped Gas Lasers. A Wavelength Table of Laser Lines," Rev. Laser Eng. (Japan), 3, 57-98 (1976); M. Rosenbluh, R. J. Temkin, and K. J. Button, "Submillimeter Laser Wavelength Tables," Appl. Opt., 15, 2635 - 2644 (1976); J. J. Gallagher, M. D.

Blue, B. Bean, and S. Perkowitz, "Tabulation of Optically Pumped Far Infrared Laser Lines and Applications to Atmospheric Transmission," Inf. Phys., 17, 43 - 55 (1977).

[50] F. R. Peterson, K. M. Evenson, D. A. Jennings, and A. Scalabrin, "New Frequency Measurements and Laser Lines of Optically Pumped CH_3OH," IEEE J. Quantum Electron., QE-16, 319 - 323 (1980).

[51] A. Scalabrin, and K. M. Evenson, "Additional CW FIR Laser Lines From Optically Pumped CH_2F_2," Opt. Lett., 4, 277 - 279 (1979).

[52] J. J. Jimenez, P. Plainchamp, A. Comeron, and A. Clairon," Submillimeter Receivers: Local Oscillators and Mixers," Proceedings of AGARD Conference on Millimeter and Submillimeter Wave Propagation and Circuits, Munich, Germany, Sept. 4 - 8 (1978).

[53] C. O. Weiss, E. Bava, A. De Marchi, and A. Godone, "Injection Locking of an Optically Pumped FIR Laser," IEEE J. Quantum Electron., QE-16, 498-499, (1980).

[54] M. Inguscio, P. Minguzzi, A. Moretti, F. Strumia, and M. Tonelli, "Stark Effect on CH_3OH and CH_3F FIR Lasers: Large Frequency Tuning Resolved Structures," Appl. Phys., 18, 261 - 270 (1979).

[55] P. E. Tannenwald, "Far Infrared Heterodyne Detectors," in Heterodyne Systems and Technology, NASA CP-2138, 1980. (Paper 28 of this compilation.)

[56] N. McAvoy and V. G. Kunde, "Detection of Atmospheric Constituents Using Submillimeter Wave (SMMW) Heterodyne Radiometry," S.P.I.E. Seminar on Far Infrared/Submillimeter Wave Tech. and Appl., Vol. 105, 112 - 116 (1977).

[57] E. J. Danielewicz, E. L. Fletcher, A. R. Calloway, and D. T. Hodges, "New CW FIR Laser Sources for Plasma Diagnostics Applications," in Proc. Japan-USA Workshop on Far Infrared Diagnostics, Cambridge, Mass., Jan. 28 - 31 (1980).

[58] M. McColl, D. T. Hodges, A. B. Chase, and W. A. Garber," Detection and Mixing at Submillimeter Wavelengths Using Schottky Diodes with Low Junction Capacitance," Third International Conference on Submillimeter Waves, Guildford, U. K., March 29 - April 1 (1978).

[59] G. A. Koepf, and N. McAvoy, "Design Criteria for FIR Waveguide Laser Cavities," IEEE J. Quantum Electron., QE-13, 418 - 421 (1977).

[60] G. A. Koepf, "Sub mm Laser Local Oscillators: Design Criteria and Results," in Heterodyne Systems and Technology, NASA CP-2138, 1980. (Paper 38 of this compilation.)

[61] H. P. Röser, and G. V. Schultz, "Development of an Optically Pumped Molecular Laser," Inf. Phys., 17, 531 - 536 (1977).

[62] G. V. Schultz, E. Sauter, H. P. Röser, and W. Reinert, "Experiments for Sensitivity Enhancement of a Heterodyne Detection System at Submm Wavelengths," Fourth International Conference on Infrared and Millimeter Waves and Their Applications, Miami, Florida, Dec. 10 - 15 (1979).

[63] H. R. Fetterman, P. E. Tannenwald, B. J. Clifton, C. D Parker, W. D. Fitzgerald, and N. R. Erickson, "Far-IR Heterodyne Radiometric Measurements with Quasioptical Schottky Diode Mixers," Appl. Phys. Lett., 33, 151 - 154 (1978).

[64] W. A. M. Blumberg, H. R. Fetterman, D. D. Peck, and P. F. Goldsmith, "Submillimeter Double Resonance Study of CH_3F Using Reradiation from Schottky Barrier Diodes," Appl. Phys. Lett., 35, 582 - 585 (1979).

[65] H. P. Röser, "The Development of an Optically Pumped Submm Laser as a Local Oscillator in a Heterodyne System," Ph. D. Thesis, University of Bonn, W. Germany (1979).

TABLE I.- CRITERIA FOR COMPARISON OF CW SMMW LOCAL OSCILLATORS

- OUTPUT POWER
- FREQUENCY RANGE
- EFFICIENCY
- TUNING BANDWIDTH
- FREQUENCY STABILITY
- LINEWIDTH
- LIFETIME
- NOISE
- SIZE
- COST AND AVAILABILITY

TABLE II.- SUMMARY OF CW SMMW SOURCES

- OPTICALLY PUMPED LASERS
- BACKWARD WAVE OSCILLATORS
- JOSEPHSON JUNCTION OSCILLATORS
- IMPATT DIODES
- HARMONIC GENERATORS
- SIDEBAND GENERATORS
- ELECTRIC DISCHARGE LASERS
- GYROTRONS

TABLE III.- PROPERTIES OF BACKWARD WAVE OSCILLATORS

- ADVANTAGES
  - CONTINUOUSLY TUNABLE ELECTRICALLY
  - WIDE RANGE OF TUNABILITY
  - NARROW LINE WIDTH
  - EASILY PHASE OR FREQUENCY LOCKED
  - LOW NOISE CHARACTERISTICS
  - COMPACT
- LIMITATIONS
  - FABRICATION PROBLEMS
  - RELATIVELY HIGH COST
  - UNAVAILABILITY
  - RAPID POWER FALLOFF WITH FREQUENCY
  - REDUCED LIFETIME AT HIGH FREQUENCIES

TABLE IV.- CHARACTERISTICS OF AVAILABLE CARCINOTRONS

WAVELENGTH (mm)	CURRENT (mA)	VOLTAGE (kV)	POWER (W)	EFFICIENCY (%)
4	65	6	38	11
2	45	6	8	4
1	30	10	1.4	0.5
0.5	35	10	15×10^{-3}	4×10^{-3}
0.4	35	10	9×10^{-3}	2×10^{-3}
0.35	45	10	0.25×10^{-3}	6×10^{-5}

TABLE V.- PROPERTIES OF IMPATT DIODES

- ADVANTAGES
  - COMPACT SIZE AND RUGGEDNESS
  - POTENTIAL LONG LIFE AND RELIABILITY
  - WIDELY TUNABLE
  - MODEST DC POWER REQUIREMENTS
  - POTENTIAL HIGH EFFICIENCY
- LIMITATIONS
  - HIGH NOISE LEVELS
  - WIDE LINEWIDTH
  - RAPID POWER FALLOFF AT HIGH FREQUENCIES
  - UNAVAILABILITY

TABLE VI.- PROPERTIES OF OPTICALLY PUMPED MOLECULAR LASERS

- ADVANTAGES
  - INHERENTLY NARROW LINEWIDTH
  - EASILY CONSTRUCTED AND WIDELY AVAILABLE
  - RELATIVELY INEXPENSIVE
  - WIDE SPECTRAL RANGE
  - HIGH FREQUENCY STABILITY
  - PHASE-LOCKED OPERATION DEMONSTRATED
  - VERSATILITY
- LIMITATIONS
  - LACK OF TUNABILITY
  - INEFFICIENT
  - HIGH POWER REQUIREMENTS
  - INSTABILITIES
  - INCREASED COMPLEXITY
  - RELATIVELY LARGE SIZE

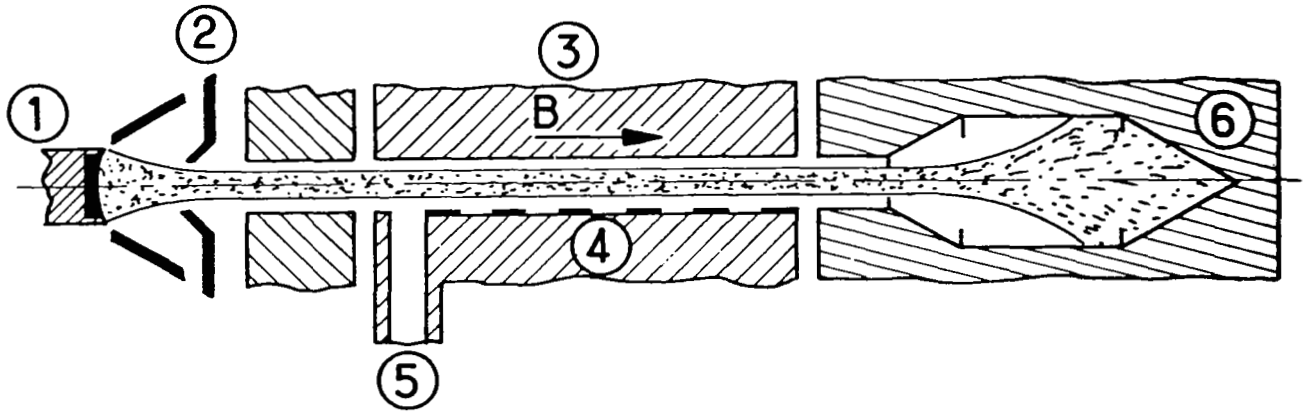

Figure 1.- Cross-sectional diagram of a backward wave oscillator (after Ref. 15).

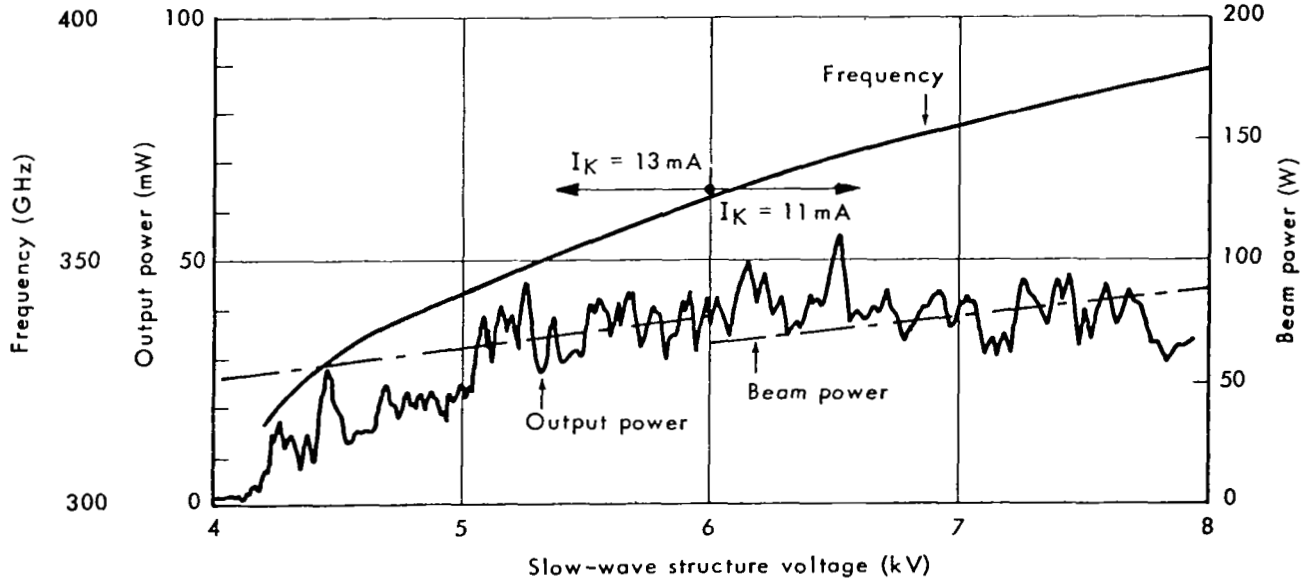

Figure 2.- Performance characteristics of a wide bandwidth medium power carcinotron (after Ref. 17).

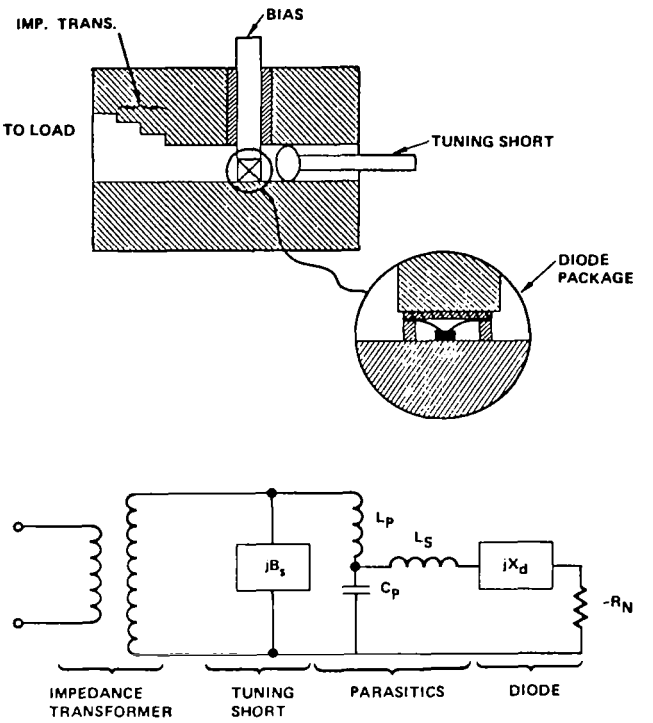

Figure 3.- Cross-sectional diagram and equivalent circuit of an IMPATT oscillator (after Ref. 24).

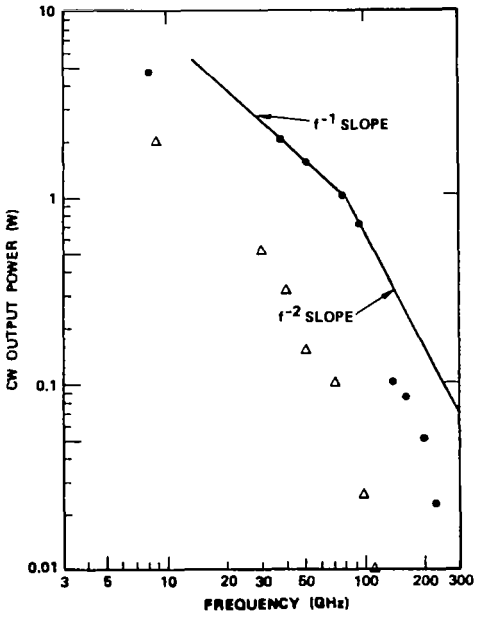

Figure 4.- State-of-the-art performance of IMPATT diodes (after Ref. 24).

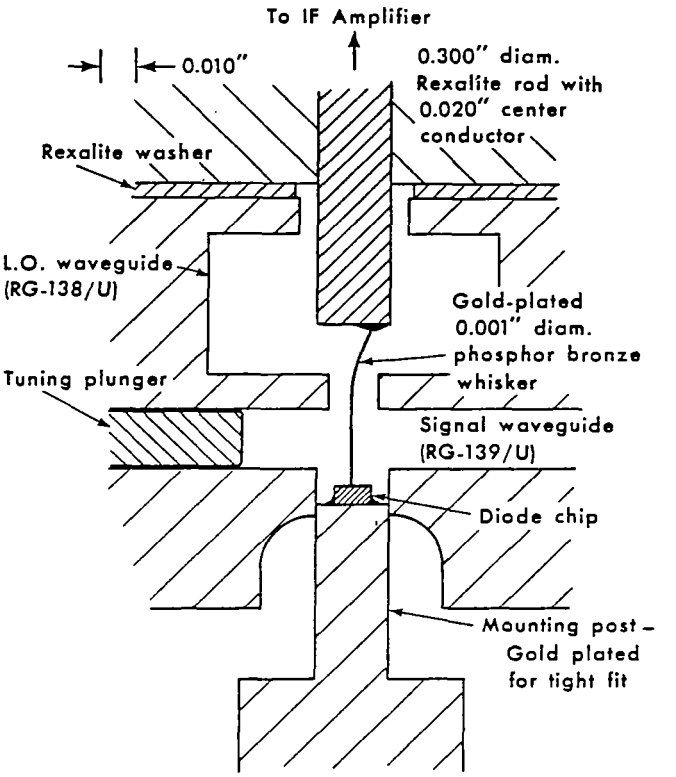

Figure 5.- Cross-sectional diagram of a crossed-waveguide mounted Schottky diode harmonic generator (after Ref. 22). 1" = 2.54 cm.

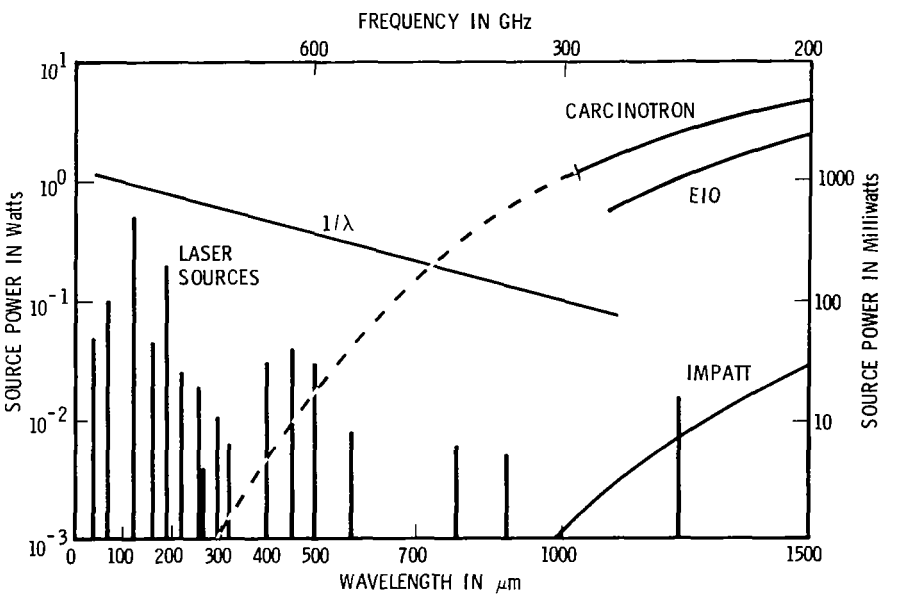

Figure 6.- Comparison of CW SMMW source technology (after Ref. 37).

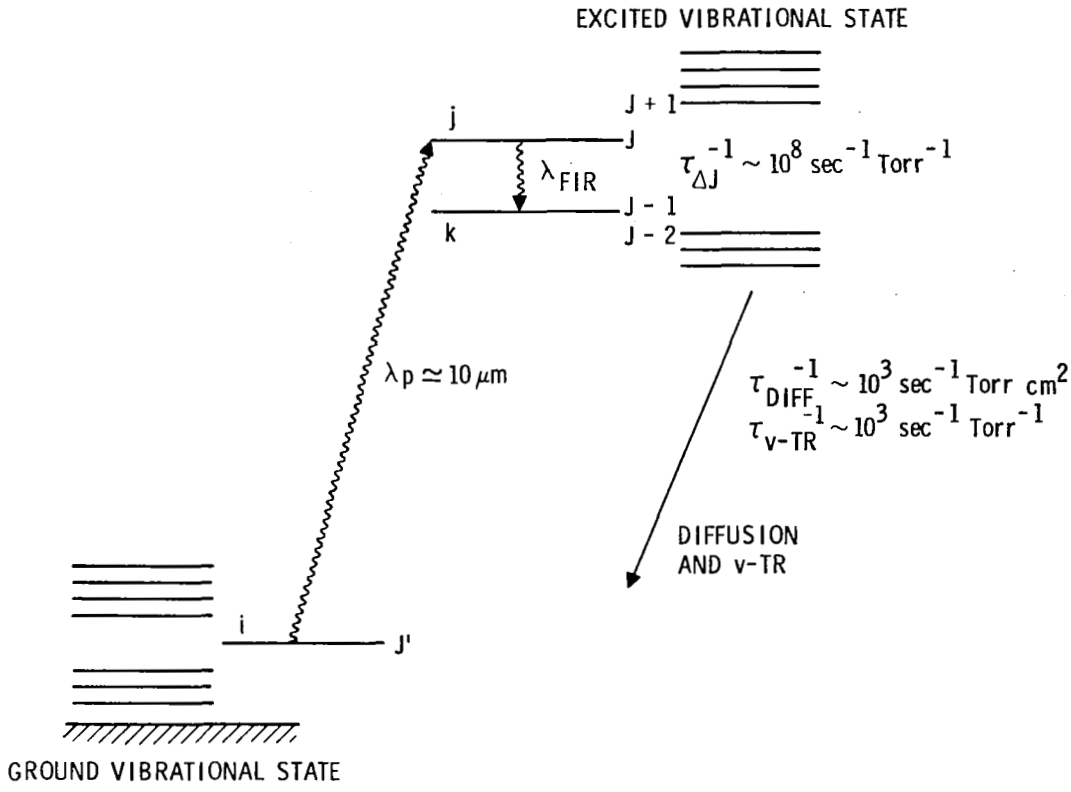

Figure 7.- Energy level diagram for an optically pumped laser.

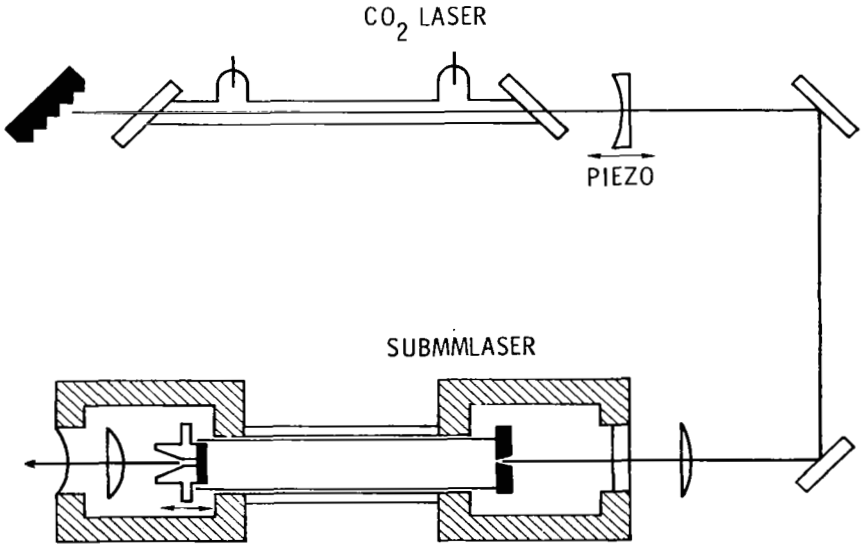

Figure 8.- Schematic of an OPM laser system.

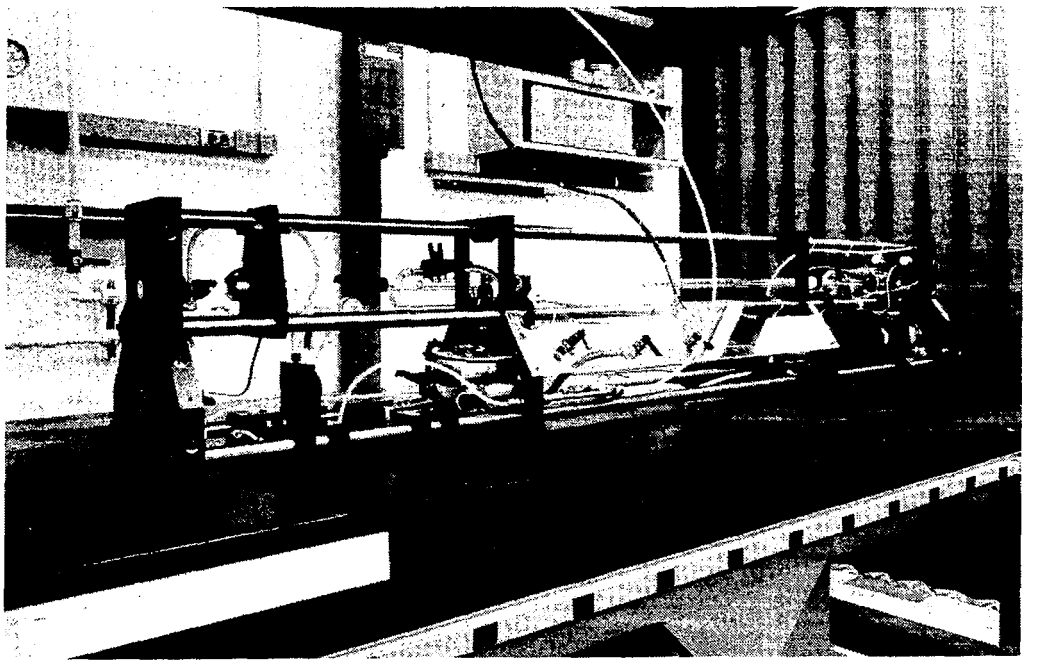

Figure 9.- Picture of Aerospace SMMW laser package.

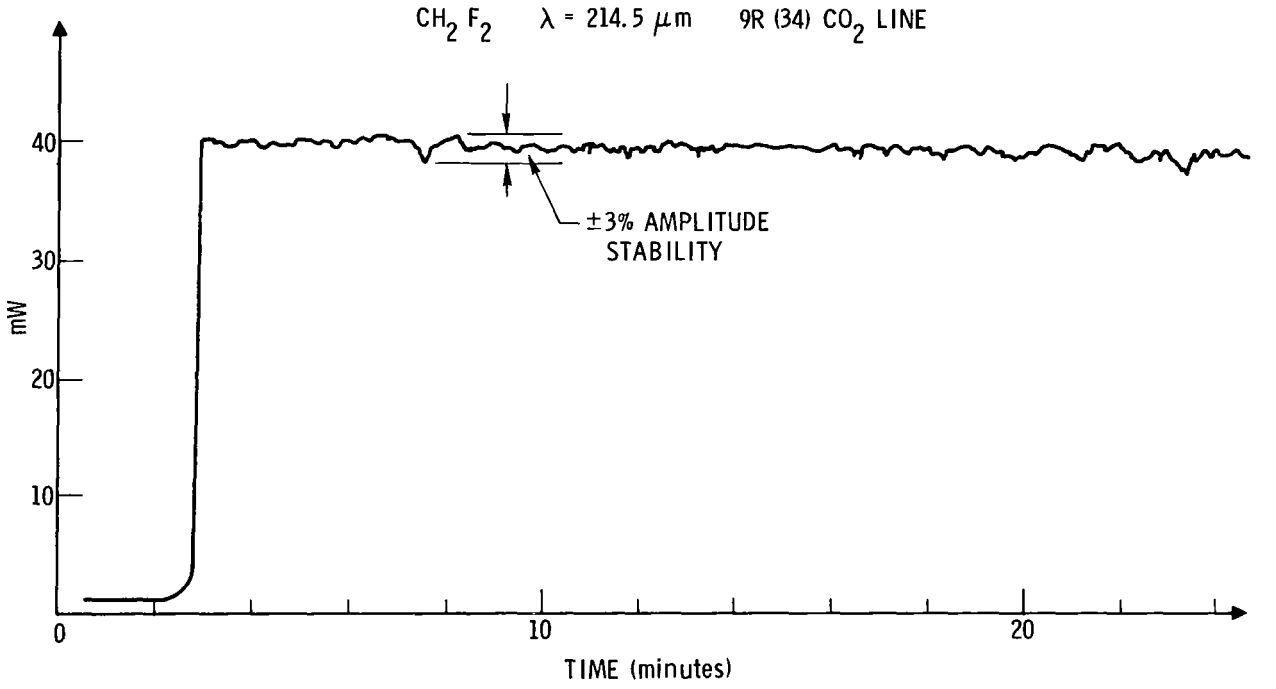

Figure 10.- Amplitude stability of OPM laser.

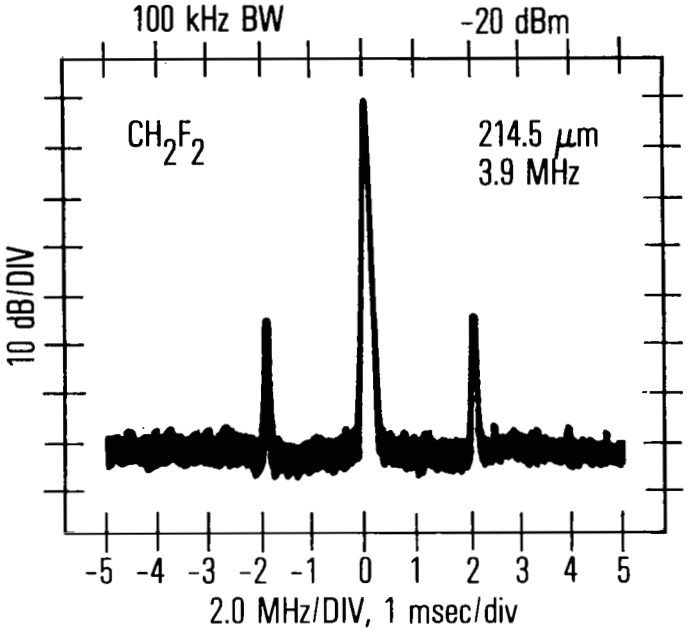

Figure 11.- Heterodyne mixing of two OPM lasers.

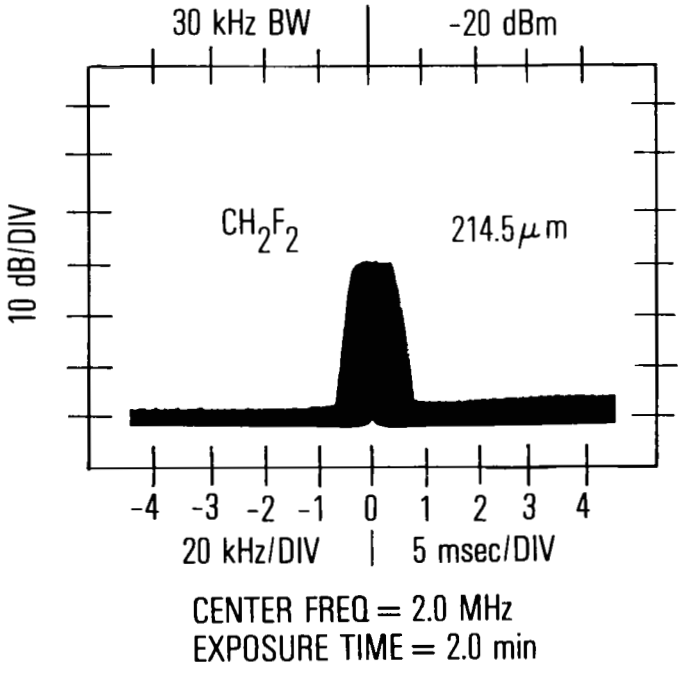

Figure 12.- Frequency jitter of heterodyne beat signal.

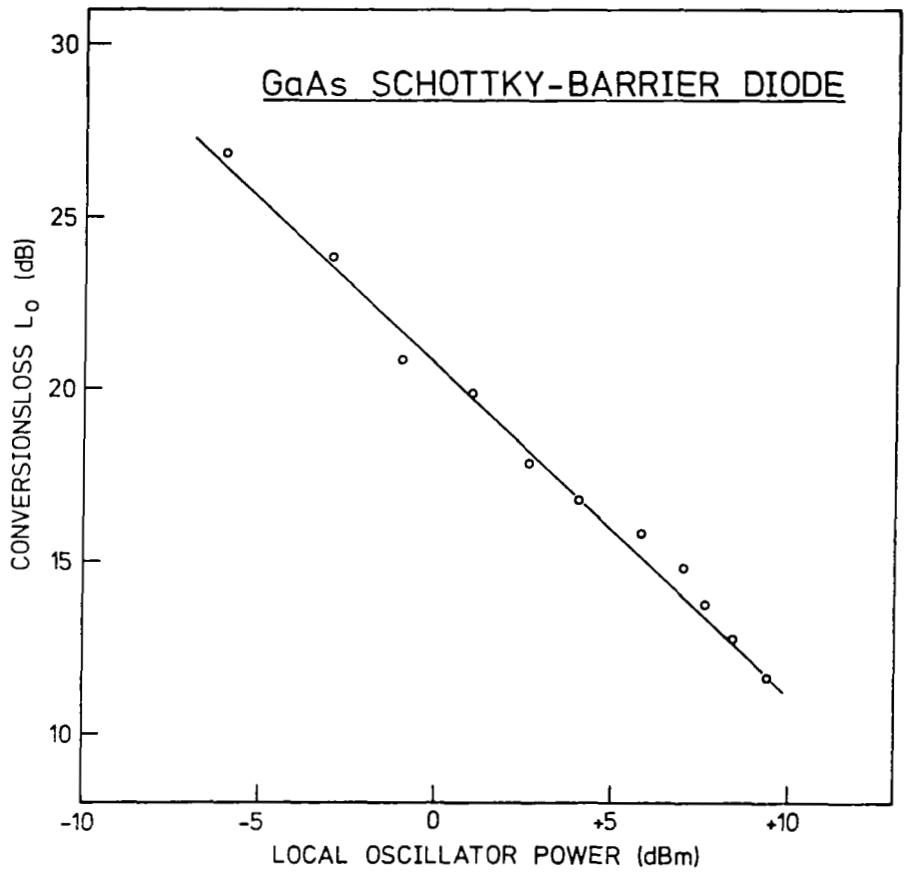

Figure 13.- Schottky diode mixer performance at 761 GHz (after Ref. 62).

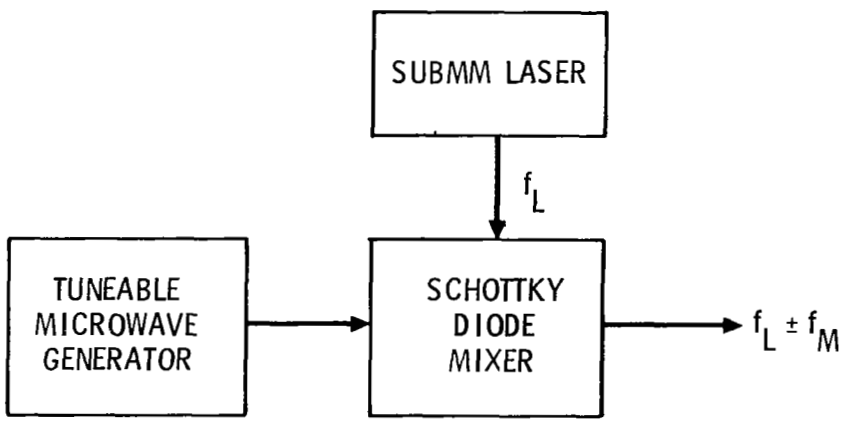

Figure 14.- Schematic diagram of a Schottky diode tuneable sideband generator.

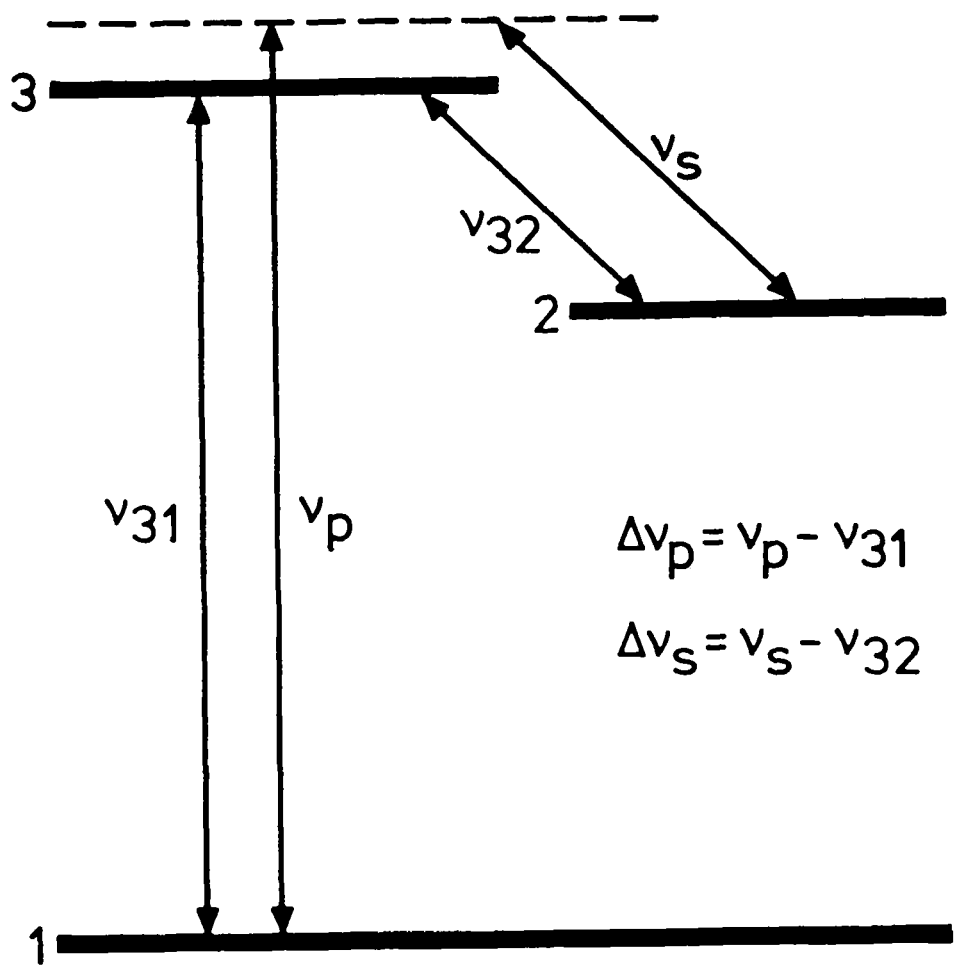

Figure 15.- Energy level diagram illustrating resonantly enhanced Raman scattering in a three-level system.

SUB MM LASER LOCAL OSCILLATORS:

DESIGN CRITERIA AND RESULTS

Gerhard A. Koepf*
Phoenix Corporation

INTRODUCTION

The main thrust in cw submillimeter (smm) laser research in the past has been toward the discovery of laser lines and toward higher output power levels. Diagnostic experiments were limited to a very small number of gases. They were directed toward the pump absorption and pressure dependence regime [1,2,3]. Very little attention has been paid to the spectral features of the smm laser emission. It was only recently that gain profile and frequency stability measurements were performed [4,5,6]. The general experience was that these lasers are quite unstable sources and in the common design not generally suitable for local oscillator applications [5,7]. The reasons for this are that (1) power and frequency changes of the CO_2 pump laser translate into power and frequency changes of the smm output, (2) that reflections of pump radiation from the smm resonator cause severe instabilities of the pump laser and (3) that smm resonator instabilities are often very critical because of resonance effects at the pump frequency. In the following, new diagnostic results will be given of the spectral features and the power conversion efficiency. As a result of these experiments, several criteria are obtained for the design of frequency stable and efficient smm lasers for local oscillator applications. Finally, a new design is described and results on the power output and power and frequency stability will be given.

*This work was performed under Contract No. NAS5-26030 for the Instrument Electrooptics Branch, NASA, Goddard Space Flight Center.

SMM LASER DIAGNOSTICS

Spectral Features

The harmonic mixing technique has been used for heterodyne diagnostics of the smm laser output at a number of laser lines ranging from 170 μm to 1221 μm. This technique has been applied before to measure the absolute frequency of smm laser lines [8,9,10]. A GaAs Schottky Barrier diode in a quasioptical mount was used to generate very high harmonics of microwave frequencies and for down conversion of the smm laser frequency [11]. With this technique we obtained frequency multiplication factors up to 145. This made diagnostics of the 170 μm line of CH_3OH possible with a signal to noise ratio of over 30 dB. The spectral features of the laser gain were studied by tuning the laser resonator while displaying the beat frequency on a spectrum analyzer screen in a high persistence mode. Several basic physical effects could be isolated by a proper choice of the laser gas, the laser gas pressure, the pump intensity and the pump frequency.

Generally, at the low operating pressures of the laser gases, the pump radiation travelling back and forth in the resonator acts velocity selective on two groups of molecules [1]. When operated at extremely low pressure, also the smm laser transition is Doppler broadened. In the absence of substantial velocity cross relaxation and power broadening, the laser gain profile consists of two distinct spikes of Lorentian shape. The separation of the spikes is tunable by the pump frequency, and their width increases with increasing saturation of the pump and the smm transition. These effects could be verified for the first time at the 496 μm line of CH_3F. One example is given in Figure 1. The difference in amplitude of the spikes is due to differing pump rates in the two directions.

Another type of gain profile splitting is due to the Autler-Townes or dynamic Stark effect [12]. The strong pump field in the laser acting on the molecules lifts the M-degeneracy of the rotational levels. The laser transition splits up into 2 (J+1) lines, where J is the rotational quantum number of the upper laser level. At normal operating pressures, these lines are collision broadened. The resulting shape of the gain profile depends on the type (P,Q,R) of the pump and laser transition on the magnitude of the pump field and the pump frequency [13]. This effect, which is well known in pulsed smm lasers, has recently been observed also in a CW amplifier and in the CH_3OH laser [4]. However, measurements of the line shape have not been reported so far. Our harmonic mixing technique revealed that dynamic Stark splitting is present at a large number of laser lines under regular operating conditions. We succeeded to isolate this effect best at the 1221 μm line of $C^{13}H_3F$ as shown in Figure 2. The observed line shape verifies the expected profile well: In this case, there are 5 pairs of M-sublevels. The largest splitting occurs for M=0 and the lowest for M=5. The highest amplitude goes with M=1. The symmetry of the two peaks indicates close to resonant pumping.

A less well known spectral feature of smm lasers is their tendency to relaxation oscillations. Such oscillations can readily be observed with fast

detectors on many lines in the time domain when the pump laser operates in a chopped mode. Generally these oscillations are of a damped kind; however, they also may occur in a continuous mode, especially when the pump laser is not well stabilized. The frequency of these oscillations is typically a few MHz. At low pressures it increases approximately with the square root of the pressure and the pump rate. At high pressure and high pump rate it approaches a fixed value. We have verified this behavior with observations in the time and frequency domain [14]. Our harmonic mixing technique allowed a clear discrimination against transverse mode beats by the existence of symmetrical frequency components and by the fact that the observed width of the gain profile is less than the oscillation frequencies.

Pump Absorption

Our concept of controlled pump beam propagation described below allows to measure the pump power reflected from the smm laser resonator. With the laser evacuated, we measured reflection of 40-50% of the pump power depending on the pump frequency. A part of these losses (about 15% per pass) are due to the tight dimension of the injection hole and the unfavorable mode of the pump laser. We also observed 5% losses per pass through the Brewster window and a total of 10-20% reflection losses at the resonator mirrors. As the laser gas pressure is decreased the reflected pump power decreases. The absorption coefficient, the transition from saturated to unsaturated absorption and the transition from Doppler broadening to homogeneous broadening is specific to each gas. Therefore, the particular dependence of the returned power versus pressure plotted in Figure 3 is not relevant. However, it shows how much or how little pump power is actually absorbed at a number of representative laser gases, when operated at their optimum pressure and at optimum pump detuning.

DESIGN CRITERIA

These diagnostic experiments provide new inputs into the question of how to improve the stability and efficiency of optically pumped smm laser local oscillators. Generally, a single mode operation on a low loss mode with high mode quality is required. This points the way to rather large diameter dielectric waveguides. The Doppler contribution and the dynamic Stark splitting should be avoided; variations of the pump frequency and pump intensity cause complicated changes of the gain profile shape. This leads to changes in the smm oscillation frequency by the cavity pulling effect. In smm lasers cavity pulling is very pronounced because the line Q and the resonator Q are of the same order of magnitude. Of the line splittings the dynamic Stark splitting by the pump field is observed more likely. Most laser lines operate well beyond the Doppler broadened regime. Therefore, low pump intensities are desirable as they are obtained by using larger waveguide diameters.

A high degree of frequency and power stability of the pump laser is a prerequisite for smm laser local oscillator applications. However, even the best known stabilization schemes are insufficient if pump power feedback from the smm resonator to the pump laser is given. CO_2 lasers are also quite sensitive to cavity pulling.

A further cause of instabilities are resonances of the pump frequency inside the smm resonator. In the common mode of optically pumping, the pump beam is reflected back and forth in the resonator in an uncontrolled way. Standing waves are built up that are highly sensitive to changes in resonator length. Such changes are translated to the smm field. As a consequence, the smm laser sensitivity to thermal and acoustical effects is greatly increased.

The criteria for high conversion efficiency of the pump power into smm radiation follow from our Figure 3. The pump power actually absorbed in the laser gas at the optimum pressure is generally only a fraction of the power provided by pump laser. This explains the rather small conversion efficiencies reported throughout the literature. The highest reported values (20-30%) are given for difluoromethane. This is a gas with an exceptionally high absorption at its operating pressure [15,16]. It is estimated that most of the power is absorbed in this gas after one round trip, such that losses into the waveguide walls and reflections are of no importance. However, if we use the power actually absorbed in the gases as given in Figure 3 as a reference, we obtain conversion efficiencies of over 25% of the theoretical values also for other gases that are rather weak absorbers. The laser design therefore should avoid a high degree of pump saturation and provide a long interaction length of the pump beam with the laser gas besides minimizing losses in the waveguide walls. The design criteria as discussed in this section are summarized in Table I.

- Stabilize pump laser in power and frequency
- Avoid feedback of pump radiation
- Minimize resonances of pump field
- Minimize cavity pulling effects due to gain profile splitting
- Control pressure and temperature
- Provide single mode operation
- Provide efficient pumping

Table I. Criteria for smm laser local oscillator design.

LASER LOCAL OSCILLATOR DESCRIPTION

The new concept of controlled pump beam propagation has been introduced a while ago [17]. A four-fold degenerate resonator configuration is chosen with two mirrors of 6m radius of curvature separated at 1.76m. The pump beam is injected through a hole that is displaced halfway between the center and the rim of the mirror. As it is shown schematically in Figure 4, the pump beam makes four roundtrips through the resonator. It diverges to a maximum diameter and converges to a beam waist before leaving the resonator through the injection hole. The total interaction length with the laser gas is 14m. No resonances and no losses into the waveguide walls occur. The outgoing beam is at an angle of about 1/2 degree. It separates from the ingoing beam after a distance and can be reflected to an absorber or to a power meter. Feedback into the pump laser and pump resonances are completely eliminated.

The smm laser head consists of a stainless steel tube that supports the 3.8mm ID glass waveguide, with flanges at each end for attachment of the mirror and window assemblies. The mode coupling losses introduced by the use of curved mirrors are minimal [18]. At wavelength below 150-200 μm, the resonator becomes Gaussian. One of the laser end assemblies is separated from the flange by vacuum bellows. It includes a large diameter differential drive centered at the axis for length tuning. The mirror assemblies are joined together by three invar rods. The thermal expansion of the rods is compensated by high expansion aluminum sleeves.

For the CO_2 laser we chose active stabilization by locking it to the resonance frequency of a temperature controlled, mechanically and thermally stable etalon. The scheme is shown in Figure 5. The pump beam passes through a ZnSe disc which is rotated close to Brewsters angle so that about 100 mW are split-off. One part of this beam serves to monitor the pump power level, the other part is matched to the confocal etalon with a lens. In addition to the tunable DC voltage, a 41 Hz dither voltage is applied to the piezoelectric translator in the etalon which modulates the transmission band. The power modulation of the transmitted beam is phase detected, and a high voltage is derived for length control of the CO_2 laser resonator. When the feedback loop is closed, the etalon DC voltage can be used to tune the pump laser frequency for maximum smm laser output power. This stabilization scheme provides a pump beam which is essentially free of modulation.

Description of Laser Performance

The output power of the smm laser and the pump laser were recorded simultaneously over extended periods. The smm laser was operated in a sealed-off mode. Due to residual leaks in the vacuum system, pressure increases of 1-2 mTorr per hour were observed. A warm-up period of one hour was allowed before making measurements. The temperature of both end assemblies, the steel tube and the invar rods were monitored with thermocouples. The readings never exceeded 2-3°C above room temperature. As a consequence, the resonator requires no re-adjustment after the warm-up period.

From the recordings a drop by 4% and by 1.5% follows for the putput power of the smm laser and the pump laser, respectively, over a period of two hours (see Figure 6). During this time the PZT voltage that controls the CO_2 laser frequency is driven through its entire range of 1000 V by the active loop circuit. It was observed that the CO_2 laser always drifts toward lower frequencies, even after several hours of operation. Relocking of the control loop at the other end of the PZT voltage range occurs automatically, sometimes within as little as 10 seconds. The somewhat larger drop of the smm power seems to be caused by pollution of the laser gas. After several hours of operation, the original power level could usually be obtained only with a freshly filled laser tube.

These results can be considered typical for lines that are pumped with the CO_2 laser operating not too far off its line center. This was confirmed by additional although less extensive measurements at a number of other lines ranging from 70 μm to 1.22mm. For detunings of more than 40 MHz from the line

center the locking of the loop is less reliable because of mode competition. The spectral range of the CO_2 laser is about 90 MHz. The output power levels at a number of characteristic lines as indicated on the scale of a Scientec power meter are given in Table II.

WAVELENGTH	LASER-GAS	READING
118 μm	CH_3OH	62.0 mW
170 μm	CH_3OH	39.0 mW
206 μm	CD_3F	25.0 mW
247 μm	CD_3F	15.0 mW
394 μm	HCOOH	38.0 mW
433 μm	HCOOH	32.0 mW
447 μm	CH_3I	32.0 mW
496 μm	$CH_3F - SF_6$	15.0 mW
513 μm	HCOOH	17.0 mW
570 μm	CH_3OH	3.5 mW
747 μm	CH_3Br	3.0 mW
1221 μm	$C\ ^{13}H_3F$	2.5 mW

Table II. Laser output power readings from Scientec power meter.

The laser output was also investigated with a wave analyzer. It was found that the dither frequency of 41 Hz produces a 0.4% modulation, while the 60 and 120 Hz components from the CO_2 discharge are below 0.3%.

With respect to matching of the laser beam to the antenna pattern of a mixer, the mode pattern of the laser beam is of importance [19]. The laser was found to operate alternately on a strong and a very weak transverse mode when the resonator length was changed. The cross section of the strong mode was recorded in the focus of a lens by a pyroelectric detector with an aperture of 1mm. This revealed an almost perfect Gaussian intensity pattern, which is surprising to some degree in view of the toroidal excitation volume of the pump beam, the hybrid hole coupler and the large number of relatively low loss modes in a waveguide resonator. The linear polarization of the mode was ensured by a polarizer.

The frequency stability of the laser was investigated by mixing the laser beam with harmonics of a very stable microwave oscillator in a Schottky diode. As compared to other similar efforts [20], a very simple approach of generating a stable reference in the smm region was chosen. The output of a stable synthesizer operating in the X-band was amplified and applied to the diode coaxially through a bandpass filter. Due to the strong nonlinearity of the diode very

large multiplication factors can be obtained. By using the 62nd harmonic, and tuning the synthesizer through a 50 MHz wide band centered at 12.25 GHz, beat signals ranging from 10 MHz to 2.5 GHz were obtained. After a second down conversion into the 150 MHz band, a frequency counter with printer and a spectrum analyzer were used to monitor the long term frequency stability of the laser line at 761 GHz of formic acid.

The short term fluctuations of the beat signal as displayed on the spectrum analyzer were typically 5-10 kHz wide, in close agreement with other measurements performed at this line [5]. In this reference, heavy pump power feedback is mentioned to have affected the stability measurements for time intervals above 0.1 second. In our laser no such effects could be observed. For long term frequency measurements, the printer was set to take samples at different time intervals. The observed frequency changes varied in rate and direction. Over a one second and a one minute time interval mean drifts of 740 Hz and 14 kHz were obtained. The Allan variance for these intervals was calculated to be $7.8\ 10^{-10}$ and $1.2\ 10^{-8}$, respectively. The lowest and highest frequencies recorded over one locking period of the CO_2 laser (two hours) were about 0.5 MHz apart.

The frequency drifts are mainly attributed to drifts of the CO_2 pump laser. Aside from the active stabilization, there are several mechanisms that can cause frequency drifts. The stability of the etalon is limited to 1.5 MHz per day. The active loop electronics are not perfectly linear and are also subject to thermal drifts. In addition, small changes in the orientation of the CO_2 laser beam were observed to shift the transmission band of the etalon. Such directional changes of the pump beam can occur as a consequence of the tuning of the CO_2 laser by the PZT mounted grating.

CONCLUSIONS

A smm laser with an amplitude and frequency stability suitable for application as a local oscillator in a high resolution heterodyne radiometer/spectrometer has been described. The mode pattern is very close to a Gaussian profile so that efficient coupling to a quasioptical mixer is possible. The laser provides sufficient output power at a large number of lines to drive the mixer into the low conversion loss regime. Radiometric integration times of several minutes with a spectral resolution of 1 MHz will be possible. With present state-of-the-art Schottky mixers and low noise preamplifiers a radiometric temperature resolution of a few ^{o}K can be expected over a spectral range from 500 to 900 GHz.

REFERENCES

[1] Hodges, D. T.; Tucker, J. R.; and Hartwick, T. S.: Basic Physical Mechanisms Determining the Performance of the CH_3F Laser. Infrared Physics, vol. 16, 1976, pp. 175-182.

[2] Weiss, C. O.: Pump Saturation in Molecular Far-Infrared Lasers. IEEE J. Quantum Electron, vol. QE-12, 1976, pp. 580-584.

[3] Henningsen, J. O. and Jensen, H. G.: The Optically Pumped Far-Infrared Laser: Rate Equations and Diagnostic Experiments. IEEE J. QE, vol. QE-11, 1975, pp. 248-252.

[4] Heppner, J.; Hubner, V.; and Weiss, C. O.: Saturated and Small Signal Gain in CW Laser-Pumped FIR Laser Gases. IV Int. Conference on Infrared and MM Waves and their Applications, Dec. 10-15, 1979, Conference Digest, pp. 161-162.

[5] Godone, A.; Weiss, C. O.; and Kramer, G.: FM-Noise Measurements on an Optically Pumped FIR Laser. IEEE J. of Quantum Electron, vol. QE-14, 1978, pp. 339-342.

[6] Plainchamp, P. M.: Frequency Instability Measurements of the CH_3OH Optically Pumped Laser at 70.5 and 118 μm. IEEE J. of Quantum Electron, vol. QE-15, 1979, pp. 860-864.

[7] Button, K.: Is there a Future for Submillimeter Lasers? Panel Discussion, Laser 78 Conference, Orlando, LF, Dec. 1978, Conference Digest, pp. 833-836.

[8] Radford, H. E.; Petersen, F. R.; Jennings, D. A.; and Mucha, J. A.: Heterodyne Measurements of smm Laser Spectrometer Frequencies. IEEE J. Quantum Electron, QE-13, 1977, pp. 92-94.

[9] Kramer, G. and Weiss, C. O.: Frequencies of some Optically Pumped Submillimeter Laser Lines. Appl. Phys. 10, 1976, pp. 187-188.

[10] Dyubko, S. F. and Fesenko, L. D.: Frequencies of Optically Pumped Submillimeter Lasers. 3rd Int. Conference on Sub MM Waves and their Applications, 28 March - 1 April 1978, Conference Digest, pp. 70-73.

[11] Fetterman, H. R.; Clifton, B. J.; Tannenwald, P. E.; and Parker, C. D.: Submillimeter Detection and Mixing Using Schottky Diodes. Appl. Phys. Lett., 24, 1976, pp. 70-72.

[12] Autler, S. H. and Townes, C. H.: Stark Effect in Rapidly Varying Fields. Phys. rev., 100, Oct. 15, 1955, pp. 703-722.

[13] Skribanovitz, N.; Kelly, M. J.; and Feld, M. S.: New Laser Technique for the Identification of Molecular Transitions. Phys. rev. A, vol. 6, 1977, pp. 2302-2311.

[14] Lawandy, N. M. and Koepf, G. A.: Relaxation Oscillations in Optically Pumped Molecular Lasers. IEEE J. of Quantum Electronics. vol. QE-16, 1980.

[15] Danielewicz, E. J. and Weiss, C. O.: New Efficient CW Far-Infrared Optically Pumped CH_2F_2 Laser. IEEE J. of Quantum Electronics, vol. QE-14, 1978, pp. 705-708.

[16] Danielewicz, E. J. et al.: High Performance at new FIR Wavelengths from Optically Pumped CH_2F_2. Optics Letters, 4, 1979, pp. 280-282.

[17] Koepf, G. A. and McAvoy , N.: Design Criteria for Optically Pumped FIR Laser Cavities. IEEE JQE, vol. QE-13, 1977, pp. 418-421.

[18] Degnan, J. J. and Hall, D. R.: Finite Aperture Waveguide - Laser Resonators. IEEE J. of Quantum Electron, vol. QE-9, 1973, pp. 901-910.

[19] Fetterman, H. R.; Tannenwald, P. E.; Clifton, B. J.; Parker, C. D.; Fitzgerald, W. D.; and Erickson, N. R.: Far IR Heterodyne Radiometric Measurements with Quasi-Optical Schottky Diode Mixers. Applied Physics Letter, 33, 1978, p. 151.

[20] Godone, A.; DeMarchi, A.; and Bava, E.: An Improved Multiplier Chain for Precise Frequency Measurements up to 20 THz. 33rd Annual Frequency Control Symposium, Atlantic City, May-June 1979.

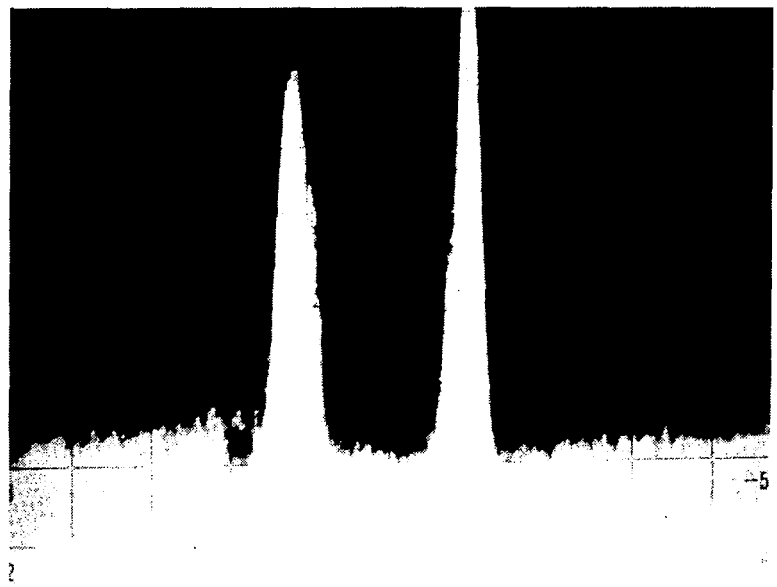

Figure 1.- Gain profile splitting due to velocity selective pumping: CH_3F pumped with 9P20 line at 3m Torr pressure; center frequency 604 GHz, 1 MHz/div.

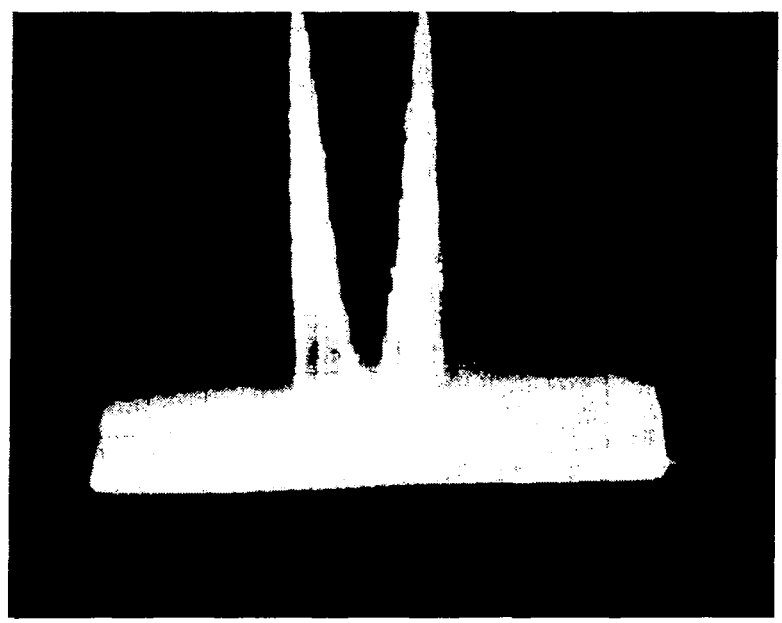

Figure 2.- Gain profile splitting due to dynamic Stark effect: $C^{13}H_3F$ pumped by 9P32 line at 36m Torr pressure; center frequency 245 GHz, 1 MHz/div.

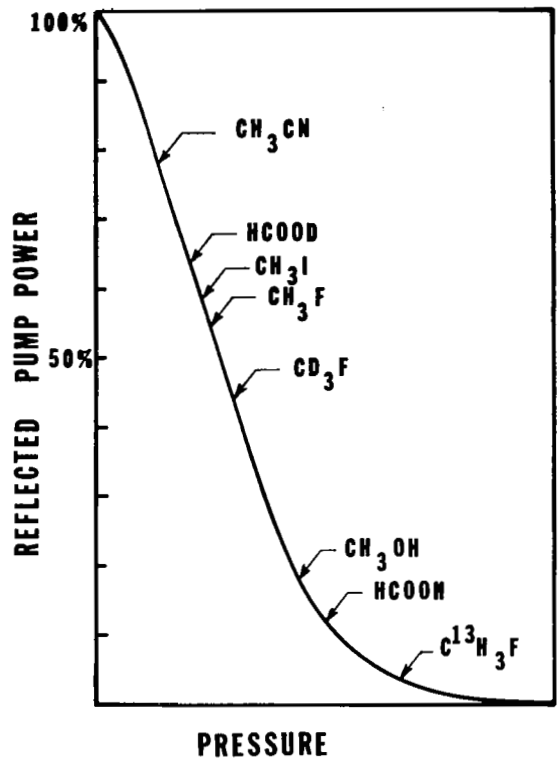

Figure 3.- Measurement of pump power reflected from resonator for representative laser gases at their respective optimum operating pressures. The pressure scale is uncalibrated.

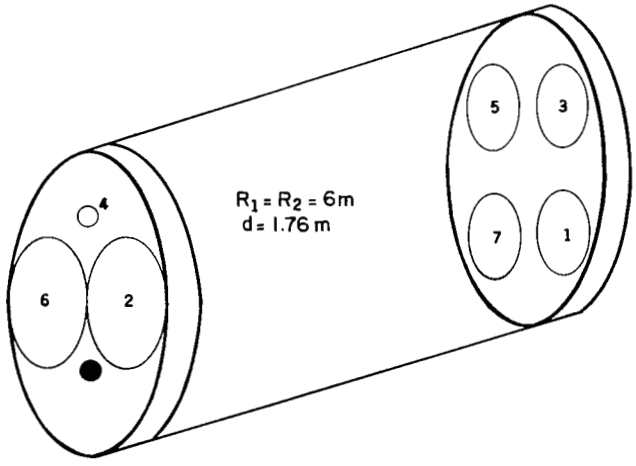

PUMP BEAM PROPAGATION IN FOURFOLD DEGENERATE RESONATOR

Figure 4.- Schematic of four fold degenerate resonator and pump beam footprints.

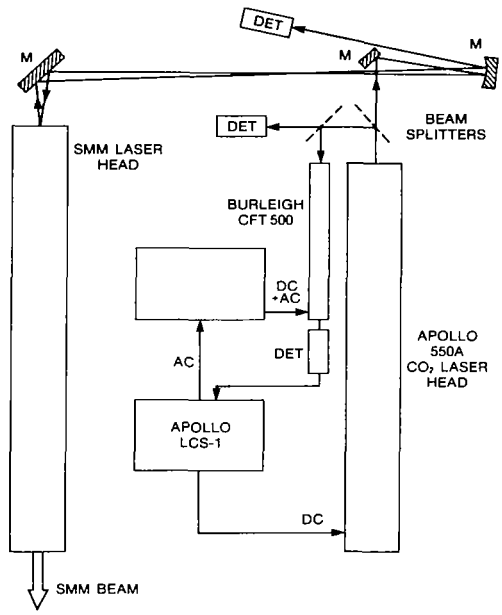

Figure 5.- CO_2 laser stabilization and pump beam propagation.

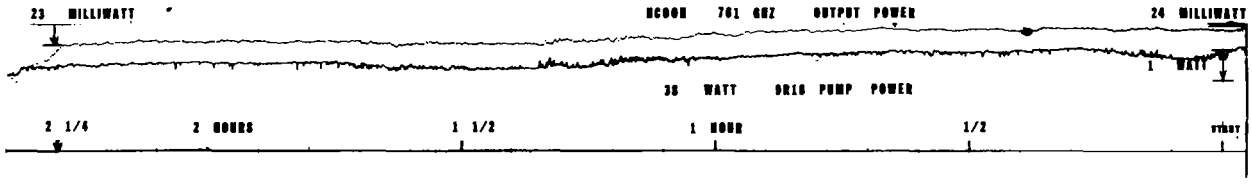

Figure 6.- Long term power stability. Upper trace: 761 GHz line of HCOOH, lower trace 9R18 pump power. Both baselines are heavily offset.

DESIGN CONSIDERATIONS FOR OPTICAL HETERODYNE RECEIVERS: A REVIEW

John J. Degnan
Instrument Electro-optics Branch
NASA Goddard Space Flight Center
Greenbelt, Maryland 20771

ABSTRACT

By its very nature, an optical heterodyne receiver is both a receiver and an antenna. Certain fundamental antenna properties of heterodyne receivers are described which set theoretical limits on the receiver sensitivity for the detection of coherent point sources, scattered light, and thermal radiation. In order to approach these limiting sensitivities, the geometry of the optical antenna-heterodyne receiver configuration must be carefully tailored to the intended application. The geometric factors which affect system sensitivity include the local oscillator (LO) amplitude distribution, mismatches between the signal and LO phasefronts, central obscurations of the optical antenna, and nonuniform mixer quantum efficiencies. The current state of knowledge in this area, which rests heavily on modern concepts of partial coherence, is reviewed.

Following a discussion of noise processes in the heterodyne receiver and the manner in which sensitivity is increased through time integration of the detected signal, we derive an expression for the mean square signal current obtained by mixing a coherent local oscillator with a partially coherent, quasi-monochromatic source. We then demonstrate the manner in which the IF signal calculation can be transferred to any convenient plane in the optical front end of the receiver. Using these techniques, we obtain a relatively simple equation for the coherently detected signal from an extended incoherent source and apply it to the heterodyne detection of an extended thermal source and to the back-scatter lidar problem where the antenna patterns of both the transmitter beam and heterodyne receiver must be taken into account. Finally, we consider the detection of a coherent source and, in particular, a distant point source such as a star or laser transmitter in a long range heterodyne communications system.

1. INTRODUCTION

Heterodyne or coherent detection can be advantageous in a variety of applications. Heterodyne receivers have at least two features which are qualitatively different from incoherent (or direct detection) receivers (ref. 1). First of all, the receiving bandwidth is determined by the IF bandwidth which, in principle, can be varied at will to give very high spectral resolution. Secondly, information related to the phase of the radiation signal is retained in the IF output and the outputs of two or more receivers can be correlated to make coherence measurements comparable to the aperture synthesis techniques of radio astronomy.

To achieve high spectral radiation with incoherent or direct detection systems, radiation filters or spectrometers must be utilized and the combination of very narrow bandwidth and high sensitivity (low loss) is usually difficult to realize. In general, a heterodyne receiver will be more sensitive than a direct detection receiver with an equivalent noise equivalent power (NEP) for spectral resolutions below a cutoff bandwidth which depends on the NEP and the infrared wavelength (refs. 1, 2). The sub-Doppler spectral resolution of heterodyne receivers can be exploited to study the molecular constituents and kinematics of remote sources yielding specific information such as altitude profiles of absolute abundance of the species, vertical temperature profiles, and wind velocities (ref. 3). In detecting extraterrestrial thermal sources, the information is gathered by passive heterodyne spectrometers whereas, in our own atmosphere or in planetary atmospheres visited by spacecraft, active backscatter lidars can be employed. In contrast to the above applications where the radiation signal is totally incoherent or only partially coherent, the signal from the laser transmitter in a heterodyne communication system (ref. 4) is coherent except as modified by atmospheric effects (ref. 5). This article attempts to present a unified theory of heterodyne receivers which addresses the optical design considerations for all of these applications.

A representative heterodyne receiver is illustrated in Figure 1. Signal radiation is collected by an optical antenna and focused, along with a local oscillator beam, onto a square-law frequency mixer operating at the radiation frequency. The latter beams have center frequencies ν_S and ν_L and powers P_S and P_L. The two frequencies mix to give an output spectrum centered at the intermediate frequency $\nu_{IF} = \nu_S - \nu_L$ where ν_{IF} is much smaller than the infrared frequencies ν_S and ν_L and typically on the order of a GHz or less. The resulting signal current is amplified by an IF amplifier of bandwidth B_{IF} and rectified by a nominally square-law detector to give a current output proportional to the power in the IF. This is usually input to a low-frequency filter or integrating circuit to further enhance the spectral resolution and/or sensitivity and is then recorded.

Although the present article will address most factors influencing the performance of the receiver in Figure 1, it will emphasize the design of the optical front end of the receiver for a variety of applications and, in particular, the manner in which the optical antenna geometry and local oscillator distribution affect system sensitivity. In Section 2 of this paper, we review the noise processes relevant to the IF signal and discuss the system signal-to-noise in the IF in terms of an as yet undefined mean square signal current. Section 3

briefly outlines the sensitivity improvement achieved by time integration techniques. In Section 4, we address the calculation of the mean square signal current in the mixer plane for a general, partially coherent, quasi-monochromatic source and, in Section 5, demonstrate the manner in which the IF signal calculation can be transferred to any convenient plane in the optical front end of the receiver. In Section 6, we apply the general result to the specific problem of coherently detecting an extended incoherent source. The results of that section are then applied to the heterodyne detection of an extended thermal source in Section 7 and to the backscatter lidar problem in Section 8 and some useful design guidelines are generated. In Section 9, we apply the results of Section 4 to the detection of a spatially coherent source such as a laser transmitter in a heterodyne communications system or a distant point source such as a star.

2. THE SIGNAL-TO-NOISE RATIO OF A HETERODYNE RECEIVER

The power signal-to-noise ratio of a heterodyne receiver is a measure of its sensitivity since setting the ratio equal to one permits calculation of the noise equivalent power (NEP). It is given, in most cases of interest, by (ref. 1)

$$\left(\frac{S}{N}\right)_{power} = \frac{\langle i_M^2 \rangle}{\langle i_S^2 \rangle + \langle i_T^2 \rangle + \langle i_B^2 \rangle + \langle i_J^2 \rangle + \langle i_A^2 \rangle} \tag{2.1}$$

We will leave the calculation of the mean square signal current $\langle i_M^2 \rangle$ to later sections and limit our present discussion to the various noise terms in the denominator of Equation (2.1).

The local oscillator induced shot noise, or quantum noise, $\langle i_S^2 \rangle$ is often the dominant noise if $h\nu >> KT_B$ where T_B is the equivalent blackbody temperature of a thermal source lying inside the antenna pattern of the receiver. Shot noise is due to fluctuations in the rate of arrival of LO photons. If the LO power is much greater than the signal power, the mean square shot noise current is given by

$$\langle i_S^2 \rangle = 2\beta e B_{IF} \bar{i}_{DC}$$

$$= \frac{2\beta e^2 B_{IF}}{h\nu} \iint_D d\vec{r}_D \, \eta_Q(\vec{r}_D) \, I_L(\vec{r}_D) \tag{2.2}$$

where $\bar{i}_{DC}$ is the DC current generated by the LO, e is the electronic charge, B_{IF} is the intermediate frequency bandwidth, and $h\nu$ is the photon energy. The integrand contains the detector quantum efficiency η_Q and the LO intensity I_L which are assumed to vary over the plane of the detector defined by the two-dimensional coordinate $\vec{r}_D$. The parameter β equals 1 for photoemissive mixers

while, for photoconductors, it equals 2 due to fluctuations in the generation and recombination of charge carriers as described by Levinstein (ref. 6).

One can rewrite Equation (2.2) in the more familiar form

$$\langle i_S^2 \rangle = \frac{2\bar{\eta}_Q \beta e^2 B_{IF} P_L}{h\nu} \tag{2.3}$$

if we define an average quantum efficiency $\bar{\eta}_Q$ by

$$\bar{\eta}_Q = \frac{\iint_D d\vec{r}_D \; \eta_Q(\vec{r}_D) \; I_L(\vec{r}_D)}{\iint_D d\vec{r}_D \; I_L(\vec{r}_D)} \tag{2.4}$$

and P_L is the local oscillator power incident on the detector.

Radiation from a thermal source contained within the receiver field of view and the receiver bandwidth B_{IF} will be coherently detected and subject to so-called "heterodyne amplification." In some experiments, such as in passive heterodyne spectrometry, this thermal source is the object of study, while in others it corresponds to unwanted background noise. We will show in later sections that it can be described by the equation

$$\langle i_T^2 \rangle = \frac{2\bar{\eta}_Q \eta_T e^2 B_{IF} P_L}{h\nu (e^{h\nu/KT} - 1)} \tag{2.5}$$

where η_T is an overall efficiency which depends in part on the design of the optical front end.

Fluctuations in background radiation, which spectrally is outside the receiver bandwidth but within the infrared response band of the mixer, will also produce noise currents, given by $\langle i_B^2 \rangle$ in Equation (2.1) as will sources of radiation outside the antenna pattern of the receiver but inside the heterodyne receiving bandwidth. McLean and Putley (ref. 7) have derived expressions for this noise component which are complicated functions of wavelength, spectral interval, detector area and temperature, and field of view. The latter noise is not amplified by the heterodyne process, however, and can be rendered negligible by choosing a large enough local oscillator power and by spatially and spectrally filtering the input radiation.

Two other important sources of noise are Johnson or thermal noise associated with the mixer and the IF amplifier. The mixer noise is given by

$$\langle i_J^2 \rangle = \frac{4KT_M B_{IF}}{R_M} \tag{2.6}$$

where T_M and R_M are the mixer's (or mixer load resistor's) temperature and resistance as seen by the IF amplifier. For most cooled mixers, this would be negligible compared with the amplifier noise given by

$$\langle i_A^2 \rangle = \frac{4KT_A B_{IF}}{MR_A} \tag{2.7}$$

where T_A and R_A are the amplifier's noise temperature and input resistance, and M is a factor less than unity which accounts for impedance mismatches between the mixer and amplifier.

Clearly, other sources of noise exist. "Excess noise" is common in receivers which employ diode laser local oscillators and generally arises from multimode effects or other non-ideal behavior in the LO. Noise can also be introduced at the electrical contacts to the mixer element or by temperature fluctuations in the mixer. These sources are unique to specific systems and will not be considered further here.

With sufficient LO power, most of the above noise sources can be made negligible relative to the quantum noise $\langle i_S^2 \rangle$ and/or the background thermal noise contribution $\langle i_T^2 \rangle$. If the mean square signal current is given by an expression of the form

$$\langle i_M^2 \rangle = 2\bar{\eta}_Q \eta_{HET} \left(\frac{e}{h\nu}\right)^2 P_S P_L \tag{2.8}$$

where P_S is the received signal power and η_{HET} is an as yet undefined heterodyne receiver efficiency, then, under strong LO illumination, the signal-to-noise ratio tends to

$$\left(\frac{S}{N}\right)_{power} = \frac{\langle i_M^2 \rangle}{\langle i_S^2 \rangle + \langle i_B^2 \rangle} = \frac{\eta_{HET} P_S}{h\nu B_{IF} \left\{\beta + \eta_T \left[\exp(h\nu/KT) - 1\right]^{-1}\right\}} \tag{2.9}$$

Setting the latter ratio equal to one and solving for P_S/B_{IF} yields the noise equivalent power per unit bandwidth; i.e.,

$$NEP\,(W/Hz) = \frac{h\nu}{\eta_{HET}} \left\{\beta + \eta_T \left[\exp(h\nu/KT) - 1\right]^{-1}\right\} \tag{2.10}$$

where η_{HET} and η_T both depend on the optical front end geometry. In the quantum noise limit ($h\nu >> KT$), Equation (2.10) reduces to

$$NEP(W/Hz) = \frac{\beta h\nu}{\eta_{HET}} \tag{2.11}$$

whereas, in the thermal limit ($h\nu << KT$), it becomes

$$NEP(W/Hz) = \frac{\eta_T}{\eta_{HET}} KT \tag{2.12}$$

If we include mixer and amplifier Johnson noise, we can write for a general photoconductor

$$NEP(W/Hz) = \frac{2h\nu}{\eta_{HET}} + \frac{\eta_T h\nu}{\eta_{HET}\left[\exp(h\nu/KT) - 1\right]} + \frac{K(T_M + T_A)}{G} \tag{2.13}$$

where G is the "conversion gain" defined by Arams et al. (ref. 8).

3. DETECTION AND TIME INTEGRATION

If the power signal-to-noise ratio in the IF is less than unity, the signal can be detected by integrating the detector output over a sufficiently long period of time. The voltage signal-to-noise ratio at the filter output in Figure 1 is linearly related to the power S/N by the equation (ref. 1)

$$\left(\frac{S}{N}\right)_V = \left(\frac{S}{N}\right)_{power} \frac{1}{\sqrt{2}} \left(\frac{B_{IF}}{B_o}\right)^{1/2} \tag{3.1}$$

The latter equation assumes that the IF amplifier has a rectangular bandpass spectrum (double sideband), the rectifying detector is an ideal square-law device, the final output filter has a noise bandwidth B_o much less than B_{IF} and the power S/N is much less than unity. Smith (ref. 9) has considered the more general case where the IF amplifier is not strictly square-law and does not have a rectangular bandpass spectrum. He has also considered power S/N ratios much greater than unity. If the output filter is a single stage RC circuit such that $B_o = \tau_o/4 = RC/4$, Equation (3.1) becomes

$$\left(\frac{S}{N}\right)_V = \left(\frac{S}{N}\right)_{power} \sqrt{2B_{IF}\tau_o} \tag{3.2}$$

4. COHERENT DETECTION OF A GENERAL QUASI-MONOCHROMATIC SOURCE

We turn now to the calculation of the mean square signal current $\langle i_M^2 \rangle$ for a general quasi-monochromatic source. This problem has been considered previously by Rye (ref. 10) and McGuire (ref. 11). With only minor modification, the derivation given here parallels that of McGuire. If we assume that the detected radiation lies within a frequency bandwidth $\Delta\nu_S$ that is narrow with respect to the center frequency ν_S, the real signal field at the mixer plane can be represented by an expression of the form

$$E_S(\vec{r}_D,t) = \sqrt{2}\ \mathrm{Re}\left\{E_S(\vec{r}_D,t)\ e^{i\omega_S t}\right\} \tag{4.1}$$

where $\omega_S = 2\pi\nu_S$ and the complex signal field envelope $E_S(\vec{r}_D,t)$ at the point $\vec{r}_D$ in the detector plane varies slowly in time relative to the exponential $\exp(i\omega_S t)$. The time dependence of the envelope might reflect the modulated output of a transmitter laser in a heterodyne communications system, the amplitude and phase fluctuations inherent in the signal from an incoherent thermal source or backscatter lidar, or even the effects of atmospheric turbulence on the signal. The envelope, through its dependence on the detector coordinate $\vec{r}_D$, also contains spatially dependent amplitude and phasefront information.

If we represent the LO field by a similar expression, the current out of the square-law mixer is given by

$$i(t) = \frac{e}{2h\nu} \iint_D d\vec{r}_D\ \eta_Q(\vec{r}_D)\left[\mathrm{Re}\left\{E_S(\vec{r}_D,t)\ e^{i\omega_S t} + E_L(\vec{r}_D,t)\ e^{i\omega_L t}\right\}\right]^2 \tag{4.2}$$

where ω_L is the LO center frequency and the integral is over the active detector area. Upon performing the quadratic multiplication of fields in Equation (4.2), we obtain both sum and difference frequencies. High-frequency sum terms varying as $\exp(\pm 2i\omega_S t)$, $\exp(\pm 2i\omega_L t)$, $\exp(\pm i(\omega_S+\omega_L)t)$, lie outside the bandwidth of the mixer and hence can be ignored. The difference terms produce two "DC" currents corresponding to the average signal and local oscillator induced currents and an additional mixing term given by

$$i_M(t) = \left(\frac{2e}{h\nu}\right)\iint_D d\vec{r}_D\ \eta_Q(\vec{r}_D)\ \mathrm{Re}\left\{E_S(\vec{r}_D,t)\ E_L^*(\vec{r}_D,t)\ e^{i\omega_{IF} t}\right\} \tag{4.3}$$

where the IF frequency $\omega_{IF} = \omega_S - \omega_L$. Squaring Equation (4.3) yields

$$i_M^2(t) = \left(\frac{2e}{h\nu}\right)^2 \iint_D d\vec{r}_D \iint_D d\vec{r}_D{}' \; \eta_Q(\vec{r}_D)\; \eta_Q(\vec{r}_D{}')$$

$$\times \mathrm{Re}\left\{E_S(\vec{r}_D,t)\; E_L^*(\vec{r}_D,t)\; e^{i\omega_{IF}t}\right\} \mathrm{Re}\left\{E_S(\vec{r}_D{}',t)\; E_L^*(\vec{r}_D{}',t)\; e^{i\omega_{IF}t}\right\}$$

$$= 2\left(\frac{e}{h\nu}\right)^2 \iint_D d\vec{r}_D \iint_D d\vec{r}_D{}' \; \eta_Q(\vec{r}_D)\; \eta_Q(\vec{r}_D{}')$$

$$\times \left[\mathrm{Re}\left\{E_S(\vec{r}_D,t)\; E_S^*(\vec{r}_D{}',t)\; E_L(\vec{r}_D{}',t)\; E_L^*(\vec{r}_D,t)\right\}\right.$$

$$\left. + \mathrm{Re}\left\{E_S(\vec{r}_D,t)\; E_S(\vec{r}_D{}',t)\; E_L^*(\vec{r}_D,t)\; E_L^*(\vec{r}_D{}',t)\; e^{i2\omega_{IF}t}\right\}\right] \qquad (4.4)$$

If we average the above expression over a time interval T short compared to the coherence times of the signal and local oscillator field (T_S and T_L) but long compared to the IF beat period, T_{IF}, we may write

$$i_M^2(t) = \frac{1}{T}\int_{t-T/2}^{t+T/2} dt\; i_M^2(t)$$

$$\approx 2\left(\frac{e}{h\nu}\right)^2 \iint_D d\vec{r}_D \iint d\vec{r}_D{}' \; \eta_Q(\vec{r}_D)\; \eta_Q(\vec{r}_D{}')$$

$$\times E_S(\vec{r}_D,t)\; E_S^*(\vec{r}_D{}',t)\; E_L(\vec{r}_D{}',t)\; E_L^*(\vec{r}_D,t) \qquad (4.5)$$

since the field envelopes can be viewed as effectively constant over this time interval and hence the terms varying as $\exp(\pm 2i\omega_{IF}t)$ in Equation (4.4) average to zero over an IF beat period. In certain applications, such as passive heterodyne spectrometry of a thermal source, the integration time can be arbitrarily long. The limit of Equation (4.5) as T approaches infinity is then

$$\langle i_M^2 \rangle = \lim_{T\to\infty} \frac{1}{T} \int_{t-T/2}^{t+T/2} dt\; i_M^2(t)$$

$$= 2\left(\frac{e}{h\nu}\right)^2 \iint_D d\vec{r}_D \iint d\vec{r}_D'\; \eta_Q(\vec{r}_D)\; \eta_Q(\vec{r}_D')$$

$$\times \langle E_S(\vec{r}_D,t)\; E_S^*(\vec{r}_D',t)\rangle \langle E_L(\vec{r}_D',t)\; E_L^*(\vec{r}_D,t)\rangle \qquad (4.6)$$

where we have invoked the fact that the signal and local oscillator fields are statistically independent and hence the fourth-order correlation function $\langle E_S(\vec{r}_D,t)\; E_S^*(\vec{r}_D',t)\; E_L(\vec{r}_D',t)\; E_L^*(\vec{r}_D,t)\rangle$ can be written as the product of two second-order functions. The second-order correlation functions can be related to quantities appearing in the theory of partial coherence by noting that the "mutual coherence function" (MCF) of a quasi-monochromatic, stationary optical signal field is defined by (ref. 12)

$$\Gamma_S(\vec{r}_1,\vec{r}_2,\tau) = \langle E_S(\vec{r}_1,t+\tau)\; E_S^*(\vec{r}_2,t)\rangle\, e^{i\omega_S\tau} \qquad (4.7)$$

Under the assumption of cross spectral purity (refs. 12, 13), the spatial and time variables are separable leading to

$$\Gamma_S(\vec{r}_1,\vec{r}_2,\tau) = J_S(\vec{r}_1,\vec{r}_2)\; g(\tau)\; e^{i\omega_S\tau} \qquad (4.8)$$

where $g(0) = 1$ and $J_S(\vec{r}_1,\vec{r}_2)$ is the "mutual intensity function" (MIF) of the signal field. From Equations (4.7) and (4.8) we note that $\langle E_S(\vec{r}_D,t)\; E_S^*(\vec{r}_D',t)\rangle = \Gamma_S(\vec{r}_D,\vec{r}_D',0) = J_S(\vec{r}_D,\vec{r}_D')$ and hence Equation (4.6) can be written in its final form

$$\langle i_M^2 \rangle = 2\left(\frac{e}{h\nu}\right)^2 \iint_D d\vec{r}_D \iint_D d\vec{r}_D'\; \eta_Q(\vec{r}_D)\; \eta_Q(\vec{r}_D')\; J_S(\vec{r}_D,\vec{r}_D')\; J_L(\vec{r}_D',\vec{r}_D) \qquad (4.9)$$

where $J_S(\vec{r}_D,\vec{r}_D')$ and $J_L(\vec{r}_D',\vec{r}_D)$ are the mutual intensity functions of the signal and local oscillator fields in the detector plane. Calculation of the mean square mixing current by means of Equation (4.9) is not always a simple task due to the difficulty in computing $J_S(\vec{r}_D,\vec{r}_D')$ for many sources of practical interest. In ensuing sections, we will demonstrate how the calculation can be carried out in optical planes other than the detector plane and the enormous simplifications that often result.

Before closing this section, it is worthwhile to note two useful properties of the mutual intensity function; i.e.,

$$J_S^*(\vec{r}_D,\vec{r}_D') = \langle E_S^*(r_D,t)\ E_S(\vec{r}_D',t)\rangle = J_S(\vec{r}_D',\vec{r}_D) \tag{4.10}$$

and

$$J_S(\vec{r}_D,\vec{r}_D) = I_S(\vec{r}_D) \tag{4.11}$$

where $I_S(\vec{r}_D)$ is the time averaged signal intensity at the point $\vec{r}_D$.

5. PROPAGATION OF THE MUTUAL INTENSITY FUNCTION

Consider the signal electric field propagating from the antenna plane in Figure 2 to the detector plane. Small angle scalar diffraction theory (ref. 12) gives the electric field in the detector plane; i.e.,

$$E_S(\vec{r}_D,t) = \iint d\vec{r}_A\ P_A(\vec{r}_A)\ E_S\left(\vec{r}_A,t - \frac{r_{AD}}{c}\right)\left(-\frac{ie^{ikr_{AD}}}{\lambda r_{AD}}\right) \tag{5.1}$$

where $k = 2\pi/\lambda$, $P_A(\vec{r}_A)$ is the antenna pupil function and the term in brackets corresponds to a Huygen's wavelet emanating from a point $\vec{r}_A$ in the antenna plane and traveling a distance r_{AD} to a point $\vec{r}_D$ in the mixer plane. Then, from the definition of the mutual intensity function (MIF), it is clear that

$$J_S(\vec{r}_D,\vec{r}_D') \equiv \langle E_S(\vec{r}_D,t)\ E_S^*(\vec{r}_D',t)\rangle$$

$$= \iint d\vec{r}_A \iint d\vec{r}_A'\ P_A(\vec{r}_A)\ P_A(\vec{r}_A')$$

$$\times \left[\frac{e^{ik(r_{AD}-r_{A'D'})}}{\lambda^2 r_{AD} r_{A'D'}}\right]\left\langle E_S\left(\vec{r}_A,t - \frac{r_{AD}}{c}\right)\ E_S^*\left(\vec{r}_A',t - \frac{r_{A'D'}}{c}\right)\right\rangle \tag{5.2}$$

For a stationary process, the time origin is of no consequence and therefore

$$\left\langle E_S\left(\vec{r}_A,t - \frac{r_{AD}}{c}\right)\ E_S^*\left(\vec{r}_A',t - \frac{r_{A'D'}}{c}\right)\right\rangle = \left\langle E_S(\vec{r}_A,t)\ E_S^*\left[\vec{r}_A',t - \frac{(r_{A'D'} - r_{AD})}{c}\right]\right\rangle \tag{5.3}$$

Now, if the transverse dimensions of the antenna and detector pupil are small compared to the coherence length of the signal radiation defined by $l = c/\Delta\nu_S$, the variation of the signal electric field over a time interval $t = (r_{A'D'} - r_{AD})/c$ is negligible and Equation (5.3) is effectively the signal MIF in the antenna plane. Equation (5.2) then becomes the propagation law for the MIF as first derived by Zernike (refs. 12, 14); i.e.,

$$J_S(\vec{r}_D,\vec{r}_D') = \iint d\vec{r}_A \iint d\vec{r}_A'\; P_A(\vec{r}_A)\; P_A(\vec{r}_A') \left[\frac{e^{ik(r_{AD}-r_{A'D'})}}{\lambda^2 r_{AD} r_{A'D'}}\right] J_S(\vec{r}_A,\vec{r}_A') \tag{5.4}$$

If we substitute Equation (4.5) in (4.9) for the mean square signal current and reverse the order of integration, we obtain

$$\langle i_M^2 \rangle = 2\left(\frac{e}{h\nu}\right)^2 \iint d\vec{r}_A \iint d\vec{r}_A'\; P_A(\vec{r}_A)\; P_A(\vec{r}_A')\; J_S(\vec{r}_A,\vec{r}_A') \times \left\{\iint d\vec{r}_D \iint d\vec{r}_D'\; P_D(\vec{r}_D)\; P_D(\vec{r}_D')\; \eta_Q(\vec{r}_D)\; \eta_Q(\vec{r}_D')\; J_L(\vec{r}_D',\vec{r}_D) \left[\frac{e^{ik(r_{AD}-r_{A'D'})}}{\lambda^2 r_{AD} r_{A'D'}}\right]\right\} \tag{5.5}$$

where $P_D(\vec{r}_D)$ is the mixer pupil function. If we now define an effective local oscillator field given by

$$E_E(\vec{r}_D',t) \equiv \eta_Q(\vec{r}_D')\; E_L(\vec{r}_D',t) \tag{5.6}$$

the corresponding effective MIF is then equal to

$$J_E(\vec{r}_D',\vec{r}_D) = \eta_Q(\vec{r}_D)\; \eta_Q(\vec{r}_D')\; J_L(\vec{r}_D',\vec{r}_D) \tag{5.7}$$

Substituting Equation (5.7) into (5.5) and comparing the resulting expression with the MIF propagation law (5.4), we note that the bracketed term in Equation (5.5) is simply the MIF of the effective local oscillator back-propagated to the antenna plane. We may therefore write for the mean square mixing current

$$\langle i_M^2 \rangle = 2\left(\frac{e}{h\nu}\right)^2 \iint d\vec{r}_A \iint d\vec{r}_A'\; P_A(\vec{r}_A)\; P_A(\vec{r}_A')\; J_S(\vec{r}_A,\vec{r}_A')\; J_E(\vec{r}_A',\vec{r}_A) \tag{5.8}$$

The physical significance of Equation (5.8) is that the calculation of mean square IF signal current can be carried out in any convenient optical plane as first pointed out by Rye (ref. 10). This has practical importance since it is usually easier, for example, to compute the backpropagation of a coherent LO electric field through an optical system than to propagate the MIF of an incoherent source in a forward direction through the system to the mixer. This fact will be well illustrated in later sections.

Although we have considered only free space propagation in the present derivation, the approach is equally valid when intervening optical elements such as lenses, mirrors, and apertures are present. The simple Huygens wavelet in Equation (5.1) is then replaced by an appropriate transmission function for the optical system (refs. 10, 12).

6. HETERODYNE DETECTION OF AN EXTENDED INCOHERENT SOURCE

The expressions derived up to this point have assumed a general, partially coherent, quasi-monochromatic source. We consider now an important practical application in which the signal radiation emanates from an extended incoherent source and propagates to the antenna plane as in Figure 3. The propagation of the MIF proceeds in precisely the same fashion as in the previous section except that there is no coherence between the Huygens wavelets emanating from the infinitesimal sources located at $\vec{r}_S$ and $\vec{r}_S'$. Thus the second-order correlation function in the source-antenna plane version of Equation (5.3) becomes

$$\left\langle E_S(\vec{r}_S,t)\; E_S^*\left[\vec{r}_S',t-\left(\frac{r_{S'A'}r_{SA}}{c}\right)\right]\right\rangle \approx \langle E_S(\vec{r}_S,t)\; E_S^*(\vec{r}_S',t)\rangle = I_S(\vec{r}_S)\;\delta(\vec{r}_S-\vec{r}_S') \tag{6.1}$$

where $I_S(\vec{r}_S)$ is the time averaged radiation intensity at the point $\vec{r}_S$ in the source plane and $\delta(\vec{r}_S-\vec{r}_S')$ is the two-dimensional Dirac delta function. It can be shown that substitution of Equation (6.1) into the source-antenna plane version of Equation (5.2) and performing the double integral over $\vec{r}_S'$ yields the propagation law for the MIF of an incoherent source (ref. 13); i.e.,

$$J_S(\vec{r}_A,\vec{r}_A') = \lambda^2 \iint_S d\vec{r}_S\; I_S(\vec{r}_S)\left[\frac{e^{ik(r_{SA}-r_{SA'})}}{\lambda^2 r_{SA}r_{SA'}}\right] \tag{6.2}$$

where the integral is over the finite dimensions of the source. We may now substitute Equation (6.2) into (5.8) and reverse the order of integration to obtain for the mean square IF signal current

$$\langle i_M^2 \rangle = 2\left(\frac{e}{h\nu}\right)^2 \lambda^2 \iint_S d\vec{r}_S \; I_S(\vec{r}_S)$$
$$\times \left\{ \iint d\vec{r}_A \iint d\vec{r}_A' \; P_A(\vec{r}_A) \; P_A(\vec{r}_A') \left[\frac{e^{ik(r_{SA}-r_{SA'})}}{\lambda^2 r_{SA} r_{SA'}} \right] J_E(\vec{r}_A', \vec{r}_A) \right\} \qquad (6.3)$$

Through use of the MIF propagation law given by Equation (5.4), we recognize the bracketed term in Equation (6.3) as the mutual intensity function of the backpropagated effective local oscillator (BPELO) evaluated at the points $\vec{r}_S = \vec{r}_S'$. But, since $J_E(\vec{r}_S, \vec{r}_S) = I_E(\vec{r}_S)$, the time averaged intensity of the BPELO in the source plane, Equation (6.3) reduces to the relatively simple expression

$$\langle i_M^2 \rangle = 2\left(\frac{e}{h\nu}\right)^2 \lambda^2 \iint_S d\vec{r}_S \; I_S(\vec{r}_S) \; I_E(\vec{r}_S) \qquad (6.4)$$

Thus we have the very useful result that the mean square IF signal current is proportional to the overlap integral of the extended incoherent source intensity with the backpropagated effective LO intensity. In the next two sections, we will apply this result to the detection of thermal radiation and to the backscatter lidar problem.

7. THERMAL SOURCE DETECTION

The total power ΔP radiated into a hemisphere, within the IF bandwidth B_{IF}, from a small area ΔA on a blackbody is

$$\Delta P = \frac{2\pi}{\lambda^2} \frac{h\nu B_{IF}}{\left[\exp(h\nu/KT) - 1\right]} \Delta A \qquad (7.1)$$

Only the power emitted in the direction of the receiver contributes to the signal MIF in the antenna plane. Thus, if the receiver is in a direction normal to the plane of the blackbody, we must multiply the above expression by a factor $1/\pi$ corresponding to the power emitted per steradian in the normal direction. We must also multiply by 1/2 to account for the fact that the heterodyne receiver detects only one polarization component. Thus, the intensity to be substituted into Equation (6.4) is given by

$$I_S = \left(\frac{1}{2}\right)\left(\frac{1}{\pi}\right)\frac{\Delta P}{\Delta A} = \frac{1}{\lambda^2} \frac{h\nu B_{IF}}{\left[\exp(h\nu/KT) - 1\right]} \qquad (7.2)$$

and Equation (6.4) becomes

$$\langle i_M^2 \rangle = \frac{2e^2 B_{IF}}{h\nu\left[\exp(h\nu/KT) - 1\right]} \iint_S d\vec{r}_S \; I_E(\vec{r}_S) \tag{7.3}$$

where the integral is simply the total backpropagated effective LO power subtended by the source.

If the dominant noise mechanism is the LO-induced shot noise given by Equation (2.3), the IF signal-to-noise ratio is

$$\left(\frac{S}{N}\right)_{power} = \frac{\langle i_M^2 \rangle}{\langle i_S^2 \rangle} = \frac{\eta_T}{\beta\left[\exp(h\nu/KT) - 1\right]} \tag{7.4}$$

where η_T is the overall heterodyne receiver efficiency for thermal source detection introduced in Equation (2.5) and defined by

$$\eta_T = \frac{1}{\bar{\eta}_Q P_L} \iint_S d\vec{r}_S \; I_E(\vec{r}_S) \tag{7.5}$$

where $\bar{\eta}_Q$ is the average mixer quantum efficiency defined by Equation (2.4) and P_L is the LO power incident on the detector. If the mixer quantum efficiency is uniform, Equation (7.5) reduces to

$$\eta_T = \frac{\eta_Q}{P_L} \iint_S d\vec{r}_S \; I_L(\vec{r}_S) \tag{7.6}$$

where we have used Equations (5.7) and (4.11). The quantity $I_L(\vec{r}_S)$ is the intensity of the actual backpropagated LO rather than the effective LO. The quantity η_T replaces the mixer efficiency in the corresponding equations in the classic paper by Siegman (ref. 15).

If the source is so large that the backpropagated LO is contained entirely within its disk radius, the integral in Equation (7.6) is simply the total LO power in the source plane. Except for an atmospheric transmission factor η_A, the latter is equal to the backpropagated LO power exiting from the antenna. Thus, the overall heterodyne efficiency (7.6) can be broken down into several components; i.e.,

$$\eta_T = \eta_Q \eta_A \eta_o \eta_R \tag{7.7}$$

where η_o takes into account routine optical losses due to reflections and scattering while η_R is a geometric efficiency which takes into account vignetting, central obstructions, LO phasefront curvature, etc. in the optical

antenna. Numerically, η_R is equal to the fraction of the original LO power which exits from the antenna during backpropagation.

As an illustration, consider the Cassegrain telescope in Figure 4. Let us assume that the mixer is illuminated by the fundamental gaussian mode of the local oscillator laser. If the gaussian mode is not truncated too badly by the mixer perimeter or by the secondary mirror, it remains gaussian until it is truncated by the primary mirror of radius a and centrally obscured by the secondary of radius b in the antenna plane. The geometric efficiency η_R is then given by

$$\eta_R = \frac{2}{\pi\omega^2}\left[2\pi \int_b^a dr\ re^{-2(r/\omega)^2}\right] = e^{-\gamma^2\alpha^2} - e^{-\alpha^2} \tag{7.8}$$

where ω is the gaussian spot radius in the antenna plane and we have defined two parameters (ref. 16) $\alpha = a/\omega$ and $\gamma = b/a$. The geometric efficiency has been plotted as a function of α and γ in Figure 5.

The important thing to note in Figure 5 is that, for a given nonzero value of the linear obscuration ratio $\gamma = b/a$, the optimum efficiency is less than what one would expect based on simple blockage of the incoming radiation by the central obscuration. For example, $\gamma = 0.5$ would imply an areal obscuration efficiency of $1 - \gamma^2$ or 75%. The peak efficiency in Figure 5, however, would only be about 47% if one were to choose an optimum gaussian spot radius corresponding to $\alpha = 1.3$. Nonoptimum choices clearly result in significantly worse performance.

Clearly, to maximize the efficiency of coherent detection of a thermal source which fills the receiver field of view, one wishes to choose an optical geometry which allows the effective backpropagated LO to exit from the telescope with near-unity efficiency. Although this is most easily accomplished with off-axis reflective telescope geometries which eliminate the central obscuration problem, one is not limited to such geometries in general. For example, if we use appropriate masks in the LO beam to create a local oscillator distribution in the mixer plane which matches the Airy pattern of the centrally obscured Cassegrain telescope in Figure 4, the backpropagated LO will form an annular disk in the antenna plane which matches the antenna pupil function and provides unity transmission. This result assumes, of course, that the mixer quantum efficiency is reasonably uniform. The transmission loss of the beam splitter in Figure 4 is included in the optical efficiency η_o.

For such large sources, the efficiency is not sensitive to the wavefront curvature of the LO beam except to the extent that it modifies the LO transmission through the antenna pupil. For example, if one considers two systems, projecting the same gaussian spot size in the antenna plane of Figure 4 but having two different radii of curvature for the LO phasefronts, the fractional transmission and hence the receiver efficiency will be the same. The system with the wider backpropagated LO divergence will detect point sources near the optic axis with less sensitivity but this will be compensated for by the

detection of additional point sources which are beyond the field of view of the receiver with the smaller backpropagated LO divergence. On the other hand, if the source is of limited spatial extent, maximum detection efficiency dictates that the backpropagated LO be contained totally within the source pupil function and hence LO phasefront curvature effects will play a more important role. For small thermal sources in the near field of the receiver, as in a laboratory experiment, this can be accomplished by choosing an optical system which effectively focuses the backpropagated LO onto the target source and provides near-unity transmission efficiency for the backpropagated LO.

8. INCOHERENT BACKSCATTER LIDAR

Consider the lidar system in Figure 6. An outgoing pulse of temporal width δ is transmitted through the atmosphere illuminating the aerosol scatterers in its path. The mixer current at time t is due to radiation scattered at a time $t - R/c$ from a volume defined by the length $c\delta/2$ within the receiver field of view as determined by the backpropagated effective LO intensity. Although the aerosol scatterers are randomly spaced and typically many wavelengths apart, the return is not strictly incoherent since the scatterers within the volume of interest are "frozen" in their positions during the passage of a short laser pulse, thereby producing a coherent or "speckle" component in the return. Thus, based on a single return, one cannot perform the long time average necessary to progress from Equation (4.5) to (4.6) in our derivation of the mean square mixing current $\langle i_M^2 \rangle$. However, if we imagine repeating the lidar experiment many times over the same source volume and obtaining an average current waveform out of the mixer, the coherent component would be expected to average to zero over the ensemble of measurements due to the random relative motions of the scatterers. After averaging a sufficiently large number of current waveforms, we would then be left with the incoherent component. Thus, if the physical process being observed is ergodic, i.e., ensemble averages are equal to time averages, the mean square mixing current will be given by $\langle i_M^2 \rangle$ where the notation now applies to either an ensemble average or time average since the two are equivalent.

With the additional argument given above, we can apply Equation (6.4) to the pulsed backscatter lidar problem. The source intensity function I_S which is now a function of range (Z coordinate) as well as the transverse coordinates, is given by

$$I_S(R,\vec{r}_S) = p\ \rho(R,\vec{r}_S)\left(\frac{c\delta}{2}\right)\frac{d\sigma(\pi)}{d\Omega}\ I_T(R,\vec{r}_S) \tag{8.1}$$

where $I_T(R,\vec{r}_S)$ is the intensity of the coherent transmitter beam at the range R and transverse coordinate $\vec{r}_S$, $d\sigma(\pi)/d\Omega$ is the differential scattering cross section in the backward direction, $c\delta/2$ is the length of the scattering volume, $\rho(R,\vec{r}_S)$ is the density distribution of scatterers, and p is a factor of order unity or less which takes into account depolarization effects. The product $\left[d\sigma(\pi)/d\Omega\right] I_T(R,\vec{r}_S)$ is the power scattered in the backward direction per steradian by a single scatterer located at the coordinates

$(R,\vec{r}_S)$ while the product $\rho(R,\vec{r}_S)(c\delta/2)$ is the number of scatterers per unit cross-sectional area in the source volume. Substituting Equation (8.1) into (6.4) gives

$$\langle i_M^2 \rangle = 2p\left(\frac{c\delta}{2}\right)\frac{d\sigma(\pi)}{d\Omega}\left(\frac{e}{h\nu}\right)^2\lambda^2\iint d\vec{r}_S\ \rho(R,\vec{r}_S)\ I_T(R,\vec{r}_S)\ I_E(R,\vec{r}_S) \tag{8.2}$$

which yields the important result that the mean square signal current is proportional to the overlap integral of three quantities - the coherent transmitter intensity, the backpropagated effective LO intensity, and the density distribution of scatterers. It is useful to note that we have not made the assumption that the transmitted and local oscillator beams are coaxial in deriving Equation (8.2). In fact, the equation can be used for bistatic lidar systems provided the transmitter and receiver optical axes are nearly parallel and an appropriate offset between transmitter and LO beams is included before computing the integral. If the transverse separation between transmitter and receiver is small relative to the spot sizes of the transmitter and BPELO at the range R, the bistatic system can be treated as coaxial to a good approximation.

As a simple numerical example, we now consider the case of gaussian transmitter and local oscillator beams described by

$$I_T(R,\vec{r}_S) = \frac{2P_T}{\pi\omega_T^2(R)}\,e^{-2\left(\frac{r_S}{\omega_T(R)}\right)^2} \tag{8.3}$$

and

$$I_L(R,\vec{r}_S) = \frac{2P_L}{\pi\omega_L^2(R)}\,e^{-2\left(\frac{r_S}{\omega_L(R)}\right)^2} \tag{8.4}$$

where P_T and P_L are the transmitter and local oscillator output powers and $\omega_T(R)$ and $\omega_L(R)$ are the corresponding guassian radii at the range R. Substitution of Equations (8.3) and (8.4) into (8.2) yields

$$\langle i_M^2 \rangle = 2\left(\frac{\eta_Q e}{h\nu}\right)^2\left\{\frac{2\pi p\left[\rho(R)\,c\delta/2\right]\frac{d\sigma(\pi)}{d\Omega}\,\lambda^2 P_T P_L}{\pi^2\left[\omega_T^2(R)+\omega_L^2(R)\right]}\right\} \tag{8.5}$$

where we have assumed a uniform scattering density $\rho(R)$ and a uniform mixer efficiency η_Q. Clearly, $\langle i_M^2 \rangle$ increases with decreasing ω_T and ω_L implying that the signal level will be maximized in a laboratory scattering experiment by focusing the transmitter and backpropagated LO into the sample.

If the scattering volume in the lidar system of Figure 6 lies in the far field of the transmitter and LO beam waists, we can use the approximations

$\omega_T(R) \approx \lambda R/\pi\omega_{TO}$ and $\omega_L(R) \approx \lambda R/\pi\omega_{LO}$ where ω_{TO} and ω_{LO} are the respective beam waists and R is the distance between the waists and the scattering volume (ref. 17). Equation (8.5) then becomes

$$\langle i_M^2 \rangle = 2\left(\frac{\eta_Q e}{h\nu}\right)^2 \left\{\frac{2\pi p\left[\rho(R)\, c\delta/2\right] \frac{d\sigma(\pi)}{d\Omega} P_T P_L}{R^2}\right\} \left(\frac{\omega_{TO}^2 \omega_{LO}^2}{\omega_{TO}^2 + \omega_{LO}^2}\right) \tag{8.6}$$

which exhibits the familiar R^{-2} dependence for the lidar equation. Equations (8.3) and (8.4) suggest the definition of an effective area for the gaussian beam waists given by $A_T = \pi\omega_{TO}^2/2$ and $A_L = \pi\omega_{LO}^2/2$. Further defining an average antenna area $A = (A_T + A_L)/2$ and letting $A_L = \varepsilon\bar{A}$ and $A_T = (2 - \varepsilon)\bar{A}$, Equation (8.6) becomes

$$\langle i_M^2 \rangle = 2\left(\frac{\eta_Q e}{h\nu}\right)^2 \left\{\frac{4P_T P_L \bar{A}}{R^2}\, p\left[\frac{\rho(R)\, c\delta}{2}\right] \frac{d\sigma(\pi)}{d\Omega}\right\} \left[\varepsilon(2 - \varepsilon)\right] \tag{8.7}$$

which has a maximum for $\varepsilon = 1$ given by

$$\langle i_M^2 \rangle_{max} = 2\left(\frac{\eta_Q e}{h\nu}\right)^2 \left\{\frac{4P_T P_L \bar{A}}{R^2}\, p\left[\frac{\rho(R)\, c\delta}{2}\right] \frac{d\sigma(\pi)}{d\Omega}\right\} \tag{8.8}$$

Thus, we have demonstrated that, if we constrain the sum of the transmitter and receiver areas to the value $2\bar{A}$, we obtain a maximum signal when $\varepsilon = 1$ or $A_L = A_T$, i.e., when the antenna areas are matched. To include optical and atmospheric transmission losses, Equation (8.3) should be multiplied by $\eta_A \eta_{TO}$ and Equation (8.4) by $\eta_A \eta_{RO}$ where η_A is the atmospheric transmission for the range R and η_{TO} and η_{RO} are the efficiencies of the transmitter and receiver optical systems.

It should be clear that, just as in the case of thermal source detection, any LO power falling on the mixer that cannot be backpropagated through the receiver optics to the source will contribute to the shot noise but not to the signal current and therefore represents a reduction in system signal-to-noise. Thus, vignetting, central obscurations, and phasefront errors can have a major impact on the lidar efficiency by (1) reducing the transmission of the back propagated LO and (2) influencing the antenna pattern of the backpropagated effective LO in Equation (8.2). The antenna patterns of vignetted, centrally obscured, and decollimated gaussian beams have been computed by Klein and Degnan (ref. 16).

9. COHERENT SOURCE DETECTION

For a spatially coherent source such as a laser or distant star, we can write for the mutual intensity function at the mixer

$$J_S(\vec{r}_D,\vec{r}_D') = \left[\varepsilon_S(\vec{r}_D)\ e^{i\phi_S(\vec{r}_D)}\right]\left[\varepsilon_S(\vec{r}_D')\ e^{-i\phi_S(\vec{r}_D')}\right] \tag{9.1}$$

where ε_S and ϕ_S are real functions which describe the signal amplitude distribution and phasefront in the mixer plane. A similar expression can be written for the laser LO. Substituting Equation (9.1) and the LO equivalent into our general expression for $\langle i_M^2\rangle$ given by Equation (4.9), we obtain for a coherent source

$$\langle i_M^2\rangle = 2\left(\frac{e}{h\nu}\right)^2 \left| \iint_D d\vec{r}_D\ \eta_Q(\vec{r}_D)\ \varepsilon_S(\vec{r}_D)\ \varepsilon_L(\vec{r}_D)\ e^{i\left[\phi_S(\vec{r}_D)-\phi_L(\vec{r}_D)\right]} \right|^2 \tag{9.2}$$

In the trivial case where the mixer efficiency and the signal and LO beams are uniform over the mixer of area A_D, Equation (9.2) reduces to the familiar form

$$\langle i_M^2\rangle = 2\left(\frac{\eta_Q e}{h\nu}\right)^2 P_S P_L \tag{9.3}$$

where $P_S = \varepsilon_S{}^2 A_D$. In the most general case, we can use Equation (2.8) to define a coherent heterodyne efficiency given by

$$\eta_{HET} = \frac{1}{\bar{\eta}_Q P_L P_S} \left| \iint_D d\vec{r}_D\ \eta_Q(\vec{r}_D)\ \varepsilon_S(\vec{r}_D)\ \varepsilon_L(\vec{r}_D)\ \exp\left\{i\left[\phi_S(\vec{r}_D) - \phi_L(\vec{r}_D)\right]\right\} \right|^2 \tag{9.4}$$

where P_S is the total signal power in the mixer plane. Equation (9.4) can also be written in the form

$$\eta_{HET} = \frac{\left| \iint_D d\vec{r}_D\ \eta_Q(\vec{r}_D)\ \varepsilon_S(\vec{r}_D)\ \varepsilon_L(\vec{r}_D)\ \exp\left\{i\left[\phi_S(\vec{r}_D) - \phi_L(\vec{r}_D)\right]\right\} \right|^2}{\left[\iint_D d\vec{r}_D\ \eta_Q(\vec{r}_D)\ \varepsilon_L{}^2(\vec{r}_D)\right]\left[\iint d\vec{r}_D\ \varepsilon_S{}^2(\vec{r}_D)\right]} \tag{9.5}$$

where we have used Equation (2.4) and the explicit expression for P_S. Degnan and Klein (ref. 18) have performed computations of η_{HET} for the case where the signal and LO phasefront curvatures are matched, the mixer efficiency η_Q is uniform and $\varepsilon_S(\vec{r}_D)$ is an Airy pattern formed by a centrally obscured, circular antenna illuminated by a plane wave from a distant point source. As the size of the central obscuration is increased, more incoming radiation is blocked by the obscuration and a smaller fraction of the radiation which reaches the mixer

plane is contained in the central lobe of the signal Airy pattern. Degnan and Klein (ref. 18) considered several illumination profiles for the LO including uniform, gaussian, and an Airy pattern matched to the signal Airy pattern. Their results are summarized in Figure 7. Optimum detection efficiency is achieved when the mixer captures the entire signal Airy pattern and a matched LO is used. In this instance, the receiver efficiency is simply $1 - \gamma^2$ (where γ is the obscuration ratio defined previously for the Cassegrain antenna in Figure 4) corresponding to the areal obscuration loss and represented by the "matched" LO curve in Figure 7. The difference between the ideal or "matched" LO curve and the uniform or gaussian curves corresponds to the heterodyne detection efficiency η_{HET}.

If the mixer is illuminated by a uniform LO, the optimum Airy disk radius (to the first null) is found to be $R_A \approx 1.35R_D$ where R_D is the mixer radius. It should be noted that the Airy disk radius varies with the obscuration ratio for an optical antenna having a given f-number (ref. 18). The optimum efficiency η_{HET} is approximately 83% for no obscuration and falls rapidly as the obscuration ratio is increased even if one chooses an optimum signal spot size. An optimized gaussian LO with waist radius $\omega = 0.64R_A$ and a central Airy signal disk which matches the mixer radius R_D yields greater sensitivity compared to the uniform LO since it more closely matches the intensity distribution of the central Airy disk for the signal. The power contained in the outer rings of the Airy pattern is lost, however, and this accounts for the major difference between the "ideal" matched LO and gaussian LO curves in Figure 7. For a more detailed discussion, and for more general plots of non-optimized geometries, the reader is referred to the original paper by Degnan and Klein (ref. 18).

It is a simple matter to compute the effects of misalignment between the signal and LO beams or of a mismatch between phasefront curvatures using the general expression (9.5). For example, if the two wavefronts are misaligned by an angle θ in the y_D direction illustrated in Figure 2, the exponential argument in Equation (9.5) is

$$\phi_S(\vec{r}_D) - \phi_L(\vec{r}_D) = (\vec{k}_S - \vec{k}_L) \cdot \vec{r}_D \approx k \sin\theta \, y_D$$

where $\vec{k}_S$ and $\vec{k}_L$ are the propagation vectors for the signal and LO beams, $|k_S| \approx |k_L| \approx k = 2\pi/\lambda$, and y_D is the y-component of the vector r_D. For cylindrically symmetric fields, Equation (9.5) reduces to a special case previously derived by Cohen (ref. 19); i.e.,

$$\eta_{HET} = \frac{\left[\int_0^{r_o} dr_D \, r_D \, \eta_Q(r_D) \, \varepsilon_S(r_D) \, \varepsilon_L(r_D) \, J_o(kr_D \sin\theta)\right]^2}{\left[\int_0^{r_o} dr_D \, r_D \, \eta_Q(r_D) \, \varepsilon_L^2(r_D)\right]\left[\int_0^{\infty} dr_D \, r_D \, \varepsilon_L^2(r_D)\right]} \qquad (9.6)$$

where r_o is the radius of the mixer, and we have used $y_D = r_D \cos \phi_D$ and the integral expression for the Bessel function $J_o(z)$, i.e.,

$$J_o(z) = \frac{1}{2\pi} \int_0^{2\pi} d\phi \; e^{iz \sin \phi} \tag{9.7}$$

Cohen (ref. 19) has generated plots of η_{HET} for a variety of source-LO illumination function combinations such as uniform-uniform, Airy-uniform, matched Airy-Airy, uniform-gaussian, and Airy-gaussian. He considered the tolerance of the various combinations to misalignment and allowed for a quadratically varying mixer quantum efficiency. The sensitivity to misalignment for the various combinations varied less than 15% relative to the most sensitive uniform-uniform case given by

$$\eta_{HET} = \eta_Q \left[\frac{2J_o(kr_o \sin \theta)}{kr_o \sin \theta} \right]^2 \tag{9.8}$$

Thus, $\eta_{HET} = \eta_Q$ for no misalignment and $\eta_{HET} = \eta_Q/2$ for $\theta = 0.5\lambda/(2r_o)$ corresponding to a half-wavelength phase difference over the mixer diameter $2r_o$. For a wavelength of 10 μm and a mixer diameter of 200 μm, the misalignment angle at which the detection efficiency is reduced by a factor of 2 is $\theta = 1.4^o$.

For a mismatch in phasefront curvatures, the exponential argument in Equation (9.5) is

$$\phi_S(\vec{r}_D) - \phi_L(\vec{r}_D) = \frac{kr_D^2}{2} \left(\frac{1}{C_S} - \frac{1}{C_L} \right)$$

where C_S and C_L are the curvatures of the signal and LO phasefronts at the mixer plane. For cylindrically symmetric beams, Equation (9.5) reduces to

$$\eta_{HET} = \frac{\left| \int_0^{r_o} dr_D \; r_D \; \eta_Q(r_D) \; \varepsilon_S(r_D) \; \varepsilon_L(r_D) \; \exp\left\{ \frac{ikr_D^2}{2} \left(\frac{1}{C_S} - \frac{1}{C_L} \right) \right\} \right|^2}{\left[\int_0^{r_o} dr_D \; r_D \; \varepsilon_L^2(r_D) \; \eta_Q(r_D) \right] \left[\int_0^{\infty} dr_D \; r_D \; \varepsilon_S^2(r_D) \right]} \tag{9.9}$$

For the uniform-uniform case,

$$\eta_{HET} = \eta_Q \left\{ \frac{\sin\left[\frac{kr_o^2}{4}\left(\frac{1}{C_S} - \frac{1}{C_L}\right)\right]}{\frac{kr_o^2}{4}\left(\frac{1}{C_S} - \frac{1}{C_L}\right)} \right\}^2 \tag{9.10}$$

and $\eta_{HET} = \eta_Q$ for $\Delta\left(\frac{1}{C}\right) = \left(\frac{1}{C_S} - \frac{1}{C_L}\right) = 0$ while $\eta_{HET} = 0$ for $\Delta\left(\frac{1}{C}\right) = 2\lambda/r_o^2$ where r_o is the mixer radius. Thus, if the local oscillator beam has a planar phasefront ($C_L = \infty$), the signal beam phasefront curvature must satisfy $C_S >> r_o^2/2\lambda$.

It should be noted in closing that we have arbitrarily chosen to perform the above calculations in the mixer plane. For a particular antenna or LO geometry, it may be more convenient to perform the computation in some other optical plane as noted previously in Section 5.

10. CONCLUDING REMARKS

This article has attempted to present a unified approach to the calculation of signal-to-noise ratios in optical heterodyne receivers for a variety of important applications. No attempt has been made to give an exhaustive review of the existing literature. The references cited are those which, in the author's opinion, either lend themselves particularly well to the development of the general theory of optical heterodyne receivers given here or have presented numerical results having widespread application. There are, for example, various uncited articles which present calculations of signal-to-noise for very specific incoherent source or backscatter lidar geometries. These have usually employed brute force computational methods that give little insight into the general approach for optimizing system sensitivity. While these provide excellent tests of the general theory, the articles were deemed to be too specialized to be included in the present review.

Clearly, no attention has been paid to the effects of the atmosphere on coherent wave propagation. Although the amplitude and phase fluctuations produced by the atmosphere are inherently included in the complex electric field envelopes introduced in Section 4, no attempt has been made here to give a quantitative assessment of their impact. In the approach taken here, the atmosphere can be viewed as simply another optical element through which the coherent backpropagated effective LO must pass to reach the signal source or vice versa. In the thermal source detection and backscatter lidar problem, the atmosphere presumably modifies the backpropagated effective LO intensity distribution thereby influencing the overlap integral in Equation (6.4). A number of papers in this area have appeared since the early work of Fried (ref. 5) including a rather extensive recent report by Capron et al. (ref. 20) applicable to coherent optical radar.

REFERENCES

1. T.G. Blaney, Space Science Reviews,17, 691 (1975).
2. J.H. McElroy, Applied Optics,11,1619(1972).
3. M.J. Mumma, T. Kostiuk, and D. Buhl, Optical Engineering, 17,50(1978).
4. J.H. McElroy, N. McAvoy, E.H. Johnson, J.J. Degnan, F.E. Goodwin, D.M. Henderson, T. A. Nussmeier, L.S. Stokes. B.J. Peyton, and T. Flattau, Proc. IEEE,65,221(1977).
5. D.L. Fried, Proc. IEEE,55,57(1967).
6. H. Levinstein,Applied Optics,4,639(1965).
7. T.P. McLean and E.H. Putley, RRE Journal,52,5(1965).
8. F.R. Arams, E.W. Sard, B.J. Peyton, and F.P. Pace, IEEE JQE, QE-3,11(1967).
9. R.A. Smith, Proc. IEEE,98,43(1951).
10. B.J. Rye,Applied Optics,18,1390(1979).
11. D. McGuire,Optics Letters,5,73(1980).
12. M.Born and E.Wolf, "Principles of Optics", 5th Ed., Chapt. 10 (Pergamon,New York, 1975).
13. L.Mandel and E.Wolf,Rev. Mod. Phys.,37,231(1965).
14. F.Zernike,Physika,5,791(1938).
15. A.E. Siegman,Applied Optics,5,1588(1966).
16. B.J. Klein and J.J. Degnan,Applied Optics,13,2134(1974).
17. A.E. Siegman,"An Introduction to Lasers and Masers", Chapter 8(McGraw-Hill,New York,1971).
18. J.J. Degnan and B.J. Klein,Applied Optics,13,2397(1974); Erratum,13,2762(1974).
19. S.C. Cohen,Applied Optics,14,1953(1975).
20. B.A.Capron,R.C. Harney, and J.H. Shapiro,"Turbulence Effects on the Receiver Operating Characteristics of a Heterodyne Reception Optical Radar", Project Report TsT-33,Lincoln Laboratory. Massachusetts Institute of Technology(1979).

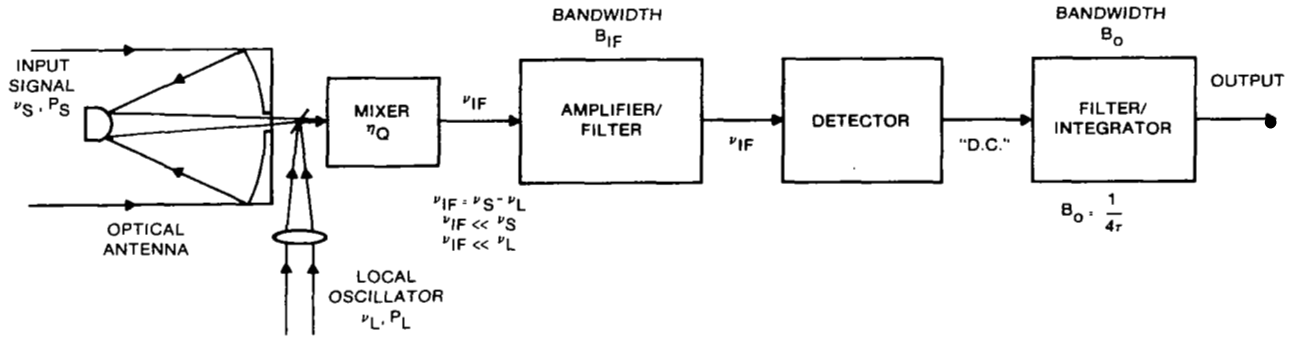

Figure 1.- Block diagram of a representative heterodyne receiver.

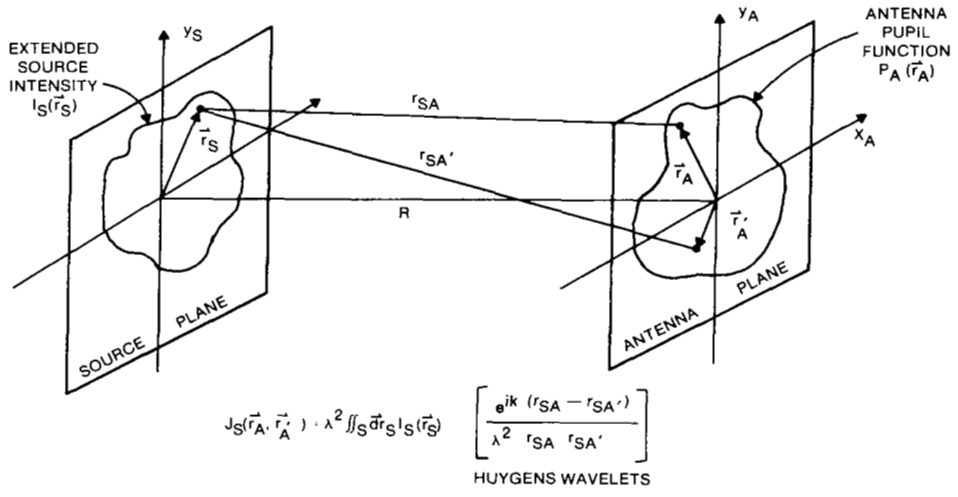

Figure 2.- Huygen's wavelet model for propagation of the mutual intensity function between the antenna and mixer plane.

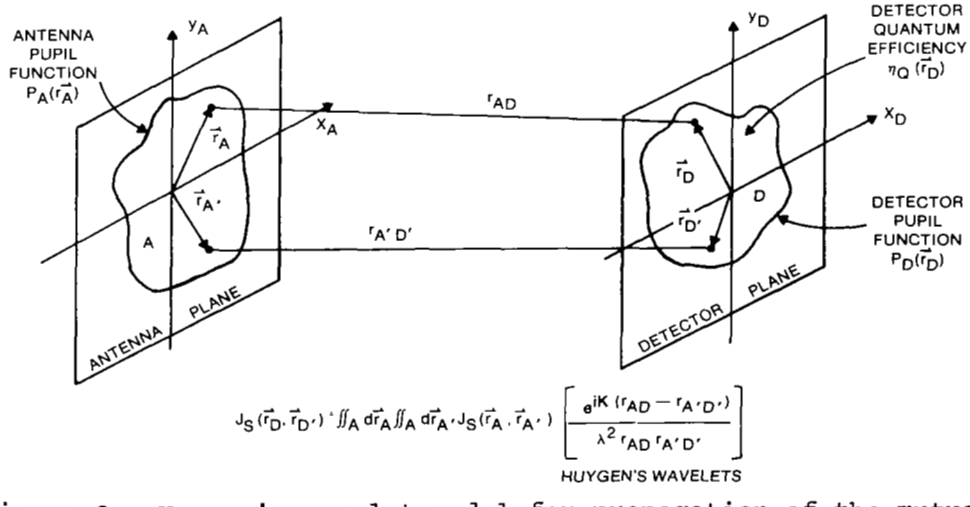

Figure 3.- Huygen's wavelet model for propagation of the mutual intensity from an extended incoherent source.

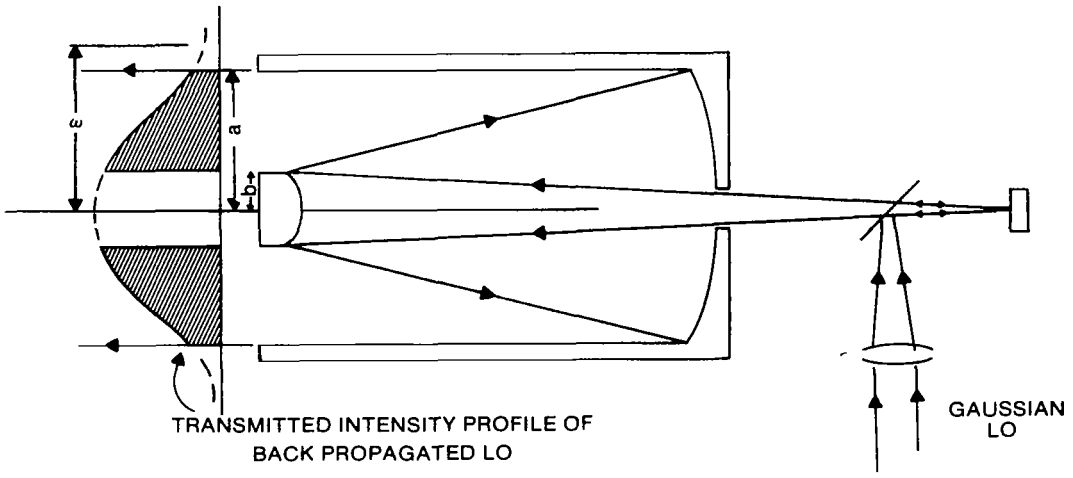

Figure 4.- Backpropagation of a gaussian local oscillator beam through a Cassegrain telescope.

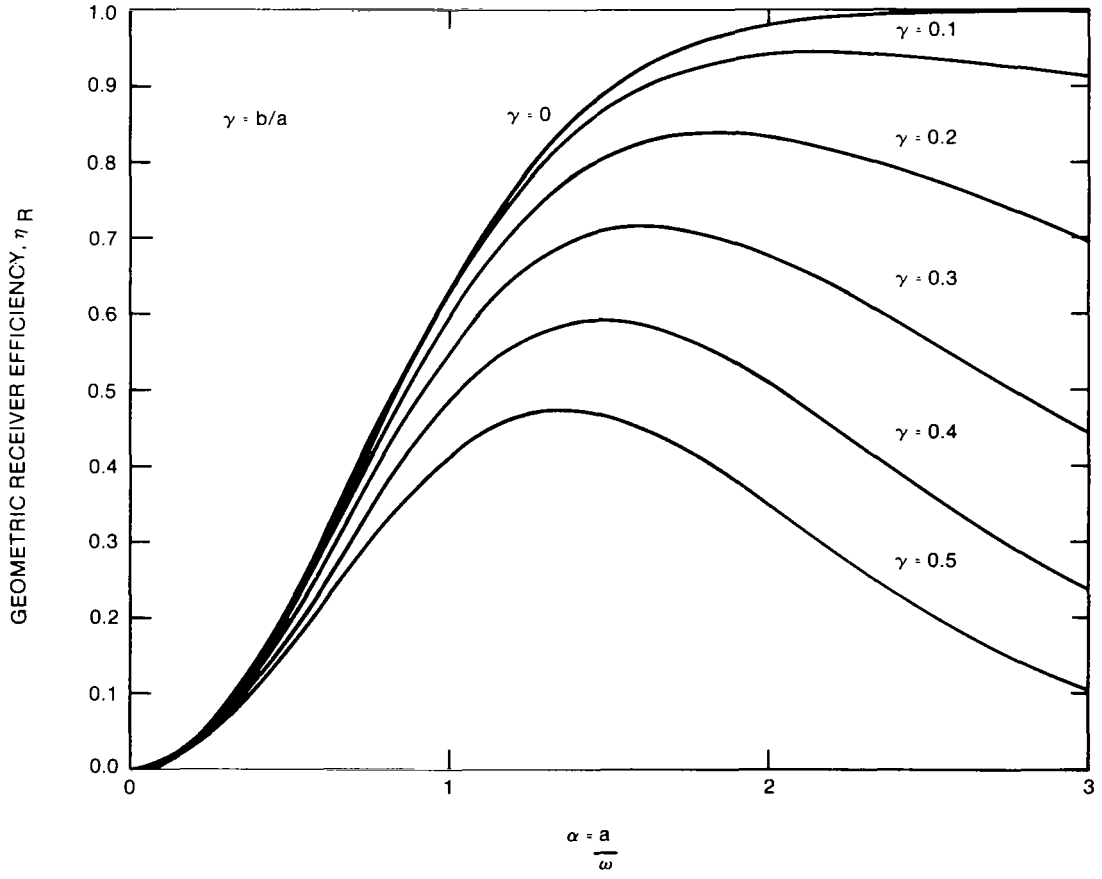

Figure 5.- Geometric receiver efficiency for a large thermal source viewed through a centrally obscured telescope by a mixer illuminated by a gaussian local oscillator beam.

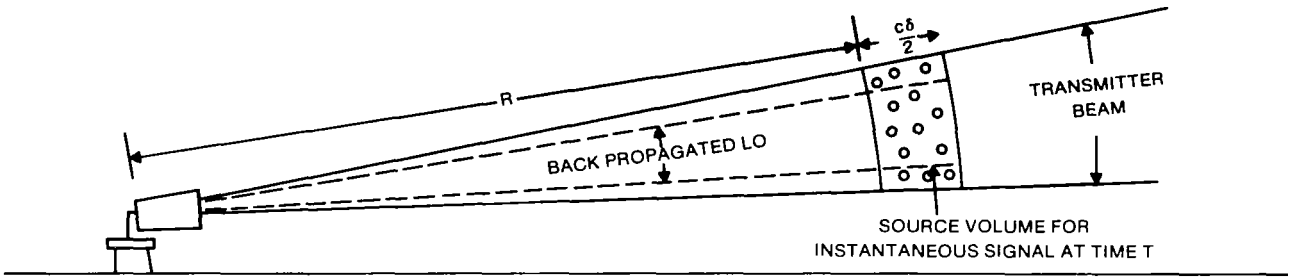

Figure 6.- Functional diagram of a heterodyne incoherent backscatter lidar system.

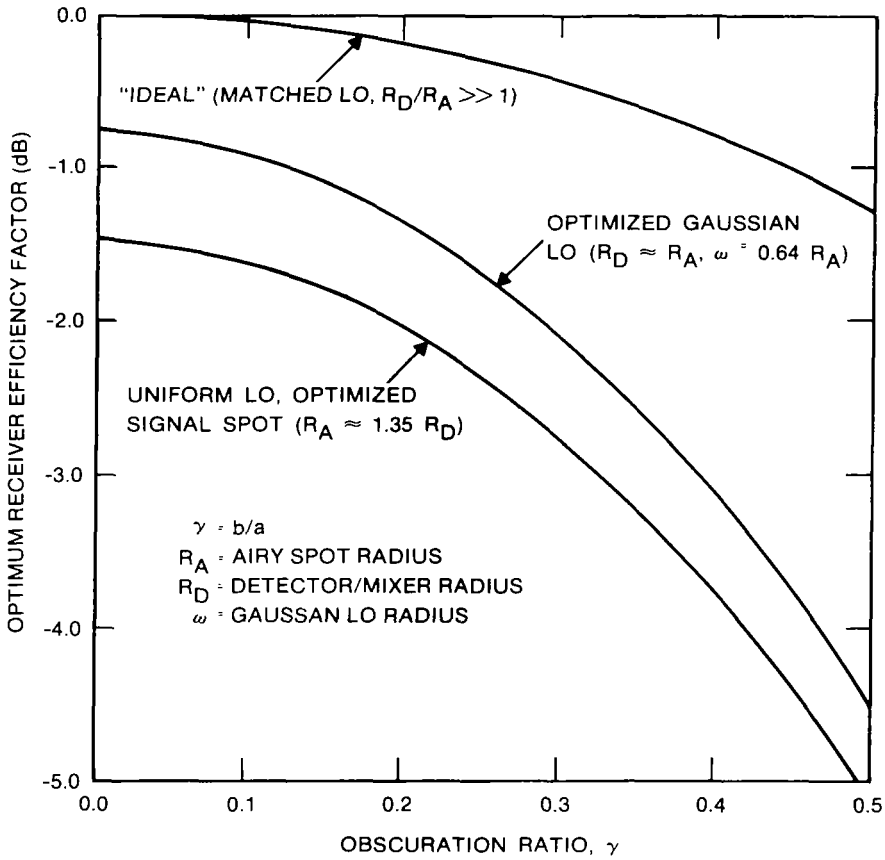

Figure 7.- Maximum receiver efficiency factors in dB for detection of a distant point source by a heterodyne receiver consisting of a general centrally obscured telescope (primary radius a, secondary radius b) as a function of linear obscuration ratio $\gamma = b/a$ and several optimized LO distributions (uniform, gaussian, and matched Airy).

MIXING EFFICIENCY IN HETERODYNE SYSTEMS

David Fink
Hughes Aircraft Company, Culver City, CA 90230

ABSTRACT

How the spatial distributions of the signal and local oscillator fields affect the heterodyne signal-to-noise ratio is examined for both a single detector and an array of detectors. For an array, the distribution of gain among the i.f. amplifiers is included. The emphasis is on understanding why the distributions are important and what is the key to maximizing the signal-to-noise ratio in any system. It is shown that for a single detector, the highest signal-to-noise ratio is obtained with an LO distribution the same as that of the signal. For an array, the product of the i.f. gain times the LO field at each detector shall have the same distribution as that of the signal field.

INTRODUCTION

The purpose of this paper is to explain how the spatial distributions of the signal and local oscillator (LO) fields affect the signal-to-noise ratio in heterodyne detection. The detailed derivations of the signal-to-noise formulae are available in References 1 and 2, but to understand the effects here, we only need the dependencies of the signal and noise photocurrents on the signal and LO field strengths over a small detector element. The time-dependent photocurrent is proportional to the power on the detector averaged over times long compared to the optical frequencies, but short compared to the difference frequency:

$$i \propto |E_s + E_\ell|^2 A \tag{1}$$

where E_s and E_ℓ are the signal and LO field strengths and A is the area of the detector. Eq. (1) can be expanded to

$$i \propto |E_s|^2 A + |E_\ell|^2 A + |E_s||E_\ell|\cos(\omega_{i.f.} t + \phi) A \tag{2}$$

where $\omega_{i.f.}$ is the angular frequency difference between the signal and LO fields and ϕ is the phase difference between the signal and LO other than that due to the exp(iωt) terms. The second term of Eq. (2) is the LO power and is the largest term; it represents the DC current. The shot noise is proportional to the square root of the number of electrons per second in the current and so is proportional to the square root of this second term:

$$i_n \propto |E_\ell| \sqrt{A} \tag{3}$$

The third term of Eq. (2) is the intermediate frequency signal current,

$$i_s \propto |E_s||E_\ell|A \tag{4}$$

With these dependencies of the signal and noise currents established, we can examine how the distributions of the signal and LO fields affect the overall signal-to-noise ratio.

THE SIGNAL-TO-NOISE RATIO

Consider the heterodyne detection situation represented by the signal and local oscillator electric field distributions of Fig. 1. As the radius of the detector is increased from 0 to A, the intermediate frequency (i.f.) signal increases. However, as the detector is increased in radius from A to B, the phase reversal of the signal causes a phase reversal in the additional i.f. signal, and the net i.f. signal decreases. Clearly, the detector should not have a radius larger than A, but should the radius even be as large as A? That part of the detector between radius A and, say, radius C collects very little signal, but it collects just as much shot noise from the local oscillator as an equal detector area nearer the center that collects a lot of signal. At some value of C, the additional signal captured by increasing the detector radius from C to A might not be worth the additional noise.

If there is such a point of diminishing returns, can we work around it and usefully capture the signal available between radii C and A? One clue is that we can work around the phase reversal of the signal at A by also reversing the phase of the LO. Then the additional i.f. signal captured between A and B will be in phase with that from 0 to A. This suggests that reducing the strength of the LO field in the C to A region might compensate for the reduction in signal field strength. Reducing the strength of the LO reduces the shot noise, but the LO field strength also multiplies the signal field strength to yield the i.f. current, so reducing it will reduce the signal by the same amount. This is just the physical reason behind the familiar result that as long as the LO is large enough that its shot noise dominates all other noises, changing the strength of the LO does not affect the signal-to-noise ratio. However, changing the strength of the LO can be used in another sense: it can be used as a weighting factor on the information in this poorer signal-to-noise region so that this information is added to that obtained from the better signal-to-noise ratio region, but not counted as heavily.

This can be made quantitative by analyzing the detector network illustrated in Fig. 2 where G_j is the gain, s_j is the signal current, and n_j is the shot noise current of the jth photomixer. Here, the individual photomixers can represent either portions of single detector or separate detectors of an array. If they represent portions of a single detector, the indicated amplifiers correspond to the LO field strength at each portion, for both the i.f. signal current and the shot noise current are proportional to the LO field strength. If the photomixers in Fig. 2 represent individual detectors, the amplifiers represent the product of the LO field strength times the actual amplification. (In either case, the amplifiers can also include a factor for any variation in

quantum efficiency.) Note that if the effect of the LO is assigned to the amplifier in the analysis, s_j is not really the signal current, but the signal current divided by the LO field strength, and n_j is the noise current divided by the LO field strength. These may be written as

$$s_j \propto |E_s| A \quad ; \quad n_j \propto \sqrt{A} \tag{5}$$

To have unique signal and LO field strengths, they must be uniform over the photomixer element. That, of course, is no problem for differential elements of a single detector, but it restricts the array analysis to small detectors. In the following, we will assume that either the phase of the LO and/or the phase of the amplifiers are set so that the signal currents add in phase.

The net power signal-to-noise ratio is given by

$$S/N = \frac{(\Sigma G_j s_j)^2}{\Sigma G_j^2 n_j^2} \tag{6}$$

Now the maximum signal-to-noise ratio may be found by adjusting the G_j. Differentiating S/N of Eq. 6 with respect to G_j and setting the derivative to zero yields

$$G_j = \frac{s_j}{n_j^2} \frac{\Sigma G_j^2 n_j^2}{\Sigma G_j s_j} \tag{7}$$

The ratio of the two sums in Eq. 7 is a constant for all the photomixers once the G_j are set, so the optimum distribution of the G_j is given by the distribution of the s_j/n_j^2. If these optimum settings for the G_j are put into the formula for the overall signal-to-noise ratio of Eq. 6, it becomes

$$S/N = \Sigma(s_j^2/n_j^2) = \Sigma(S/N)_j \tag{8}$$

That is, every additional piece of information (signal) increases the total signal-to-noise ratio no matter how poor the S/N of the additional information, if the additional information is weighted according to Eq. 7.

THE OPTIMUM LO FIELD DISTRIBUTION

It was noted above that s_j is proportional to the product of the signal field strength times the area and n_j in this analysis is not really the noise current, but the noise current divided by the LO field strength. n_j is therefore proportional to only the square root of the area, and the optimum weighting, s_j/n_j^2, is proportional to only the signal field strength at each location. For a single detector, the weighting mechanism is simply the LO field strength, so we have the result that the maximum signal-to-noise ratio is obtained by setting the LO field distribution equal to the signal field distribution. For an array of small detectors, the product of the LO field strength at each element multiplied by the gain of that element's amplifier should have the same distribution

as the signal field.

THE GENERAL SOLUTION

References 1 and 2 draw these same two conclusions for the optimum use of a single detector and an array by first deriving the signal-to-noise ratio equations for general signal and local oscillator field and amplifier distributions. For a single detector, the signal-to-noise ratio is given by

$$S/N = \frac{\eta P_S}{h\nu B} \frac{\left| \int_A |U_S||U_L| \exp(i\phi)\, dA \right|^2}{\int^{\infty} |U_S|^2 dA \int_A |U_L|^2\, dA} \tag{9}$$

where η is the quantum efficiency, P_S the total signal power available for detection, h Planck's constant, ν the optical frequency, B the i.f. bandwidth, U_S and U_L the complex field distribution functions for the signal and local oscillator (not including the $\exp(i\omega t)$ dependence), ϕ the phase difference between U_S and U_L, $\int_A$ indicates an integration over the area of the detector, and $\int^{\infty}$ indicates an integral over the whole detector plane to include all available signal power. The coefficient of $\eta P_S/h\nu B$ is called the heterodyne efficiency, γ.

The equation for an array simply replaces $|U_L|$ with $|U_L|U_j$ and ϕ with $\phi-\psi_j$, where U_j and ψ_j are the gain distribution and phase shifts of the i.f. amplifiers. The integrals over A are then over the sensitive area of the array. For both a single detector and an array, the maximum heterodyne efficiency obtainable is equal to the fraction of the signal power falling on the sensitive area of the detector.

SPECIAL CASES

Reference 1 calculates the heterodyne efficiency for two special cases with the following results:

Case I Signal and LO are matched Airy functions over a circular detector. The heterodyne efficiency is just equal to the fraction of the signal power falling on the detector:

$$\gamma = 1 - J_0^2(x) - J_1^2(x) \tag{10}$$

where J_0 and J_1 are Bessel functions, $x = \pi r/F\lambda$, where r is the radius of the detector, F the f/number of the collection optics, and λ the wavelength of the light. This heterodyne efficiency is plotted in Fig. 3. It is a monotonically increasing function of the detector size and is equal to 0.84 for a detector the same size as the Airy disk.

Case II Signal is an Airy function, LO is uniform over a circular detector. The heterodyne efficiency is given by

$$\gamma = 4\left[1 - J_0^2(x)/x^2\right] \qquad (11)$$

where the symbols are as defined for Case I. This heterodyne efficiency is also plotted in Fig. 3. Its peak is 0.72 at a radius of 72% of the radius of the Airy disk. If the detector is increased in size to match the Airy disk, the efficiency drops to 0.54.

REFERENCES

1. D. Fink, Coherent Detection Signal-to-Noise, Appl. Opt., 14, 689 (1975).

2. D. Fink and S. N. Vodopia, Coherent Detection SNR of an Array of Detectors, Appl. Opt., 15, 453 (1976).

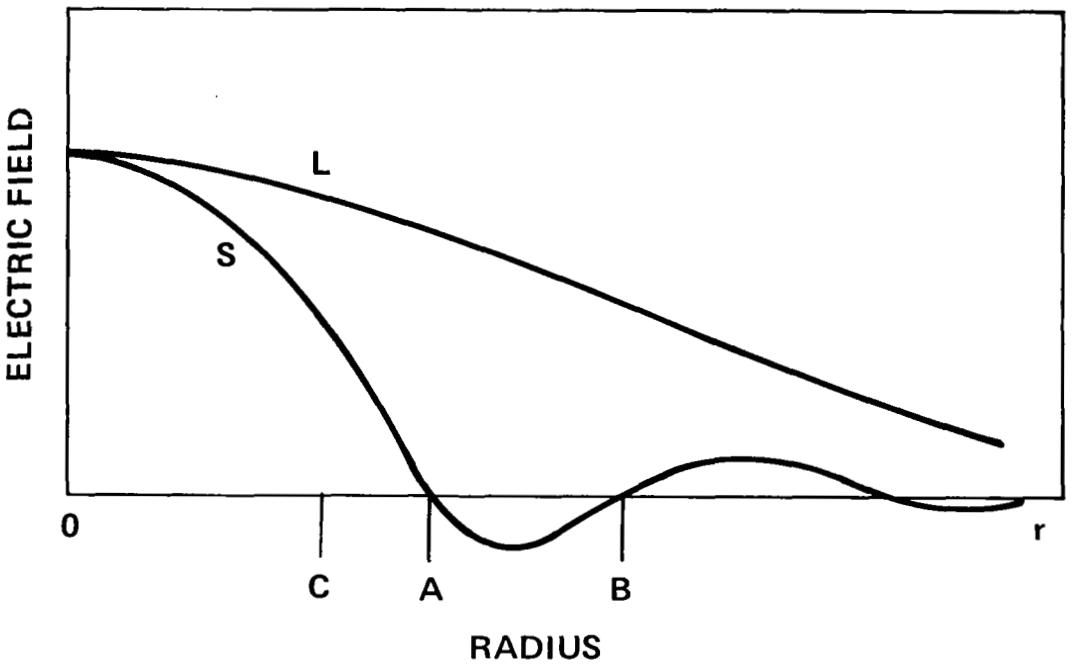

Figure 1.- Representative electric field distributions of signal (S) and local oscillator (L).

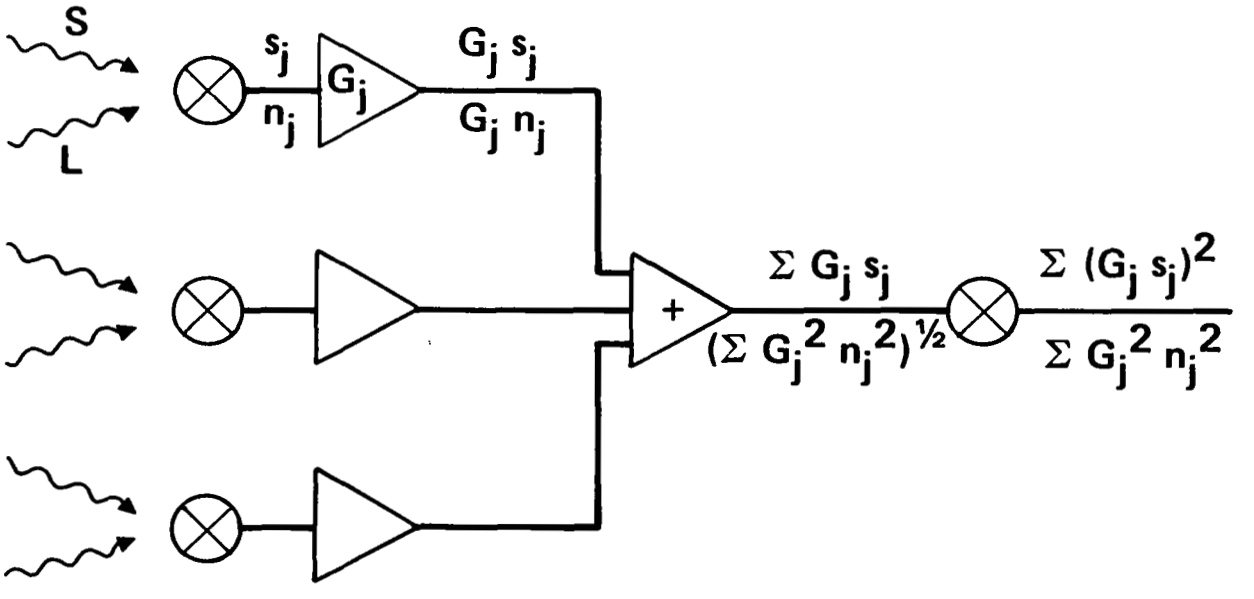

Figure 2.- Photomixing detector network.

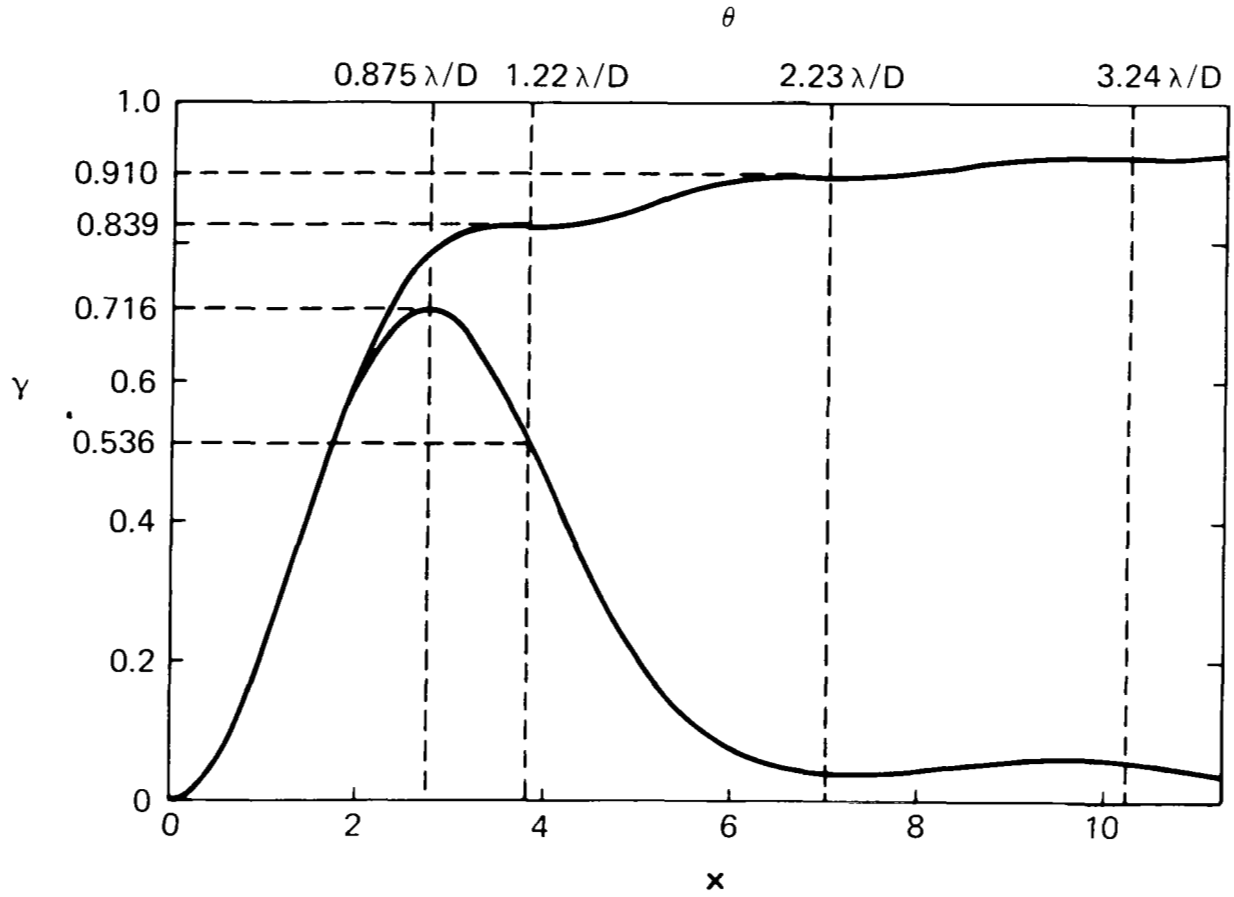

Figure 3.- Heterodyne efficiency for Airy function signal distribution on circular detector. Both curves are for circular detector of radius $r = F\lambda x/\pi$ and Airy function signal field distribution. Upper curve is for matched local oscillator field distribution on detector, which gives maximum possible signal-to-noise ratio. Lower curve is for usual case of uniform local oscillator field distribution on detector. Angular radius detedtor is indicated on upper axis for peak of lower curve (x = 2.75) and first three Airy dark rings (x = 3.83, 7.02, and 10.2).

SPATIAL FREQUENCY RESPONSE OF AN OPTICAL HETERODYNE RECEIVER

Carl L. Fales and Don M. Robinson
Langley Research Center

SUMMARY

The principles of transfer function analysis have been applied to a passive optical heterodyne receiver to obtain the modulation transfer function (MTF). MTF calculations have been performed based of an optical platform which is imaging vertically varying profiles at worst case shuttle orbit altitudes. An analysis of the derogatory effects of sampling (aliasing) and central obscurations on both resolution and heterodyne efficiency is given.

INTRODUCTION

One measure of performance of an optical imaging system is its ability to reproduce an object distribution with sufficient signal-to-noise ratio and resolution so as to make the information contained within the image useful. Generally, such a system may be characterized by its optical transfer function (OTF) or, in certain cases, by the modulation transfer function (MTF) (ref. 1).

For conventional imaging systems using either coherent or incoherent illumination, one usually assumes linearity in the imaging process so that the cascading property of transfer function analysis applies (ref. 2). Under this assumption, the MTF's of the individual subsystems (i.e., optics, detector, electronics, etc.) can be multiplied to give the overall transfer function.

In this paper, the principles of transfer function analysis have been applied to a passive optical heterodyne receiver which is assumed to be imaging vertically varying spatial profiles at worst-case shuttle orbit altitudes. Results of the analysis show some interesting departures from the properties described above; namely, that the cascading property must be carefully applied and that optical receivers having obscurations, such as a Cassegrains, are not optimum for heterodyne-type detection.

THEORETICAL ANALYSIS

Imaging Considerations

Consider an optical receiver which is imaging an object amplitude distribution as shown in figure 1. Using scalar diffraction theory, the signal amplitude, E_s, in the detector plane, $\underline{r}$, is given by (ref. 3)

$$E_s(\underline{r}) = E_g(\underline{r}) \circledast h(\underline{r}) = \int_{-\infty}^{+\infty} d^2s\, E_g(\underline{s})h(\underline{r} - \underline{s}) \tag{1}$$

where $h(\underline{r})$ is the impulse response of the imaging optics and $E_g(\underline{r})$ is the amplitude of the geometrical image of the object. The shift invariance of $h(\underline{r})$ can be justified for the heterodyne applications discussed here by a careful examination of the various phase factors appearing in the impulse response function.

For mixing of two deterministic optical beams in an ideal detector, the mean-square heterodyne current power at the difference frequency, $f = |\nu - \nu_o|$ is (ref. 4)

$$I_{het}^2 = \frac{2\eta^2 e^2}{(h\nu)^2} \left| \int_{det} d^2r\, E_o^*(\underline{r})\, E_s(\underline{r}) \right|^2 \tag{2}$$

where $E_o(\underline{r})$ is the local oscillator amplitude distribution in the detector plane, η is the quantum efficiency, e is the electronic charge, and $h\nu$ is the photon energy. A simple-minded classical approach is taken to obtain the correct expression from which the spatial frequency analysis may begin. We recognize that the geometrical image field, $E_g(s,\nu)$, is a stochastic process which we synthesize by discrete frequency components with random phases. Now, for a deterministic L.O. field and a quasi-monochromatic optical signal, equation (1) and the generalization of equation (2) combine to give

$$I_{het}^2 = \frac{2\eta^2 e^2}{(h\nu)^2} \sum_f \int_{-\infty}^{+\infty} d^2s d^2s' \langle E_g(\underline{s}, f+\nu_o) E_g^*(\underline{s}', f+\nu_o) \rangle \left[\int_{det} dr^2 E_o^*(\underline{r}) h(\underline{r}-\underline{s}) \right]$$

$$\left[\int_{det} d^2r' E_o(\underline{r}') h^*(r'-s') \right] \tag{3}$$

where $\langle\ \rangle$ represents an average over the ensemble of signal fields. It is assumed that the source, i.e., the sun, of the image field on the detector is spatially incoherent. The appropriate substitutions are

$$\langle E_g(\underline{s}, \nu) E_g^*(\underline{s}', \nu) \rangle \rightarrow \Delta f\, \lambda^2 P_g(\underline{s}, \nu) \delta(\underline{s} - \underline{s}')$$

$$I_{het}^2 \rightarrow I_{het}^2(f)\Delta f$$

where P_g represents the image spectral radiance at the detector plane in $W/m^2/str/Hz$ and $I_{het}^2(f)$ is the current spectral power density in A^2/Hz.

Equation (3) becomes

$$I_{het}^2(f) = \frac{2\eta^2 e^2 \lambda^2}{(h\nu)^2} \int_{-\infty}^{+\infty} d^2s [P_g(\underline{s}, \nu_o + f) + P_g(\underline{s}, \nu_o - f)] \left| T_o^*(\underline{s}) \circledast h(-\underline{s}) \right|^2$$

where $f \geq 0$ and we note that the L.O. mixes with the signal field components at $\nu_o + f$ and $\nu_o - f$. Here, we have expressed the detector overlap integral of the L.O. field and the impulse response function as

$$\int_{-\infty}^{+\infty} T_{det}(\underline{r}) E_o^*(\underline{r}) h(\underline{r} - \underline{s}) d^2r = T_o^*(\underline{s}) \circledast h(-\underline{s})$$

where $T_{det}(\underline{r})$ is the aperture function of the detector geometry and the product $T_{det}(\underline{r}) E_o^*(\underline{r}) = T_o^*(\underline{r})$ is simply that portion of the L.O. that is transmitted by the detector aperture.

Referring to the detector scheme of figure 2, the output current from the synchronous detector is

$$I_{sync} = \frac{2Te^2\eta^2\lambda^2}{(h\nu)^2} \int_{-\infty}^{+\infty} d^2s \int_{(f>0)} df \left| H_{het}(f) \right|^2 [P_g(\underline{s}, \nu_o + f) + P_g(\underline{s}, \nu_o - f)] \left| T_o^*(\underline{s}) \circledast h(-\underline{s}) \right|^2$$

where H_{het} is the total heterodyne transfer function defined by

$$\left| H_{het}(f) \right|^2 = \left| H_m \right|^2 \left| H_d \right|^2 \left| H_{ifa} \right|^2$$

and T is the optical transmission factor. The various contributions to H_{het} are (1) the signal/L.O. mixing transfer function, H_m, representing carrier diffusion and transit time effects in the detector; (2) the photodetector transfer function, H_d, comprised of contributions due to capacitance, resistance and inductance; and (3) the I.F. amplifier and filter transfer function, H_{ifa}. The square-law detector is assumed to have a unity transfer function ($H_{sq} = 1$). The shot noise transfer function, H_{tr}, is due only to transit time effects as opposed to H_m.

Heterodyne Transfer Function

In this paper, we are interested in the spatial frequency response of the heterodyne receiver to a vertically varying object profile as shown in figure 1. This is different from the I.F. considerations discussed previously other than a knowledge of the total I.F. power. To obtain the spatial frequency response and, ultimately, the system modulation transfer function (MTF), we assume the object scene radiance (and, consequently, the image scene) is linearly translated due to motion of the optical receiver, e.g., an orbiting platform. This induces a translation of the image coordinates by an amount

$$\underline{s} \rightarrow \underline{s} - \underline{r}(t)$$

and

$$P_g(\underline{s}, \nu_o \pm f) \rightarrow P_g(\underline{s} - \underline{r}, \nu_o \pm f)$$

Further, we define

$$P_g(-\underline{r}) \equiv \int_{(f>0)} df \left|H_{het}(f)\right|^2 [P_g(\underline{r}, \nu_o + f) + P_g(\underline{r}, \nu_o - f)]$$

Since the impulse response, h, is invariant, we have the output current from the synchronous detector as

$$I_{sync}(t) = I_{sync}[\underline{r}(t)] = \frac{2Te^2\eta^2\lambda^2}{(h\nu)^2} \int_{-\infty}^{+\infty} d^2s \; P_g(\underline{r} - \underline{s}) \left|T_o^*(\underline{s}) \circledast h(-\underline{s})\right|^2 \qquad (4)$$

Equation (4) is of the form of a convolution

$$I_{sync}[r(t)] = \frac{2Te^2\eta^2\lambda^2}{(h\nu)^2} P_g(\underline{r}) \circledast \left|T_o^*(\underline{r}) \circledast h(-\underline{r})\right|^2$$

Decomposition of I_{sync} into its spatial frequency components is obtained by the Fourier transformation

$$\hat{I}_{sync}(\underline{K}) = \int_{-\infty}^{\infty} e^{-i2\pi \underline{K}\cdot\underline{r}} I_{sync}(\underline{r}) d^2r$$

Using the convolution theorem, we have

$$\hat{I}_{sync}(\underline{K}) = \frac{2Te^2\eta^2\lambda^2}{(h\nu)^2} G_g(\underline{K}) [G_o^*(-\underline{K})H(-\underline{K}) \circledast G_o(\underline{K})H^*(\underline{K})] \quad (5)$$

where $\underline{K}$ is the spatial frequency vector variable defined by its rectangular components (K_x, K_y), $G_g(\underline{K})$ is the object, or more specifically, the geometrical image spectrum, $G_o(\underline{K})$ is the detector pupil function modulated L.O. spectrum, and $H(\underline{K})$ is the coherent transfer function of the system (ref. 3).

Equation (5) illustrates the departure of the transfer function obtained in a heterodyne system with that obtained in conventional imaging systems. Remembering that the coherent transfer function, $H(\underline{K})$, is equal to the pupil function of the optical receiver (with a suitable change in variables) (ref. 3), the conventional optical transfer function is proportional to

$$G_{det}(\underline{K}) [H(-\underline{K}) \circledast H^*(\underline{K})]$$

where $G_{det}(\underline{K})$ is the Fourier transform of the detector aperture function, $T_{det}(\underline{K})$. In equation (5), however, we see that $H(\underline{K})$ is modified by the spectrum of the L.O./detector combination, $G_o(K)$. The normalized convolution of the product $G_o(\underline{K})H^*(\underline{K})$ with its negative argument complex conjugate is defined as the heterodyne transfer function, G_H. Functionally, then, we define a normalized heterodyne transfer function by

$$G_H(\underline{K}) \equiv \frac{G_o^*(-\underline{K})H(-\underline{K}) \circledast G_o(\underline{K})H^*(\underline{K})}{[G_o^*(-\underline{K})H(-\underline{K}) \circledast G_o(\underline{K})H^*(\underline{K})]_{\underline{K}=0}} \quad (6)$$

or

$$G_H(\underline{K}) = \frac{\int d^2K' G_o(\underline{K}')H^*(\underline{K}')G_o^*(\underline{K}'-\underline{K})H(\underline{K}'-\underline{K})}{\int d^2K' |G_o(\underline{K}')|^2 |H(\underline{K}')|^2}$$

Heterodyne Efficiency Factor

The denominator of equation (6) indicates that the product $G_o(\underline{K})H(\underline{K})$ represents the optics/L.O. detector amplitude spectrum that is transferred to the detector. Using Parseval's theorem, the integral $\int d^2K |G_o(\underline{K})|^2 |H(\underline{K})|^2$ is thus the power available for heterodyning out of a total L.O.-detector power of $P_o = \int d^2K |G_o(\underline{K})|^2$. For a uniform extended source, we may thus define an efficiency factor

$$\chi \equiv \frac{\int d^2K |G_o(\underline{K})|^2 |H(\underline{K})|^2}{\int d^2K |G_o(\underline{K})|^2} \leq 1 \tag{7}$$

With this definition, the current spectrum for the synchronous detector (equation (5)) becomes

$$\hat{I}_{sync}(\underline{K}) = \frac{2Te^2\eta^2\lambda^2}{(h\nu)^2} P_o \chi G_H(\underline{K}) G_g(\underline{K}) \tag{8}$$

Equation (8) may be related to a more conventional form of heterodyne efficiency found in the literature (ref. 5). The synchronous detector current is the inverse Fourier transform of equation (8), i.e.,

$$I_{sync}(\underline{r}) = \int_{-\infty}^{+\infty} d^2K \, \hat{I}_{sync}(\underline{K}) \, e^{i2\pi \underline{K}\cdot\underline{r}}$$

For a stationary scene, i.e., before translation of the image coordinates, we have $\underline{r} = 0$ so that

$$I_{sync}(0) = \int_{-\infty}^{+\infty} \hat{I}_{sync}(\underline{K}) \, d^2K \tag{9}$$

Substitution of equation (8) into equation (9) and assuming a blackbody source of geometrical shape factor, $A_g(\underline{r})$, and radiance $P_g(\underline{r})$, we have

$$P_g(\underline{r}) = \frac{2h\nu \, B_{HIF}}{\lambda^2 (e^{h\nu/KT} - 1)} A_g(\underline{r})$$

and

$$I_{sync}(\underline{r} = 0) = \frac{4Te^2\eta^2 P_o B_{HIF}}{h\nu(e^{h\nu/KT} - 1)} \chi \int_{-\infty}^{+\infty} d^2K \, \hat{A}_g(\underline{K}) G_H(\underline{K}) \tag{10}$$

where mixing occurs over an effective bandwidth $2B_{HIF}$ centered at the L.O. frequency, a polarization loss factor of 0.5 is included, and $\hat{A}_g(\underline{K})$ is the Fourier transform of $A_g(\underline{r})$. The integral portion of equation (10) has the form of a throughput, i.e., that portion of the image passed by the heterodyne

transfer function. The product of χ and this integral is an efficiency

$$\chi_{het} \equiv \chi \int_{-\infty}^{+\infty} d^2K \, \hat{A}_g(\underline{K}) G_H(\underline{K}) \tag{11}$$

so that equation (10) becomes

$$I_{sync}(r = 0) = \frac{4Te^2\eta^2 P_o B_{HIF} \chi_{het}}{h\nu(e^{h\nu/KT} - 1)}$$

If now, we define a shot noise level due to the L.O. by

$$N = \frac{2\eta e^2}{(h\nu)} P_o B_{SIF}$$

then the signal-to-noise ratio in the shot noise limit becomes

$$\frac{S}{N} = \frac{I_{sync}(r = 0)}{N} = \frac{2T}{(e^{h\nu/KT} - 1)} \eta_{het} \cdot \frac{B_{HIF}}{B_{SIF}}$$

where we have defined

$$\eta_{het} \equiv \eta \, \chi_{het} \leq \eta$$

as the heterodyne quantum efficiency and B_{SIF} is the effective shot noise bandwidth. Note that for a uniform extended source, $A_g(\underline{K}) = \delta(\underline{K})$ and equation (11) reduces to $\chi_{het} = \chi$ and $\eta_{het} = \eta\chi$. In this case, the efficiency factor, χ, which we have defined in equation (7) is equivalent (to within the D.C. quantum efficiency, η) to the heterodyne quantum efficiency, η_{het}, found in the literature (ref. 5).

System Transfer Function

Results from the previous section may now be used to calculate the system transfer function, including the low-pass filter (see figure 2), for the specific case of imaging a one-dimensional object through an optical receiver which has rectangular symmetry. This case has some physical significance since the resolution elements of interest in an orbiting heterodyne receiver are vertically varying stratospheric layers. In addition, to avoid scaling difficulties in the calculations we will use angular coordinates defined by (see figure 1)

$$\theta = \frac{X}{d_i} \; ; \; \phi = \frac{Y}{d_i} \quad \text{(radians)}$$

$$K_\theta = K_X d_i \; ; \; K_\phi = K_Y d_i \quad \text{(cycles/radian)} \tag{12}$$

and

$$\theta_F = \frac{\ell_X}{d_i} \quad \text{(radians)}$$

where θ_F is the geometrical instantaneous field of view (I.F.O.V.) of the optical receiver.

Using equations (12) and the one-dimensional geometry, equation (6) becomes

$$G_H(K_\theta;K_c,\theta_F) = \frac{[\mathrm{sinc}(\theta_F K_\theta)\,\mathrm{RECT}(\frac{K_\theta}{2K_c})] \circledast [\mathrm{sinc}(\theta_F K_\theta)\,\mathrm{RECT}(\frac{K_\theta}{2K_c})]}{\{[\mathrm{sinc}(\theta_F K_\theta)\,\mathrm{RECT}(\frac{K_\theta}{2K_c})] \circledast [\mathrm{sinc}(\theta_F K_\theta)\,\mathrm{RECT}(\frac{K_\theta}{2K_c})]\}_{K_\theta=0}} \tag{13}$$

where

$$\mathrm{sinc}(X) \equiv \frac{\sin \pi X}{\pi X} \quad \text{and} \quad \mathrm{RECT}(\frac{X}{2\ell}) \equiv \begin{cases} 1 \; , & |X| \leq \ell \\ 0 \; , & |X| > \ell \end{cases}$$

Equation (13) assumes a plane wave local oscillator incident of the detector so that the detector/L.O. transfer function becomes simply the Fourier transform of the detector aperture. Further, the coherent transfer function for the optics is the pupil function (rectangular in shape) having a coherent cut-off frequency of $K_c = D_A/2\lambda$, where D_A is the diameter of the receiver aperture and λ the wavelength. This convolution process is shown in figure 3.

Equation (13) along with equation (8) gives the system transfer function up to the low-pass filter. Expressing $G_H(K_\theta;K_c,\theta_F)$ and $\chi(K_c,\theta_F)$ (equation (7)) in integral form, we have

$$G_H(K_\theta;K_c,\theta_F) = \frac{\int_{-\infty}^{+\infty} \mathrm{sinc}(\theta_F K'_\theta)\,\mathrm{RECT}(\frac{K'_\theta}{2K_c})\,\mathrm{sinc}[\theta_P(K'_\theta-K_\theta)]\,\mathrm{RECT}(\frac{K'_\theta-K_\theta}{2K_c})\,dK'_o}{\int_{-\infty}^{+\infty} \mathrm{sinc}^2(\theta_F K_\theta)\,\mathrm{RECT}(\frac{K_\theta}{2K_c})\,dK_o} \tag{14}$$

and

$$\chi(K_\theta,\theta_P) = \theta_P^2\left[\int_{-\infty}^{+\infty} \mathrm{sinc}^2(\theta_F K_\theta)\,\mathrm{RECT}\left(\frac{K_\theta}{2K_c}\right)dK_\theta\right]^2 \tag{15}$$

Finally, inclusion of the low-pass filter transfer function, H_{LP}, (i.e., the integration time, τ) which, in this case is modeled as a running mean integrator, we have

$$H_{LP}(K_\theta) = \mathrm{sinc}\left(\frac{v_o \tau}{Z} K_\theta\right)$$

where v_o is the vertical component of the orbital velocity, z the receiver-object distance, and τ the integration time. The total transfer function is then the modulation transfer function

$$MTF(K_\theta) = \left|G_H(K_\theta)H_{LP}(K_\theta)\right|$$

Equations (14) and (15) can be evaluated in terms of tabulated functions yielding the following relations which will be used for computational purposes

$$MTF\left(K_\theta;\theta_F,K_c,\frac{v_o\tau}{Z}\right) = (N)\,\mathrm{RECT}\left(\frac{K_\theta}{4K_c}\right)\left|\mathrm{sinc}\left(\frac{v_o\tau}{Z}K_\theta\right)\right\{\left(\frac{\cos(\pi\theta_F K_\theta)}{\pi\theta_F K_\theta}\right) X$$

$$\left[C_{in}\left(\left|2\pi\theta_F K_\theta - 2\pi\theta_F K_c\right|\right) - C_{in}(2\pi\theta_F K_c)\right] +$$

$$\left.\left(\frac{\sin(\pi\theta_F K_\theta)}{\pi\theta_F K_\theta}\right)\left[s_i(2\pi\theta_F K_c\left|\right. - s_i(2\pi\theta_F K_\theta - 2\pi\theta_F K_c)\right]\right\}\right| \tag{16}$$

$$\chi(\theta_F,K_c) = \frac{4}{\pi^2}\left[s_i(2\pi\theta_F K_c) - \frac{1-\cos(2\pi\theta_F K_c)}{2\pi\theta_F K_c}\right]^2 \quad \text{and} \quad N = (\pi\chi^{1/2})^{-1}$$

In the above equations, the functions $C_{in}(X)$ and $s_i(X)$ are defined as (ref. 6)

$$s_i(X) = \int_o^X \frac{\sin t}{t}\,dt \quad \text{and} \quad C_{in}(X) = \int_o^X \frac{1-\cos t}{t}\,dt$$

RESULTS AND DISCUSSION

MTF Calculations

Equations (16) and (17) may now be evaluated for some specific parameter values which are applicable to the optical receiver in a space-lab type of scenario. A worst-case set of orbital values would be for the receiver platform to be at an orbital height of $R = 400$ Km and a tangent height, H_T, of 10 Km. At these values, we assume that the receiver is operating in a solar occultation mode where the sunrise or sunset velocity due to orbital motion is $v_o = 2$ Km/sec. The MTF and χ calculations (equations (16) and (17)) will be done for an I.F.O.V. of $\theta_F = 0.5 \times 10^{-3}$ rad , an equivalent optical receiver aperture of $D_A = 2.0"$, and values of integration time of $\tau = 0.2$ sec , and 0.4 sec. Further, the value of $D_A = 2.0"$ at a wavelength of $\lambda = 11.152$ μm (HNO_3 line) corresponds to an optics cut-off frequency of $K_c = D_A/2\lambda = 2278$ cycles/radian. These parameters are compatible with the values for an LHS type experiment using a tunable diode laser as the L.O. and associated optics for coupling this type radiation to a detector having the required time-frequency response (ref. 7).

The calculations are shown in figure 4. It can be shown that, for values of τ greater than roughly 0.2 sec., the optical (heterodyne) transfer function dominates the MTF; and, for τ somewhat less than 0.4 sec., the low pass filter is the dominant frequency limiting factor. Note that the angular frequency values can be converted to linear spatial frequency (cycles/Km) by the relationships of equation (12) by appropriately scaling image and object space by the ratio of image distance, d_i, to object distance, z. For the orbital values assumed, z = 2262 Km and consequently a value of 2262 cycles/rad corresponds to an object spatial frequency of 1 cycle/Km. Examination of the MTF curves shows that resolutions of the order of 1.5-2.0 Km may be expected for the various integration times.

Efficiency Calculations

The efficiency factor (heterodyne efficiency) given by equation (17) is shown plotted in figure 5 for the case of the plane-wave L.O.. Two geometries are shown: rectangular optics (as has been previously assumed) and circular optics adjusted for equal optics and detector areas. The significance of the abscissa ($2\pi\theta_F K_c$) relative to heterodyne efficiency becomes apparent when it is noted that at the value of $2\pi\theta_F K_c \cong 7.7$ corresponds approximately to an image (sun) size filling the detector of one Airy Disk of the receiver aperture. In this region, the efficiency is in excess of 80%.

Sampling Error

The calculations shown plotted in figure 5 do not include any sampling errors which may occur. Suppose we sample the output of the low-pass filter, which has been modeled as a running mean integrator, at a rate of the inverse of the integration time. This is equivalent to a sampled mean integration scheme. Under this constraint, it may be shown that for certain values of τ the signal is undersampled. This results in an aliasing or foldover error which can be significant relative to the desired signal. For example, shown in figure 6 is the total MTF for the values of orbital and system parameters previously stated. Two integration times are considered: $\tau = 0.2$ sec and $\tau = 0.4$ sec. If we define the sampling error as the ratio of the "foldover" amplitude on the MTF plot to the amplitude of the MTF itself, i.e., a white signal spectrum, we see that the error for 0.4 sec. is approximately 40% at 0.5 cycle/Km frequency and considerably worse for higher values of spatial frequency. Conversely, for $\tau = 0.2$ sec and the correspondingly higher sampling rate, the sampling error is negligible.

Heterodyne Receivers With Obscurations

Telescopes having central obscurations such as Cassegrains are often used for imaging a source. If this type receiver is used as a collector for heterodyne-type detection, one needs to compare the efficiency, χ, and the heterodyne transfer function, G_H, with that obtained for the unobscured case.

In figure 7, we consider the effects of receiver apertures having obscuration ratios of 0 and 20% for $\theta_F = 0.2 \times 10^{-3}$ and 0.5×10^{-3} rad. Note the enhancement of response in the 2000 cycles/rad region at the expense of that near 1000 cycles/rad for 20% obscuration and $\theta_F = 0.5 \times 10^{-3}$ rad. The effects of obscurations are more pronounced for square as opposed to circular geometries. An unobscured conventional MTF discussed earlier is plotted for $\theta_F = 0.5 \times 10^{-3}$ rad showing a somewhat reduced frequency response characteristic from the heterodyne MTF. For a smaller detector ($\theta_F = 0.2 \times 10^{-3}$ rad), a 20% obscuration tends to assume the shape of a conventional MTF.

In figure 5, we assume a receiver aperture having obscuration ratios of 20% and 50%. For the values of θ_F and K_c used earlier, $X = 2\pi\theta_F K_c \cong 7.2$, and comparison of the various efficiency curves at this value shows striking differences. For the 50% case, one sees that the heterodyne efficiency is virtually zero while for the 20% case a relative efficiency of slightly greater than 0.2 is achieved. This compares with a value of greater than 0.8 in the unobscured case. Note further there is a "peaking" of the efficiency curves for obscured systems. The rule-of-thumb requirement of one Airy disk on the detector for "good" efficiency no longer holds but rather the source image needs to be less than this value to achieve the maximum efficiency for that particular system. The effect can be explained on the basis of the overlap integral (equation (2)) of the L.O. field and signal field

distributions. Thus, the diffracted field due to the central obscuration is out of phase with that of the primary diffracted field and, as the size of the detector and/or optics increases, the cancellation tends to be more complete.

CONCLUDING REMARKS

The analysis of a passive heterodyne receiver with respect to its imaging performance (transfer function) and its heterodyne efficiency shows some interesting departures from the results which are obtained in strictly coherent or incoherent imaging systems. For example, the cascading property of MTF analysis must be carefully applied since the coherent transfer function of the optical receiver and that due to the L.O.-detector combination are not separable but are related by the convolution of their products. Application of these results to the specific case of a space-lab type optical heterodyne receiver (LHS) shows that resolutions of the order of 1.5-2.0 Km are possible for worst-case type orbital scenarios.

Further, comparison of obscured-type receivers (e.g., Cassegrains) with unobscured receivers shows that both resolution and efficiency are severely degraded in an obscured-type receiver and consequently should not be used for a passive heterodyne detection scheme.

REFERENCES

1. Smith, F. Dow: Optical Image Evaluation and the Transfer Function. Applied Optics, vol. 2, no. 4, April 1963, pp. 335-350.

2. Wolf, William L.; Zissis, George J.; Editors: The Infra-Red Handbook. U.S. Government Printing Office, Washington, D.C., 1978.

3. Goodman, J. W.: Introduction to Fourier Optics. McGraw-Hill, New York, 1968.

4. Yura, H. T.: Optical Heterodyne Signal Power Obtained from Finite Sized Sources of Radiation. Applied Optics, vol. 13, no. 1, Jan. 1974, pp. 150-157.

5. Siegman, A. E.: The Antenna Properties of Optical Heterodyne Receivers. Proc. IEEE, vol. 54, no. 10, Oct. 1966, pp. 1350-1356.

6. Abramowitz, M.; Stegun, I.; Editors: Handbook of Mathematical Functions. National Bureau of Standards Applied Mathematics Series, vol. 55, June 1964, p. 231.

7. Allario, Frank; Katzberg, Stephen J.; Larsen, Jack C.: Sensitivity Studies and Laboratory Measurements for the Laser Heterodyne Spectrometer Experiment. Heterodyne Systems and Technology, NASA CP-2138, 1980. (Paper 17 of this compilation.)

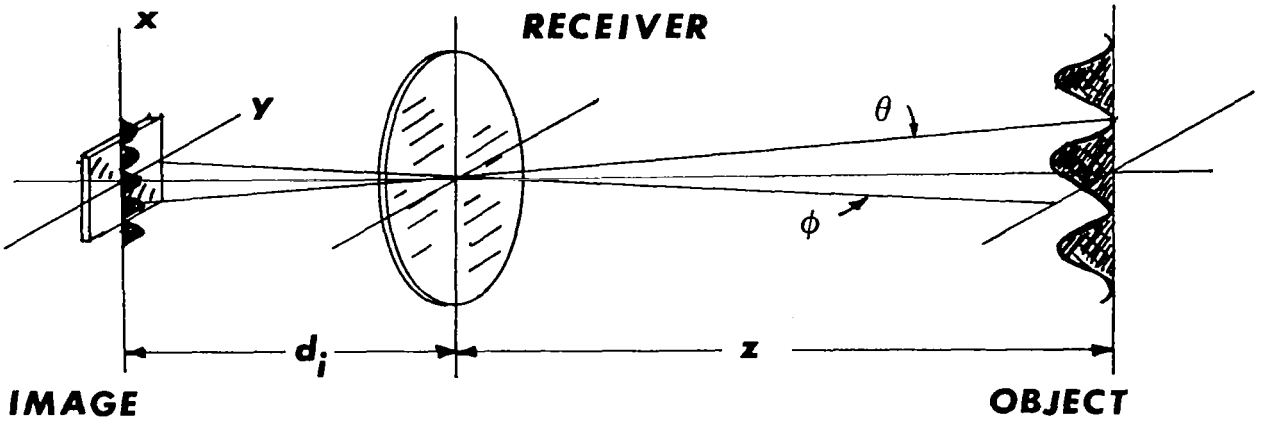

Figure 1.- Imaging geometry.

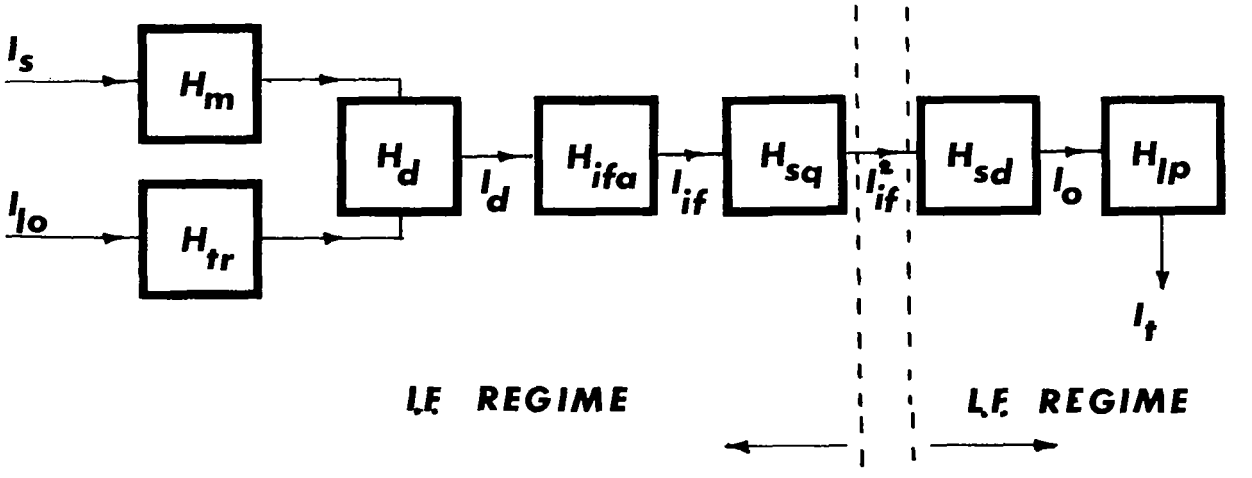

Figure 2.- System transfer functions.

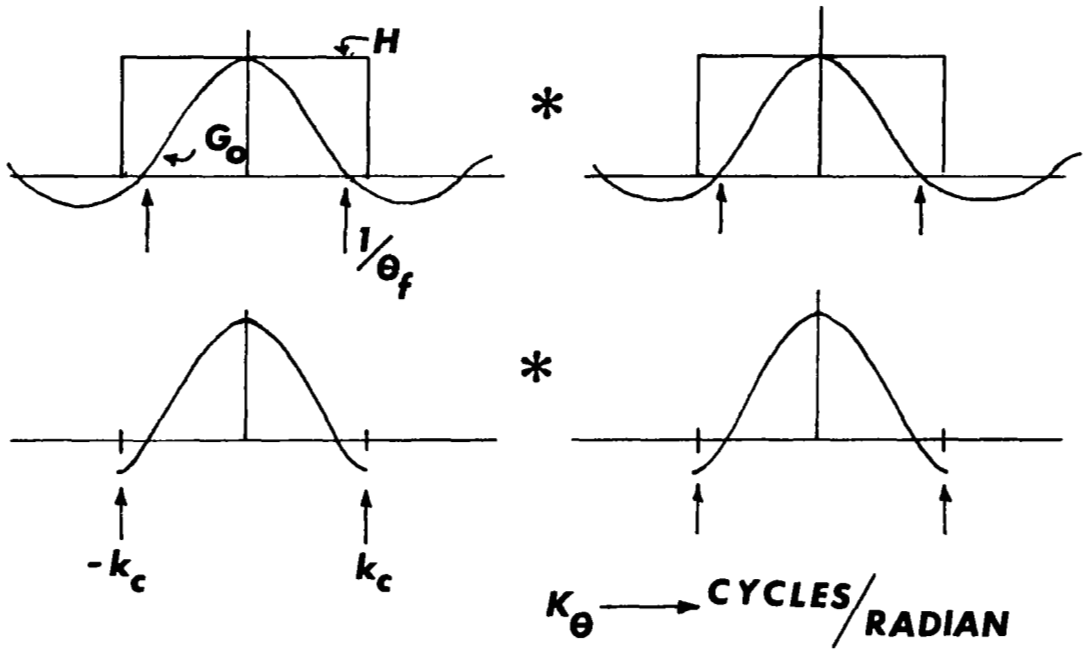

Figure 3.- Graphical interpretation of heterodyne transfer function.

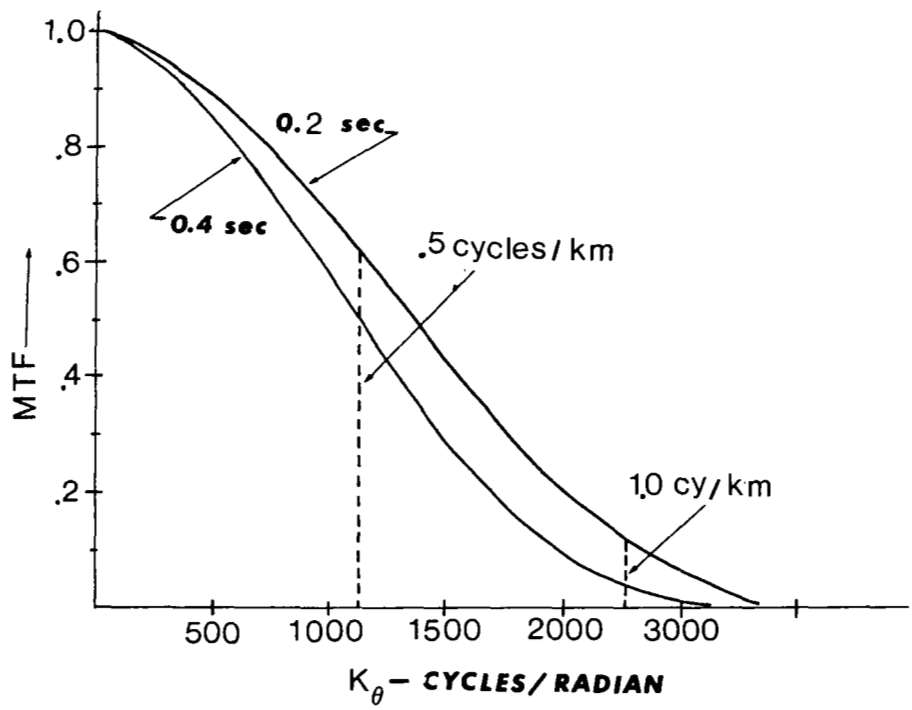

Figure 4.- Total MTF for worst-case shuttle orbit and two values of integration time.

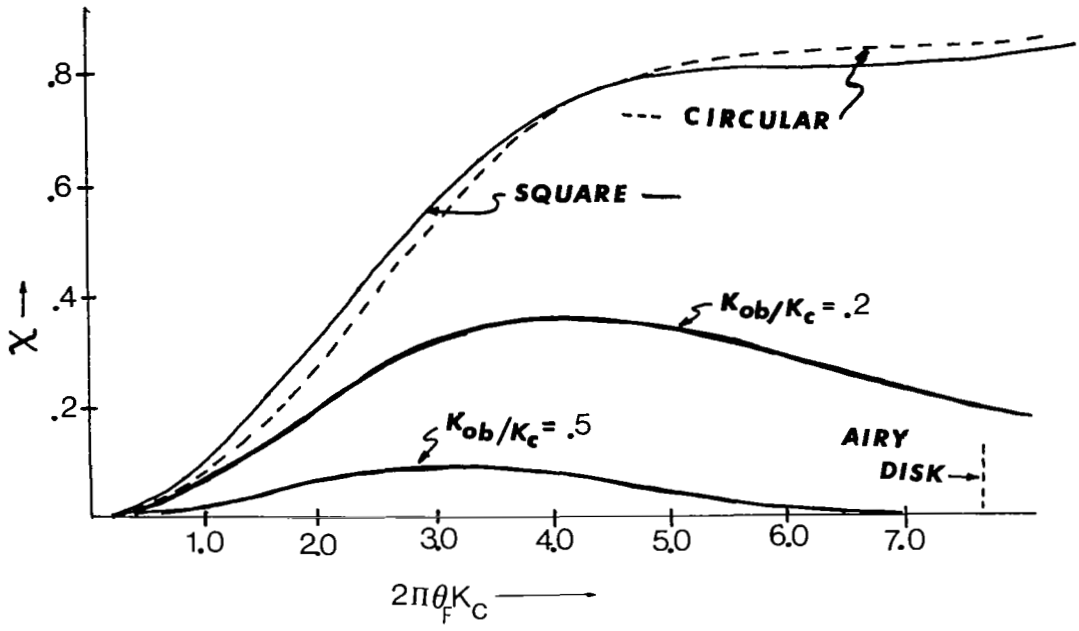

Figure 5.- Efficiency factor, χ, versus system parameter $2\pi\theta_F K_c$ for various receiver geometries.

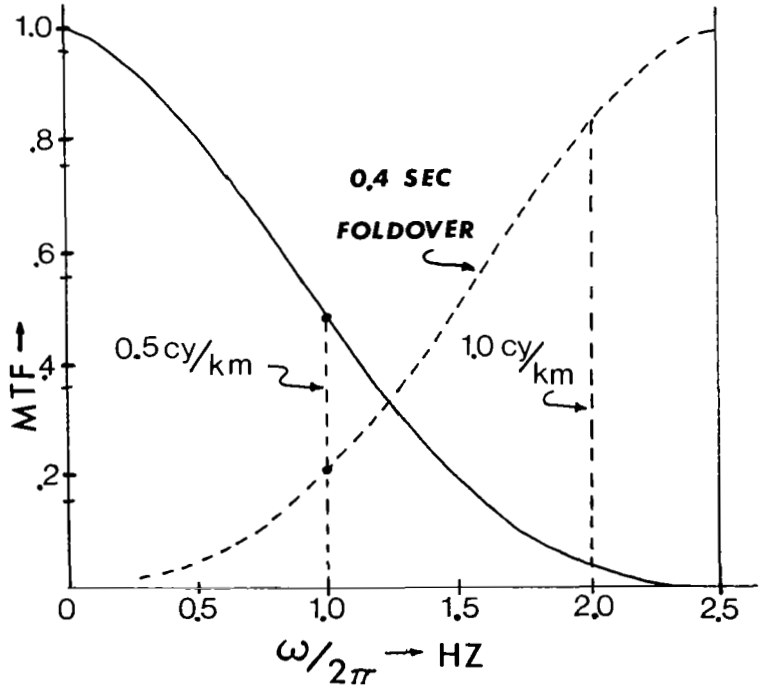

Figure 6.- Aliasing error for 2.5 Hz sampling rate at worst-case shuttle orbit.

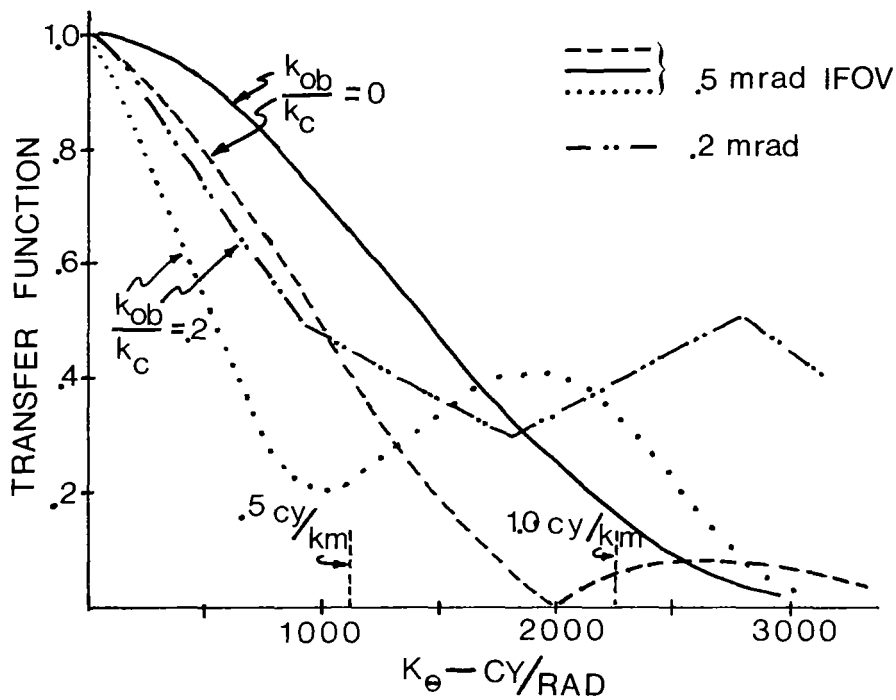

Figure 7.- Comparison of transfer functions for various geometries. Dashed curve represents conventional MTF with 0.5 mrad I.F.O.V.

HIGH PRESSURE GAS LASER TECHNOLOGY FOR ATMOSPHERIC REMOTE SENSING

A. Javan*
Laser Development Corporation
Lexington, Mass.

ABSTRACT

High pressure gas laser technology offers the possibility for stable lasers at finely controlled tunable frequencies and power levels needed for atmospheric remote sensing. Broadly tunable precision CW lasers for LHS or CW DIAL measurements, or repetitively pulsed high intensity lasers with the required characteristics for high-resolution DIAL observation of pressure-broadened pollutant line-profiles (to obtain altitude discrimination) are possible. A fixed frequency chirp-free and highly stable intense pulsed laser can be made for Doppler wind velocity measurements with accurate ranging. The talk will review the related technologies in the 10 μm region. The review will be in the form of a progress report presenting an on-going research and engineering effort.

INTRODUCTORY REMARKS

This talk was presented in two parts. The first part gave the details of the work relating to the generation of intense IR laser pulses at highly stable (and chirp-free) single frequency for Doppler wind velocity measurements. It took place at a workshop (chaired by Dr. Robert Menzies) on the evening of March 26. The second talk presented the work addressed to energy extraction from a high pressure CO_2 laser at a tunable single-mode frequency. It took place on March 27 at the session on Coherent Applications (chaired by Dr. Frank Goodwin). Both talks reviewed the status of a project currently in progress. Future publications (and final reports to NASA) will give extensive details of the various phases when completed. For this proceeding, the viewgraphs shown in the two talks are submitted as figures along with detailed descriptions outlining the presentations.

GENERATION OF INTENSE CO_2 LASER PULSES AT A STABLE CHIRP-FREE SINGLE FREQUENCY

Frequency Stabilization by Transient Injection Locking

With transient injection locking (TIL), the laser energy from an intense gain-switched CO_2 pulsed plasma can be extracted at a single-mode frequency triggered by an injected (weak-field) radiation. With an internal low pressure CO_2 gain cell, the TIL laser oscillation occures on a single mode of the resonator lying near the center of a CO_2 amplifying transition. The identity of

*Permanent address: Massachusetts Institute of Technology, Cambridge, Massachusetts 02139.

the laser field inside the resonator as an oscillating sinusoidal field is established after two or three transits across the length of the resonator (after the gain onset). Subsequent oscillation buildup in the single mode (near the line-center) will occur as in a free-running oscillator, without an interference from the (weak) injected field.

In the course of transient oscillation buildup, the oscillating laser frequency ω is subject to time variations caused by refractive index changes of the medium. It is known that by far the dominant source of refractive index change arises from shock waves due to the intense current-pulse producing the high density CO_2 laser plasma. Rapid deposition of energy in the medium causes the shock waves, which propagate at sound speed. However, the onset of violent refractive index changes due to this cause generally occurs at late times (because of propagation at sound speed) exceeding tens of μsec after the current pulse. Accordingly, this effect can result in sizable chirping mainly at the tail of a long duration (several μsec) pulse. In practice, the magnitude of this chirping effect can be minimized by operating at a low plasma-current pulse; this, however, will be at the expense of a reduction in energy-deposition capacity and energy-conversion efficiency.

Another cause of frequency chirping is saturation of the amplifying transition. This effect occurs during a laser pulse if the resonator mode on which laser oscillation occurs is appreciably detuned from the transition center. This chirping effect is largest in the buildup portion (the leading edge) of the pulse. At line-center, however, there will be no contribution to chirping due to this source.

From the above it appears that the chirping will be at a minimum on line-center and for a moderate laser excitation (sacrificing energy-conversion efficiency), particularly for pulse durations below several μsec. However, the studies reported here have revealed additional causes leading to small time dependent refractive index changes during the pulse and, hence, frequency chirping. The dominant process arises from a time dependent change in molecular composition of the medium taking place during each laser pulse. The intense current pulse produces sizable molecular decomposition. The resultant unstable constituents of the gas subsequently evolve (after each current pulse) toward the equilibrium gas mixture. In addition, the effect of redistribution of populations in the low-lying excited molecular states also contributes to a time-varying refractive index change during the laser pulse. Although the refractive index variations due to these causes are small, the resultant frequency chirping can be sizable.

Under the best conditions, the chirping rate on line-center (for a several hundred millijoule laser) can be reduced to a fraction of one MHz/μsec for pulses below one μsec duration. On the tail of the pulse, extensive heterodyne observations show that the chirp rate will build up to values larger than several MHz/μsec at times beyond five or ten μsec after the onset of the leading edge of the laser pulse. At this stage of the art, it appears difficult to reduce the frequency chirping below this observed limiting value reported here. It is also to be noted that refractive index variations leading to frequency chirping will be larger in a higher energy laser.

Doppler wind velocity measurements (and other accurate Doppler Lidar applications) require a laser pulse of several μsec duration at a chirp rate below 100 kHz/μsec. A proposed method is described below, offering the possibility of removing the residual frequency chirping from the laser output pulse.

Figure 1 shows the experimental arrangement employed in heterodyne observations of TIL frequency characteristics. Two methods are employed. The first relates to the studies of single-mode TIL operation near line-center obtained with an internal low pressure CO_2 gain cell. In this case, the single-frequency laser output is heterodyned against an external CO_2 laser local oscillator to observe the frequency characteristics. For a variety of reasons, it is advantageous to achieve single-mode TIL energy extraction employing an external CW CO_2 laser master oscillator for TIL driver, as shown in figure 1. (In this case, the internal CW CO_2 gain cell is switched off). The advantages include the possibility of employing the CW TIL driver laser also as the local oscillator in heterodyne detection of the Lidar return signal.

If the external TIL driver laser is detuned from the peak of the resonator mode of the pulsed power oscillator, the TIL laser osciallation occurs at a frequency shifted to the peak of the resonator mode. In the extensive studies of frequency chirping and the related effects, the injected frquency, ω_{Inj}, is detuned by a known amount from the peak of the power oscillator resonator mode. The TIL laser output is heterodyned against the same CO_2 laser employed as the TIL driver laser (see fig. 1).

Detuning of the external TIL driver laser from the center frequency, ω_o, of the power oscillator resonator mode is obtained as follows: With the intense pulsed plasma switched off, the internal CW CO_2 gain cell is employed to obtain CW laser oscillation at the center frequency ω_o, of the power oscillator resonator mode. (With PZT tuning, the mode is centered on the internal low-pressure CO_2 gain profile.) With heterodyne observation, the TIL driver laser is detuned from ω_o by a preselected known amount. Rugged and stable resonator configurations are used to avoid appreciable long term drifts (as verified by frequent heterodyne observations in the course of an experiment). Once the known detuning is achieved, the internal CO_2 gain cell is switched off. The TIL energy extraction and heterodyne observations are then performed at the known detuned injected frequency.

It is necessary to decouple radiatively the power oscillator laser totally from LO (and external TIL driver). A ring resonator with appropriate suppressor-mirror (to avoid backward oscillation) and appropriate padding with attenuators are employed.

In accurate observation of frequency chirping, it is important to employ adequate optical isolation and electrical shielding of the high intensity plasma-current pulses (and the LO laser power supply); otherwise, the local oscillator will suffer (due to optical feedback or spurious electrical pickup currents) small frequency variations, rendering the measurements invalid. To verify the absence of such a spurious LO chirping, another LO is used to probe the frequency of the first LO during the short observation time (while the energy extraction from TIL power oscillator occurs). One arrangement to achieve this is shown in figure 1.

It is essential to study frequency chirping effect (due to refractive index variation) at late times (about 5-to-10 μsec). After the onset of TIL laser pulse the tail of the gain-switched pulse generally provides a weak, slowly decaying, laser output at such late times. Although the intensity on the tail is considerably below the main laser pulse, it can be readily detected with heterodyne detection and employed in the studies of frequency chirping. Figure 2 shows typical oscilloscope traces of a photopreionized single-mode TIL laser output (at several hundred millijoule energy per pulse) heterodyned with a CW LO; the heterodyne beatnote (in the MHz range) appears superimposed on the pulse profile. The main pulse is below one μsec and has a long tail. The upper figure is displayed to show the general features of the observation. In the lower trace, the oscilloscope is triggered at about five μsec after the main pulse. It shows an initial zero beat and a subsequent increase in beatnote. At about 10-to-11 μsec after the pulse, the chirp rate has increased to a value of about 3 MHz/μsec. This displays the limiting chirp rate obtainable in a typical several hundred millijoule photopreionized TIL CO_2 laser. As noted, lasers at higher pulse energies will suffer larger chirp rates. At early times after the onset of the laser pulse, however, the chirp rate can be considerably below the value stated here. This can be obtained by carefully centering the power oscillator resonator mode near the line-center and at a somewhat reduced energy deposition efficiency and uniform excitation across the cross section of a (seed gas) photopreionized CO_2 laser. For a one μsec pulse, the chirp rate can be as low as a fraction of one MHz/μsec.

Removal of Residual Frequency Chirping From Output Laser Pulse; A Proposed Method

The proposed chirp removal method employs electro-optic modulation of the laser output at an rf frequency. The modulating rf voltage is obtained from a laser beatnote produced by mixing a small fraction of the intense laser pulse with the output of a stable CW laser. In one embodiment, the stable CW laser frequency (or the frequency of the high-energy pulsed laser) is tuned so that the beatnote appears at a convenient rf range. (This heterodyning is accomplished at large input radiation signals incident on the mixer element, hence the beat voltage across the mixer appears at a sizable signal level). The resultant beatnote, after amplification in a broadband rf amplifier (when necessary), is applied to an electro-optical modulator to produce frequency modulation of the output laser pulse. Inspection will show that one of the rf sidebands will be free from laser chirp. The block diagrams in figures 3 and 4 give a summary description. A variable optical delay is provided to make up for small delays in the rf amplifier circuit. It can be shown that if this delay is not totally corrected, the chirping effect, although reduced by orders of magnitude, will not be totally eliminated; the remaining chirp will be $(d\omega/dt)\tau$, where $(d\omega/dt)$ is the chirp rate at the output of the pulsed laser and τ is the delay time. (In practice, τ can be reduced to values below several nsec.)

In an ultimate design it is possible to employ single sideband e.o. modulation, converting more than 50 percent of a (e.g., ten joule) laser output pulse to a nearly chirp-free sideband. Depending on the laser intensity, it will also

be possible to use the e.o. modulator in the form of a thin (possibly waveguide type) sample to achieve high conversion efficiency at reduced modulator rf voltages.

Other applications require a pulsed chirp-free master-oscillator unit at a reasonably large output power level; the master-oscillator unit can then be used in a MOPA configuration to extract a chirp-free amplified output from a high energy power amplifier. If the master oscillator provides a reasonably large output power, the requirements for multipass power amplification will be enormously relaxed. (In the existing MOPA systems, multipass amplification with intricate isolation stages are needed because of low-level power outputs of the existing stable master oscillators. This is the main reason for complexities of the existing high energy MOPA systems.) A longitudinally excited low pressure Q-switched CO_2 laser, for example, can be used in the chirp-removal system suggested here. Such a Q-switched CO_2 laser, after chirp removal, can be used as a master oscillator at a relatively high peak intensity in a MOPA system.

This proposed method, yet to be developed, was presented in the conference workshop because of its potential application in generation of chirp-free radiation for accurate Doppler Lidar.

ENERGY EXTRACTION FROM GAIN-SWITCHED HIGH PRESSURE CO_2 LASER AT A STABLE TUNABLE MONOCHROMATIC FREQUENCY

Energy extraction by Transient Injection Locking (TIL) at a tunable frequency requires the utilization of an external tunable master oscillator, driving an intense pulsed power oscillator at the tunable frequency. In this sytem a weak radiation field (from the tunable master oscillator) is introduced in the resonator of the pulsed power oscillator at the frequency of a selected resonator mode. As the power oscillator gain is rapidly switched on, under appropriate conditions, laser oscillation buildup occurs at the single-mode selected by the frequency of the weak injected field. This is a transient process and appreciably differs from the previously known steady state injection locking. The transient injection locking under consideration in this talk is an extension of the well known art of superregenerative amplification in the microwave region, where enormously large gains are obtained with a (repetitively pulsed) gain-switched microwave (or rf) oscillator, driven by a weak (input) signal.

An important feature of the TIL process relates to its transient nature: the oscillation "buildup" at the selected single mode will "hold on" only for a limited time duration. The oscillator will switch after a short time interval (determined by the injected field) into its free-running oscillation mode.

If the weak-field injected radiation is introduced at the frequency of one of the resonator modes lying near the peak of a high-gain line - consider, e.g., a power oscillator with a grating resonator tuned to the high-gain line - the time duration of switchover (to the steady-state oscillating mode) is generally long. However, if the selected mode is appreciably detuned from the peak of the high-gain line, unless the injected field has sufficient intensity, the

switchover from the selected mode to the free-running oscillating mode (or modes) will occur in the early times during transient oscillation buildup.

For a power oscillator with a resonator employing broadband reflectors (without a grating), injection of a weak field at the frequency of a low-gain transition of the CO_2 amplifying band will cause initial oscillation buildup to occur on the selected mode of the low-gain line. The free-running oscillation (without the injected field), however, occurs on several modes of the high-gain line of the amplifying band. Accordingly, the switchover from the TIL on the low-gain line will generally occur to multimode oscillation on the line with the highest gain.

Energy extraction at the frequency of a resonator mode selected by TIL will be complete if the switchover time to free-running oscillation occurs at late times after the main pulse (i.e., it takes place on the decaying tail of the laser pulse). If appropriate conditions are not satisfied, the switchover time will be in the early buildup time (or at a time during the main pulse), in which case TIL energy extraction at the desired frequency will not be complete.

Complete-versus-partial TIL energy extraction is a subject requiring extensive scrutiny for a tunable TIL laser. This important problem is not encountered for a TIL gain-switched CO_2 laser with an internal low pressure gain cell (causing line-center TIL). The internal low pressure gain cell selects a mode near the center of a high-gain line and, hence, as noted previously, the switchover time to the free-running oscillating mode (which may be, e.g., another resonator mode adjacent to or in the vicinity of the selected mode) will take place at late times on the tail of the pulse. However, the switchover process can be an important effect if the injected radiation is introduced at a frequency where the gain of the medium is lower than the peak gain (even by as much as five or ten percent).

The switchover time duration critically depends on several parameters. They consist of: (a) Intensity of the injected radiation, (b) the gain-above-loss-factor at the mode selected by the injected field compared to the gain-above-loss factor in the region where free-running oscillation can occur, (c) the detuning of the frequency of the injected field from center-frequency of the selected resonator mode, and (d) the saturation parameters of the medium determined by pressure effect.

For the power-oscillator laser at a fixed pressure, and a given resonator loss factor, the condition for complete energy extraction by TIL can be described by a threshold intensity, I_{th}, of the injected field inside the resonator. This threshold is defined by the intensity of the injected radiation causing the switchover time to take place at times not shorter than two or three times the duration of the main pulse. Accordingly, the threshold intensity (for complete TIL energy extraction) will depend on the gain factor at the injected frequency, and the detuning of it from the peak of the selected resonator mode.

The work of colleagues (ref. 1) in Canada on TIL of a gain-switched CO_2 laser (and the other workers) have addressed the problem of line-center TIL on a high-gain line. Energy extraction in such a system is always in the "complete

regime". The previous works have not dealt with TIL energy extraction at a tunable frequency, requiring an understanding of the complete-versus-partial TIL energy extraction presented here (for the first time).

In the experimental studies discussed here, the TIL process is explored in the line-center region, as well as at frequencies appreciably detuned from the CO_2 line centers. In the line-center observations, an external line-tunable low pressure CW CO_2 laser is used as the TIL driver master oscillator. In this case, e.g., complete-versus-partial energy extraction on a low-gain line is explored by TIL of a gain-switched power oscillator employing a broadband resonator. In this case the switchover from line-center TIL on the low-gain line will take place to free-running multimode oscillation on the highest gain line.

The energy extraction at frequencies appreciably detuned from CO_2 line centers are studied employing an external line-tunable low pressure N_2O laser as the TIL driver master oscillator. It is known that the N_2O and CO_2 amplifying bands (in the 10.6 μm region) overlap one another. Several N_2O laser lines lie at known frequencies detuned from the center frequencies of nearby CO_2 lines. With a gain-switched CO_2 power oscillator at varying pressures (corresponding to varying collision broadened linewidths), off-line center TIL is studied employing the N_2O TIL driver laser. This process is also studied using the CO_2 power oscillator with a grating tunable resonator containing within it a low pressure N_2O gain cell.

Figure 5 is a schematic of well-known TIL with an internal low pressure gain cell. Observation of a smooth output pulse is a good indication of TIL. This is observed with the low pressure gain cell switched on. Without the low-pressure gain cell, the output is accompanied with beatnotes originating from multimode operation.

Figure 6 is schematic of a tunable TIL employing an external (tunable) master oscillator.

Figures 7, 8, and 9 relate to complete-versus-partial TIL energy extraction. The upper trace in figure 7 is a computer modeling theoretical estimate for a case in which an injected field at 20 mW intensity is introduced in the resonator of a gain-switched CO_2 power oscillator at the frequency of the P(10) line (with the power oscillator laser employing broadband resonator reflectors). The main pulse shows buildup and decay of the P(10) line. Full scale absissa is 10 μsec. The gain-switched pulse is followed by a long tail (caused by transfer from N_2O to CO_2). The switchover to the free-running oscillation on the P(18), the high-gain line, is also displayed (the lower trace). In this case (which corresponds to a non-complete energy extraction), the total laser output will consist of a superposition of the two curves, with the main peak dominantly consisting of the P(10) line and an early switchover on the tail to the P(18) line. This figure 7 also shows experimentally observed near-complete TIL energy extraction with about one mW injected radiation in the P(12) line. The switchover occurs to the P(18) line on the tail of the pulse. When this occurs, the P(18) line appears (as in a free-running oscillator) with multimoding. The breaking into a multimode operation seen on the decaying portion of the observed pulse is due to the switchover from single mode TIL P(12) line to multimode free-running

P(18) line. For clarity of presentation, the lower figure is a hand drawing of the somewhat faint (high speed) oscilloscope picture of the experimental trace shown.

Figure 8 shows the observed pulses described in figure 7, except the injected field intensities are varied. The two traces in figure 8 show the control of switchover time by injected field intensity.

Figure 9 shows the observed pulses described in figure 7 for about 50 mW injected radiation, showing complete energy extraction (with the switchover time delayed to late times on the tail not appearing on the trace). The intensities of the injected field for figures 7, 8, and 9 correspond to the injected frequency, ω_{Inj}, tuned to the center frequency of the power oscillator resonator mode (via the method described in the explanation of figure 1). Additional details of figures 7, 8, and 9 will be published by S. Nazemi and A. Javan.

Figure 10 lists several N_2O laser lines at frequencies differing by known amounts from CO_2 line centers.

Figure 11 illustrates that the threshold injected field intensity for complete energy extraction (I_{th}) depends on the parameter N given in the figure. As is seen, the parameter N in turn depends on pressure broadened linewidth as shown. I_{th} at a fixed detuned frequency is considerably lower for a broader line (higher pressure).

Figure 12 gives the TIL threshold intensity, I_{th}, for complete energy extraction at a detuned frequency employing the R(10) N_2O line (at 1980 MHz removed from P(16) CO_2 line center). The threshold injected intensity (value for inside resonator), I_{th}, is given at 3 different pressures. At about one atmosphere pressure, larger than 50 mW is required for complete TIL energy extraction. At about 2.5 atmospheres, on the other hand, 3 μW is sufficient for complete energy extraction (at the detuned N_2O frequency). The threshold values are given for the injected field carefully tuned to the peak of the power oscillator resonator mode, with the method extensively described in the explanation of figure 1, employing CW N_2O lasers (and gain cell) instead of CW CO_2 lasers (and gain cell), see figure 1.

We mention here, with great emphasis, that an important aspect of engineering of a tunable TIL CO_2 laser is control of the power oscillator resonator mode with respect to the frequency of the tunable injected radiation. Based on extensive component-by-component experimental investigations, a frequency tracking unit, complete with fine control and calibration, has been designed and is under consideration by NASA LaRC for possible implementation. Future publications will describe the control system.

Tunable frequency energy extraction by TIL from an energetic gain switched CO_2 laser can be achieved with a TIL driver input consisting of a frequency tunable laser pulse (low energy) with a duration as short as about ten nsec (or longer). A grating tunable photopreionized high pressure CO_2 laser can be reliably operated (with seed gas photoionization) at output energies in the ten to fifty mj range. Such a high pressure laser can be tuned to frequencies appreciably detuned from CO_2 line centers. However, the spectrum of the grating

tunable high pressure pulsed CO_2 laser is generally broad. It consists of multimode oscillation spread over a range of about 2000 MHz. This laser, by itself, is inadequate for use as a driver TIL master oscillator. On the other hand, if it is followed by an appropriate Fabry-Perot filter, it is possible to reproducibly select one (or two) oscillating modes for use as a tunable TIL driver master oscillator. (Controlling the tuning can be achieved with simultaneous - ganged - laser grating and Fabry-Perot filter tuning.)

In the system employed, the selected (filtered) oscillating modes appeared (after the filter) at a pulse duration somewhat below 100 nsec at a peak intensity of about 0.1 to 1 kW. The CO_2 power oscillator was triggered at a (variable) delayed time with respect to the pulsed driver master oscillator. The pulsed injected field is introduced in the gain-switched CO_2 power oscillator during the early buildup time. By varying the delay, it is found that about 100 nsec time window is readily available to achieve TIL with the injected pulse. This experiment has been successfully performed. However, detailed observations (and the possible utilization in a remote sensing experiment) are presently postponed for a later date.

A short pulse TIL driver master oscillator cannot be used at the same time for heterodyne detection of the Lidar return signal. (The return signal arrives at a delayed time.) Such a system would require a separate LO laser (such as a tunable diode laser) in the Lidar detection system.

A gain-switched CO_2 power oscillator operating at a multiatmospheric pressure, driven with an appropriate TIL driver master oscillator, can offer frequency tunable output in ranges considerably detuned from CO_2 line centers. An isotopic high pressure CO_2 laser can be operated closed cycle (sealed off) with catalytic CO_2 regeneration. Such an isotopic CO_2 laser, reliably operating with seed gas photopreionization (refs. 2 and 3), offers broad frequency tuning at about 3 atmospheres pressure.

An important tunable master oscillator available for TIL driver is the system consisting of a line tunable CW CO_2 laser followed by a tunable microwave e.o. modulator (ref. 4). The tunable microwave sidebands have sufficient intensity for TIL energy extraction.

With a tight control of the power oscillator resonator mode and its centering on the injected frequency, it should also be possible to employ a tunable diode laser as the tunable TIL driver master oscillator.

Another possibility (sugested by A. Mooradian of Lincoln Laboratory) is parametric mixing of a CO and CO_2 laser to generate discretely tunable radiation (by about 150 MHz spacing) over a broad region in the 10 μm range.

A tunable TIL in the CO_2 line center region (applied to an atmospheric differential remote sensing experiment) has been reported (ref. 5) by R. Menzies with a tunable (by several hundred MHz) waveguide CO_2 laser.

An ideal widely tunable master oscillator for a differential absorption (ref. 6) experiment, however, is a miniature e-beam sustained CO_2 laser currently under extensive development.

PRECISION MINI E-BEAM-SUSTAINED TUNABLE CW CO_2 LASER; A COMPONENT-BY-COMPONENT DESIGN STUDY

A design-study project is in progress to construct a miniature e-beam sustained tunable CW CO_2 laser, with a thin pencil-like plasma volume (of about 10 cm × 1 $(mm)^2$), capable of operating at pressures as high as 3 to 4 atmospheres. Such a laser will offer a fine frequency-tuning characteristic, with a single-mode output at a CW output power up to about 50 watts. The removal of deposited heat energy (necessary for CW operation) is achieved by rapid transverse gas flow. The thin cross-section of the pencil-like plasma facilitates the heat removal at a subsonic flow. The design calls for operation at a sustainer voltage below avalanche breakdown, where the totality of the electrons in the thin pencil-like CO_2 plasma is produced by the secondaries from the incident primary e-beam. The e-beam is in the form of a thin ribbon transmitted through a thin foil.

The operating pressure under consideration is up to 3 to 4 atmospheres, where broad tuning can be obtained, as in reference 3, with an isotopic CO_2 gas mixture.

It is necessary to employ a low-Fresnel number resonator with a short mirror spacing (13 cm in the present design).

The requirement for a short low-Fresnel number resonator together with the miniature nature of the device calls for novel design considerations within severe space limitations (of the miniature laser). The short resonator of the laser facilitates energy extraction at a minimum diffraction loss.

The electron gun is of the plasma cathode design. Figure 13 shows internal components of the electron gun made visible by removal of the anode. The hollow cathode and its concentric shield are precisely aligned inside the vacuum box (left) by means of two high voltage feedthroughs which are not seen in this view. The anode plate is 2 cm thick to allow for water cooling channels. A wide slot is cut out of the central portion of the anode. This is covered on the vacuum side by a thin narrowly slotted plate to permit electron passage into the 2 cm long field free region. A 0.3 mil thick aluminum window seals the outside of the wide anode slot. This device produces a uniform, stable, cw electron beam 9 cm long and 0.2 cm wide at a current density of 300 $\mu A/cm^2$ and energy of 30 keV.

Figure 14 is an electron gun similar to that shown in figure 13 in operation with the ribbon-like beam emerging into the atmosphere. In this view the two H.V. feedthroughs are visible emerging from the vacuum chamber. Also visible is the glow of ionized air in the path of the electron beam. The uniformity of the glow reflects the uniformity of the emergent beam.

The author expresses acknowledgment to the Spectroscopy Branch, LaRC, Virginia, headed by R. V. Hess, for continued encouragement and support. The program has extensively benefited from the modeling estimates and other investigations of the branch, specifying the various requirements.

REFERENCES

1. Lachambre, J.; Lavigne, P.; Otis, G.; and Noel, M.: Injection Locking and Mode Selection in TEA-CO_2 Laser Oscillators. IEEE J.Q.E., vol. QE-14, no. 3, p. 756, March 1978. Lachambre, J.; Lavigne, P.; Verreault, M.; and Otis, G.: Frequency and Amplitude Characteristics of a High Repetition Rate Hybrid TEA-CO_2 Laser IEE J.Q.E., vol. QE-14, no. 3, p. 170, March 1978.

2. Gibson, R. B.; Javan A.; and Boyer K.: Sealed Multiatmospheric CO_2 TEA Laser: Seed-Gas Compatible System Using Unheated Oxide Catalyst, Appl. Phys. Lett., vol 32 (726), 1978.

3. Gibson, R. B.; Javan, A.; and Boyer, K.: Mixed Isotope Multiatmospheric CO_2 Laser, IEEE J.Q.E., Nov. 1979.

4. Cheo, P. K.: Generation and Applications of 16 Ghz. Tunable Sidebands from a CO_2 Laser. Proceedings of 3rd International Conference on Laser Spectroscopy, Jackson Lake Wyoming, July 4-8, 1977. Sachse, G. W.; and Cheo, P. K.: A Microwave Tunable Laser Source for the Infrared. Conference on Laser and Electro Optical Systems, San Diego, California, February 26-28, 1980.

5. Menzies, R. T.; and Shumate, M. S.: Tropospheric Ozone Distributions Measured with an Airborne Laser Absorption Spectrometer. Journal of Geophysical Research, vol. 83, no. 18, August 20, 1978.

6. Brockman, P.; Hess, R. V.; Staton, L. D.; and Bair, C. H.: DIAL With Heterodyne Detection Including Speckle Noise: Aircraft/Shuttle Measurements of O_3, H_2O, and NH_3 With Pulsed Tunable CO_2 Lasers. Heterodyne Systems and Technology, NASA CP-2138, 1980. (Paper 39 of this compilation.)

Work reported is in part performed in collaboration with J. S. Levine, and M. Guerra, LDC, Lexington, Mass., and with S. Nazemi and C. Davis, MIT, Cambridge, Mass. The development and engineering of lasers for remote sensing is done at LDC under sponsorship of NASA LaRC; the MIT work has been under NSF support.

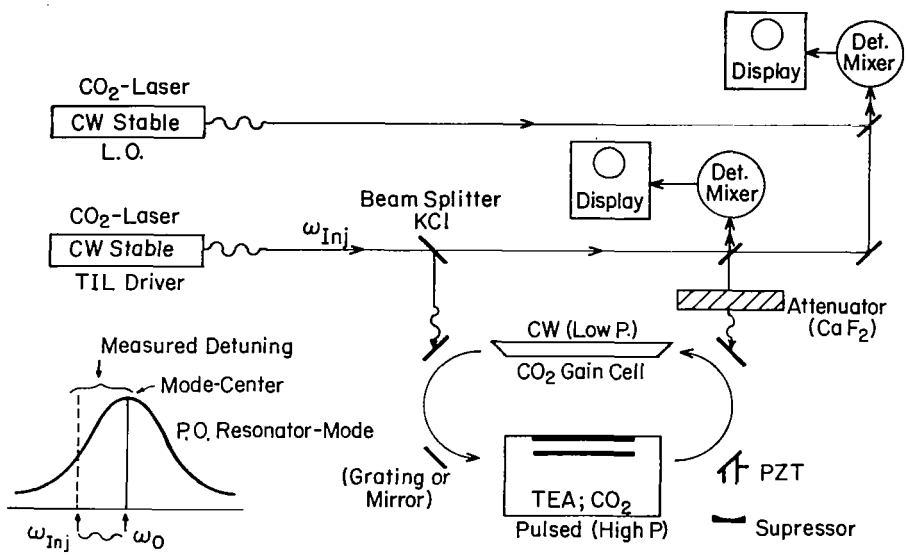

Figure 1.- TIL characteristics; heterodyne observations in the CO_2 line-center region.

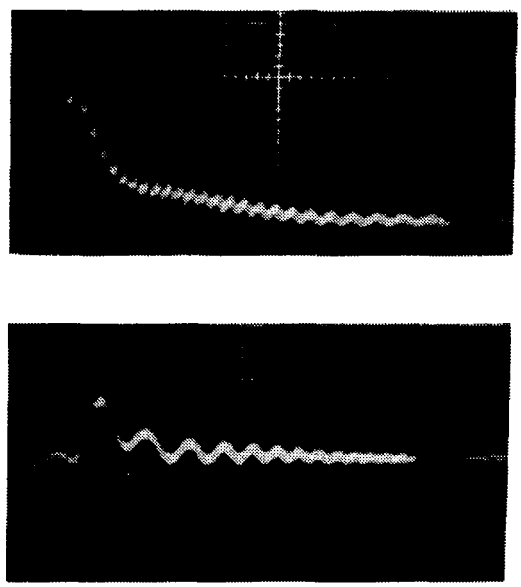

1 μsec/cm

Figure 2.- Heterodyne signal ring power oscillator (TIL) display of chirping at late times.

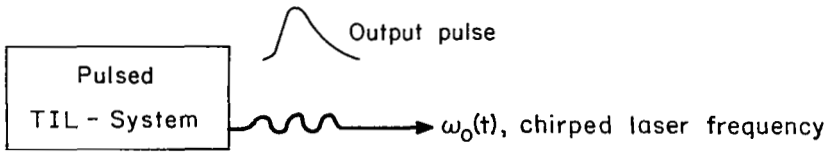

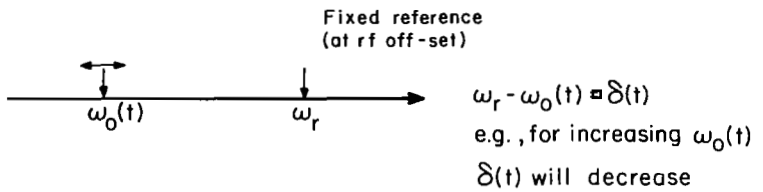

Suppose could generate radiation exactly at
$\omega_0(t) + \delta(t)$; This will be chirp-free
$\omega_0(t) + [\omega_r - \omega_0(t)] = \underline{\underline{\omega_r}}$

Figure 3.- A method for removal of frequency chirp from a pulsed laser: concept.

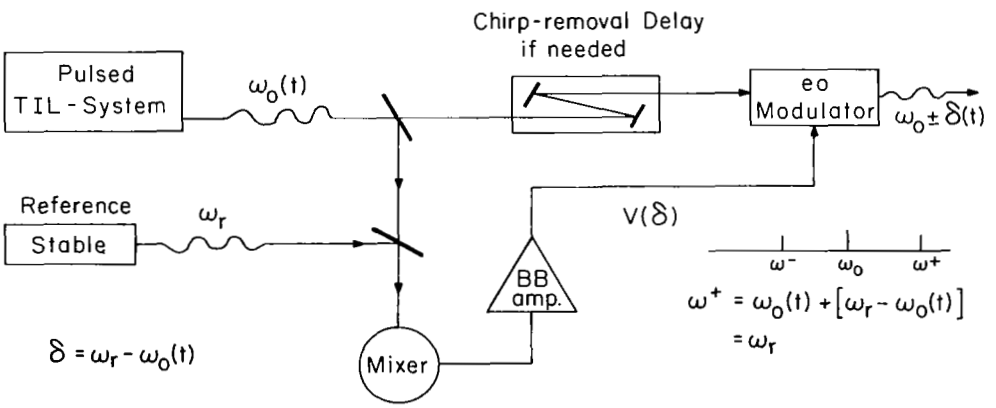

Can be shown that a delay $d\tau$
will leave a residual chirping:

$$\omega^+ = \omega_r + \frac{\partial \omega_0}{\partial t}\,\tau$$

e.g. for (conservative) $\frac{\partial \omega_0}{\partial t} = 1\ \text{MHz}/\mu\text{sec}$ and $\tau < 10\ \text{nsec}$

Figure 4.- A method for removal of frequency chirp from a pulsed laser: experimental arrangement.

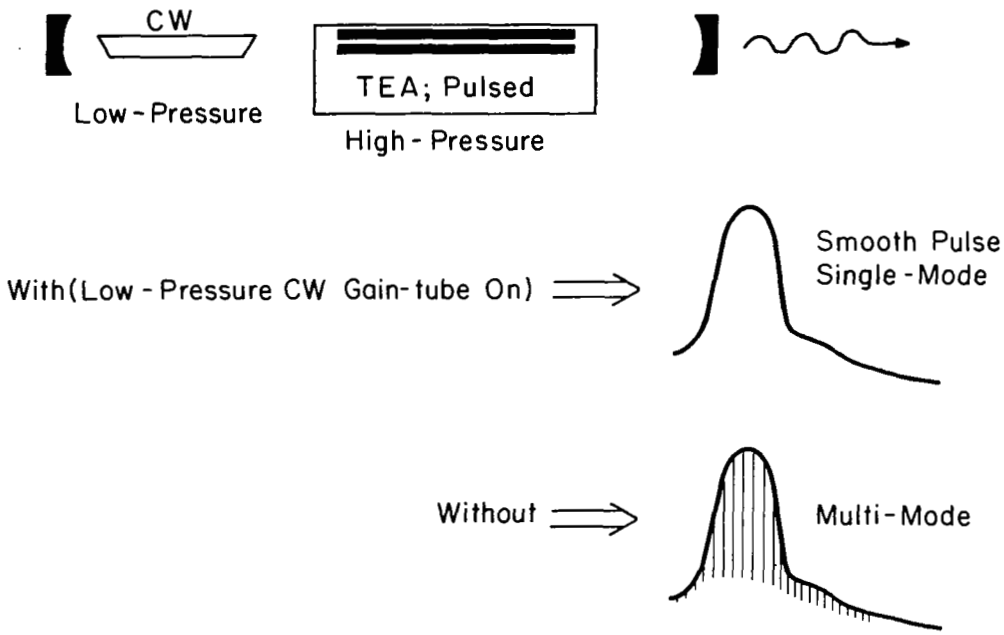

Figure 5.- Pulse-smoothing: TIL with an internal gain-tube.

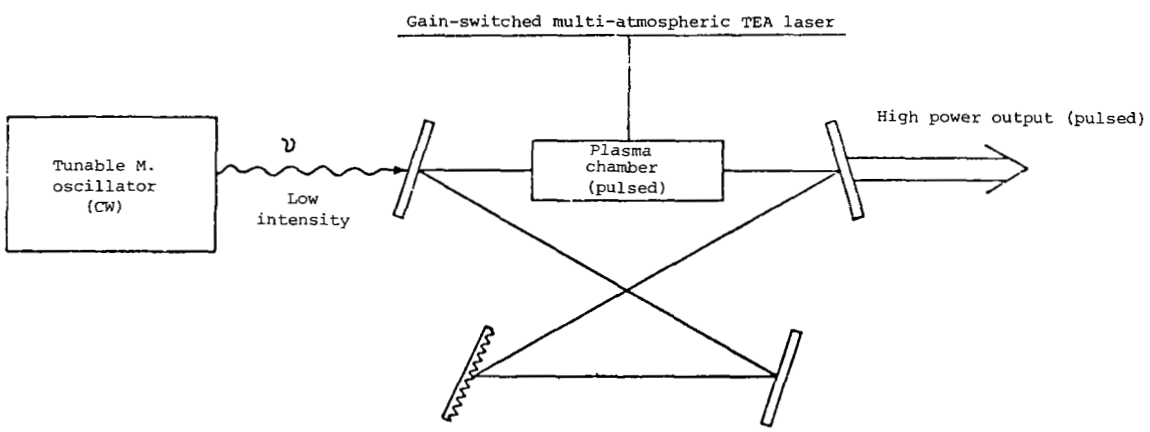

Ring Resonator Grating Is Broadly Tuned To The Desired Frequency Region. The Injected Weak Input, Tuned To The Appropriate Frequency, Will Cause Near-Complete Energy Extraction At A Single-Mode Frequency (Close To The Injected Frequency)

Figure 6.- Schematic of tunable Transient Injection Locking.

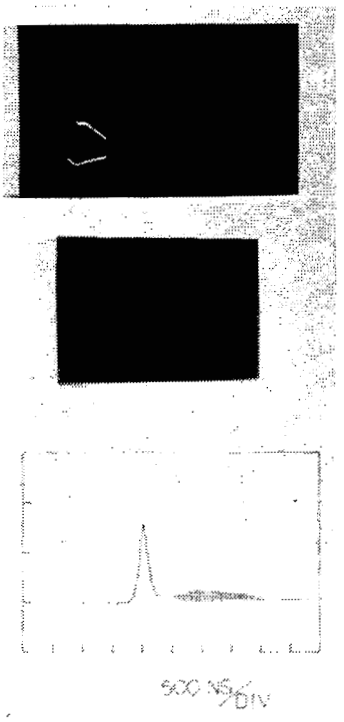

Figure 7.- Theoretical and experimental energy extraction by Transient Injection Locking.

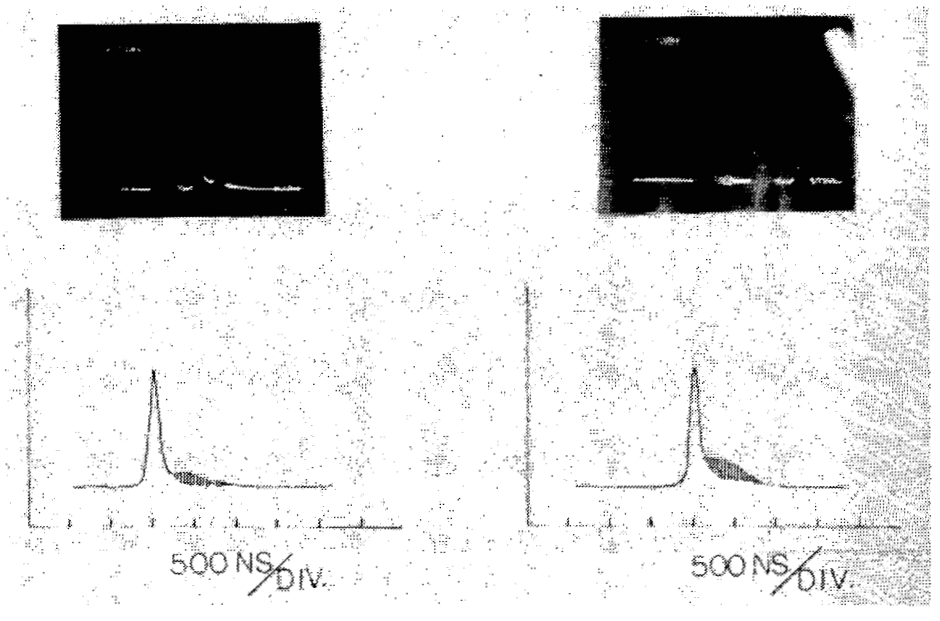

Figure 8.- Effect of varying injected power on the time-of-onset of multimoding.

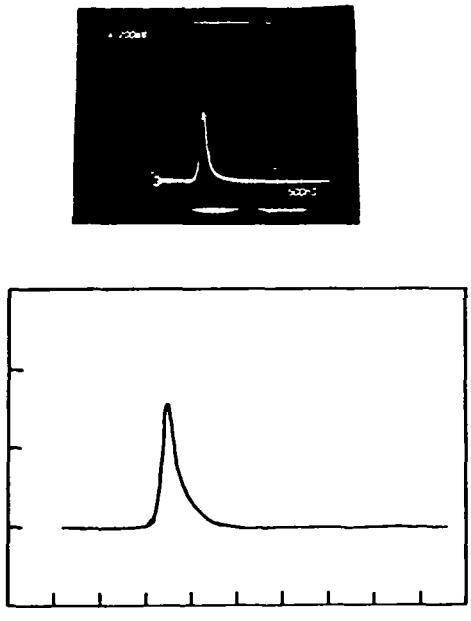

Figure 9.- Complete energy extraction by Transient Injection Locking for the case of strong injected radiation.

$\delta = \nu_0(N_2O) - \nu_0(CO_2)$

N_2O R(10) CO_2 P(16)	δ = 1986 MHz
N_2O P(7) CO_2 P(32)	δ = -586 MHz
N_2O R(21) CO_2 P(6)	δ = 4844 MHz
N_2O R(16) CO_2 P(10)	= -10891 MHz

Figure 10.- Difference frequencies for some N_2O and CO_2 laser lines.

$$N = \frac{g(\omega_o) - g(\omega_{INJ})}{g(\omega_o)}$$

I_{TH} = THRESHOLD INJECTED INTENSITY FOR COMPLETE ENERGY EXTRACTION BY TIL

I_{TH} DEPENDS ON N

(SWITCHOVER TIME DEPENDS ON N)

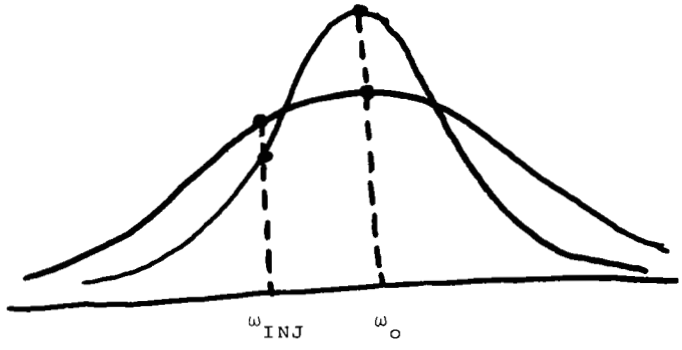

Figure 11.- Threshold for complete energy extraction versus detuning from line center.

I_{TH} VERSUS PRESSURE

$\delta = \omega - \omega_o$

= 1980 MHz

P(in PSI)	15	27	40
I_{th}	> 50 mW	3 mW	3 μW

Figure 12.- TIL at detuned frequencies: I_{TH} versus pressure.

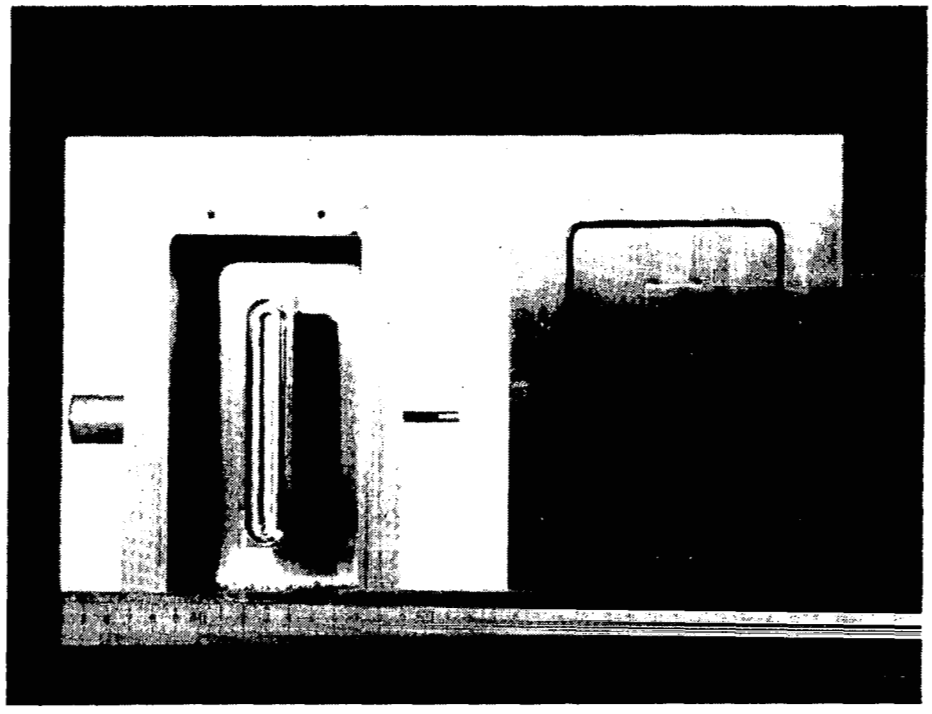

Figure 13.- Internal view of plasma cathode electron gun.

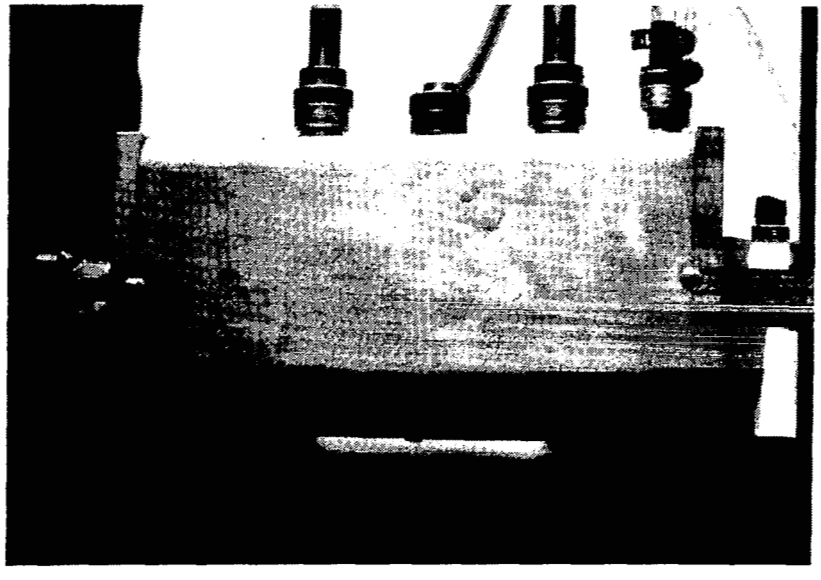

Figure 14.- Plasma cathode electron gun operating in air.

AN AIRBORNE DOPPLER LIDAR

Charles A. DiMarzio
Raytheon Company

James W. Bilbro
Marshall Space Flight Center

ABSTRACT

A Pulsed CO_2 Doppler Lidar has been developed for airborne measurements of atmospheric wind fields. This device has been successfully utilized in the detection and measurement of mountain-wave turbulence and wind shear, and in the generation of time histories of wind-field variations in smooth flight. This Lidar is now in the process of being configured for measurement of the atmospheric flow fields surrounding severe convective storms.

This paper will provide a brief description of the system, a discussion of the Lidar System's Capabilities, a brief look at typical data provided by the system, and an overview of near-term program plans.

INTRODUCTION

The coherent pulsed Doppler Lidar, shown in figure 1, was built by the Raytheon Co. for NASA Marshall Space Flight Center in 1971 (ref. 1). This unit was originally designed for the detection of clear air turbulence (CAT) and was flown on a shake-down flight in 1972 and in a search for CAT in 1973. The system succeeded in measuring clear air returns up to an altitude of 6 kilometers, and, on one occassion, detected mountain-wave turbulence, which was verified by penetration with the aircraft (ref. 2). The Lidar was found to be operating considerably under its theoretical expectations and was extensively refurbished, incorporating a number of changes including an offset local oscillator to allow ground-based operation with stationary targets. A series of ground tests was undertaken in 1977 and 1978, and the Lidar was flown in another CAT flight series in early 1979. Data analysis from this test series is still underway, so this paper will provide only representative selections of the types of information being obtained.

The Lidar is currently being modified to perform flow-field mapping of the non-precipitating regions of severe storms. This primarily involves the incorporation of a scan system, central timing and control system, new signal processing electronics, and a new telescope. An extensive measurement program is being planned for the summer of 1981.

SYSTEM DESCRIPTION

A block diagram of the Lidar is shown in Figure 2. It is a CO_2, pulsed, coherent Lidar operating at 10.6μm. Its configuration is known as a MOPA, (master oscillator power amplifier). To obtain an understanding of how the system operates, it is perhaps best to follow through the block diagram. First, the master oscillator is a continuous wave (CW) laser providing approximately 8 watts of linearly polarized radiation at 10.6μm. A small portion of this output is picked off for use in frequency stabilization of the master laser and for use in an offset locking loop used to maintain the offset-local-oscillator laser at a 10 MHz frequency offset from the master laser. The main portion of the master-laser output is directed to an electro-optic CdTe modulator, where it is chopped into a pulse train of variable width and rate. The width may be selected at 2,4, or 8 μs and the rate may be varied from 1 to 200 pulses per second. The resultant pulse train passes through an indium-antiomonide isolator which prevents reflections from the secondary mirror of the telescope from entering the master laser cavity. The pulse train, after being expanded to a diameter of 15mm, is then directed into a 6-tube power-amplifier array which provides approximately 40 dB of gain. The pulse train next passes through a Brewster window, a quarter-wave plate (which converts the polarization from linear to circular) and into a collimated 30cm diameter telescope where the pulse train is expanded to approximately 24 cm ($1/e^2$) and directed into the atmosphere. These pulses are scattered by particulates on the order of from 1 to 10 μm in size which are naturally entrained in the atmosphere. Some of the scattered light returns along the same optical path as the incident beam, after having been Doppler shifted in frequency by an amount proportional to the radial component of the aerosol velocity, and reversed in its direction of circular polarization. Measurement of this Doppler Shift in frequency is the primary purpose of the Lidar. The backscattered beam is collected by the telescope, passed through the quarter-wave plate and reflected by the Brewster window to the HgCdTe detector, where it is mixed with the LO beam. The reflection from the Brewster plate is enhanced by the change in polarization at the target, which results in linear polarization of the scattered beam at 90° to the polarization of the transmitter.

SYSTEM CAPABILITY SUMMARY

The System's range capability is determined by characteristics of the atmosphere and of the system. At the present time, the system's minimum range is 3 kilometers, due to detector saturation caused by the backscattering of transmitted light from the secondary mirror. Except for highly reflective targets such as clouds or the ground, the usual maximum range at which signals are received is limited by beam propagation effects to less than 15 kilometers. In the recent flight tests useful signals were obtained with backscatter coefficients estimated at $2 \times 10^{-9} m^{-1} steradian^{-1}$ or less. Particle sampling measurements have been used to predict CO_2 backscatter coefficients, and these analyses indicate a wide spread in the atmospheric backscatter coefficients. A new measurement program is being planned to make quantitative backscatter measurements at different altitudes, locations, and times to more accurately determine the operational capability of the system.

The resolution of the system in space, velocity and time may be varied within some limitations. Typical operation of the system during the CAT flight tests used an 8 microsecond pulse, resulting in a velocity resolution of 0.5 m/sec and a range resolution of 1.2 kilometers. The actual range or velocity estimate for a target may be improved by approximately $\sqrt{N}$ by integrating N pulses and them employing adaptive thresholding and statistical analysis.

The pulse repetition frequency of the system is typically 140 pulses per second, and, in typical operation, 25 to 50 pulses are integrated to produce a single data sample. This results in 3 to 6 data samples per second. During previous tests each data sample has included complete spectral data over a 10 megahertz (50 m/sec) bandwidth for a single selected range gate. A new processor, presently being installed, will provide processed spectral parameters for each range gate over the same range of data rates. Thus, while complete spectral data will not be available, parameters from all range gates will become available at the specified update rate. This will result in considerably more efficient use of the available data.

The display capabilities of the system include the real-time analog displays of processor outputs, near-real-time displays of algorithm results from the on-line mini computer, and more detailed displays which may be obtained at the completion of a mission. The real-time analog displays include the RVI, IVI, and A-Scope. These displays are shown in Figure 3. The top display is the RVI, which displays range on the horizontal axis, velocity on the vertical axis, and amplitude with intensity modulation of the display. At short ranges, the display in the

figure shows the saturation effect mentioned previously. At longer range, it shows a velocity which decreases and then increases with increasing range, along with varying amplitudes and spectral widths, and a distant return from a cloud or solid object. While this three-dimensional display is useful for a qualitative evaluation of the system, and for locating interesting features, it is not amenable to quantitative analysis. For these purposes, two-dimensional displays are more useful, and two such displays may be obtained by looking at slices of the RVI display, as indicated by the lines in the figure. The IVI shows the spectrum of the return at a selected range. The logarithm of the intensity is plotted as a function of frequency (velocity). This represents a vertical slice at a selected range through the RVI display. The A-Scope provides the opposite type of displays, showing the variations in intensity as a function of range at a selected velocity. In the indicated display, the atmospheric return has contributions at the selected velocity at two different ranges. The range scale is selectable, but is generally set at 16 kilometers, full scale. The on-line mini computer provides a means for recording the Lidar processor data, ancillary data from other sources, time and run number, and provides selected parameter displays. For example velocity, spectral width, or amplitude could be plotted with respect to time, range, or other parameters. The mini computer provides a number of default displays, and additional displays can be selected by the operator. All data are recorded on magnetic tape for more detailed analysis with the mini computer or with an off-line large-scale computer.

AIRBORNE MEASUREMENTS

During the 1979 flight tests, many different measurements were made to verify the different operational capabilities of the system. Calibration measurements were made using reasonably uniform hard targets, such as the desert floor to determine the system sensitivity. Velocity comparisons were made to verify measurements of the correct Doppler frequency. Power spectral density measurements of the atmospheric velocity were made as well as actual measurements of clear air turbulence encounters. This section will describe one of each of these types of measurements.

Several approaches were made at various solid targets to establish the sensitivity of the system. The most consistent results were obtained from the desert sand at Edwards AFB. Knowing the reflectivity $\rho(\pi)$ of the solid target and the pulse length, $\Delta\ell$, it is easy to calculate the atmospheric backscatter coefficient which would produce the same signal;

$$\beta_1 (\pi) = \rho (\pi)/\Delta\ell. \qquad (1)$$

The minimum detectable backscatter coefficient is in the same ratio to this as the minimum detectable signal is to the calibration signal;

$$\frac{\beta_{min}\ (\pi)}{\beta_1\ (\pi)} = \frac{SNR_{min}}{SNR_1} \qquad (2)$$

From this, the estimate of $\beta_{min}\ (\pi) = 2 \times 10^{-9} m^{-1} steradians^{-1}$ was obtained.

A comparison of the ground speed as measured by the Doppler Lidar to that measured by the aircraft Inertial Navigation System (INS) is shown in figure 4. These measurements were made during flight 28 on March 26, 1979. The aircraft plot was constructed by simply plotting the ground speed as measured by the aircraft INS. The Lidar plot was somewhat more complicated to construct, since the ground return had to be tracked in range as the dive progressed. This was accomplished by scanning in range, identifying the ground return in each scan by its amplitude characteristics, and calculating the mean of the signal spectrum through an automatic thresholding routine. The ground speed was then determined by multiplying the resultant velocity by the cosine of the pitch angle, taking into account the -1.5 degree offset for the pointing of the Lidar pod. The average difference in these ground speed measurements is 4.52 meters per second with a standard deviation of 0.6 meters per second. During the flight, comparison of airborne digital data acquisition system (ADDAS) with cockpit data indicated that the ADDAS-system velocity data were approximately 3 meters per second slow. The remaining 1.5 meters per second difference between the Lidar and the aircraft velocity measurements lies well within the error bounds of the aircraft measurement system.

A 13-minute segment of the mean wind-velocity component in the direction of the aircraft heading is shown in figure 5. This was measured 3 kilometers in front of the aircraft at an altitude of approximately 8.5 kilometers. Overall variations of approximately 8 m/s are indicated for the duration of the sample. This plot was produced by calculating the mean velocity of the spectrum, averaged over 50 pulses, at a rate of roughly 3 times a second. This time history has been corrected for ground-speed component in the measurement direction. This was obtained by multiplying the ground speed by the cosine of the drift angle (the angle between the aircraft heading and the actual direction of travel).

The power spectral density plot for this sample is shown at the bottom of figure 5. This plot was produced using a 2048 point FFT with Blackman windowing and the mean extracted. As can be seen from the plot, the -5/3 slope, predicted by Kolmogorov, is followed rather well out to a frequency of about .15 Hz

where it tends to level off to noise. At an airspeed of approximately 235 m/s this corresponds to a spatial length of about 1.5 kilometers, which corresponds reasonably well to the pulse length of about 1.2 km. It was anticipated that turbulence length scales below this length would not be resolved by this technique. However, turbulence length scales below this limit do contribute to the spectral spread of the Lidar signal. Consequently by combining this technique with spectral processing of the Lidar signal, turbulence length scales from several hundred kilometers (such as the case above) down to several meters can be measured. The lower limit is determined by such inherent effects as signal-to-noise ratio, processor bandwidth, and spectral broadening caused by system characteristics.

An example of spectral broadening associated with clear air turbulence is shown in figure 6. This figure shows, on a single plot, the spectral broadening due to turbulence length scales less than the pulse length and the accelerations actually encountered by the aircraft. In this case, the broadening of the spectrum occurs about 20 seconds before the turbulence encounter. An automated analysis of selected turbulence encounters and additional analysis of power spectral densities at the longer turbulence scales are in the process of being implemented.

FUTURE PROGRAMS

The Lidar is presently being modified to perform measurements of the clear-air regions around severe storms. The transmitter will be overhauled and a new off-axis telescope obtained, which will eliminate the saturation effects at near ranges (caused by reflections from the secondary mirror in the present telescope). A scan system is being constructed which will allow the scan pattern shown in figure 7. This type of scanning will allow the measurement of the mean wind velocity components in a region from two different view angles, thereby allowing resolution of the horizontal vector wind velocity.

A new signal processing system is being installed which will calculate the spectral power, mean frequency, and width for each range gate for every integration period. This information will be fed to a central timing and control system, which incorporates the location data from the scanner and the aircraft and interfaces to an on-line PDP11-35 computer for processing.

The output of this measurement will be in the form of a two-dimensional vector map of the velocities in the horizontal plane at the altitude of the aircraft.

A flight test of this system is planned for June and July of 1981. Successful results in this test will, in all probability, lead to additional measurements being performed in 1982

and 1983.

Because of the importance of atmospheric-backscatter-coefficient levels to system operations, a test program has been undertaken to develop and fly a compact, CW, Doppler Lidar. This program is aimed specifically at establishing the backscatter-coefficient variation with altitude and location. A long-term program to attempt to establish the temporal as well as spatial variation over the next 3 years is being planned.

SUMMARY

An airborne Doppler Lidar has been described which has been used successfully to detect turbulence and to perform large-scale wind variation measurements. The airborne measurement program, which took place in January through March 1979, was conducted by personnel from the Raytheon Company and Marshall Space Flight Center. The real-time and post-processing software utilized in obtaining the selected data samples were provided by the M&S Computing Corporation. Post-processing software for data generated on the Univac 1108 computer was provided by Computer Science Corporation. The flight operations were performed by Ames Research Center and meteorological support was provided by Dryden Flight Research Center, the United States Air Force, Stanford Research Institute and Marshall Space Flight Center. Particulate studies were performed by Alabama A&M University.

REFERENCES

1. Development of CO_2 Laser Doppler Instrumentation for Detection of Clear Air Turbulence, Final Report 10 February 1972 - 27 December 1978, ER78-4392-1 NASA Contract NAS8-28424, C.E. Harris, A.V. Jelalian

2. Huffaker, R.M., "CO_2 Laser Doppler Systems for the Measurement of Atmospheric Winds and Turbulence," Atmospheric Technology, NCAR, Winter, 1974-75.

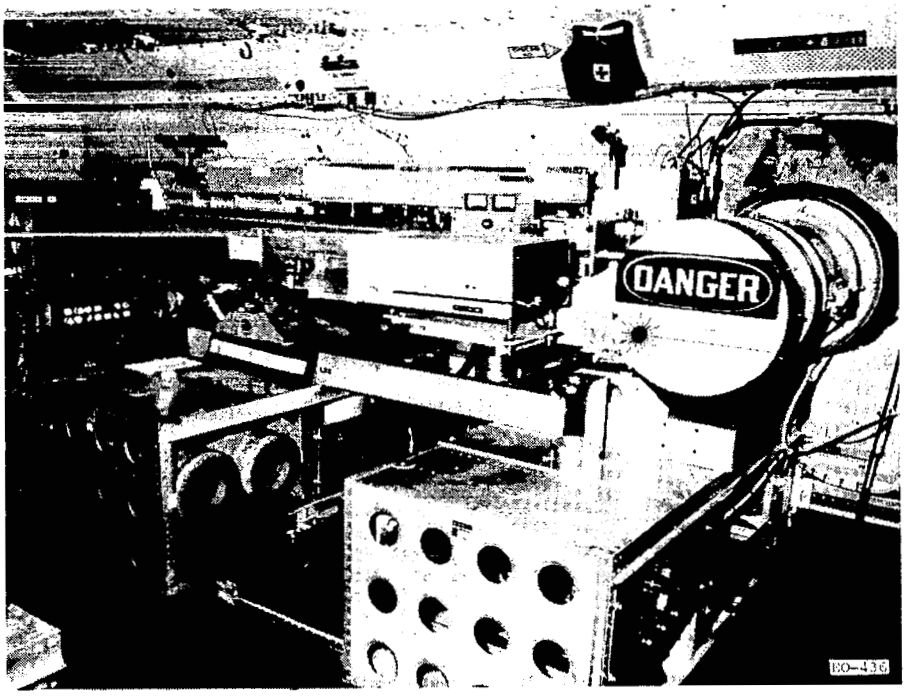

Figure 1.- Pulsed CO_2 Doppler Lidar in aircraft.

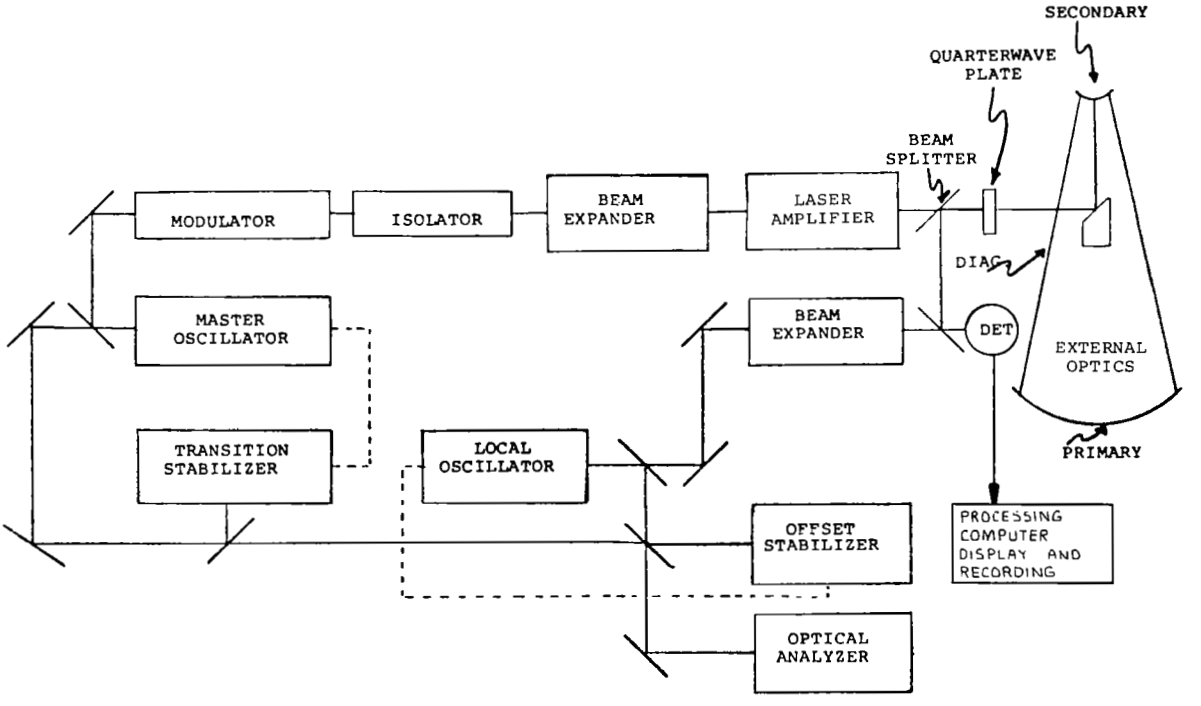

Figure 2.- Pulsed CO_2 Doppler Lidar block diagram.

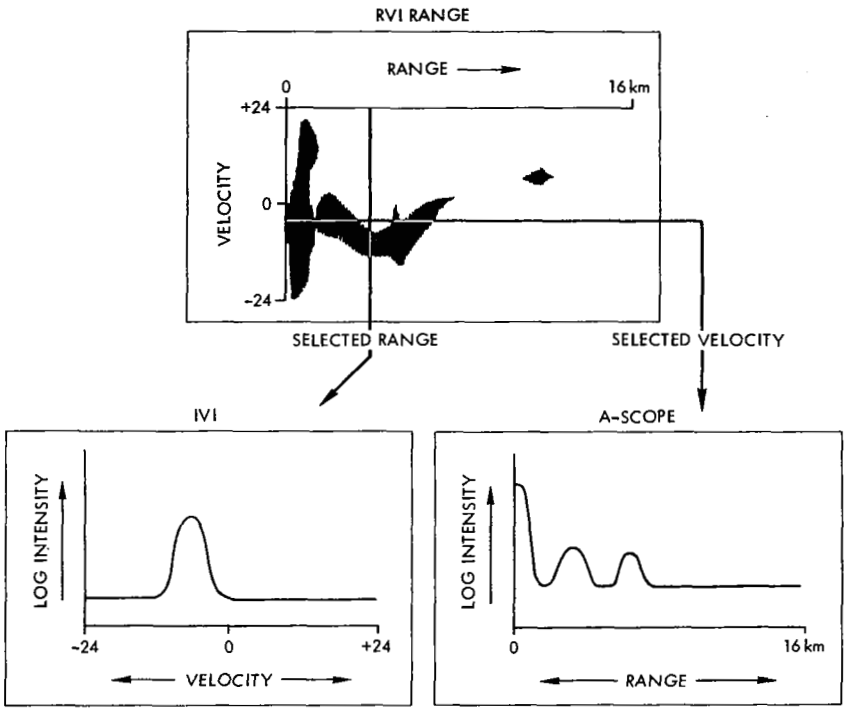

Figure 3.- CAT detection real-time displays.

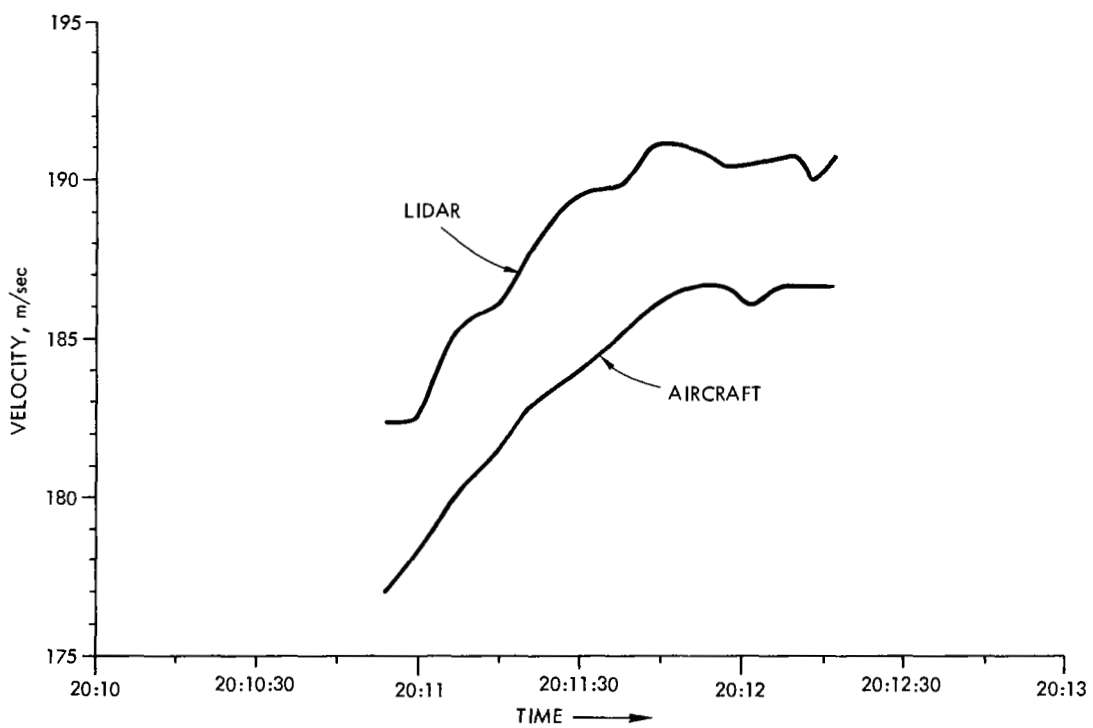

Figure 4.- Pulsed CO_2 Doppler Lidar velocity comparison using ground as a target.

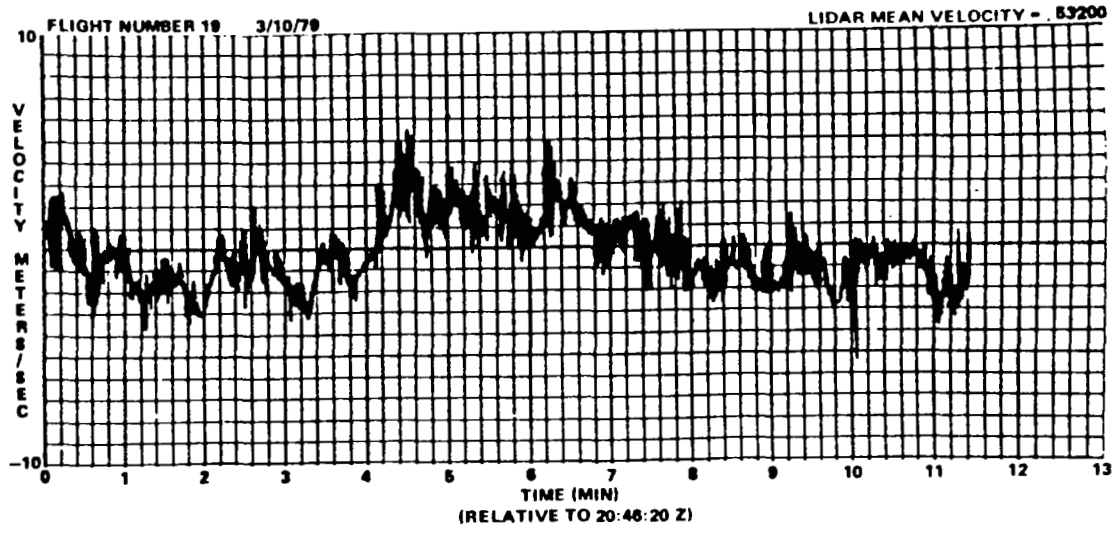

A. VELOCITY TIME HISTORY

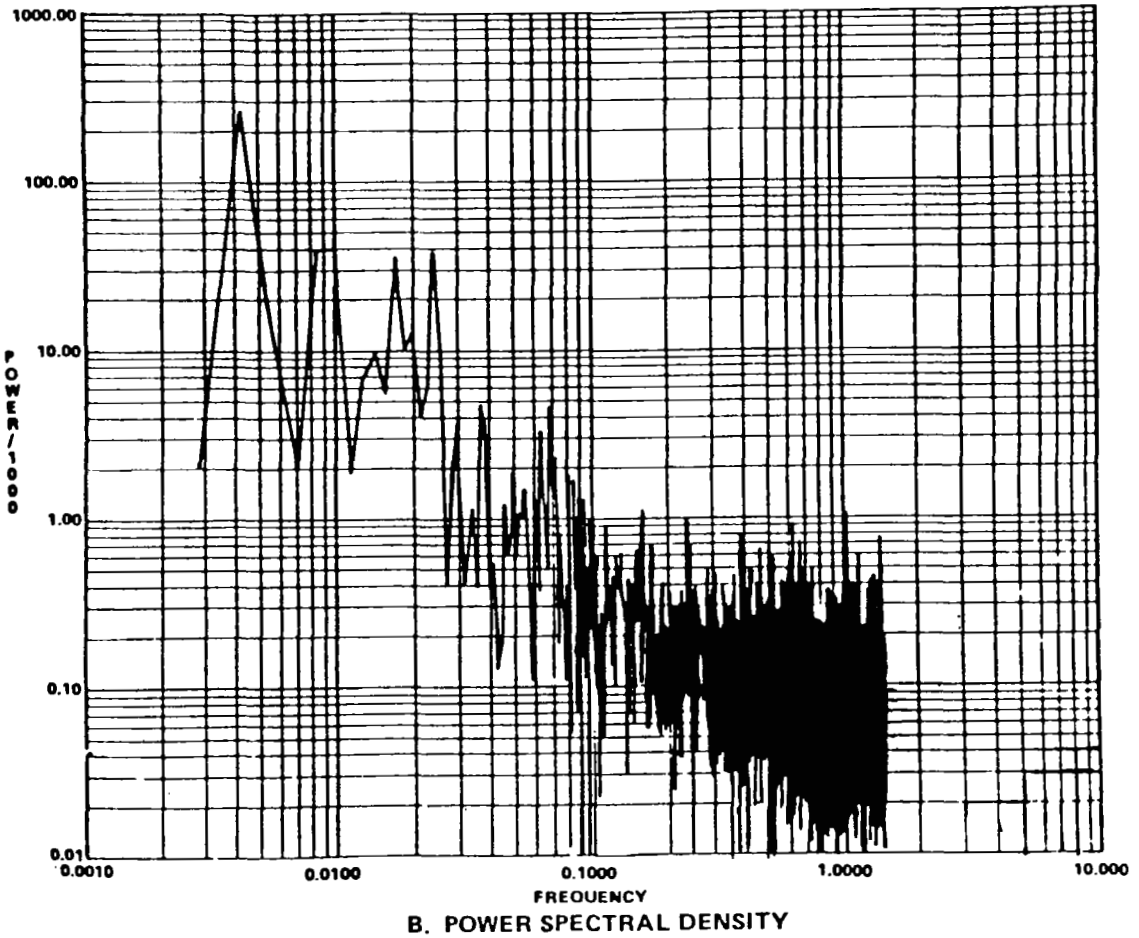

B. POWER SPECTRAL DENSITY

Figure 5.- Atmospheric-velocity measurements with a pulsed CO_2 Lidar.

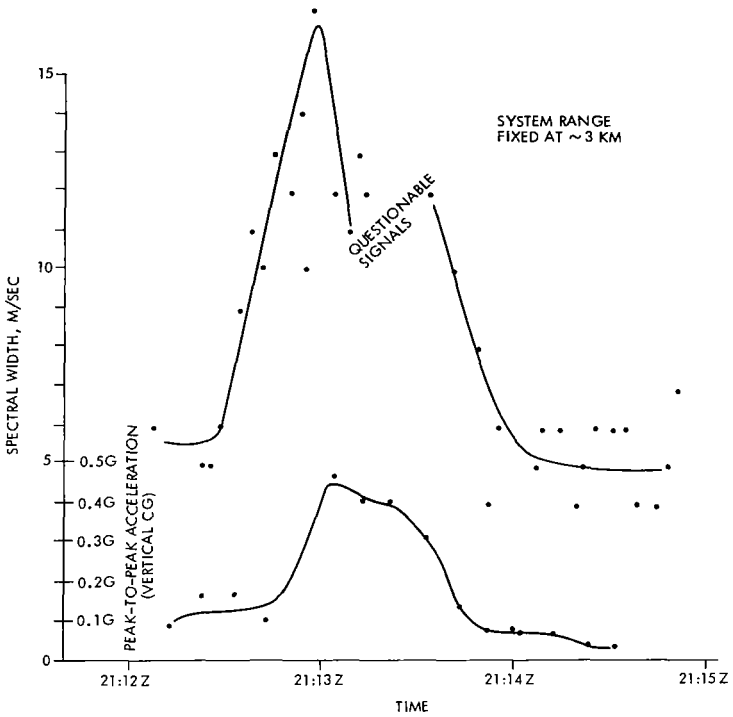

Figure 6.- Time history of a CAT encounter.

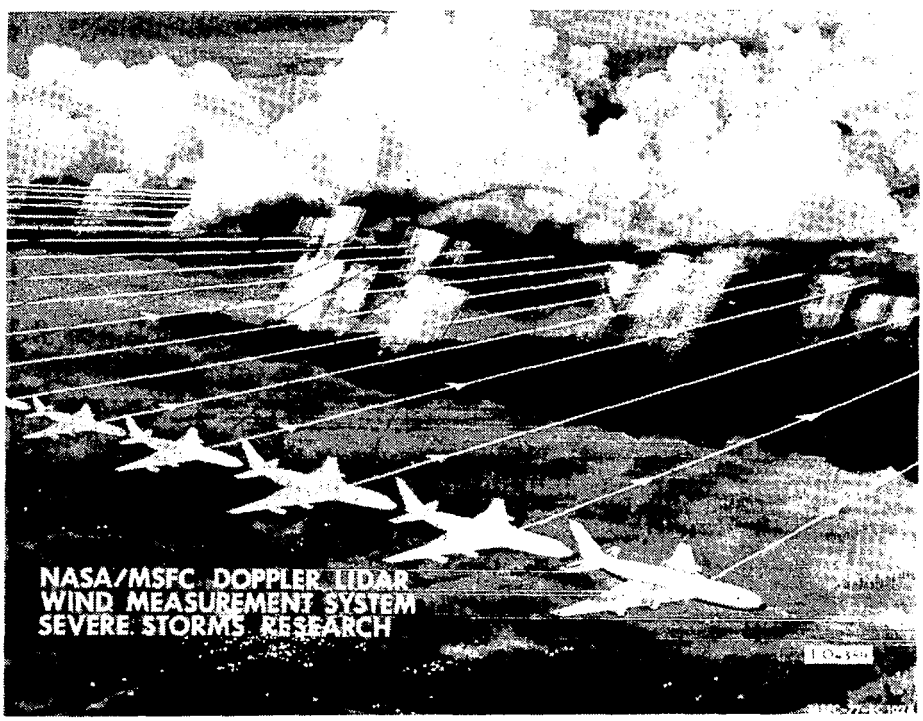

Figure 7.- Severe storm measurement concept.

SURFACE RELIEF STRUCTURES FOR MULTIPLE BEAM LO GENERATION WITH HETERODYNING DETECTOR ARRAYS*

Wilfrid B. Veldkamp
Massachusetts Institute of Technology
Lincoln Laboratory
Lexington, Massachusetts 02173

SUMMARY

Linear and binary holograms have been developed for use in heterodyne detection with 10.6μm imaging arrays. These devices match the amplitude and phase of the local oscillator to the received signal and thus maximize the system signal-to-noise ratio and resolution and minimize heat generation on the focal plane. In both the linear and binary approaches, the holographic surface-relief pattern is coded to generate a set of local oscillator beams when the relief pattern is illuminated by a single plane-wave. Each beam of this set has the same amplitude shape distribution as, and is collinear with, each single element wavefront illuminating array.

INTRODUCTION

High-resolution infrared laser radars (ref. 1) often suffer from considerable loss of image quality due to speckle noise. This speckle noise is caused by the constructive and destructive interference of wavefronts reflected from a rough target and from the large spatial coherence of the laser radiation source. The only feasible way, at present, to improve the speckle-degraded image quality is to average a number of frames of the scanned image, pixel by pixel. The frame-averaging requirement is for very high scan rates. The use of a detector array reduces this requirement; i.e., it reduces the scan rate while increasing the frame rate.

A problem in high-efficiency heterodyne detection with detector arrays is the loss of heterodyne efficiency due to the misalignment of signal and local-oscillator (LO) wavefronts away from the optical axis when a single uniform local oscillator wavefront is used. The heterodyne efficiency, which is proportional to the vector dot product of the

*This work was sponsored by the Department of the Air Force.

signal (ref. 2) and the local oscillator wavefronts integrated over the entire detector area, decreases rapidly with angular misalignment of signal and LO wavefronts. When this angular misalignment approaches $\theta \approx \lambda/d$ where d is the detector diameter, the detection efficiency falls to approximately zero. This destructive interference imposes a restriction on the maximum number, n, of detector elements in an array with detector separation, s, and at a distance, ℓ, away from a signal exit aperture,

$$n << \frac{\lambda}{d} \cdot \frac{\ell}{s} \tag{1}$$

This type of detection efficiency loss can be alleviated considerably with the use of a cylindrical LO wavefront. Other sources of detection efficiency degradation are mismatches between signal and LO wavefront amplitude distributions and between optimum detector size, d, and the signal diffraction limited Airy spot size. These detection efficiency losses can be quite severe, particularly for telescopes with high obscuration ratio's (see figure 1). Finally the use of a uniform-intensity local oscillator not only reduces the S/N by creating excess LO noise but also generates excess focal-plane heat and lowers the heterodyning system's spatial frequency resolution. Thus, the desirability of an amplitude and angular phase-matched set of LO's is clear.

In our approach, we used a holographic surface-relief grating to generate a set of LO's. A uniform plane-wave of a single LO illuminates the grating so that the reflected light, after passing through the detector focussing lens, consists of a fan of N plane waves focussed on each of the N detectors in the array in phase with the incoming signal (see figure 2). In addition, if the virtual exit aperture calculated for the signal beam path is replaced by a real aperture, then the size of the holographic grating can be chosen to equal or exceed the size necessary to obtain diffraction-limited LO amplitude distributions of the same size as the signal amplitude distribution. The LO amplitude distribution then must have enough spatial frequency bandwidth in the Fourier domain to exceed the spatial frequency bandwidth set by the real exit aperture acting as a low-pass filter. Consequently, the optical signal wavefronts and the LO wavefronts are space-limited by the same low-pass filter and exact signal-to-LO diffraction-limited amplitude matching occurs.

Two techniques were developed to generate the necessary high-accuracy optical-phase relief gratings. The first approach, called the linear or optical technique used the classical concept of holographic recordings in photosensitive materials (positive photoresist). In the recording step, an optical wavefront simulating the LO wavefronts is recorded in photoresist at a blue or near UV wavelength that matches the resist sensitivity. In the reconstruction step, a scaled IR optical wavefront simulating the LO's is generated by reilluminating the recording with an IR (10.6μm) plane wave.

The second approach called the binary or synthetic technique uses a real non-negative coding scheme to generate a complex wavefront with binary π-phase steps deposited on a reflective substrate. When this substrate is

reillluminated with a plane wavefront of the appropriate wavelength, a uniform set of uniform plane LO wavefronts is generated without any need for a previous optical recording.

HOLOGRAPHIC GRATING FABRICATION

The Linear Technique

In the linear (optical) technique (see figure 3), a phase-holographic recording of a reference wavefront and an information wavefront are made in photoresist (AZ 1350-J) with the use of an Argon ion laser beam tuned to 4579 Å. The information beam consists of a set of N plane-waves generated by a scaled metallic mask containing apertures simulating the detector array. Each aperture in the mask acts as a point source that generates a plane-wave by lens Fourier transformation or by propagation, depending on the size of the apertures. The information beam is mixed with a uniform plane-wave at an angle θ_b, and the interference pattern is recorded on a pretreated substrate coated with photoresist (see figure 4). The coherent exposure records the interference pattern in the photoresist by deactivating a photoactive inhibitor compound with a deactivation density proportional to the optic field intensity distribution. In the following resist development step, the light exposure distribution is transformed into a relief pattern at a rate of approximately 1500 Å/sec (ref. 3). The relief depth controls the ultimate diffraction efficiency of the grating (refs. 4 and 5). Because of the mechanical instability of the resist, the relief pattern must be transferred to a mechanically stable and highly reflective substrate. This can be done by ion-beam etching chemical wet etching, or electroplating.

Reillumination of the holographic relief grating with IR light will recreate a set of N uniform plane-wavefronts scaled in angles θ_{IR} and in spatial coordinates X_{IR} in the image domain according to the first-order expressions shown in figure 4. It can be shown that of the Seidel aberrations caused by the mismatch of the three wavefronts, only distortion can not be avoided in Fourier holograms undergoing a wavelength transformation. (ref. 4). However, the positions of the apertures in the object mask simulating the detector array have been calculated and predistorted to compensate for this mismatch.

Typical mask apertures used in these experiments were 8μm in diameter and positioned at approximately 25μm intervals. Position accuracy was better than 1μm. The large wavelength scaling ratio $\lambda_{IR}/\lambda_b \approx 23$ caused the interference angle θ_b to be very small, approximately 1.3°, and required the use of a Mach-Zehnder interferometer recording arrangement with a beam expander and spatial filter in one branch and the metallic mask in the other. Better than $\lambda/50$ optics were used throughout the recording arrangement.

The three problem areas of the technique are (1) substrate reflections, (2) resist deposition flatness quality, and (3) dynamic range of the optic field and resist non-linearities. We chose SKN-5 glass as a substrate material and AR coated the back side with 1/4 λ MgF_2 to avoid the formation of serious interference nodes in the plane of the resist due to reflection from the resist-substrate and substrate-air boundaries. The refractive index of SKN-5 glass closely matches that of AZ-1350J resist ($n \approx 1.675$). Of course, refractive index matching with the liquid glycerol in contact with black chrome can reduce reflections even more. The deleterious effects of substrate reflections are important - - even a 1% residual reflection can cause a 20 or 30% change in developed relief height.

Microfinish and macroflatness are also important for good reconstruction image quality. Microfinish imperfections cause a random relief pattern in the developed photoresist rather than a smooth etching surface and in turn cause a noisy LO background. The deposition of a uniformly thick resist on a one-inch substrate was an extremely difficult problem in our effort to develop high quality (i.e., large array) linear holographic beam formers. To some extent, all our samples exhibited the characteristic doughnut resist spinning profile together with resist redepositions from scattering in the spinner bowl (even in an acetone atmosphere). These nonuniformities are very destructive for holographic recordings where the lowest and incremental spatial frequencies are 0.25 lines/mm.

A third problem concerns the large-intensity dynamic range of the information beam and the limited materials linearity. The material nonlinear distortions have been studied by many researchers (refs. 6 and 7). They are particularly severe in thick resist layers. A coherent superposition of plane-waves leads to a $[\sin Nx / \sin x]^2$ intensity distribution. The minimum dynamic range that needs to be recorded is 23 db. The only feasible way to reduce the dynamic range of the information beam is to introduce randomizing phases in each of the apertures forming the mask. Considering the microscopic size of the mask, this is not an easy task.

Figure 5 shows a single HgCdTe detector scan past the focussed IR(10.6μm) image of a three-element mask that forms a three-beam amplitude-shaped LO. These three LO beams are separated by 530μm, using the magnification of a 12 cm focal length lens, exhibit a very low optical noise background, and produce an optical conversion efficiency of approximately 12%. The width of the LO beams is controlled by the low-pass filtering characteristics of the exit aperture or by the relief hologram's size.

It is our experience that with this technique and its severe limitations of photoresist linearity and large dynamic intensity range of the optic field, a maximum of 8- to 10-high optical-quality LO beams per linear dimension with an arbitrary spatial distribution can be generated. This number of LO's can, of course, be increased somewhat if lower and lower power conversion efficiencies can be tolerated.

The Binary Technique

In the binary (computer lithographic) technique (see figure 3), a grating is formed by a reflective substrate on which a series of small reflective strips separated by an air gap have been deposited. The position and width parameters of these strips can be used to code a complex object wavefront using the phase detour principle in a real non-negative functional form so that the wavefront can be regenerated by optical means.

Our goal is to generate a fan of N uniform plane-waves that are focussed by the system's exit lens onto each of the N elements of a detector array with equal intensity. This approach requires a Fourier superposition of plane-waves of the form,

$$\frac{1}{N} \sum_{n=1}^{N} A_o \, e^{2\pi j n \alpha x} \tag{2}$$

where the propagation vector $k = 2\pi\alpha$ is determined by the detector configuration and the focal length, f, of the lens. That is,

$$\lambda f \alpha = d + s \tag{3}$$

where d + s is the detector spacing (see figure 6). The system's exit lens focal length is in turn determined by the necessary signal and LO spot sizes to be matched to the detector size, i.e.,

$$\frac{2.44\ \lambda f}{D} \approx 0.75\ d \tag{4}$$

for a grating size of diameter D. The combination of expressions 3 and 4 yields a spatial frequency of $\alpha \approx 0.437\ 10^{3}$ 1/meter from our system parameters.

To avoid overlap with the strong undiffracted beam components, this collection of plane-waves must be placed on a spatial carrier frequency that diffracts the light at an angle β. This carrier frequency (or equivalently, diffraction angle) must be chosen judiciously so that no signal aliasing occurs between the different diffraction orders, yet must be large enough so that the fringe periodicity is not limited by the pattern generator resolution. From a simplified analysis outlined in figure 6, one can determine that for a diffraction angle β of only a few degrees, the fringe accuracy over a 750 mils holographic grating must be in the order of 500 Å if a 10% LO misalignment can be tolerated. This is a very high accuracy requirement.

There is, however, another choice: the grating carrier frequency of period T can be changed from either parallel (x direction) to or orthogonal (y direction) to the carrier frequency 1/T. After the orthogonal placement of carrier and information spatial frequencies, β_{max} equals $N\alpha/2$, and the grating tolerance is greatly relaxed to an accuracy of a few μm over the holographic surface.

The required phase of the LO wavefront $\phi(y)$ can, therefore, be described by

$$e^{j\phi(y)} \sim \sum_{n=-N/2}^{N/2} e^{2\pi jn\alpha y} \tag{5}$$

or

$$e^{j\phi(y)} \sim [1 + 2 \sum_{n=1}^{N/2} \cos 2\pi n\alpha y]$$

Unfortunately, the phase $\phi(y)$ that describes the plane-wave superposition cannot be extracted in real form for substitution in a phase detour equation. This problem can be remedied by creating a composite grating of period T and shifting its reflection by a phase $\exp(j\pi/2)$ or, equivalently, a T/2 period. If this plane-wave distribution generated by the composite grating is equated to the required superposition of plane-waves, one finds the holographic phase modulation $\phi(y)$ of each fringe, i.e.,

$$\phi(y) \sim \sin^{-1} [m(\frac{1}{2} + \sum_{n=1}^{N/2} \cos 2\pi n\alpha)] \tag{6}$$

where m is proportional to the modulation depth of the fringes.

The dynamic range of this phase distribution and that of the generated optic field can be reduced considerably by introducing a randomizing phase factor $\exp(j\psi_n)$ to each of the plane-waves in N/2 conjugate pairs,

$$\phi(y) = \sin^{-1} [\frac{m}{\sqrt{2N}} (\frac{1}{2} + \sum_{n=1}^{N/2} \cos(2\pi n\alpha y + \psi_n))] \tag{7}$$

In our system, we have chosen a deterministic binary phase code (ref. 8), $\psi_n(0,0,0,\pi,0,0,\pi,0)$ that yields a dynamic range reduction of at least $(\sqrt{2N})^{-1}$. Many other binary and polyphase codes exist (ref. 9) that bound the amplitude dynamic range of a plane-wave superposition. This randomizing phase factor has the same effect as introducing microscopic phase plates in the mask apertures in the optical technique. It simply randomizes the phases between the LO's but maintains a constant phase over each detector surface.

Each plane-wave component of this sum, therefore, interferes with the incident reference wavefront $\exp(2\pi j\, x/\lambda \sin\beta)$. Using the Bragg condition, the reference wavefront is $\exp(2\pi j\, x/T)$. The resulting interference forms a fringe pattern that satisfies the following periodic equations (phase detour principle):

$$x = \frac{-\phi(y)}{2\pi} T + nT$$

$$x = \frac{\phi(y) + \pi}{2\pi} T + nT \qquad (8)$$

where T is the periodicity or distance between two homologous points along the grating. A partial, strongly aberrated, visible-light (HeNe) reconstruction of a 17-element LO array is shown in figure 7.

A high resolution pattern generator uses equation (7) to generate a hologram large enough to satisfy the required space-bandwidth product by repeatedly plotting the fringe pairs of equations (8). The holographic patterns were initially generated at 5X magnification on a Kodak emulsion plate using a Mann 1600-A pattern generator. The building block rectangle size was 38 x 2 mils with 0.5 mil accuracy on a 5X reticle. In order to use a pattern generator with this limited accuracy we had to enhance its accuracy and resolution artificially. This was done by plotting a reticle of a single square holographic unit cell and by a 5X photoreduction. Then with a step-and-repeat process, the hologram was built up of these unit cells to its diffraction-limited size. Another 5X photoreduction brought the mask down to its final size while maintaining the absolute spatial frequency of the grating. This process, of course, also reduced pattern generation time considerably to approximately 8 1/2 hours.

The resulting phase quantization of the highest image spatial frequency component was 80 and the amplitude quantization was 20. The effects of these quantizations are difficult to analyze (ref. 10). If, however, the quantization errors are assumed to be uniformly random, then it can be shown that optimum-magnitude quantization depends on the number of phase quantizations, N_p, via $[\sin(\pi/N_p)/(\pi/N_p)]$, i.e., amplitude-phase coupling between errors exists (ref. 11).

After completion of the pattern in the primary emulsion mask it is replicated in thin positive resist on a chrome-coated conformable mask and is chemically etched. A photograph of a section of such a mask is shown in figure 8. The period between two homologous points in the x direction (vertical) is 2 mils, whereas the y direction (horizontal) carries the information, i.e., the phase modulation $\phi(y)$. The final substrate is then coated with thick resist (approximately $1/4\ \lambda \cos\theta$, where θ is the angle of incidence) and is exposed through this conformable mask in intimate contact and is developed. The close contact is essential to avoid degradation of the thick resist side-walls and to maintain the high

acuity. Ion beam bombardment of the relief surface transfers the developed resist pattern into a stable substrate. The ion beam etching applies to both linear holograms (where the resist is not developed away down to the substrate) and binary holograms (where it is). By choosing a suitable substrate with a high ion-beam-etch ratio compared to the resist, we can take advantage of the resist-substrate-etch magnification ratio, i.e., AZ1350:ST-quartz:Poly-GaAs = 150:279:575 Å/min. The cleanup of the residual resist and organics was performed by immersing the sample in a plasma of 97% He and 3% O_2. Figure 9 shows these processing steps for both the linear and binary techniques. A final 800 Å chrome-gold coating provides the needed reflection for efficient power conversion (see figure 10).

These binary gratings were also tested by scanning the focussed first-order diffracted wavefront with a single HgCdTe detector obscured by a 10μm pinhole. The result of this one-dimensional scan of the 17-element LO beam profile is shown in figure 11. The LO beams were separated by 112μm, consistent with the detector separation in the array. They exhibited low optical background noise. The orientation and periodicity (T = 3 mils) of this grating were chosen such that a 90° relationship existed between the incident wave and the first diffraction order. The nonuniformities between the different LO elements are assumed to be due to the inaccuracies in the step-and-repeat process that generated the grating from the individual unit cells. This step-and-repeater had a position accuracy of only 0.5 mils (approximately one wavelength) and imposed a periodic modulation on the LO amplitudes, whereas the low amplitude of the center LO was traced to a mathematical error in the program that generated the mask.

DISCUSSION

We have shown the feasibility of generating a set of LO's that are matched in amplitude distribution and angular phase with the incident signal wavefronts on 1- or 2-D detector arrays with the use of holographic relief gratings by two different techniques.

The number of LO's that can be generated with linear holograms in the optical technique is limited by the high dynamic range of the optic field and by resist linearity. Therefore, this technique, although useful, is restricted to small detector arrays (a maximum of 10 detectors per linear dimension) such as symmetrical detector configurations used for tracking purposes.

The binary technique has its limitations also, even though it eliminated or reduced the problems of substrate reflections, resist flatness, and dynamic range that hampered the optical technique. The major problems with the binary technique are pattern generator accuracy, resolution, and generation time. In addition, at high diffraction angles or low periodicities the fringe duty cycle and the phase modulation depth must be reduced more and more. When the fringe spacing becomes comparable to the wavelength

(i.e., $< 5\lambda$), the concept (in terms of constructive interference of waves that are specularly reflected) on which this theory is based no longer applies to surface dimensions comparable to the wavelength of the illuminating light. For instance, in figure 8, a picture of an earlier mask with $T \approx 50\mu m$, $m = 1$ and 20% fringe duty cycle (i.e., T/10 fringe width), we still observed strong polarization effects, resonances, and possibly surface plasmon effects (ref. 12). Reducing the grating periodicity and phase modulation range unfortunately also reduces the diffraction efficiency. The coding method we have discussed is by no means the only or most efficient one. Many more elaborate codes exist (ref. 13). It seems feasible to illuminate a 100-element heterodyning linear detector array with LO beams from a single binary grating with reasonable power efficiency.

REFERENCES

1. R. J. Hull and S. Marcus, Proceedings of IEEE National Aerospace and Electronics Conference, Dayton, Ohio, 662 (May 1978).

2. D. Fink, Appl. Opt. 14, 689 (1975).

3. S. Norman and M. Singh, Appl. Opt. 14, 818 (1975).

4. H. Smith, Principles of Holography, Wiley-Interscience (1969).

5. R. Bartolini, Appl. Opt. 13, 129 (1974).

6. M. Beesley and J. Castledine, Appl. Opt. 9, 2720 (1970).

7. A. Neureuther and F. Dill, Proceedings of Symposium on Optical and and Acoustical Micro-Electronics, Polytechnique Institute of New York, 223 (April 1974).

8. W. Rudin, Proc. of Am. Math, Soc 10, 855 (1959).

9. H. Akahori, Appl. Opt. 12, 2336 (1973).

10. R. Gabel and B. Lui, Appl. Opt. 9, 1180 (1970).

11. W. Dallas, Appl. Opt. 13, 2274 (1974).

12. K. Utagawa, J. Opt. Soc. Am. 69, 333 (1979).

13. C. Hsueh and A. Sawchuk, Appl. Opt. 17, 3874 (1978).

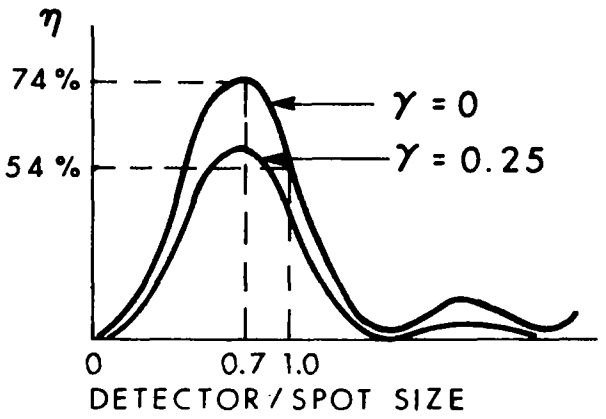

(a) Uniform LO illumination.

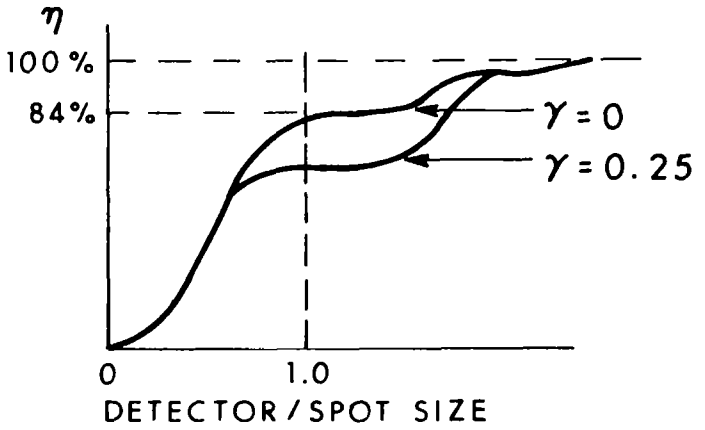

(b) Amplitude shape matched LO illumination.

Figure 1.- Heterodyne efficiency as a function of detector/signal-spot-size ratio.

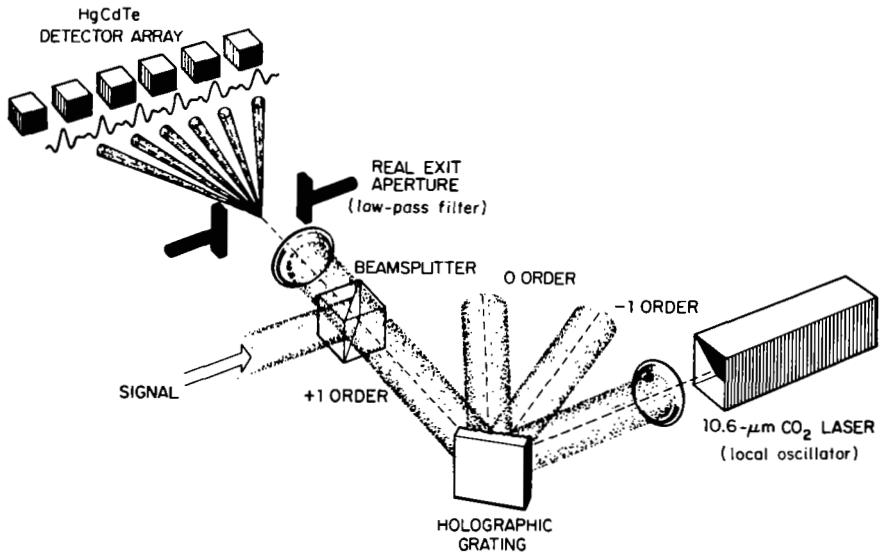

Figure 2.- Holographic generation of a multibeam local oscillator.

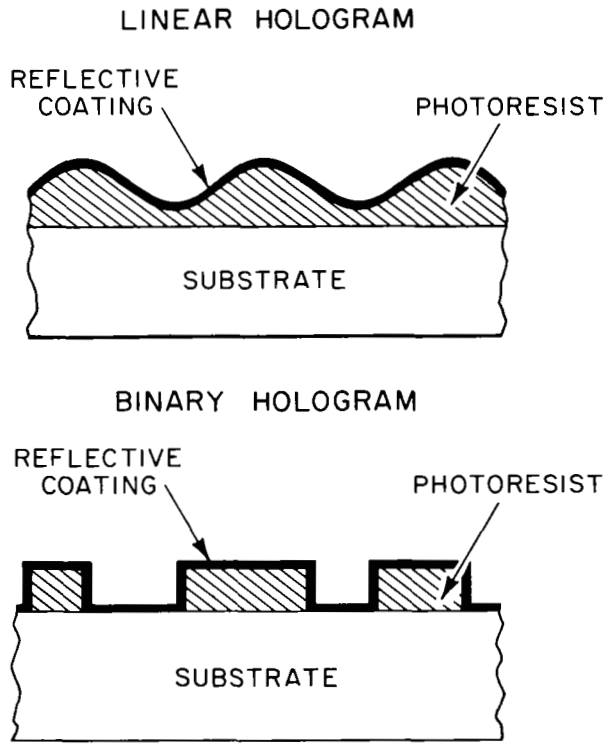

Figure 3.- Characteristics of linear and binary reflection holograms.

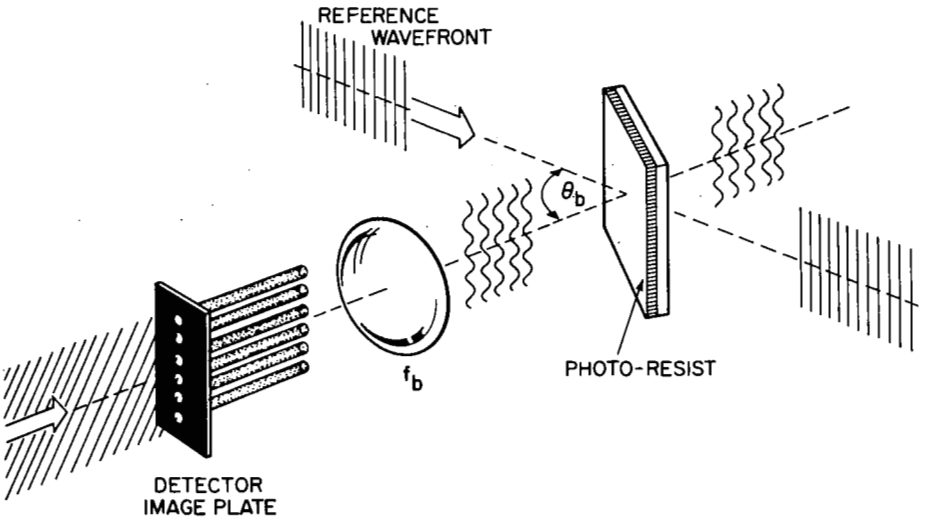

$$\text{TO FIRST ORDER:}\quad \theta_{IR} = \frac{\lambda_{IR}}{\lambda_b}\,\theta_b$$

$$X_{IR} = \frac{\lambda_{IR}}{\lambda_b}\cdot\frac{f_{IR}}{f_b}\cdot X'_b$$

Figure 4.- Formation of a linear holographic grating.

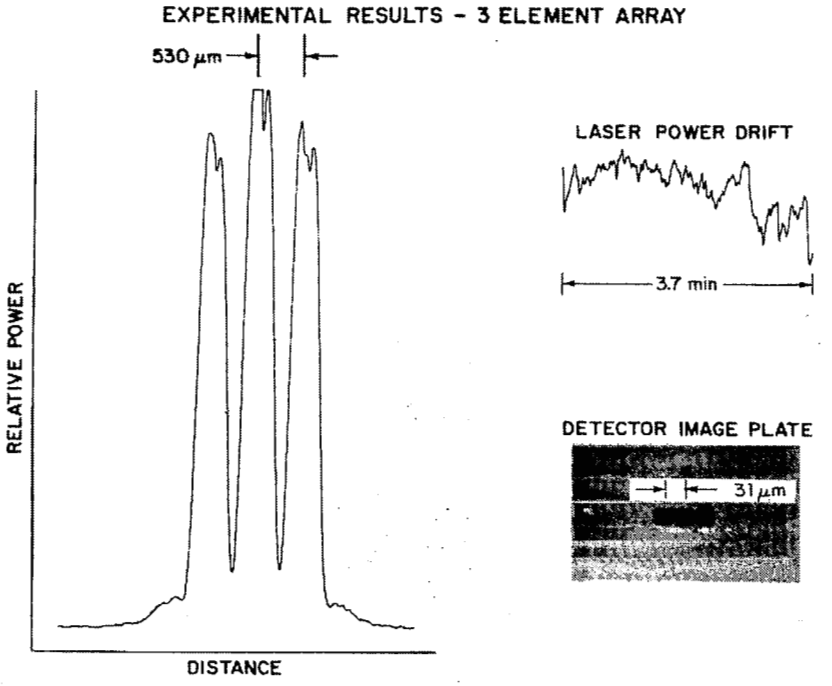

Figure 5.- An intensity scan past a three-element IR (10.6μm) local oscillator generated by a linear holographic grating.

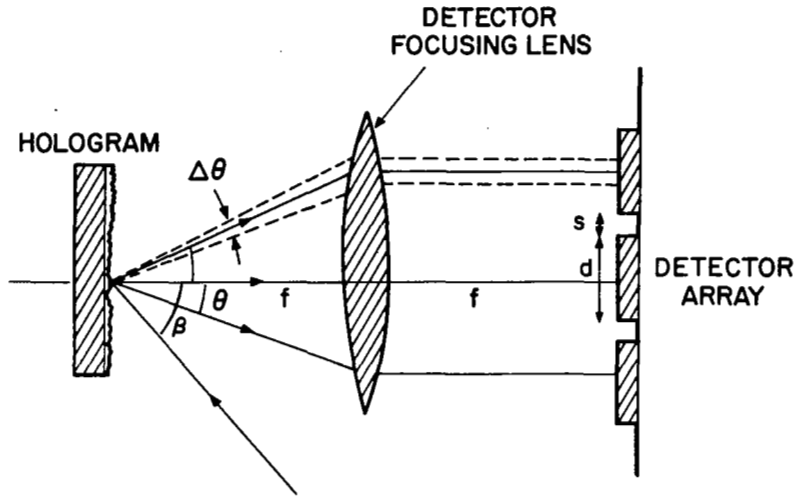

$$\text{GRATING LAW: } T = \frac{\lambda}{\sin\beta}$$

$$\text{GRATING TOLERANCE: } \Delta d_s = \frac{\cos\beta}{(\sin\beta)^2} \cdot \lambda \cdot \Delta\theta$$

$$\text{L.O. ALIGNMENT } \Delta\theta \leq \widehat{\tan}\left[\frac{d+s}{10f}\right]$$

Figure 6.- LO alignment dependence on fringe position accuracy.

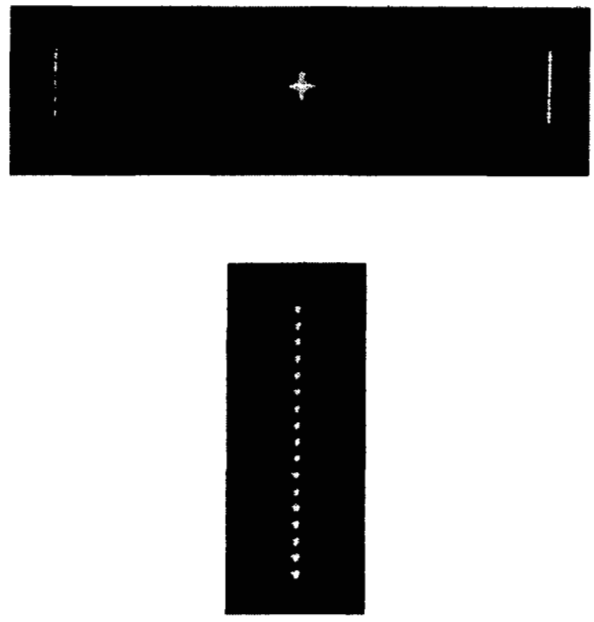

Figure 7.- A strongly magnified, aberrated, visible light (HeNe) reconstruction of a 17-element LO beam from a binary grating.

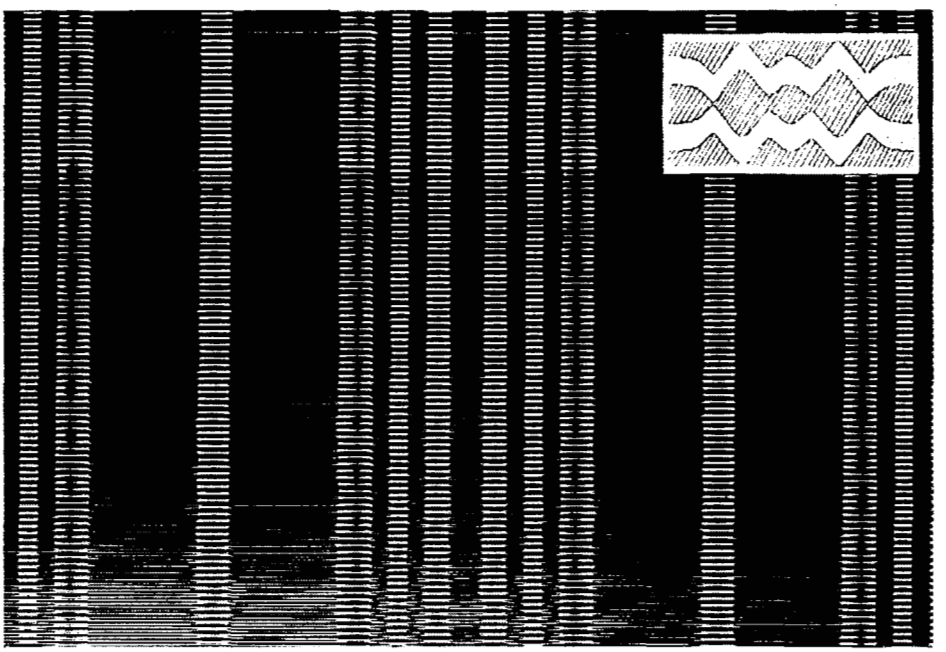

Figure 8.- Enlarged photograph of a section of a binary mask, T = 50μm, m = 1. The insert shows a section of a compressed conjugate fringe pair.

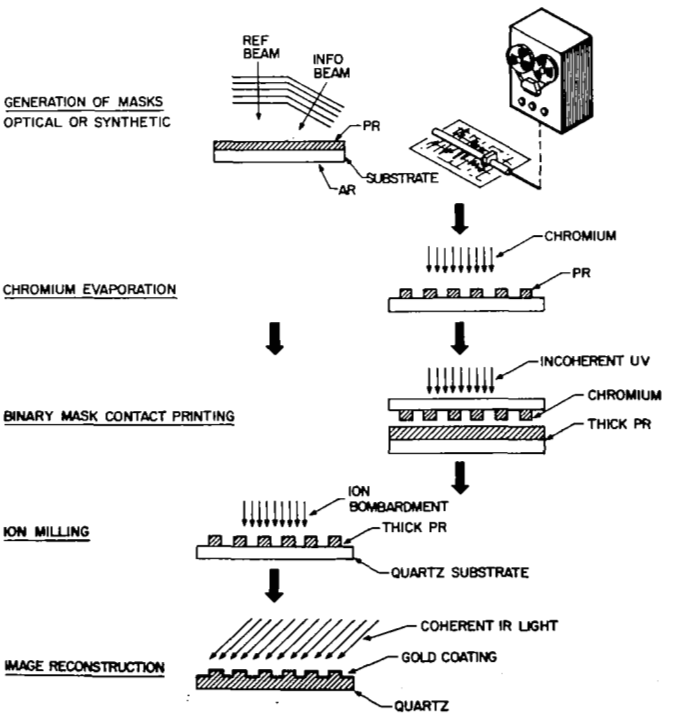

Figure 9.- Processing steps in the formation of linear and binary relief gratings.

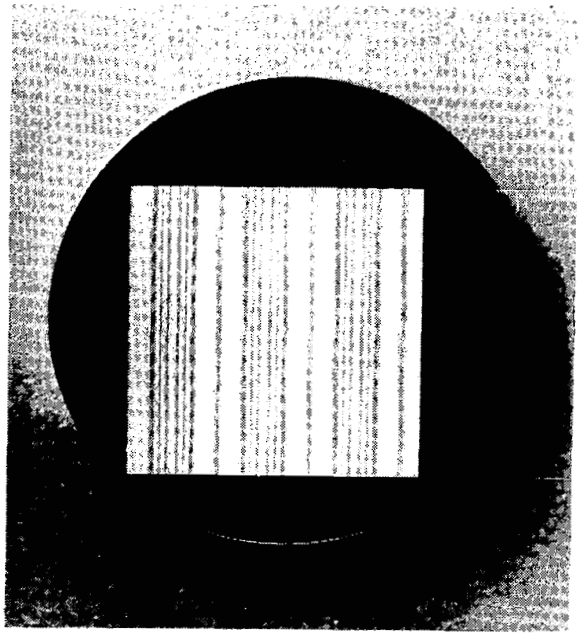

Figure 10.- A photograph of a 3/4 inch gold coated binary holographic grating on a poly-GaAs substrate.

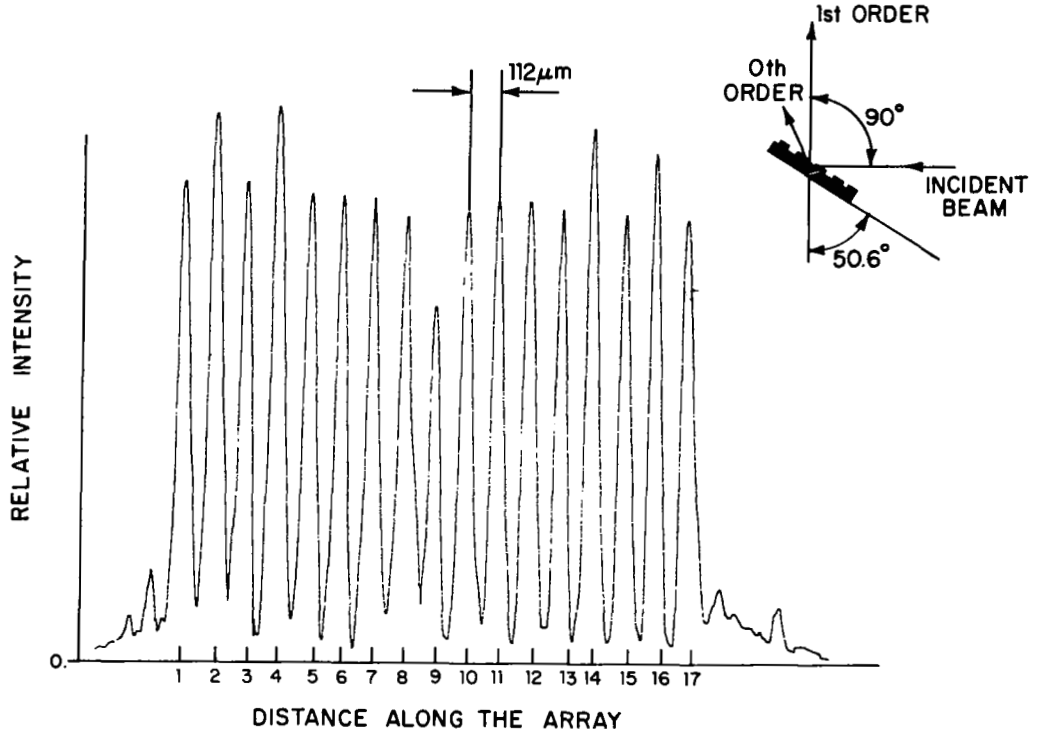

Figure 11.- An IR (10.6μm) detector scan past a focussed wavefront generated by a 17-element holographic binary grating.

DIAL WITH HETERODYNE DETECTION INCLUDING SPECKLE NOISE: AIRCRAFT/SHUTTLE MEASUREMENTS OF O_3, H_2O, AND NH_3 WITH PULSED TUNABLE CO_2 LASERS

Philip Brockman, Robert V. Hess, Leo D. Staton, and Clayton H. Bair
Langley Research Center

INTRODUCTION

There is great need for atmospheric trace constituent measurements with higher vertical resolution than attainable with passive radiometers. Infrared (IR) DIAL, which depends on Mie scattering from aerosols, has special advantages for tropospheric and lower stratospheric applications and has great potential importance for measurements from Shuttle (ref. 1) and aircraft. Differential-absorption LIDAR data reduction involves comparing large amplitude signals which have small differences. The accuracy of the trace constituent concentration inferred from DIAL measurements depends strongly on the errors in determining the amplitude of the signals. Thus, the commonly used SNR expression (signal divided by noise in the absence of signal) is not adequate to describe DIAL measurement accuracy and must be replaced by an expression which includes the random coherent (speckle) noise within the signal (refs. 2, 3, and 4). A comprehensive DIAL computer algorithm (ref. 5) is modified to include heterodyne detection and speckle noise. Results of a parametric study are presented and comparisons with direct detection are discussed. Examples are given for monitoring vertical distributions of O_3, H_2O, and NH_3 using a ground-, aircraft-, or Shuttle-based pulsed tunable CO_2 laser DIAL system.

ANALYSIS OF DIAL SENSITIVITY WITH HETERODYNE DETECTION

The expectation value P of the number of measured photons from one coherence area of a scattering cell at range R of length Δr is

$$P = \frac{\eta\Gamma E\Delta r A\beta}{h\nu R^2} \exp \int_o^R -2(\xi + \sigma\rho)dr \qquad (1)$$

where η = detector efficiency, Γ = optical efficiency, E = laser energy, β = 180° backscatter coefficient per length per steradian, Δr = cell length = $\frac{cT}{2}$, T = integration time, ν = frequency, A = transmitter area (= receiver area for heterodyne system with single detector), ξ = extinction coefficient (total minus that of measured gas), σ = absorption coefficient of measured gas, and ρ = density of gas being measured.

In differential absorption, measurements are made of two frequencies selected to maximize signal and differential absorption of the species being measured while minimizing interference effects. The double ratio of signals at

adjacent scattering cells at two frequencies yields information about absorption in the region between the scattering cells.

$$\int_{R_1}^{R_2}(\rho\Delta\sigma)dr = \ln\left(\frac{P_{22}\,P_{11}}{P_{12}\,P_{21}}\right) + \ln\left(\frac{\beta_{12}\,\beta_{21}}{\beta_{11}\,\beta_{22}}\right) - 2\int_{R_1}^{R_2}(\Delta\xi)\,dr \qquad (2)$$

where P_{ij} = expectation value of measured return from cell j at frequency i. β_{ij} = backscatter coefficient from cell j at frequency i, $\Delta\sigma$ = absorption coefficient difference between frequencies 1 and 2, $\Delta\xi$ = extinction coefficient difference between frequencies 1 and 2 (not including gas being measured) i = 1 or 2 frequencies on or off absorption line, respectively, and j = 1 or 2 for distances R_1 and R_2, respectively. For scattering cells of equal length the resolution length $R_2 - R_1$ equals the scattering cell length Δr. The term $\ln \frac{\beta_{12}\,\beta_{21}}{\beta_{11}\,\beta_{22}}$ is a correction term due to changes in backscattering with frequency across scattering cells. The term $2\int_{R_1}^{R_2}(\Delta\xi)\,dr$ is a correction due to interferent species. Variation in backscatter and interferent absorption at the two frequencies will result in biases in the inferred concentrations. These biases can be reduced by careful frequency selection and partially corrected by using a priori information and auxiliary measurements. For an optically thick species, a series of "on" frequencies is required to maximize sensitivity at various altitudes.

The random error in ρ, which is calculated assuming that signal plus background are measured during each pulse and that background is measured between pulses and subtracted, will depend on the random error in the measurement of P_{ij}. The uncertainty in the inferred concentration $(\delta\rho)^2$ is given by

$$(\delta\rho)^2 = \left(\frac{1}{2\Delta\sigma\Delta r}\right)^2 \frac{1}{N} \sum_{i=1}^{2} \sum_{j=1}^{2} \left[\frac{1}{(SNR)_{ij}^2} + \text{system error terms}\right] \qquad (3)$$

where N is the number of pulse pairs per measurement and SNR is the single pulse signal-to-noise ratio. For heterodyne detection, the major errors in P_{ij} are due to quantum noise in the local oscillator and fluctuation noise in the return signal.

The heterodyne signal-to-noise ratio for a single coherence volume $\frac{P_{ij}}{P_{ij} + BT}$ is limited to 1.0 due to the speckle noise in the return signal. The number of coherence lengths per scattering cell is BT. The number of coherence areas viewed by the detector is M, where M is the ratio of receiver to transmitter area. For heterodyne detection an individual detector is required for each coherence area. The single pulse signal-to-noise ratio for determining the signal from a scattering cell is then

$$SNR = \frac{P_{ij}}{P_{ij} + BT}\sqrt{BTM} \qquad (4)$$

where BTM is the number of statistically independent samples from a scattering cell for a single pulse. The post-detection bandwidth B is constrained by matching with pulse duration ($B \leq 1/T_p$) and by the width of atmospheric spectral lines. The integration time T is constrained by vertical resolution requirements. Neglecting the system error terms, the random error in density for heterodyne detection with bandwidth B, integration time T, N pulse pairs, and M coherence areas with one detector per coherence area is

$$(\delta\rho)^2 = \frac{1}{(2\Delta\sigma\Delta r)^2} \sum_{i=1}^{2} \sum_{j=1}^{2} \left[\frac{P_{ij} + BT}{P_{ij} \sqrt{BTNM}} \right] \tag{5}$$

For N pulse pairs and M detectors, the SNR $\frac{P_{ij}}{P_{ij} + BT} \sqrt{BTNM}$ is maximized for a given total laser energy per measurement ($\propto NMP_{ij}$) when the laser energy per pulse per detector is selected so that $P_{ij} \approx BT$. For that condition an approximate solution to equation (5) is

$$\delta\rho \backsim \frac{2}{\Delta\sigma\Delta r} \frac{1}{\sqrt{BTNM}} \propto \frac{1}{\Delta\sigma (\Delta r)^{3/2} \sqrt{BNM}} \tag{6}$$

This equation illustrates that $\delta\rho$ is independent of ρ and proportional to $1/\Delta\sigma$ within the constraint that the two-way integrated absorption through the atmosphere does not limit P_{ij} to less than BT. Equation (6) also indicates the strong effect of range resolution on measurement error. The number of pulse pairs required to maintain a constant measurement error is proportional to the inverse cube of the range resolution.

COMMENTS ON DIRECT DETECTION

Direct detection can have advantages over single-detector heterodyne detection when signal levels are high since direct detection allows averaging over multiple coherence areas with a single detector. The major disadvantage of direct detection is background noise which is limited by optical filters ($\sim 10^{11}$ Hz) compared with the electronic filters (10^6 to 10^9 Hz) for heterodyne detection. Reducing the background noise by reducing the field of view will result in an increase in speckle noise.

The direct detection signal-to-noise ratio can be written as a function of M, the number of coherence areas, and the total direct detected signal $P'_{ij} = MP_{ij}$. The SNR for direct detection (assuming zero detector noise, ref. 3) is

$$(SNR)_{DD} = \frac{P'_{ij} \sqrt{BT}}{\left(P'_{ij} BT + (GDMT)BT + \frac{P'^{2}_{ij}}{M} \right)^{1/2}} \tag{7}$$

Equation (7) includes a speckle term P'^2_{ij}/M, a Poisson term $P'_{ij}BT$, and a background term $(GDMT)BT$. In equation (7), G is the background signal in detected photons/sec/Hz per coherence area, M is the number of coherence areas, and D is the bandwidth in Hz of the optical filter. Maximization of the direct detection SNR with respect to the number of coherence areas occurs when M is selected so that the background and speckle terms are equal:

$$(SNR)_{DD\ max} \approx \frac{\sqrt{BTM}}{\sqrt{2}} \quad \text{with} \quad M = \frac{P'_{ij}}{\sqrt{GBD}\ T} \tag{8}$$

For this condition, the criterion for direct detection SNR to exceed the single-detector heterodyne large signal SNR of $\sqrt{BT}$ is for $P'_{ij} > 2T\sqrt{GBD}$.

SENSITIVITY ANALYSIS FOR DIAL MEASUREMENT USING HETERODYNE DETECTION WITH A SINGLE DETECTOR

A comprehensive computer algorithm is used to calculate the expectation values of P_{ij} for various measurement conditions. Pressures, temperatures, and gas species densities are input from a midsummer midlatitude atmospheric model. Trace gas species densities can be modified using card inputs. Line absorption parameters are accessed from a comprehensive data base. Sources for line data are given in reference 6. At each altitude, molecular absorption at ν_1 and ν_2 is calculated for each species by summing contributions from absorption lines in the vicinity of the laser frequency. Lorentz, Voigt, or Doppler line shapes are used at appropriate altitudes. Water vapor continuum absorption is added to the line absorption. Extinction due to particulate and molecular scattering is summed with molecular absorption at each altitude to give the total loss in each scattering cell. The integrated two-way loss is calculated by summing contributions from altitude layers between the laser and the cell being considered. The backscattering coefficient β is calculated by combining a Rayleigh term, which is small at infrared frequencies, and a Mie term. Mie backscatter and extinction for the cases shown here are calculated using parameters of Deirmendjian's Haze L size distribution (ref. 7). The vertical aerosol distribution is based on reference 8 with a ground level concentration (350 particles/cm^3) corresponding to a 23-km visibility. Figure 1 shows the Mie contribution to the volume backscatter coefficient used in this study as a function of altitude for $\nu = 927.61\ cm^{-1}$.

For all simulations presented, the overall system efficiency, which is the product of optical and quantum efficiency, is set at 12.5%. The system errors due to amplification and digitization are set at 0.1%. For aircraft and ground-based cases, telescope area is 0.1 m^2 and bandwidth 10^8 Hz; for Shuttle cases, telescope area is 1 m^2 and bandwidth 10^7 Hz. Bandwidths have been constrained by atmospheric line parameters and by laser limits. Pulse energies are selected within practical laser constraints to match signal to bandwidth and the number of pulse pairs N is adjusted to obtain reasonable measurement accuracy. The "on" and "off" frequencies have been selected to be within the range of a single rare isotope multiatmospheric CO_2 laser line. Use of rare isotope lines minimizes interference by atmospheric CO_2 and use of

closely spaced "on" and "off" frequencies minimizes error due to variations in backscatter and interfering species absorption.

Figure 2 displays O_3 concentration in STP-ppb and measurement error in the same units versus altitude for measurement from Shuttle at 250 km. The pulse energy is 5 joules per pulse with 1000 pulse pairs per measurement. Telescope area is 1 m^2, bandwidth is 10^7 Hz, resolution is 1.5 km below 30 km and 3 km above 30 km. Simulations are for an "off" frequency of 1058.01 cm^{-1} and "on" frequencies of 1058.17, 1058.11, and 1058.19 cm^{-1}. It should be noted that a fine tuning of the "on" frequency results in a sharp variation of altitude at which the best measurement can be accomplished.

Figure 3 displays ozone concentration and error in STP-ppb for a measurement from aircraft at 10.5 km looking either upward or downward. Pulse energy is 0.05 joules, telescope area is 0.1 m^2, bandwidth is 10^8 Hz, and "on" frequency is 1058.20 cm^{-1}. In the case of aircraft measurements the "on" frequency selection is simplified since the signal does not have to pass through the ozone bulge. Two cases are presented in order to illustrate the strong influence of range resolution on number of pulses required for a measurement. The solid error line is for 3000 pulse pairs with a resolution of 0.5 km below 6 km, 1 km from 6 to 10 km, and 3 km above 10 km. The dashed error line is for 100 pulse pairs with a resolution of 1.5 km. The errors are nearly identical at low altitude, which is expected (see equation (6)) since the number of pulses has been increased by approximately the cube of the inverse of the range resolution.

Figure 4 displays NH_3 concentration and error in STP-ppb for 300 pulse pairs with operation from Shuttle at an altitude of 250 km with 1 joule per pulse and from aircraft at an altitude of 10 km with 0.05 joules per pulse. Since NH_3 is not heavily attenuated, only one set of frequencies is required. The resolution for both cases is 1.5 km.

Figure 5 displays NH_3 concentration and error in STP-ppb for a ground-based measurement. The vertical NH_3 distribution is the same as shown in figure 4. For this case, the telescope area is 0.1 m^2, bandwidth is 10^8 Hz, "on" frequency is 927.32 cm^{-1}, and "off" frequency is 927.61 cm^{-1}. The error curves are for a range resolution of 1.5 km using 300 pulse pairs. The two error curves are for laser energies of 0.05 J and 0.5 J. Note that for the cases in which E = 0.5 J, the large signal limit $\left(\frac{P_{ij}}{P_{ij} + BT} \approx 1\right)$ is achieved throughout the entire measurement range and therefore the error is nearly independent of altitude.

Figure 6 is for the same conditions as shown in figure 5 with the exception that the NH_3 concentration has been reduced by a factor of 5. The error is plotted only for the E = 0.05 J case. Comparison of figure 6 with the 0.05 joule curve in figure 5 illustrates the effect of concentration on measurement error. At low altitude, $P_{ij} \geq BT$ and the measurement errors are independent of concentration. At higher altitudes $P_{ij} < BT$ and the increased integrated absorption at the higher concentration (fig. 5) results in an increased measurement error for that case. These NH_3 distributions are

typical values from Langley Research Center ground-based infrared heterodyne radiometer measurements (ref. 9).

Figure 7 displays percent error in measurement of water vapor concentration versus altitude for measurement from 250 km for a midsummer, midlatitude water vapor distribution. Measurement conditions are 1 joule per pulse, 100 pulse pairs, 10^7 Hz bandwidth, and 1 m^2 telescope. Two "on" frequencies are used at 948.25 and 948.30 cm^{-1}. The "off" frequency is at 948.35 cm^{-1}. Tropospheric water vapor is particularly amenable to measurement from space since the concentration rapidly increases towards the ground. Thus, absorption is high at low altitudes and the integrated absorption from space to low altitudes is relatively low. For measurement of water vapor at higher altitudes, the number of pulses would have to be increased.

CONCLUDING REMARKS

High vertical resolution measurement of atmospheric trace species can be achieved using CO_2 laser DIAL with heterodyne detection. This study indicates that maximum sensitivity at minimum laser energy per measurement requires multiple pulse operation with the energy per pulse selected so that the measure photon rate is approximately equal to the detector IF bandwidth. Measurement sensitivities can be maximized and interference effects minimized by fine adjustment of measurement frequencies using the tunability of high-pressure laser The use of rare isotope lasers minimizes loss due to CO_2 atmospheric absorption

REFERENCES

1. Shuttle Atmospheric Lidar Research Program - Final Report of Atmospheric Lidar Working Group. NASA SP-433, 1979.

2. Jakeman, E.; Oliver, C. J.; and Pike, E. R.: Optical Homodyne Detection Advances in Physics. Europhysics Journal, vol. 24, no. 3, May 1975.

3. Elbaum, M.; and Teich, M. C.: Heterodyne Detection of Random Gaussian Signals in the Optical and Infrared: Optimization of Pulse Duration. Optics Communications, vol. 27, Nov. 1978.

4. Rye, B. J.: Differential Absorption Lidar System Sensitivity With Heterodyne Reception. Appl. Optics, vol. 17, no. 24, Dec. 15, 1978.

5. Remsberg, E. E.; and Gordley, L. L.: Analysis of Differential Abosrption Lidar From the Space Shuttle. Appl. Optics, vol. 17, no. 4, Feb. 15, 1978.

6. Park, J. H.: Optical Measurement in the Middle Atmosphere. Pageoph, vol. 117 (1978/79).

7. Deirmendjian, D.: Electromagnetic Scattering on Spherical Polydispersions. American Elsevier Publishing Co., New York, NY, 1969.

8. McClatchey, Robert A.; and Selby, John E. A.: Atmospheric Attenuation of Laser Radiation From 0.76 to 31.25 μm. AFCRL-TR-74-0003, U.S. Air Force, Jan. 1974.

9. Hoell, J. M.; Harward, C. M.; and Williams, B. S.: Remote Infrared Heterodyne Radiometer Measurements of Atmospheric Ammonia Profiles. Geophys. Res. Lett., Vol. 7, No.5, May 1980, pp. 313-316.

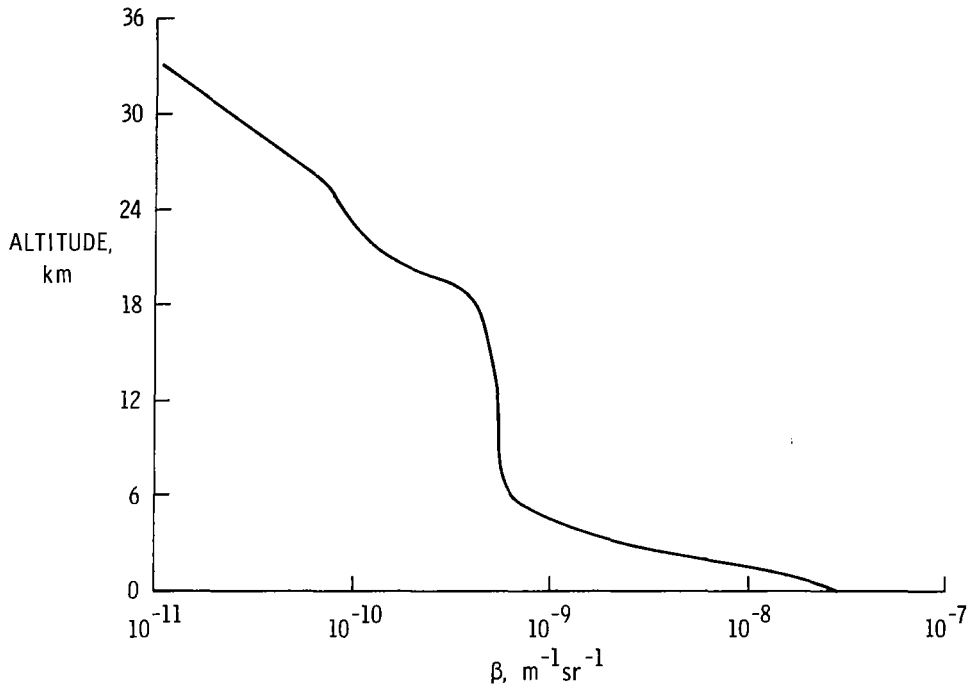

Figure 1.- Aerosol volume backscattering coefficient as a function of altitude for ν = 927.61 cm^{-1}.

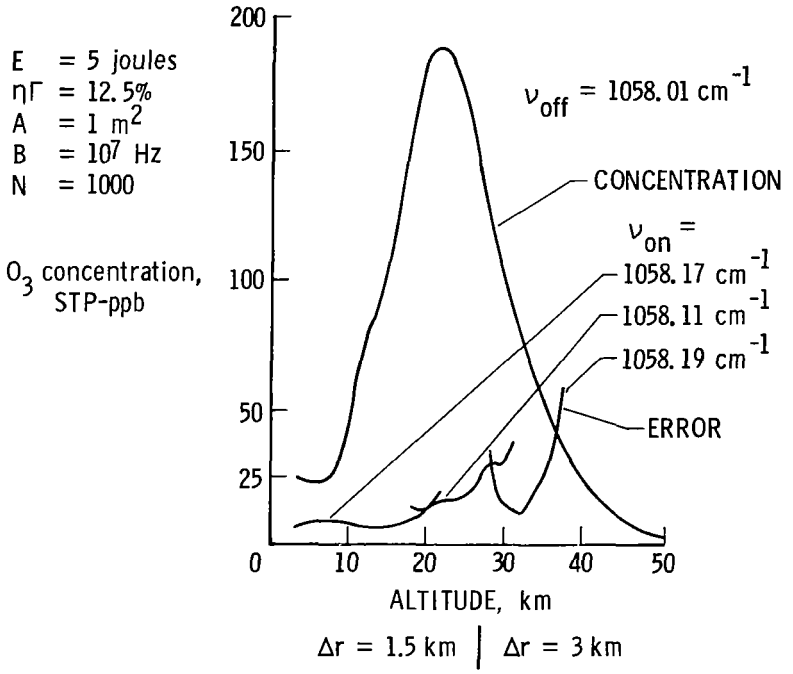

Figure 2.- Ozone measurement from 250 km.

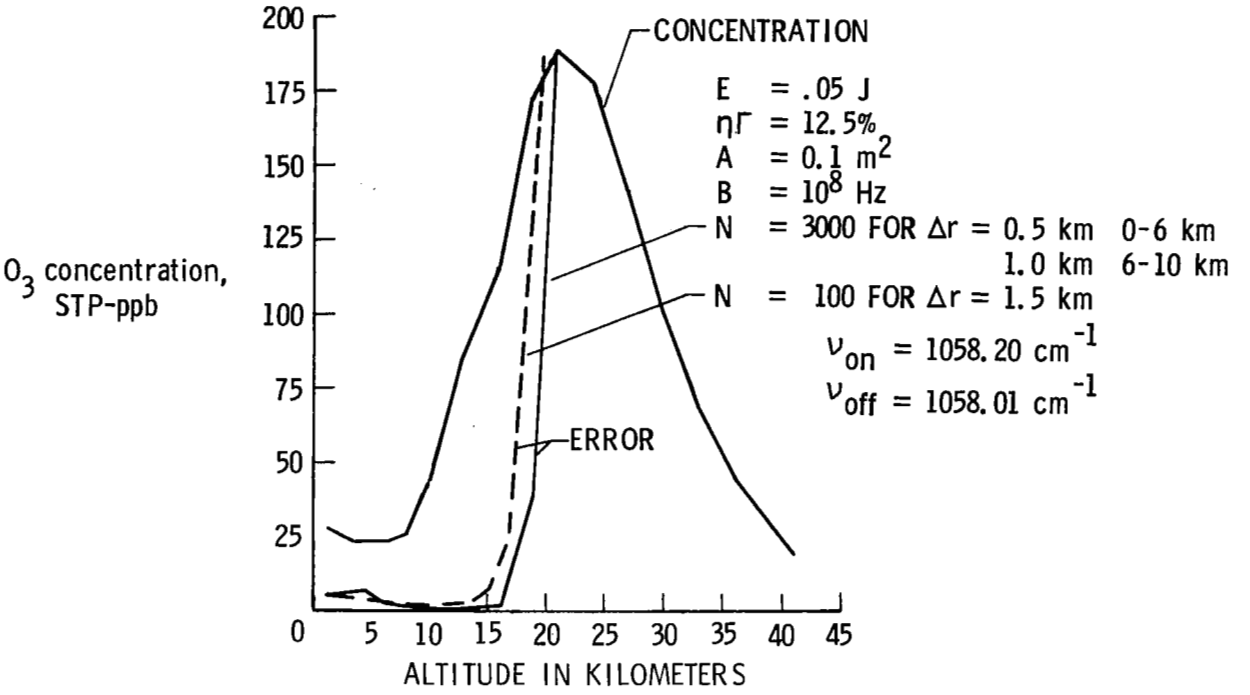

Figure 3.- Ozone measurement from 10.5 km.

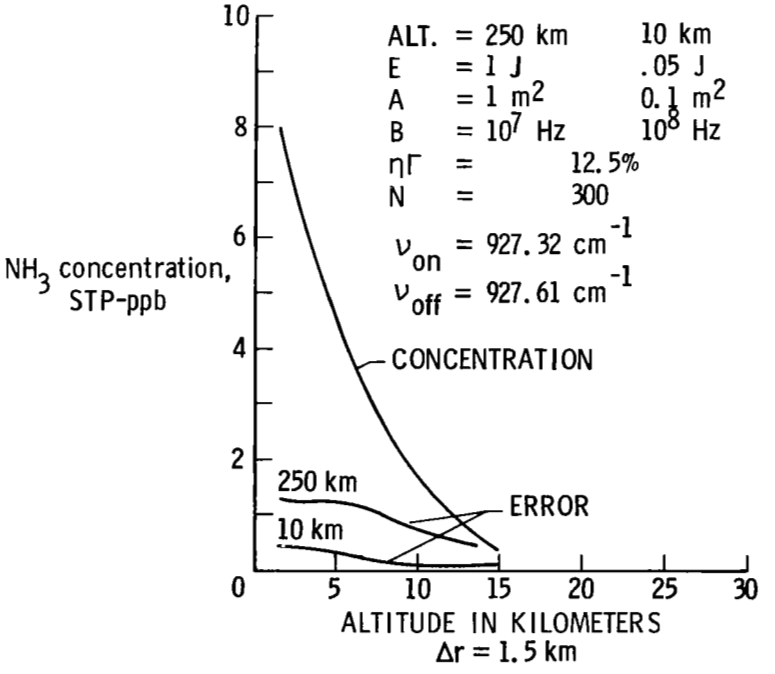

Figure 4.- NH_3 measurement from 10 and 250 km.

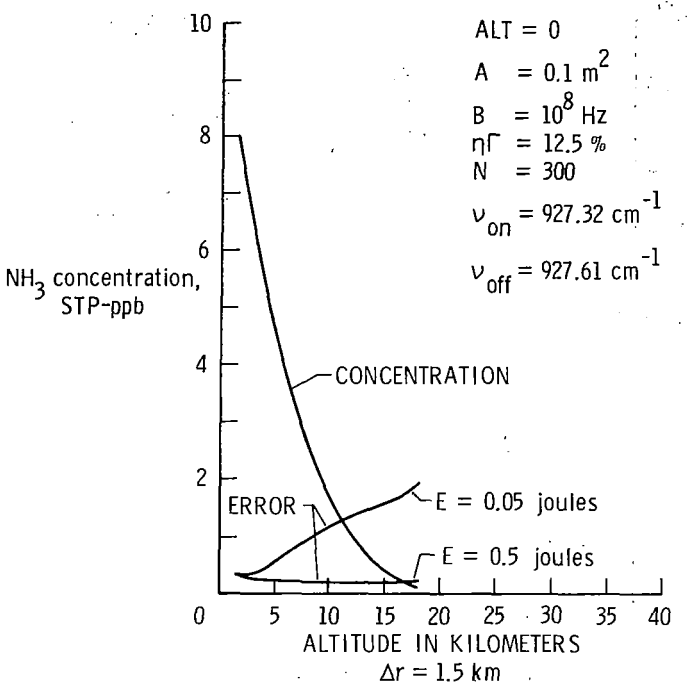

Figure 5.- NH_3 measurement from ground for E = 0.5 and 0.05 J.

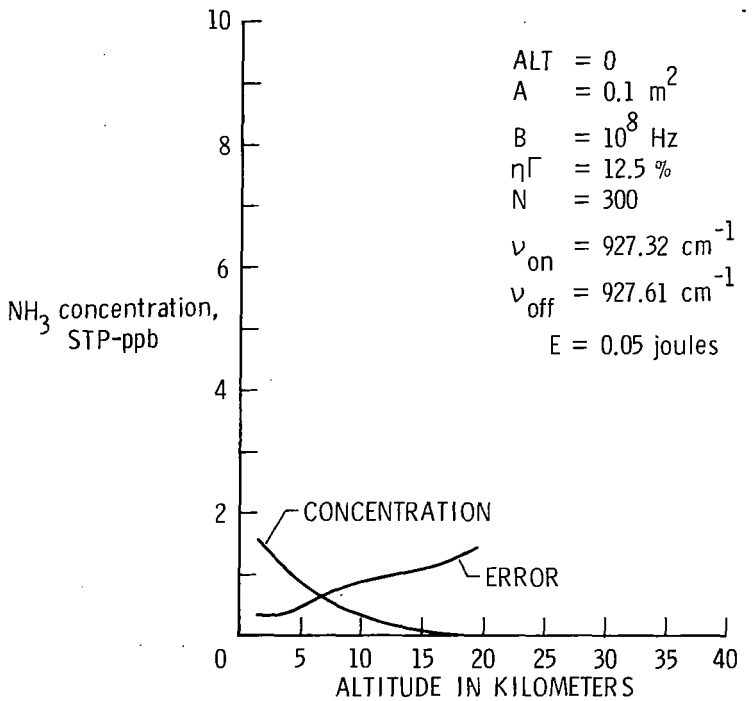

Figure 6.- NH_3 measurement from ground for E = 0.05 J.

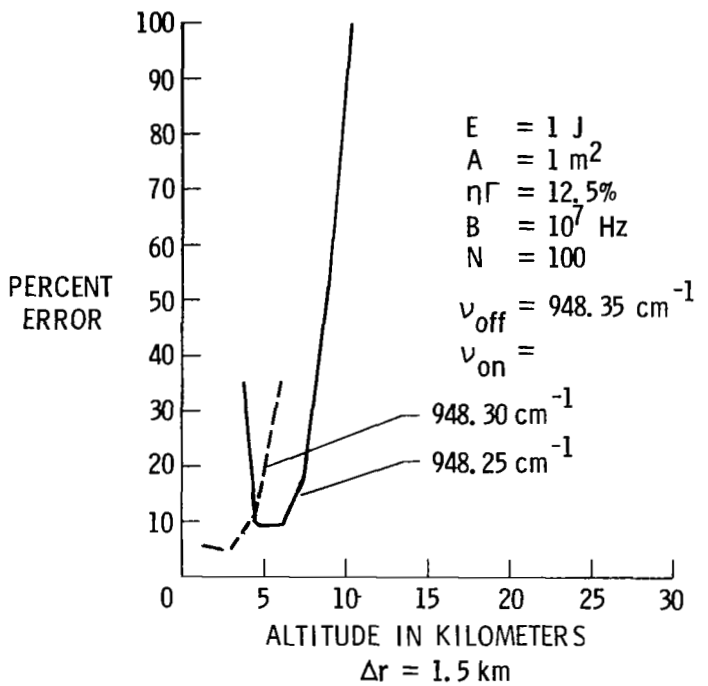

Figure 7.- Water vapor measurement from 250 km.

HETERODYNE SIGNAL-TO-NOISE RATIOS IN ACOUSTIC MODE SCATTERING EXPERIMENTS

William R. Cochran
Youngstown State University
Youngstown, Ohio

SUMMARY

A study has been made of the relation between the SNR obtained in heterodyne detection of radiation scattered from acoustic modes in crystalline solids and the scattered spectral density function. It is shown that in addition to the information provided by the measured frequency shifts and line widths, measurement of the SNR provides a determination of the absolute elasto-optical (Pockel's) constants. Examples are given for cubic crystals, and acceptable SNR values are obtained for scattering from thermally excited phonons at 10.6 microns, with no external perturbation of the sample necessary. The results indicate the special advantages of the method for the study of semiconductors.

ANALYSIS AND DISCUSSION

The ratio of mean square signal current to mean square noise current obtained at the frequency f when laser radiation of frequency ν_o is mixed on the surface of a photoconductor with a spectrum $G(\nu)$ can be expressed (ref. 1) in the form

$$\frac{S}{N} = \eta G(\nu_o \pm f). \tag{1}$$

G is expressed in numbers of photons per second per frequency interval into a coherence area and η is the photoconductor quantum efficiency. If I_1 represents the number of electrons produced per second by light with frequencies in a bandwidth $\Delta\nu$ and solid angular spread Ω falling on area A, then

$$G(\nu) = \frac{I_1 \lambda^2}{A\Omega\Delta\nu} . \tag{2}$$

I_1 is the total energy incident per second, P, divided by the energy per photon, multiplied by the number of electrons produced by one photon, i.e.,

$$I_1 = \frac{P\eta}{h\nu} . \tag{3}$$

If the source of P is the scattering of laser radiation from acoustic waves or phonons propagating through a crystalline sample, then equation (1)

can be written in the convenient form

$$\frac{S}{N} = \eta P_o \frac{P_s/P_o}{A\,\Omega} \frac{\lambda^2}{h\nu} \frac{1}{\Delta\nu} , \tag{4}$$

where P_o represents the total power incident on the sample, P_s the total scattered power, and $\Delta\nu$ the width of the scattered line. The scattering of radiation by propagating thermally excited phonons in crystalline solids has been analyzed by Born and Huang (ref. 2), specialized for birefringent crystals by Gammon and Cummins (ref. 3), and for cubic crystals by Benedek and Fritsch (ref. 4). For small angles the power scattered into solid angle Ω at the point R by the acoustic fluctuation of wavevector $\vec{K}$ is related to the autocorrelation function of the scattered field,

$$P_s(\vec{K},R) = \frac{C}{8\pi} \left\langle \left| E(\vec{K},t) \right|^2 \right\rangle R^2\Omega, \tag{5}$$

where (ref. 4, equation 46)

$$\left\langle \left| E(\vec{K},t) \right|^2 \right\rangle = {E_o}^2 \left(\frac{\omega_o}{C}\right)^4 \frac{{\varepsilon_o}^4}{R^4} \frac{V}{4\pi^2} \frac{kT}{\rho} \sum_{\mu=1}^{3} \left|\xi^\mu\right|^2 \frac{K^2}{{\omega_\mu}^2(K)} \tag{6}$$

Here μ denotes a particular acoustic mode (μ = 1, 2, 3 for cubic crystals), ω_μ the frequency of mode μ, V the scattering volume, ε_o the dielectric constant, and ρ the density of the sample. ξ^μ is in effect a weighting factor which determines the relative intensity of the radiation scattered by mode μ, and is itself determined by the absolute elasto-optical constants. If the illuminated volume of the crystal is written as $V = LA_i$, where A_i is the cross-sectional area of the incident beam and L the scattering length, then for mode μ

$$\frac{P_s/P_o}{\Omega} = \pi^2 \left(\frac{\nu_o}{C}\right)^4 \frac{{\varepsilon_o}^4 LkT}{\rho} \frac{\left|\xi^\mu\right|^2}{{v_\mu}^2} , \tag{7}$$

where

$$P_o = \frac{C}{8\pi} {E_o}^2 A_i . \tag{8}$$

The final expression for the SNR can then be written

$$\frac{S}{N} = \eta P_o \left(\frac{\pi}{C}\right)^2 \nu_o \frac{{\varepsilon_o}^4 LkT}{hA\rho} \frac{\left|\xi^\mu\right|^2}{{v_\mu}^2} \frac{1}{\Delta\nu_\mu} . \tag{9}$$

For a given experimental configuration all quantities in this expression are known except $\Delta\nu_\mu$, ξ^μ, and v_μ. $\Delta\nu_\mu$ is directly observable, while v_μ is determined by the measured frequency shift of the scattered radiation for a given scattering angle (ref. 5). Thus a measure of the SNR allows ξ^μ to be found, which in turn leads to values of the absolute elasto-optical constants. For

example, inverting the relation between the elasto-optical constants and the ξ^{μ} given by Benedek and Fritsch (ref. 4), and using numerical values for scattering at 3° from acoustic waves propagating in the [110] plane of potassium chloride (the elastic constants are needed in the calculation), results in the relations for the elasto-optical constants p_{11}, p_{12}, and p_{44}

$$\begin{aligned} p_{11} &= 2\,\xi^1 - 56.8\,\xi^2 + 1.72\,\xi^3 \\ p_{12} &= 1.72\,\xi^3 - 56.8\,\xi^2 \\ p_{44} &= 2\,\xi^1 - 113.6\,\xi^2 + 1.43\,\xi^3 \end{aligned} \qquad (10)$$

Potassium chloride is one of the few substances for which the absolute elasto-optical constants are known (ref. 6), and substitution of the known values into equations (9) and (10) result in an expected SNR of 4.6 for scattering of 40 watts of 10.6 micron radiation from the longitudinal ($\mu = 3$) mode. A value of 0.4 has been used for the quantum efficiency for purposes of calculation; in addition, an inverse square frequency dependence for sound wave attenuation has been assumed in order to estimate the expected line width (about 12 kc), such a dependence being characteristic of relaxation phenomena in solids, especially in the megacycle range.

This optimum value of the SNR will be obtained only if the distance z from the scatterer to the detector is related to the detector aperture radius b through the wavevector k according to the expression

$$b \simeq \sqrt{\frac{z}{k}} \quad ; \qquad (11)$$

otherwise the above SNR must be multiplied by an appropriate reduction factor (ref. 7). For a detector of 3 mm diameter the optimum SNR would be obtained for a source detector distance of 1.3 meters, a typical experimental configuration.

Thus a careful determination of the SNR provides a unique method for obtaining the absolute elasto-optical coefficients of crystalline samples, with no external perturbation or acoustic excitation required. The favorable results at 10.6 microns imply the method will be useful for the study of semiconductors having band gaps less than 0.12 eV, which are inaccessible to study by the usual optical methods.

REFERENCES

1. A. T. Forrester, J. Op. Soc. Amer. 51, 253 (1961).

2. M. Born and K. Huang, Dynamical Theory of Crystal Lattices (Oxford: Clarendon Press (1954).

3. R. W. Gammon and H. Z. Cummins, Johns Hopkins University, Department of Physics, Technical Report No. 2 (1967).

4. G. B. Benedek and K. Fritsch, Phys. Rev. 149, 647 (1966).

5. L. Brillouin, Ann. Phys. (Paris) 17, 88 (1922).

6. Elias Burstein and Paul L. Smith, Phys. Rev. 74, 229 (1948).

7. H. T. Yura, Appl. Opt. 13, 150 (1974).

HETERODYNE SYSTEMS AND TECHNOLOGY CONFERENCE

PROGRAM COMMITTEE

DR. ROBERT H. KINGSTON, Chairman
M.I.T. Lincoln Laboratory
C-174 - P.O. Box 73
Lexington, MA 02173
(617) 862-5500

FRANK ALLARIO
M/S 401A
NASA Langley Research Center
Hampton, VA 23665
(804) 827-2576

JAMES M. HOELL, JR.
M/S 283
NASA Langley Research Center
Hampton, VA 23665
(804) 827-2818

STEPHEN J. KATZBERG
M/S 473
NASA Langley Research Center
Hampton, VA 23665
(804) 827-3661

SHELBY G. TILFORD
Mail Code EBT-8
NASA Headquarters
Washington, DC 20546
(202) 755-8617

DAVID L. SPEARS
Lincoln Laboratory
Box 73
Lexington, MA 02173
(617) 862-5500

FRANK GOODWIN
Space and Comm. Group
Hughes Aircraft
Bldg. 366/W 322
P.O. Box 92919
Los Angeles, CA 90009

ARAM MOORADIAN
Lincoln Laboratory
Box 73
Lexington, MA 02173
(617) 862-5500, ext. 184

ROBERT T. MENZIES
Jet Propulsion Laboratory
Mail Code 169-332
4800 Oak Grove Dr.
Pasadena, CA 91103
(213) 354-3787

JAMES A. HUTCHBY
Research Triangle Institute
P.O. Box 12194
Research Triangle Park, NC 27709
(919) 541-6000, ext. 5900

COL. MALCOLM R. O'NEILL
DARPA-STO
1400 Wilson Blvd.
Arlington, VA 22209

R. MILTON HUFFAKER
NOAA/ERL/WPL
Code R45X2
Boulder, CO 80302
(303) 499-1000

ALBERT BETZ
University of California
366 Le Conte Hall
Berkley, CA 94720

MICHAEL J. MUMMA
Mail Code 693
NASA Goddard Space Flight Center
Greenbelt, MD 20771
(301) 344-6994

HETERODYNE SYSTEMS TECHNOLOGY CONFERENCE

ATTENDANCE LIST

March 25-27, 1980

Mian M. Abbas
Drexel University
Philadelphia, PA 19104

NASA Langley Research Center
Attn: 401A/Frank Allario
Hampton, VA 23665

W. Altman
RCA Astro
P. O. Box 800 - MS 56
Princeton, NJ 08540

NASA Langley Research Center
Attn: 433/Robert D. Averill
Hampton, VA 23665

NASA Langley Research Center
Attn: 283/Clayton H. Bair
Hampton, VA 23665

Bruce J. Bartholomew
General Dynamics/Convair
P. O. Box 80847, M/Z 42-6210
San Diego, CA 92138

Bob Benson
Hughes Aircraft Company
Building 6 - M/S 121
5651 Sumnerway
#111 Centinella & Teale Sts
Culver City, CA 90230

NASA Langley Research Center
Attn: 474/Alfred G. Beswick
Hampton, VA 23665

Albert Betz
University of California
Department of Physics
Berkeley, CA 94720

Russell Bigelow
GTE Sylvania
Mountain View, CA 94042

James W. Bilbro
NASA Marshall Space Flight Center
Mail Code EC32
Marshall Space Flight Center, AL 35812

NASA Langley Research Center
Attn: 401B/Robert E. Boughner
Hampton, VA 23665

Peter Bratt
Santa Barbara Research Center
75 Coromar Drive
Goleta, CA 93017

NASA Langley Research Center
Attn: 473/Roger A. Breckenridge
Hampton, VA 23665

NASA Langley Research Center
Attn: 283/Philip Brockman
Hampton, VA 23665

David Buhl
NASA Goddard Space Flight Center
Code 693
Greenbelt, MD 20771

Apostle Cardiamenos
Alpha Industries
20 Sylvan Road
Woburn, MA 01801

NASA Langley Research Center
Attn: 234/William P. Chu
Hampton, VA 23665

NASA Langley Research Center
Attn: 473/Ivan O. Clark
Hampton, VA 23665

William R. Cochran
Youngstown State University
Department of Physics and Astronomy
410 Wick Avenue
Youngstown, OH 44555

NASA Langley Research Center
Attn: 475/Kenneth H. Crumbly
Hampton, VA 23665

Edward J. Danielewicz
The Aerospace Corporation
P. O. Box 92957
Los Angeles, CA 09990

John J. Degnan
NASA Goddard Space Flight Center
Code 723
Greenbelt, MD 20771

Robert L. DelBoca
USA-Avionics R&D Activity
M/S DAVAA-E
Ft. Monmouth, NJ 07703

C. A. DiMarzio
Raytheon Company
430 Boston Post Road
Wayland, MA 01778

Reinhard Dirscherl
MBB Apparate
Postfach 801149
8000 München 80
W. GERMANY

Gerald F. Dionne
MIT Lincoln Lab
P. O. Box 73
Lexington, MA 02173

NASA Langley Research Center
Attn: 235/Howard B. Edwards
Hampton, VA 23665

NASA Langley Research Center
Attn: 235A/Reginald J. Exton
Hampton, VA 23665

NASA Langley Research Center
Attn: 473/Carl L. Fales, Jr.
Hampton, VA 23665

David Fink
Hughes Aircraft Company
Culver City, CA 90230

Pierre H. Flamant
Laboratoire de Meteorologie Dynamique
Ecole Polytechnique
91128 Palaisean
FRANCE

Chris Flanagan
Honeywell
2 Forbes Road
Lexington, MA 02173

Clifton Fonstad
MIT
Rm. 13-3062
77 Mass Avenue
Cambridge, MA 02139

Charles Freed
MIT
244 Wood Street - Room B-259
Lexington, MA 02173

NASA Langley Research Center
Attn: 473/Archibald L. Fripp, Jr.
Hampton, VA 23665

NASA Langley Research Center
Attn: 475/Joseph H. Goad, Jr.
Hampton, VA 23665

Frank Goodwin
Hughes Aircraft Company
366/W322
P. O. Box 92919
Los Angeles, CA 90009

Stanley H. Gordon
Applied Physics Lab/JHU
Johns Hopkins Road
Laurel, MD 20810

Walter J. Graham
Naval Surface Weapons Center
White Oak Laboratory
F-46
Silver Spring, MD 20910

Lawrence Greenberg
The Aerospace Corporation
P. O. Box 92957
Los Angeles, CA 90009

Howard W. Halsey
General Electric Company
Rm. L9163 VFSC
P. O. Box 8555
Philadelphia, PA 19101

NASA Langley Research Center
Attn: 158/Jack E. Harris
Hampton, VA 23665

Charles N. Harward
Dept. of Physics, School of Science
& Health Professions
Old Dominion University
Norfolk, VA 23508

NASA Langley Research Center
Attn: 433/Kenneth D. Hedgepeth
Hampton, VA 23665

NASA Langley Research Center
Attn: 499/Herbert D. Hendricks
Hampton, VA 23665

NASA Langley Research Center
Attn: 283/Robert V. Hess
Hampton, VA 23665

John J. Hillman
NASA Goddard Space Flight Center
Code 693.1
Greenbelt, MD 20771

E. David Hinkley
Jet Propulsion Laboratory
4800 Oak Grove Drive
Pasadena, CA 91103

NASA Langley Research Center
Attn: 283/James M. Hoell, Jr.
Hampton, VA 23665

Henry Hofheimer
ELTEK Corporation
7 Woodland Avenue
Larchmont, NY 10538

NASA Langley Research Center
Attn: 235A/John C. Hoppe
Hampton, VA 23665

James A. Hutchby
Research Triangle Institute
P. O. Box 12194
Research Triangle Park, NC 27709

NASA Langley Research Center
Attn: 473/Daniel J. Jobson
Hampton, VA 23665

Gordon B. Jacobs
General Electric Company
Electronics Park
Syracuse, NY 13221

Ali Javan
MIT
77 Mass Avenue
Cambridge, MA 02139

Clarence Jensen
Ball Aerospace
4790 Lee Circle
Boulder, CO 80303

C. R. Jones
North Carolina Central University
Physics Department
Durham, NC 27707

NASA Langley Research Center
Attn: 433/Irby W. Jones
Hampton, VA 23665

NASA Langley Research Center
Attn: 235/William B. Jones
Hampton, VA 23665

Majorie Katz
Honeywell
2 Forbes Road
Lexington, MA 02173

NASA Langley Research Center
Attn: 473/Stephen J. Katzberg
Hampton, VA 23665

NASA Langley Research Center
Attn: 364/Lloyd S. Keafer, Jr.
Hampton, VA 23665

John G. Kepros
General Dynamics/Convair
P. O. Box 80847
M/Z 42-6210
San Diego, CA 92138

Robert Kingston
MIT
P. O. Box 73
Lexington, MA 02173

Gerhard A. Koepf
Phoenix Corporation
1700 Old Meadow Road
McLean, VA 22102

NASA Langley Research Center
Attn: 490/Herbert R. Kowitz
Hampton, VA 23665

R. T. Ku
MIT
P. O. Box 73
Lexington, MA 02173

Ronald Lange
AIL Div. - Eaton Corporation
Melville, NY 11747

Jack Larsen
Systems and Applied Sciences Corp.
M/S 401A
NASA Langley Research Center
Hampton, VA 23665

NASA Langley Research Center
Attn: 284A/Thomas J. Lash
Hampton, VA 23665

R. E. Lawrence
1815 Melbourne Drive
McLean, VA 22101

K. F. Linden
Laser Analytics
25 Wiggins Avenue
Bedford, MA 01730

Marvin M. Litvak
JPL
4800 Oak Grove Drive
Pasadena, CA 91103

Wayne Lo
General Motors Corporation
G. M. Research Labs
G. M. Tech Center
Warren, MI 48090

Dennis M. Loger
Alpha Industries
20 Sylvan Road
Woburn, MA 01801

J. G. Lundholm, Jr.
NASA
Code RSI-5
Washington, DC 20546

NASA Langley Research Center
Attn: 117/William D. Mace
Hampton, VA 23665

NASA Langley Research Center
Attn: 475/Lemuel E. Mauldin, III
Hampton, VA 23665

Larry Majorana
Old Dominion University
Norfolk, VA 23508

Nelson McAvoy
NASA Goddard Space Flight Center
Code 723.0
Greenbelt, MD 20771

NASA Langley Research Center
Attn: 236/Royce F. McCormick
Hampton, VA 23665

NASA Langley Research Center
Attn: 234/Leonard R. McMaster
Hampton, VA 23665

C. Lynn Mears
University of Virginia
Department of Electrical Engineering
Charlottesville, VA 22901

Gérard J. Megie
Service D' Aeronomie Du CNRS
BP 3
91379 Verrieres Le Buisson
FRANCE

Harvey Melfi
NASA Goddard Space Flight Center
Code 940
Greenbelt, MD 20771

Robert T. Menzies
JPL
4800 Oak Grove Drive
MS 183-301
Pasadena, CA 91103

NASA Langley Research Center
Attn: 473/Barry D. Meredith
Hampton, VA 23665

Perry A. Miles
Raytheon Company MSD
Hartwell Road
Bedford, MA 01730

Matthew Miller
Perkin Elmer
M/S 283
Mail Avenue
Norwolk, CT 06856

Robert J. Mongeon
United Technologies Research Center
Silver Lane
East Hartford, CT 06108

Aram Mooradian
MIT
P. O. Box 73
Lexington, MA 02173

NASA Langley Research Center
Attn: 476/William M. Moore
Hampton, VA 23665

Salvatore C. Moreno
Honeywell
2 Forbes Road
Lexington, MA 02173

Michael J. Mumma
NASA Goddard Space Flight Center
Code 693.0
Greenbelt, MD 20771

John Nella
TRW
One Space Park - M/S R1-1062
Redondo Beach, CA 90278

NASA Langley Research Center
Attn: 474/Arthur L. Newcomb, Jr.
Hampton, VA 23665

T. Nguyen-Duy
Societe Anonyme de Telecommunications
%Eltek Corporation
7 Woodland Avenue
Larchmont, NY 10538

Van O. Nicolai
Office of Naval Research
800 Quincy
Arlington, VA 22217

NASA Langley Research Center
Attn: 235A/Stewart L. Ocheltree
Hampton, VA 23665

Milton E. Parrish
Phillip Morris
P. O. Box 26583
Richmond, VA 23261

Lauren M. Peterson
Environmental Research Institute of Michigan
P. O. Box 8618
Ann Arbor, MI 48107

Bud Peyton
AIL Division
Eaton Corporation
Melville, NY 11747

Robert E. Phelps
Applied Physics Lab
Johns Hopkins Road
Laurel, MD 20810

Herbert M. Pickett
JPL
4800 Oak Grove Drive
Pasadena, CA 91103

Henry Plotkin
NASA Goddard Space Flight Center
Mail Code 940
Greenbelt, MD 20771

Sherman K. Poultney
Perkin-Elmer Corporation
M/S 965
100 Wooster Heights Road
Danbury, CT 06810

John P. Rahlf
TRW
One Space Park
Redondo Beach, CA 90278

NASA Langley Research Center
Attn: 475/Don M. Robinson
Hampton, VA 23665

NASA Langley Research Center
Attn: 283/Robert S. Rogowski
Hampton, VA 23665

Herman Rothermel
Max Planck Institute für Physik und Astrophysik
8046 Garching bei München, W. GERMANY

Shlomo Rotter
MIT
77 Mass Avenue
Cambridge, MA 02139

NASA Langley Research Center
Attn: 473/Carroll W. Rowland
Hampton, VA 23665

Michael J. Rudd
Bolt, Beranek, and Newman, Inc.
50 Moulton Street
Cambridge, MA 02238

NASA Langley Research Center
Attn: 473/Stephen L. Ruggles
Hampton, VA 23665

NASA Langley Research Center
Attn: 235A/Glen W. Sachse
Hampton, VA 23665

Michael G. Savage
Eaton Corporation
AIL Division
Walt Whitman Road
Melville, NY 11747

NASA Langley Research Center
Attn: 470/Rodolfo Segura
Hampton, VA 23665

James F. Shanley
Honeywell
2 Forbes Road
Lexington, MA 02173

Koji Shinohara
Fujitsu Laboratories, Ltd.
2-38, 1-Chrome,
Gosho-dori, Hyogo-ku,
Kobe, 652, JAPAN

NASA Langley Research Center
Attn: 283/Barry D. Sidney
Hampton, VA 23665

Michael Sirieix
Societe Anonyme de Telecommunications
%ELTEK Corporation
H. Hofheimer
7 Woodland Avenue
Larchmont, NY 10538

David L. Spears
MIT
P. O. Box 73
Lexington, MA 02173

Alexander Stein
Exxon Res. & Eng. Co.
1600 E. Linden Avenue
P. O. Box 45
Linden, NJ 07036

NASA Langley Research Center
Attn: 430/Robert L. Swain
Hampton, VA 23665

J. B. Tammerdahl
Research Triangle Institute
Research Triangle Park, NC 27709

Wayne Tanaka
Naval Weapons Center
Mail Code 3311
China Lake, CA 93555

Peter E. Tannenwald
MIT
P. O. Box 73
Lexington, MA 02173

Malvin C. Teich
Columbia University
Department of Electrical Engineering
1320 Seeley W. Mudd Building
New York, NY 10027

John S. Theon
National Aeronautics & Space Admin.
Mail Code EBT-8
Washington, DC 20546

Richard D. Tooley
Northrop Corporation
Electro Mechanical Division
400 East Orangethorpe Avenue
Anaheim, CA 92801

Charles H. Townes
University of California
Department of Physics
366 Le Conte Hall
Berkeley, CA 94720

George Tucker
New York State Department of Health
Division of Laboratories & Research
Empire State Plaza
Albany, NY 12201

Wilfrid Veldkamp
MIT
Wood Street
Lexington, MA 02173

Robert J. Wayne
United Technologies Research Center
Silver Lane
M/S 85
East Hartford, CT 06108

Joseph S. Wells
National Bureau of Standards
Time and Frequency Division
325 S. Broadway
Boulder, CO 80303

NASA Langley Research Center
Attn: 284A/Burnie S. Williams
Hampton, VA 23665

NASA Langley Research Center
Attn: 284A/Jerry A. Williams
Hampton, VA 23665

NASA Langley Research Center
Attn: 475/David C. Woods
Hampton, VA 23365

Robert M. Young
The Aerospace Corporation
P. O. Box 92957
Los Angeles, CA 90009

Dave Yustein
4202 Minstrell Lane
Fairfax, VA 22030

1. Report No.	2. Government Accession No.	3. Recipient's Catalog No.
NASA CP-2138, Part 2		

4. Title and Subtitle	5. Report Date
HETERODYNE SYSTEMS AND TECHNOLOGY	August 1980
	6. Performing Organization Code
7. Author(s)	8. Performing Organization Report No. L-13849
	10. Work Unit No. 506-61-53-04
9. Performing Organization Name and Address NASA Langley Research Center Hampton, VA 23665	11. Contract or Grant No.
	13. Type of Report and Period Covered Conference Publication
12. Sponsoring Agency Name and Address National Aeronautics and Space Administration Washington, DC 20546	14. Sponsoring Agency Code

15. Supplementary Notes

16. Abstract

This report is a compilation of papers presented at the International Conference on Heterodyne Systems and Technology held March 25-27 at Williamsburg, Virginia. It includes papers that cover various aspects of optical heterodyning including active and passive systems, local oscillators, tunable diode lasers, detectors, and related systems.

17. Key Words (Suggested by Author(s))	18. Distribution Statement
Heterodyne Optical Laser Photomixer	Unclassified - Unlimited Subject Category 36

19. Security Classif. (of this report)	20. Security Classif. (of this page)	21. No. of Pages	22. Price*
Unclassified	Unclassified	327	A15

For sale by the National Technical Information Service, Springfield, Virginia 22161

NASA-Langley, 1980